UNIVERZA V LJUBLJANI
FAKULTETA ZA MATEMATIKO IN FIZIKO

DOKTORSKA DISERTACIJA

Eva Ribežl

2015

UNIVERSITY OF LJUBLJANA
FACULTY OF MATHEMATICS AND PHYSICS
DEPARTMENT OF PHYSICS

Eva Ribežl

SEARCH FOR $X(3872)$ PRODUCTION IN e^+e^- COLLISIONS WITH BELLE

Doctoral thesis

ADVISER: Doc.Dr. Rok Pestotnik
COADVISER: Doc.Dr. Anže Zupanc

Ljubljana, 2015

UNIVERZA V LJUBLJANI
FAKULTETA ZA MATEMATIKO IN FIZIKO
ODDELEK ZA FIZIKO

Eva Ribežl

ISKANJE DELCA $X(3872)$ V TRKIH ELEKTRONOV IN POZITRONOV Z DETEKTORJEM BELLE

Doktorska disertacija

MENTOR: doc. dr. Rok Pestotnik
SOMENTOR: doc. dr. Anže Zupanc

Ljubljana, 2015

IZJAVA O AVTORSTVU

Podpisana Eva Ribežl izjavljam:

- da sem doktorsko disertacijo z naslovom *Iskanje delca $X(3872)$ v trkih elektronov in pozitronov z detektorjem Belle* izdelala kot rezultat lastnega raziskovalnega dela pod mentorstvom doc.dr. Roka Pestotnika in somentorstvom doc.dr. Anžeta Zupanca,
- da je tiskani izvod dela identičen z elektronskim izvodom in
- da Fakulteti za matematiko in fiziko Univerze v Ljubljani dovoljujem objavo elektronske oblike svojega dela na spletnih straneh.

Eva Ribežl

ACKNOWLEDGMENTS

First and foremost, I would like to thank my PhD adviser, doc. dr. Anže Zupanc, for his ever enduring will to help me, whether with introducing me to various analysis techniques, discussing results or correcting my reports and presentations. His dedication to the field of experimental particle physics will always remain the highest standard for whatever path my professional career will take in the future. I am grateful for his support and encouragement especially in the final stages of writing this PhD.

I also thank my second adviser, doc. dr. Rok Pestotnik. His optimistic approach to problem solving helped me overcome times of uncertainty and doubt in various stages of analysis and assured me in the can-do attitude.

Several other people contributed to this work, most notably dr. Marko Petrič, who helped me in the first stages of the MC generation, when the progress seemed utterly slow and the goal far ahead. His help will not be forgotten.

During the years spent working at the Department of experimental particle physics, I had an opportunity to meet many interesting people. Coworkers of the department F9 made a workplace worth going to each morning. For that I especially thank Andreja, Ruben, Tara, and Marko.

One of the nicest experiences in the course of this PhD studies was teaching. Joyful discussions on preparation and results of exams with dr. Tomaž Podobnik and dr. Simon Čopar represent a very special and dear memory to me.

My friends and family supported me on every step of the way, knowing when to encourage me to work more and when to work less.

And last, but far from the least, I thank Teo. A path to obtaining a PhD is not only about the research subject, it is also a great personal journey. I thank Teo for sharing this path with me.

POVZETEK

Izmerili smo inkluzivno razvejitveno razmerje za Br(B $\rightarrow$ $\psi(2S)$ + karkoli) = $(2.817 \pm 0.032(\text{stat.}) \pm 0.104(\text{sist.}))\ 10^{-3}$. Rezultat se ujema s prejšnjimi meritvami.

V meritvi Br($B \rightarrow X(3872)$ + karkoli) $\times$ Br($X(3872) \rightarrow J\psi\pi^+\pi^-$) prvič opazimo inkluzivno produkcijo X(3872) v razpadih mezonov B. Tudi meritev Br($B \rightarrow X(3872)$ + karkoli) $\times$ Br($X(3872) \rightarrow J\psi\pi^+\pi^-$) je prva tovrstna meritev.

$$\text{Br}(B \rightarrow X(3872) + \text{karkoli}) \times \text{Br}(X(3872) \rightarrow J\psi\pi^+\pi^-) = (2.79 \pm 0.37(\text{stat.}) \pm 0.11(\text{sist.})) \times 10^{-5}.$$

Produkt preseka za takojšnjo produkcijo $\psi(2S)$in razvejitvenega razmerja za razpad v $J/\psi\pi^+\pi^-$, $\sigma_{e^+e^-\rightarrow\psi(2S)+\text{ karkoli}} \times \text{Br}(\psi(2S) \rightarrow J/\psi\pi^+\pi^-)$ je bil izmerjen v razdelkih po gibalni količini v težiščnem sistemu trka. Rezultat za takojšnjo produkcijo $\sigma_{e^+e^-\rightarrow\psi(2S)+\text{ karkoli}}$ daje

$$\sigma_{e^+e^-\rightarrow\psi(2S)+karkoli} = (0.694 \pm 0.046 \pm 0.083)\ \text{pb}.$$

Tudi študija takojšnje produkcije X(3872) je bila narejena v razdelkih po gibalni količini v težiščnem sistemu trka, določena je bila zgornja meja za produkcijo $\sigma_{e^+e^-\rightarrow X(3872)+\text{ karkoli}} \times \text{Br}(X(3872) \rightarrow J/\psi\pi^+\pi^-)$, 8.5 10^{-3} pb pri stopnji zanesljivosti 90%.

Ključne besede:
Produkcija hadronov v interakcijah elektronov in pozitronov, kvarkonij, eksotični mezoni, detektor Belle

PACS:
13.66.Bc, 14.40.Pq, 14.40.Rt, 13.66.Bc, 14.20.Pt

ABSTRACT

The inclusive branching fraction for Br(B $\to \psi(2S)$ + anything) was measured to be $(2.817 \pm 0.032(\text{stat.}) \pm 0.104(\text{syst.})) \times 10^{-3}$. Result is in accordance with previous measurements.

The measurement of $\text{Br}(B \to X(3872) + \text{anything}) \times \text{Br}(X(3872) \to J\psi\pi^+\pi^-)$ is the first observation of inclusive production of X(3872) in B decays and also a first measurement of $\text{Br}(B \to X(3872) + \text{anything}) \times \text{Br}(X(3872) \to J\psi\pi^+\pi^-)$.

$$\text{Br}(B \to X(3872) + \text{anything}) \times \text{Br}(X(3872) \to J\psi\pi^+\pi^-) = (2.79 \pm 0.37(\text{stat.}) \pm 0.11(\text{syst.})) \times 10^{-5}.$$

The $\sigma_{e^+e^- \to \psi(2S)+ \text{ anything}} \times \text{Br}(\psi(2S) \to J/\psi\pi^+\pi^-)$ was measured in bins of momentum in the CMS frame of the collision and the cross section for the prompt production was determined to be

$$\sigma_{e^+e^- \to \psi(2S)+anything} = (0.694 \pm 0.046 \pm 0.083) \text{ pb}.$$

The prompt production of X(3872) was studied in the bins of momentum in the CMS frame of the collision and the upper limit for the prompt production of X, $\sigma_{e^+e^- \to X(3872)+ \text{ anything}} \times \text{Br}(X(3872) \to J/\psi\pi^+\pi^-)$ was determined at 8.5×10^{-3} pb at 90% confidence level.

Keywords:

Hadron production in e^+e^- interactions, heavy quarkonia, exotic mesons, the Belle detector

PACS:
13.66.Bc, 14.40.Pq, 14.40.Rt, 13.66.Bc, 14.20.Pt

CONTENTS

LIST OF FIGURES

LIST OF TABLES

1

THE X(3872)

The story of the X(3872) started in 2003 when the Belle Collaboration observed an unexpected peak in the invariant mass distribution of $J/\psi\pi^+\pi^-$ while studying exclusive decays of $B^\pm \to K^\pm\pi^+\pi^- J/\psi$ [1]. The discovery sparked immediate attention amongst the high energy physics community and its confirmations by other experiments followed within months. The BaBar found the X(3872) in decays of B mesons [2], while CDF II and D0 collaborations found theX(3872) in $p\overline{p}$ production [3, 4]. Up to date, the article [1] is the most cited paper of the Belle Collaboration, topping over 1000 citation in 12 years (INSPIRE database [5]). The curious nature of X(3872) has proved a problem of great interest for both the theorist and experimentalists alike. Even after more than a decade of research, some fundamental issues (e.g., exact quark composition, branching ratios of interesting decay modes, presence of prompt production, etc.) have not been resolved and the research of X(3872) remains one of the most exciting fields in hadron spectroscopy.
The following text is divided into two main parts. In the first part, some necessary theoretical introduction is given; a very brief introduction to hadrons is followed by the description of charmonium where quantum numbers J^{PC} are introduced, the spectrum of charmonium is discussed and an overview of charmonium production is given. The second part summarizes of the experimental efforts in the research of the nature of the X(3872). Several models for the composition of the X(3872) are given and some of the most used experimental techniques are explained. Finally, experimental results for the single and double charmonium production are discussed.

1.1 THEORETICAL INTRODUCTION

1.1.1 *Extremely short introduction to hadrons*

Hadron spectroscopy emerged as a new field in the 1930s when the neutron was discovered [6]. The quest of the nuclear physics - to understand how nucleons are bound inside atomic nucleus - has been slowly replaced with the research of the strong interactions. Already in 1935, the existence of the pion was suggested by Yukawa [7], who introduced the concept of the meson as a carrier of the strong force, not as a strongly interacting composite object. The first mesons discovered

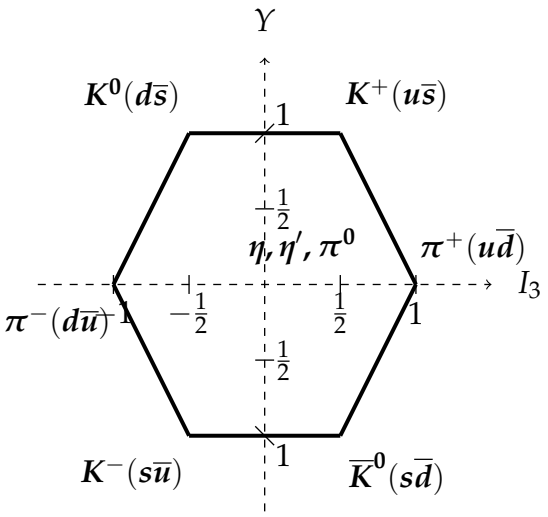

Figure 1: Example of the CQM for the combination of quarks u, d, and s. Here, the pseudoscalar nonet is portrayed. Pseudoscalar mesons have the J^P assignment of 1^- (see Subsec. 1.1.3 for explanation). On the x-axis, the third component of isospin (I_3) is plotted, on the y-axis, the values of the hypercharge (Y) is given. The Y and I_3 are connected to the (electromagnetic) charge via relation $Q = Y + \frac{I_3}{2}$.

were in fact the pions [8]. In the following years, number of other hadrons were discovered (e.g., kaons, Δ, etc.).

Witnessing an abundance of strongly interacting particles, Zweig [9] and Gell-Mann [10] in the 1960s independently suggested that all observed strongly interacting particles are in fact composite particles, built of *quarks*. The hadrons (composite objects of two or three constituent quarks) are classified today into multiplets according to the constituent quark model (CQM) where mesons are bound states of a quark and an anti-quark and baryons bound states of three quarks. At the time, three flavors of quarks were introduced, u, d, and s, all being fermions with a spin 1/2 and a non-integer charge. The model was very successful both in accounting for the already observed particles as well as in predicting some new. An example of a model of states, comprised of quarks u, d, and s is shown on Fig. 1.

After 50 years, the quark model now encompasses 6 quarks: up (u), down (d), strange (s), charm (c), bottom (b) and top (t). They belong to three families, separated by the mass of the quarks. No free quark has ever been observed so the masses of the quarks, given in Table 1 are results of various calculations in the framework of quantum chromodynamics. QCD is a field theory, used to describe interactions between quarks and gluons, the mediators of the strong force. The QCD analogue of the electric charge is the color, described in more detail in Subsec. 1.1.4. The Langrangian, describing strong interaction, is given in the Eq. 1 where ψ is the quark field, G are the gluon field tensors and γ are the Dirac matrices.

$$\mathcal{L}_{qcd} = \overline{\psi_i}\left(i\left(\gamma^\mu D_\mu\right)_{ij} - m\delta_{ij}\right)\psi_j - \frac{1}{4}G_a^{\mu\nu}G^a_{\mu\nu}. \tag{1}$$

quark	mass	charge [in e_0 units]
u	$2.3^{+0.7}_{-0.5}$ MeV	2/3
d	$4.8^{+0.5}_{-0.3}$ MeV	-1/3
c	1.275 ± 0.025 GeV	2/3
s	95 ± 5 MeV	-1/3
t	$173.21 \pm 0.51 \pm 0.71$ GeV	2/3
b	4.18 ± 0.03 GeV	-1/3

Table 1: Charge and mass of quarks. The $u-$, $d-$, and $s-$quarks masses are *current-quark masses*, while $c-$ and $b-$ quark masses are *running* masses. Only the top quark mass is measured directly [11].

The perturbation approaches to predicting masses, transitions, decays, etc. for the hadron states proved imprecise at best at the scales corresponding to the binding between quarks in the hadrons. The reason for this non-perturbative nature of the QCD is in the coupling constant of the interaction which increases at lower energies (i.e., at the long distance). Hence at the typical energy transfers involved in the hadron transitions one has to rely on models. Alternatively, the lattice QCD (LQCD) is hoped to give more exact predictions once the computing power catches pace with demands of the LQCD approaches. Numerically extremely difficult, the LQCD relies on the sets of calculations, done on a discrete sets of points, which demand the use of supercomputers.

1.1.2 *Conventional charmonium*

The quarkonium is a meson, comprised of a quark and an antiquark of the same flavor. Most studied quarkonia include J/ψ (an example of charmonium, bound state of c and $\bar{c}$) and $\Upsilon(nS)$ resonances (bound states of b and $\bar{b}$). The toponium does not exist because the top quark decays weakly before it is able to form a bound state. Usually, the term quarkonium is used just for the bound states of $c\bar{c}$ and $b\bar{b}$ and not for the lighter states.
The existence of the *charm* quark has been predicted by Glashow, Iliopoulos and Maiani in 1970 [12] and the first $c\bar{c}$ state, J/ψ, has been discovered independently by two groups in November 1974[1]. At Stanford, group of B. Richter collided positrons and electrons and named the discovered particle ψ [13]; at the same time, group led by S. Ting at Brookenhaven used protons colliding with a berillium target and named the discovered particle J [14].
From a theorist point of view, charmonium is interesting because of the large mass of the quarks that contributes to their small relative velocity, making such systems an appropriate playground for the non-perturbative and the perturbative

1 A period, later nicknamed *the November revolution.*

QCD approaches alike. Experimentally, the states in the spectrum of charmonium are well separated in contrast to the spectrum of the bound states of the lighter quarks (u, d, and s), where the physical states actually seen in the experiments are quantum mechanical mixtures of the light quark states.

1.1.3 *Charmonium spectroscopy*

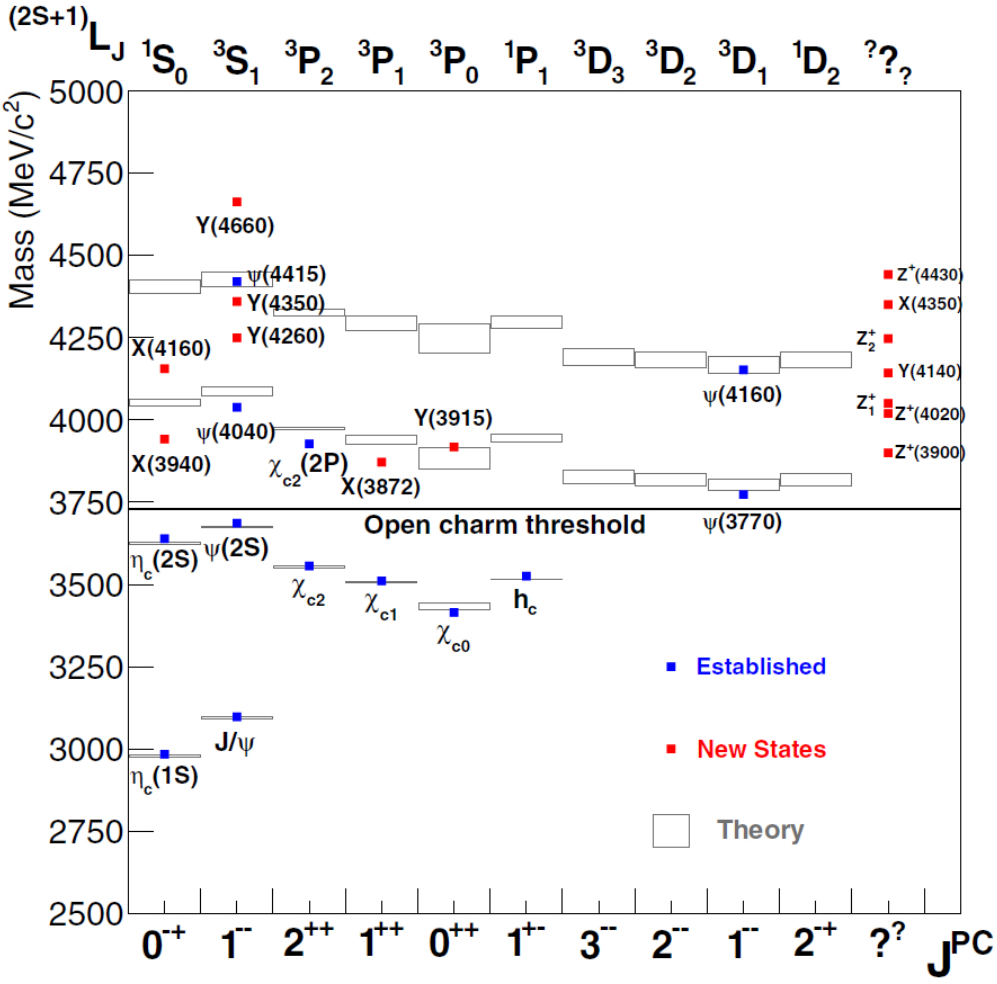

Figure 2: Energy levels of charmonium; 'Established' marks the states that have been theoretically predicted and with measured properties matching the predicted ones. 'New states' marks a plethora of exotic states (either in J^{PC} or in some other properties) that were found experimentally but still lack sufficient theoretical explanation. Recent theoretical predictions (mostly lattice) are marked with 'Theory'. The open charm threshold is also drawn [15].

The quarkonium levels are conventionally described with the spectroscopic notation $n^{2s+1}L_J$. Here, n stands for the radial quantum number, s for the spin of quarks ($s = 0, 1$) and l for the orbital angular momentum between quarks (labelled with S ($l = 0$), P ($l = 1$), D ($l = 2$), etc.). The decays of the quarkonium are governed by quantum numbers, the conservation of parity and the charge

conjugation. Because only the spin of the quarkonium can be measured, quantum numbers J^{PC} are also used to describe the spectrum. Here, J is the quarkonium spin ($|l - s| \leqslant J \leqslant l + s$).
The parity (P) is a flip of sign of spatial coordinates, a point reflection. For constituent quarks, the spatial eigenfunctions are spherical harmonics (Y_l^m), which under parity behave as $P = (-1)^l$. The corresponding antifermion (i.e. antiquark) has the opposite parity. For quarkonium, the operation of the space reflection (the parity operator) thus yields

$$P = (-1)^{l+1}. \tag{2}$$

The charge conjugation (C) effectively exchanges the two constituents (fermion by its antifermion); but because having two fermions, the charge conjugation also affects the spin part of the wave function. Applying the charge conjugation to a bound state of two fermions, one can derive the relation between C, spin and angular momentum:

$$\begin{aligned} C|f\overline{f}\rangle = (-1)^l(-1)^{s+1}(-1)|f\overline{f}\rangle = (-1)^{l+s}|f\overline{f}\rangle\,; \\ C = (-1)^{l+s}. \end{aligned} \tag{3}$$

Fig. 2 summarizes our current knowledge of the spectrum of charmonium. Some of the very basic properties of the spectrum can be derived via the Schrödinger equation using the potential between the quarks. One of the models, the Cornell potential, describes the two asymptotic behaviors: at short distances, the ultraviolet, i.e. Coulomb-like term, and the infrared, the linear increase of confining potential at large distances:

$$V(r) = kr - \frac{4}{3}\frac{\alpha_S}{r}. \tag{4}$$

It can be observed that the splitting between the states (f.e., the hyperfine splitting between the 0^{-+} and 1^{--} states) is much smaller than the mass of the very states. This a enables non-relativistic approach for treating the quarkonia. One important feature of the plot is the existence of the open charm threshold. The open charm states result from the breakup of the charmonium into a pair of mesons via strong decay, one containing the charm quark plus a light antiquark and the other containing the anticharm quark plus a light quark. For example, the D meson family contains a charm quark plus one of the light antiquarks (i.e., up, down, or strange). States above the threshold are therefore significantly wider than the states below.

Fig. 3 shows charmonium transitions and decays. Widths of the states below the open charm threshold are significantly narrower than the states above (e.g., $\psi(2S)$ has decay width $\approx$ 300 keV/c^2; $\psi(3770)$, state just above the threshold, $\approx$ 30 MeV/c^2). Width of the former can be explained by the OZI rule which was

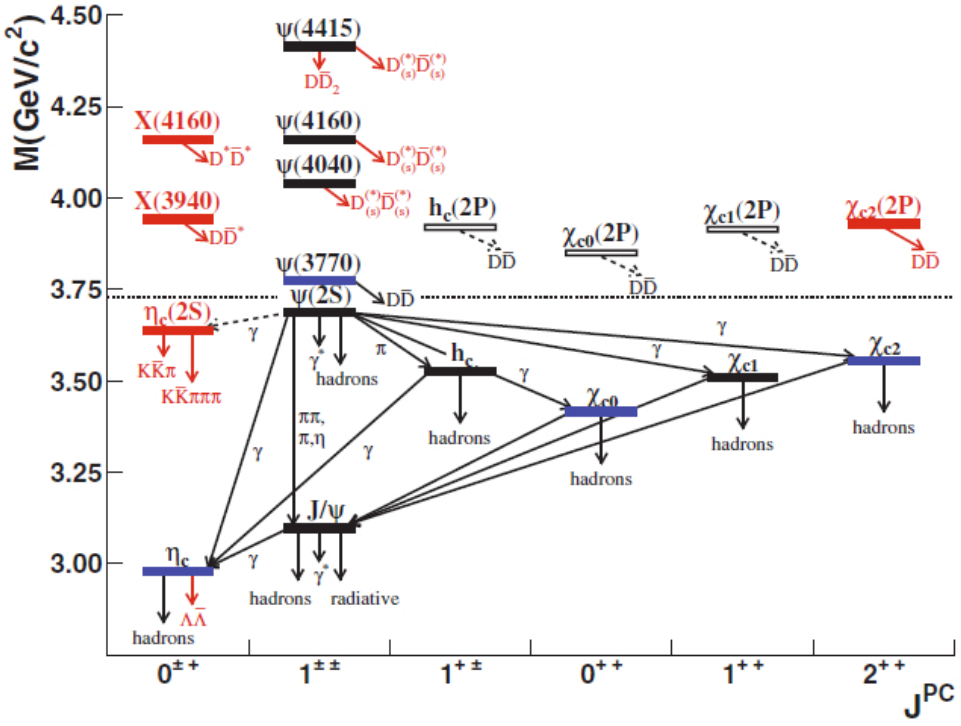

Figure 3: The charmonium spectrum and the scheme of charmonium transitions and decays. The red bands correspond to the newly observed states at the *B*-factories, the blue bands show states where the *B*-factories have made a substantial contribution to the accurate measurement of parameters, while the white bands represent the yet unobserved states. The arrows show charmonium transitions and decays: the decay modes newly observed at the *B*-factories are shown in red [15].

independently proposed by Okubo, Zweig and Iizuka in the 1960s [16, 17, 18]. When represented graphically (see Fig. 4), it states that any strongly occurring process will be suppressed if its Feynman diagram can be split in two by cutting only the internal gluon lines. In terms of the QCD, the OZI rule is a consequence of a decrease of the coupling constant with increasing energy (or momentum transfer). The gluons in OZI suppressed channels have a high q^2 and the coupling constant will appear small to such gluons. In the case of the charmonium, the quarks in the states above the D meson threshold do not need to annihilate, but can be propagated to the final state. Only two gluons are required, their total energy being the energy of quark-antiquark pair, which is created in order to get two D mesons. In the states lower than the open charm threshold, the original quark states cannot propagate to the final state. The quark line is cut, the decay has to proceed with virtual gluons mediating the interaction, each of which having enough energy to produce a quark-antiquark pair. Thus the former case is much lower in energy of two gluons than the one with three gluons of the latter, OZI-suppressed annihilation. The suppression arises from both the smaller values of the QCD coupling constant at high energies and the greater number of interaction vertices.

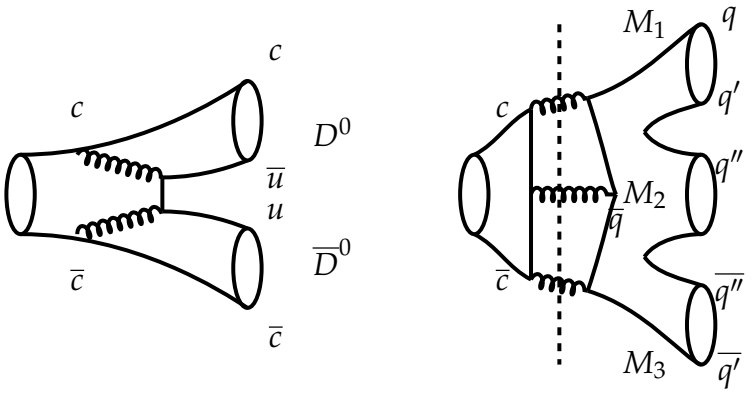

Figure 4: The OZI rule. The dashed line on the right sketch shows the cutting of the gluon lines and thus dividing the diagram in two parts, resulting in suppression. On the left sketch, simply cutting the internal gluon lines does not separate the diagram in two distinct parts.

1.1.4 *SU(3) color group*

Already in the early years of the quark model, physicists have been puzzled by the existence of the Δ^{++} baryon. It carries a spin of $3/2$, which means it requires three (up) quarks with parallel spins and a vanishing orbital angular momentum. The Pauli exclusion principle tells us that the wave function of a baryon has to be antisymmetric under exchange of any two quarks. This is clearly not possible in the case of the Δ^{++}; an additional (hidden) quantum number had to be introduced, later called the color charge. Today, our knowledge about interactions between quarks mediated by gluons is described by quantum chromodynamics. Both quarks and gluons are assigned a color charge.
The color charge can be adequately described in terms of the SU(3) group, which is a special unitary group, a group of 3×3 matrices with a determinant 1. There are 8 generators of the group, traceless 3×3 matrices. Usually, the Gell-Mann matrices are used, which are analogues of the Pauli matrices for $n = 3$. Of those, only λ_3 and λ_8 are diagonal (see Eq. 5).

$$\lambda_1 = \begin{bmatrix} 0 & 1 & 0 \\ 1 & 0 & 0 \\ 0 & 0 & 0 \end{bmatrix} \qquad \lambda_2 = \begin{bmatrix} 0 & -i & 0 \\ i & 0 & 0 \\ 0 & 0 & 0 \end{bmatrix}$$

$$\lambda_3 = \begin{bmatrix} 1 & 0 & 0 \\ 0 & -1 & 0 \\ 0 & 0 & 0 \end{bmatrix} \qquad \lambda_4 = \begin{bmatrix} 0 & 0 & 1 \\ 0 & 0 & 0 \\ 1 & 0 & 0 \end{bmatrix}$$

$$\lambda_5 = \begin{bmatrix} 0 & 0 & -i \\ 0 & 0 & 0 \\ i & 0 & 0 \end{bmatrix} \qquad \lambda_6 = \begin{bmatrix} 0 & 0 & 0 \\ 0 & 0 & 1 \\ 0 & 1 & 0 \end{bmatrix}$$

$$\lambda_7 = \begin{bmatrix} 0 & 0 & 0 \\ 0 & 0 & -i \\ 0 & i & 0 \end{bmatrix} \qquad \lambda_8 = \frac{1}{\sqrt{3}} \begin{bmatrix} 1 & 0 & 0 \\ 0 & 1 & 0 \\ 0 & 0 & -2 \end{bmatrix} \tag{5}$$

The eigenstates represent the color charge itself. Here, R stands for red, G for green and B for blue:

$$|R\rangle = \begin{bmatrix} 1 \\ 0 \\ 0 \end{bmatrix}, \quad |G\rangle = \begin{bmatrix} 0 \\ 1 \\ 0 \end{bmatrix}, \quad |B\rangle = \begin{bmatrix} 0 \\ 0 \\ 1 \end{bmatrix}.$$

Raising and lowering operators are defined to rotate the color states:

$$\begin{aligned} \frac{1}{2}(\lambda_1 + i\lambda_2)|G\rangle &= |R\rangle, \\ \frac{1}{2}(\lambda_4 + i\lambda_5)|B\rangle &= |R\rangle, \\ \frac{1}{2}(\lambda_6 + i\lambda_7)|B\rangle &= |G\rangle. \end{aligned} \tag{6}$$

Strong interaction is invariant to rotations in the color space where rotations describe changes of type $|R\rangle \leftrightarrow |G\rangle$, $|R\rangle \leftrightarrow |B\rangle$ and $|G\rangle \rightarrow |B\rangle$. Conservation of the color charge (see Fig. 5) is the consequence of the SU(3) symmetry as shown by the Noether theorem.

The gluons, mediators of the strong interaction, are massless particles with a spin 1. The SU(3) structure,

$$3 \otimes 3 = 8 \oplus 1, \tag{7}$$

shows that gluons can exist either as a color octet or as a singlet state. The former can be symbolically written as $G\overline{B}$, $R\overline{B}$, $G\overline{R}$, $R\overline{G}$, $B\overline{R}$, $B\overline{G}$, $\frac{1}{\sqrt{6}}\left(R\overline{R} + G\overline{G} - 2B\overline{B}\right)$, $\frac{1}{\sqrt{2}}\left(R\overline{R} - G\overline{G}\right)$, while the latter is $\frac{1}{\sqrt{3}}(R\overline{R} + G\overline{G} + B\overline{B})$. Gluon in a singlet state is a case of a particular interest; being in a singlet state also means to be invariant to the rotations in the color space, therefore being unable to carry the force. Physical gluons are therefore the representatives of the octet.

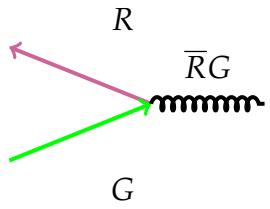

Figure 5: Conservation of color charge.

The hadrons, however, have to be colorless. The color singlet can be understood as a color part of the wave-function of the quark and anti-quark. Particles of type $q\overline{q}$ (mesons) are colorless and observed in nature, the color part of the wave function is $\Psi_c^{q\overline{q}} = \frac{1}{2}(r\overline{r} + g\overline{g} + b\overline{b})$. Similar can be said for the states of $qq\overline{q}$ (baryons); color part of wave function also reads $\Psi = \frac{1}{\sqrt{6}}(rgb - rbg + gbr - grb + brg - bgr)$. Since the color singlet state has an antisymmetric wave function, this satisfies the Pauli exclusion principle in the case of the Δ^{++} baryon. Even more exotic combination

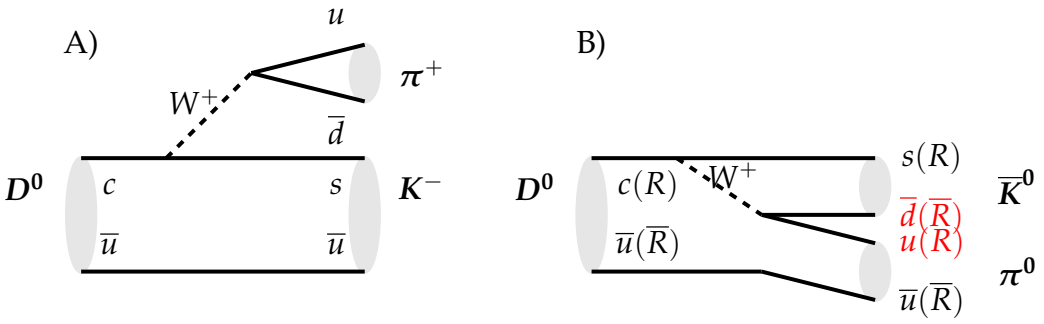

Figure 6: An example of a color suppressed decay. Feynmann diagrams for decays $D^0 \to \pi^+ K^-$ and $D^0 \to \pi^0 K^0$. In case A, color of the quarks from D^0 at the start transfers to the quarks in K^-. The quarks in resulting π^+ can be any of the combinations $R\overline{R}$, $G\overline{G}$ or $B\overline{B}$. This is not the case in example B, a color suppressed decay. Colors of the quarks coming from the weak boson W^+ have to be exactly anti-colors to quarks of the starting D^0 meson.

of quarks and mesons are allowed, as long as the demand for colorlessness is fulfilled. Combinations as $q\bar{q}q\bar{q}$, $qqqq\bar{q}$, gg and $gggg$ are possible from the point of view of neutral color charge. The X(3872) is an example of such a state - although its nature is still under debate, it has to be in the color singlet state, regardless of the quark composition.

A direct consequence of colorlessness is a smaller probability of certain decays, e.g. color-suppressed decays. Comparing similar decays, $D^0 \to \pi^0 K^0$ and $D^0 \to \pi^+ K^-$; in both cases, the D^0 decays weakly via a charged weak meson W^+ and same elements of the CKM matrix contribute to the decay matrix. However, the color has to be conserved along the quark line, therefore the amplitude for the former decay is expected to be three times smaller than the amplitude for the latter (Eq. 8). In the case of $D^0 \to \pi^+ K^-$, any colorless combination suffices ($R\overline{R}$, $G\overline{G}$, $B\overline{B}$). In the case of $D^0 \to \pi^0 K^0$, only one color can be used - the one that has been set with the initial state of the D^0 (see Fig. 6).

$$\frac{\mathrm{Br}(D^0 \to \pi^0 K^0)}{\mathrm{Br}(D^0 \to \pi^+ K^-)} \sim \frac{1}{9} \tag{8}$$

The color content should be carefully analyzed also when studying the prompt production of the charmonia, as explained in the following paragraphs.

1.1.5 *The prompt production of charmonium in e^+e^- annihilation*

The term prompt production of charmonium usually refers to the charmonium that do not originate from the decays of B mesons. The prompt production of charmonium can be divided into four separate processes shown on Fig. 7. Two different types are the production of a single $c\bar{c}$ state and the production of either a bound $c\bar{c}$ state or open charm mesons alongside the first charmonium.

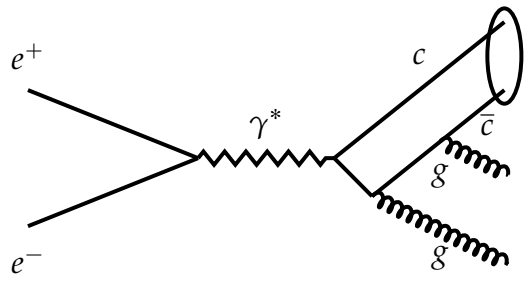

(a) The color singlet production, formation of the bound state $c\overline{c}$ in the singlet state.

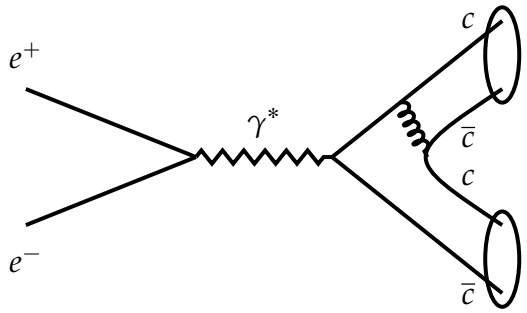

(b) An example of the double charmonium production with 2 resulting bound $c\overline{c}$ states.

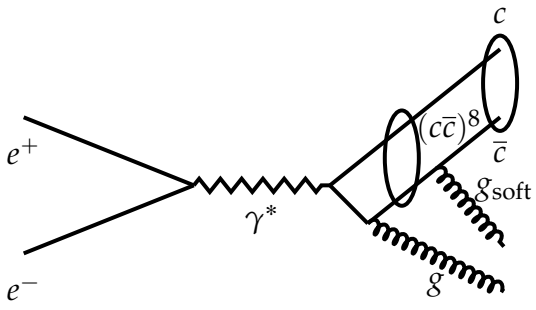

(c) The color octet production, formation of the bound state $c\overline{c}$ in the octet state, radiation of a soft gluon and transfer of a meson to the color singlet state.

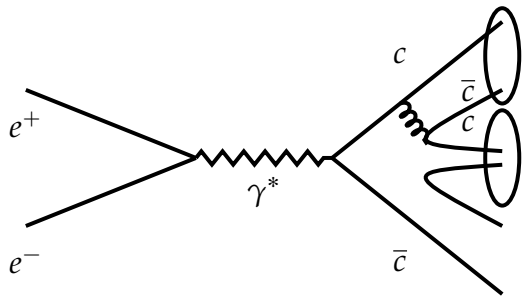

(d) An example of the double charmonium production with 1 bound $c\overline{c}$ state and 2 D mesons in the final state.

Figure 7: Examples of production mechanisms for the prompt charmonium production.

1.1.5.1 *The production of a single charmonium*

The bound states of a heavy-quark(Q) and a heavy-antiquark ($\overline{Q}$) are characterized by the velocity v of the Q or $\overline{Q}$ in the $Q\overline{Q}$ rest frame; a system is said to be nonrelativistic if $v \ll 1$. Typical values are $v^2 \sim 0.1$ for the $b\overline{b}$ and ~ 0.3 for the $c\overline{c}$ systems. Further on, a hierarchy of energy scales exists: the mass m of the heavy quark *(hard scale)*, the typical relative momentum $p \sim mv$ (in the meson rest frame, *soft scale*), and the typical binding (or kinetic) energy $E \sim mv^2$ *(ultra soft scale)*. Quarkonium annihilation and production take place at the scale m, quarkonium binding takes place at the scale mv, which is the typical momentum exchanged inside the bound state, while the very low-energy gluons and the light quarks live long enough that a bound state has time to form and, therefore, are sensitive to the scale mv^2. Existence of various scales calls for an effective field theory, in the case of quarkonium annihilation and production, this is the nonrelativistic QCD (NRQCD).

FACTORIZATION APPROACH The relevant scale for the direct quarkonium production is also the hard scale m, therefore this process can be described by a local interaction in the NRQCD. The aim of the approach is to calculate the

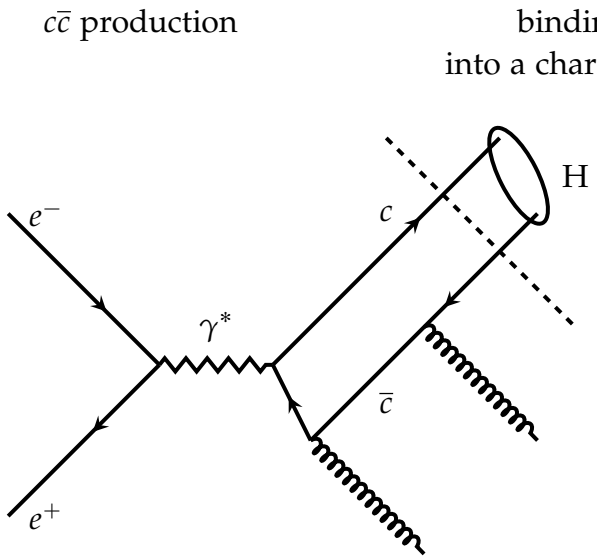

Figure 8: A schematical approach to factorization.

inclusive cross section for the production of a bound state of $c\bar{c}$, called H at the large momentum in the center-of-mass frame. The *factorization* procedure [19] proves to be the effective approach. The two processes are treated separately - first, the production process at the partonic level is described, afterwards the quark pair hadronization is taken into account.
More generally, the H can be written as a sum of products of the NRQCD matrix elements and the short-distance coefficients:

$$\sigma[H] = \sum_n \sigma_n \left(\kappa_n^{4\ \text{fermions}} \right). \tag{9}$$

In Eq. 9, σ_n are the short-distance coefficients, process-dependent partonic cross sections for production of a $Q\overline{Q}$ pair. The matrix elements $\kappa_n^{4\ \text{fermions}}$ are the vacuum-expectation values of objects similar to the four-fermion operators in the decay, containing both the color singlet and the color octet contributions (see [15]). There are no limitations to the created $Q\overline{Q}$ state; colorwise, it can be either in a singlet or an octet state; spinwise, either a singlet or a triplet state are allowed.
The NRQCD approach has been proven only at next-to-next-to-leading order in α_S. Several other methods have proven to be competitive to the approach.
One of the most commonly used methods is the *color singlet model*, which can be related to Eq. 9 by keeping only the color singlet contributions at the leading order in v. The process $e^+e^- \rightarrow c\bar{c}gg$ is an example of a color singlet process (see Fig. 8). Two hard gluons are emitted alongside the bound state of $c\bar{c}$, pushing the mass of $c\bar{c}$ into the charmonium region. Radiation of two gluons is suppressed by the factor of α_S^2. The produced $c\bar{c}$ can be projected directly into a physical state (e.g.,J/ψ).
Considering the case of an S-wave bound state H, where $c\bar{c}$ state with relative

momentum p is denoted as $|c\bar{c}\,(p)\rangle$, the production amplitude $\mathcal{A}$ where T is a general transfer matrix is written as:

$$\begin{aligned}\mathcal{A} &= \\ &= \langle Hgg|T|e^+e^-\rangle \\ &= \sum_p \langle H|c\bar{c}\,(p)\rangle\langle c\bar{c}\,(p)\,gg|T|e^+e^-\rangle \\ &= \int d^3p\psi\,(p)\,A\left(e^+e^- \to c\bar{c}\,(p)\,gg\right). \end{aligned} \tag{10}$$

In the non-relativistic limit, $A\left(e^+e^- \to c\bar{c}\,(p)\,gg\right)$ does not depend on the momentum. Only the wave function has to be considered for the integration:

$$\mathcal{A} = A\left(e^+e^- \to c\bar{c}gg\right) \times \int d^3p\psi\,(p) = A\left(e^+e^- \to c\bar{c}gg\right) \times \psi\,(0)\,, \tag{11}$$

$$\sigma\left(e^+e^- \to c\bar{c}gg\right) = \sum_{\text{phase space}} |A\left(e^+e^- \to c\bar{c}gg\right)|^2 \times |\psi(0)|^2. \tag{12}$$

In Eq. 12, the first term of the result describes the short distance part while the second part describes the long distance part. Few additional remarks are necessary: first, only the $c\bar{c}$ pairs in the color singlet state with the same quantum numbers as the bound state H $\left(c\bar{c}\left[^{2S+1}S_J\right]^{[1]} \to H\left(^{2S+1}S_J\right)\right)$ were considered. Secondly, in the computation of $A\left(e^+e^- \to c\bar{c}gg\right)$ the relative momentum p has been neglected.

Evidently, the color singlet model suffers from a few inconsistencies and the color-octet production has to be allowed as well (see Fig. 7, part C). Without a strict mathematical proof, the idea behind the color octet production is as follows [20]: the infrared divergence arises when a gluon in the decay becomes soft. However, the infrared divergence cannot appear if the gluon is attached to a line that is off-shell by an amount of order m_c. The effect is factorized into the long distance part. Effectively, this means that a bound state is first produced as a color-octet state and is transformed into a final color-singlet state via soft gluon emission.

A comparison has been made between the predictions of different models and the CDF results (as shown on Fig. 9). Although applied to the results in the $p\bar{p}$ production, the contribution on the color-octet model is significant and should be taken into account when studying the prompt charmonium production.

The Belle collaboration has measured the total cross section for the process $e^+e^- \to J/\psi + \mathrm{X}(\mathrm{non} - c\bar{c})$ [21]: $0.43 \pm 0.09 \pm 0.09$ pb. The theoretical predictions using the NRQCD factorization [22],[23] give

$$\sigma(e^+e^- \to J/\psi + \mathrm{X}(\mathrm{non} - c\bar{c})) = 0.99 \pm 0.35 \text{ pb}.$$

The NRQCD might not describe the $p_T < 3$ GeV region well; since most of the Belle data comes from that region, this could be the source of the slight discrepancy between theory and experiment.

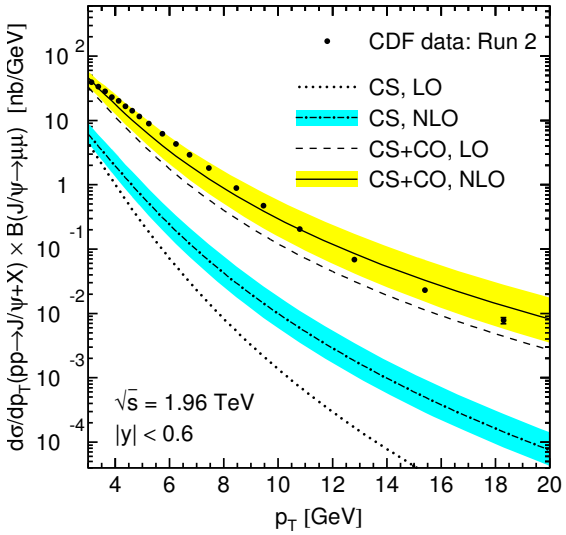

Figure 9: Comparison of the next-to-leading order fits to the CDF data [24]. The global fit to the CDF data is from Butenschon and Kniehl [22]. *CS* stands for the color-singlet contribution and *CO* for the color-octet contribution.

1.1.5.2 *The double charmonium production*

The color singlet model should also be accurate in describing the e^+e^- annihilation to exactly two charmonia [25]. The main idea is to use the electromagnetic annihilation decay rate of either H or another state related to H by spin symmetry for determination of the NRQCD matrix element. The cross section for double charmonium production can therefore be predicted up to corrections suppressed by powers of v^2 without any unknown phenomenological factors. However, the cross section for the double charmonium production is very small at energies where perturbative QCD has sufficient predictive power.
Naïvely, the cross section for $J/\psi + \eta_C$ can be defined in units of the cross section for $\mu^+\mu^-$ as

$$R\left[J/\psi + \eta_C\right] \sim \alpha_S^2 \left(\frac{m_C v}{E_{\text{beam}}}\right)^6. \tag{13}$$

Considering calculation with E_{beam} of the Belle experiment: $E_{\text{beam}} = 10.6$ GeV, $v^2 \sim 0.3$, $\alpha_S = 0.2$ and $m_c = 1.4$ GeV. The estimate shows that the expected ratio is $R\left[J/\psi + \eta_C\right] = 4 \times 10^{-7}$. More detailed calculations are gathered in Table 2.

H_2/H_1	J/ψ	$\psi(2S)$	$h_C(1P)$	$\psi_1(1D)$	$\psi_2(1D)$
η_c	3.78 ± 1.26	1.57 ± 0.52	0.308 ± 0.017	0.106 ± 0.025	1.04 ± 0.23
$\eta_c(2S)$	1.57 ± 0.52	0.65 ± 0.22	0.128 ± 0.007	0.044 ± 0.01	0.43 ± 0.09
$\chi_{c0}(1P)$	2.40 ± 1.02	1.00 ± 0.42	0.053 ± 0.019		
$\chi_{c1}(1P)$	0.38 ± 0.12	0.16 ± 0.05	0.258 ± 0.064		
$\chi_{c2}(1P)$	0.69 ± 0.13	0.29 ± 0.06	0.017 ± 0.002		
$\eta_{c2}(1D)$	0.35 ± 0.05	0.14 ± 0.02			

Table 2: A cross section in fb for e^+e^- annihilation into double-charmonium states $H_1 + H_2$ without relativistic corrections. The errors are only those from variations in the NLO pole mass 1.4 ± 0.2 GeV [25]. Note that the predictions are significantly lower than the actually measured cross sections. For instance, the sum of the cross section in the first column is much lower than the measured cross section for $e^+e^- \to J/\psi c\bar{c}$ ($\sigma = 0.74 \pm 0.08$ pb) [21].

1.2 EXPERIMENTAL RESULTS

1.2.1 *The X(3872) in a nutshell*

The X(3872) was the first exotic charmonium-like state discovered. In November 2003, Belle published a paper [1] in which a clear peak is seen in the mass difference $m_{\pi^+\pi^-l^+l^-} - m_{l^+l^-}$ distribution while studying exclusive decays of $B^\pm \to K^\pm\pi^+\pi^- J/\psi$ (see Fig. 11). The variables ΔE and M_{bc} (see Fig. 12) show that the newly discovered particle originates from the decay of B mesons. The decay process in [1] can be naively described with a spectator type Feynman diagram, as seen on Fig. 10, where the bound $c\bar{c}$ state is $\psi(2S)$. The name, X(3872), originates from the mass of the newly discovered particle, ≈ 3.872 GeV. In the following years, several precise measurements of the mass were performed, mainly to establish a relation to the open charm threshold. Fig. 13 sums up the measurements of mass, all in the channels with a J/ψ. The mass measurements in the channels where X(3872) decays to D mesons sparked some controversy, which is discussed in Subsec. 1.3.1. The current PDG value [11] gives 3871.69 ± 0.17 MeV for the mass of X(3872).

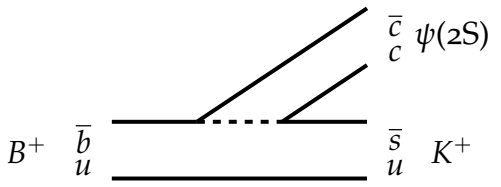

Figure 10: The spectator model for the decay.

The discovered particle, X(3872), was first speculated to be a bound $c\bar{c}$ state because of the similarity of the decay with the decay of the $\psi(2S)$. However, there was no obvious candidate in the spectrum of charmonia, as shown in Fig. 2. The exotic nature of the state has also been hinted by the narrowness of the state

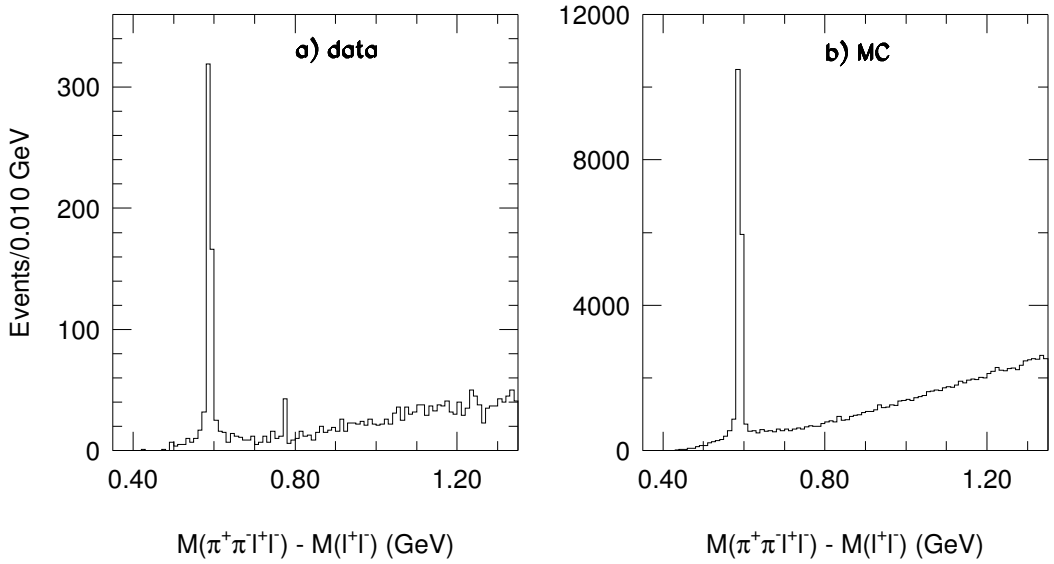

Figure 11: Distribution of mass difference, $m_{\pi^+\pi^- l^+ l^-} - m_{l^+ l^-}$. Left data, right MC simulation. On the left plot, the left peak belongs to (expected) $\psi(2S)$, the right peak has not been accounted for before (as also seen from the MC simulation) [1].

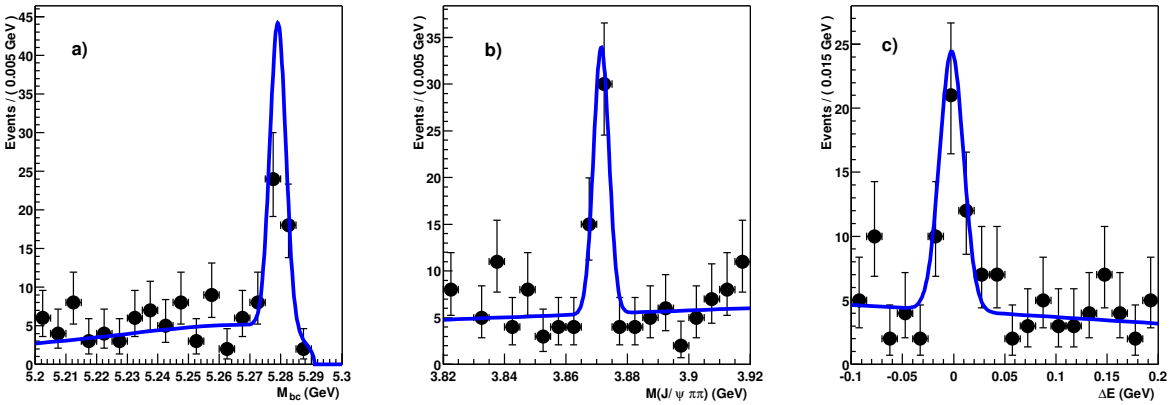

Figure 12: Distribution of beam constrained mass, mass of combination $J/\psi\pi\pi$, and ΔE for the newly discovered state X(3872)[1]. ΔE is defined as $\sum_i \sqrt{p_i^2 + m_i^2} - E_{\text{beam}}$, while beam constrained mass is defined as $M_{bc} = \sqrt{E_{\text{beam}}^2 - |p_B|^2}$ where p_i and p_B are momenta of particles in the CMS.

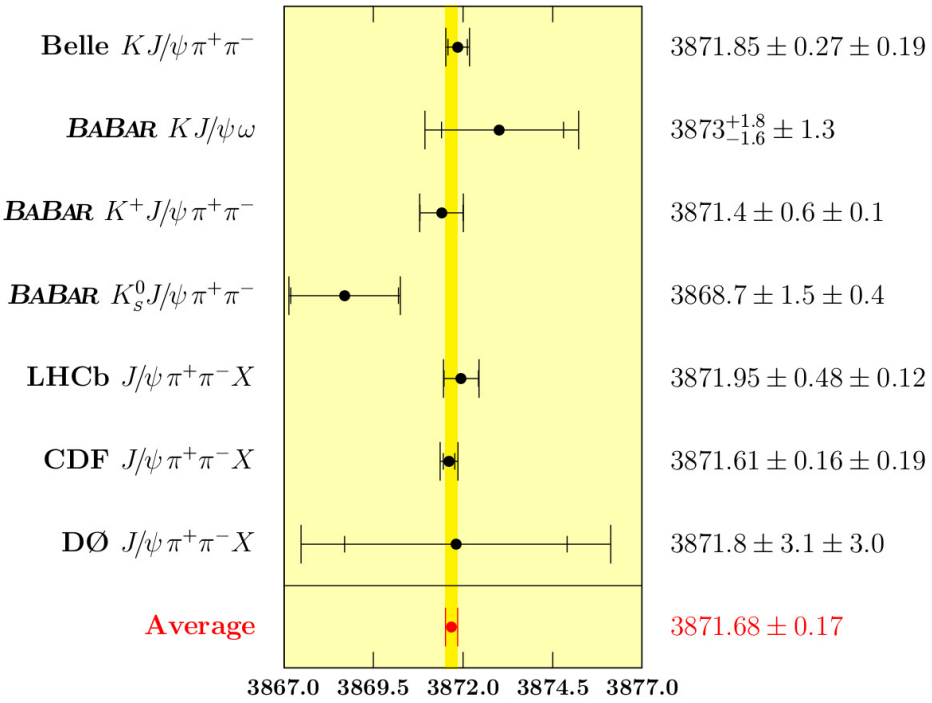

Figure 13: Collected results of measurement of mass. The decay channel is given, along with the experiment, which performed the measurement [15]. The first error is statistical, the second systematic.

($\Gamma_{X(3872)} < 2.3$ MeV/c^2 [1]), despite being slightly above the open charm threshold. From early on, four hypotheses about the X(3872)'s nature have been formed:

- *yet unidentified $c\bar{c}$ state*; the first attempts of explanation focused on trying to accommodate the X(3872) within the existing quark model, more precisely within the spectrum of charmonia (as seen on Fig. 2). In order to do that, the J^{PC} quantum numbers had to be determined, as explained in Subsec.1.2.2.

- *hybrids*; bound states of a quark and an anti-quark plus a number of constituent gluons. Such states could have quantum numbers that cannot be assumed by quarkonia (e.g., $J^{PC} = 0^{+-}, 1^{-+}$). Some initial calculations (model or lattice) show that 1^{-+} would be the lightest states and therefore the easiest ones to distinguish from the conventional quarkonia. It is assumed that signature decays would be either to two open charm mesons (one in P and one in S state) or to a conventional charmonium plus a pion. This hypothesis is also discussed in Subsec.1.2.2.

- *molecules*; hypothetical objects in which two mesons are bound, usually represented as $[Q\bar{q}][q'\bar{Q}]$; Q representing a heavy quarks and q a light quark. Some calculations show that both $Q = c$ or $Q = b$ states could be possible and that such states would decay via configuration mixing. If the X(3872) is a molecule, a decay to two D mesons would be observed. The hypothesis is discussed in Subsec.1.3.1.

- *tetraquarks*; are composite particles in which a bound quark pair neutralizes its color with a bound antiquark pair, usually represented as $[Qq][\overline{q}'\overline{Q}]$. A large number of states are expected for each spin-parity. The discovery of such states would be a clear signal of existence of tetraquarks (see Subsec.1.3.2).

1.2.2 *Determination of the J^{PC}*

Determination of the J^{PC} was crucial to the understanding of the nature of the X(3872).
First, the charge conjugation C had to be determined. As explained in the 1.1.3, C is a multiplicative quantum number. One searches for the decays X(3872) $\rightarrow J/\psi\gamma$; since C for both J/ψ and γ is negative, observing the decay would mean a positive C for the X(3872). Both Belle [26] and BaBar [27] found such a decay. Also, an upper limit has been set on the branching fraction of the decay X(3872)$\rightarrow \chi_{c1}\gamma$. χ_{c1} has a positive intrinsic C-parity and an observation of the decay X(3872)$\rightarrow \chi_{c1}\gamma$ would mean a negative C for the X(3872). With the determination of $C = 1$, possibilities of accommodating the X(3872) to the charmonium spectrum have been narrowed, but there were no limitations set to the hypothesis that the X(3872) is a molecule.
J^P assignment proved harder to establish. From early on, analyses excluded all the possible J^{PC} except for the two competitive hypotheses: either 1^{++} or 2^{-+}. The final determination was done via two complementary procedures, the careful angular analysis and the determination of the dipion mass distribution, both in the decay channel X(3872)$\rightarrow J/\psi\pi^+\pi^-$. In general, distributions over selected angles in the decay have to be calculated. The problem of decays $B^{\pm} \rightarrow K^{\pm}X(3872)$; X(3872)$\rightarrow J/\psi\pi^+\pi^-$; $J/\psi \rightarrow l^+l^-$ is in general a five-dimensional problem with three helicity angles (θ_X, $\theta_{\pi\pi}$, $\theta_{J/\psi}$) and two angles between the decay planes ($\Delta\phi_{X,\pi\pi}$, $\Delta\phi_{X,J/\psi}$). The LHCb analysis [28] was the first to perform a complete analysis; both the CDF [29] and Belle [30] have simplified the problem to 3D because of low statistics.
In 2006, the CDF [29] analyzed the decay X(3872)$\rightarrow J/\psi\pi^+\pi^-$. Such decay is an example of a strong decay that conserves parity (P) and angular momentum (L). Analysis clearly shows that dipion mass peaks at high values close to mass of ρ ($\sim$ 770 MeV, see Fig. 14). Intrinsic parity of both J/ψ and ρ is negative, to calculate parity of X(3872), the angular momentum also has to be considered: $P_X = P_{J/\psi}\, P_\rho\, (-1)^L$. At the time, $L = 0$ (and consequently positive parity) was the most likely value; however, $L = 1$ hypothesis could not be excluded with given statistics.
The updated Belle analysis of X(3872)$\rightarrow \pi^+\pi^- J/\psi$, using the full 711 fb^{-1} $\Upsilon(4S) \rightarrow BB$ data sample [30] confirmed the CDF result on the dipion mass and again narrowed the possibilities for J^{PC} to either 1^{++} or 2^{-+}. For the angular correlation studies, the definition of angles is shown in Fig. 15. The x-axis is the direction opposite to the kaon, the $x-y$ plane is defined by the kaon and π^+ and the z-axis completes a right-handed coordinate system. χ is defined as an angle between

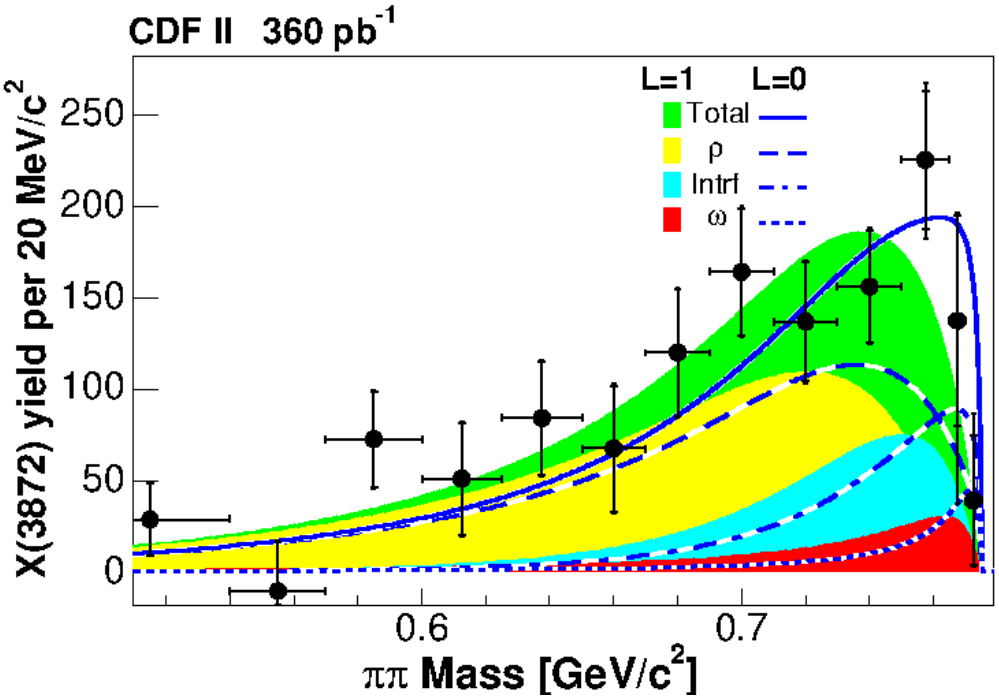

Figure 14: Measurement of the dipion mass, done by the CDF [29]. The pion pair arises from the intermediate ρ or ω meson, the interference of the two, and the total sum of the three contributions. Simulations for the $L = 0$ options are marked with lines, simulations for the $L = 1$ option with shaded regions.

the π^+ direction and the x-axis and the θ_l is the angle between the positive lepton and the z-axis. θ_X is the angle between the J/ψ and the direction opposite to the kaon in the X(3872) rest frame. It can be shown that for the 1^{++} hypothesis, the expected distribution over θ_l and χ is

$$\frac{d^2N}{d\cos\theta_l d\cos\chi} \propto \sin^2\theta_l \sin^2\chi. \tag{14}$$

The measurements can be seen on Fig. 15. For the 2^{-+} assignment, two separate combinations of L and S are expected in the final state: the $L = 1, S = 1$ possibility is labelled as B_{11} and the $L = 1, S = 2$ as B_{12}. This[2] leads to three simplified predictions for the distribution over $\cos\theta_X$:

$$\frac{dN}{d\cos\theta_X} = \begin{cases} \sim (1 + 3\cos^2\theta_X) & \text{for } B_{12} = 0, \\ \sim \text{flat} & \text{for } |B_{11}| \simeq |B_{12}|, \\ \sim \sin^2\theta_X & \text{for } B_{11} = 0. \end{cases}$$

Fig. 15 also shows the results for the 2^{-+} hypothesis. MC simulations were developed for the $B_{11}/B_{12} = 1.5e^{60°i}$, which turned out to be the best match. At the time, Belle was not able to exclude the 2^{-+} hypotheses and both possibilities for the J^{PC} remained valid.

It took 10 years from the discovery to the final determination of J^{PC} for the

2 Assuming only the lowest L to be of relevance due to the suppression of higher partial waves.

X(3872). In 2013, the LHCb collaboration established $J^{PC} = 1^{++}$. The analysis was done on the event-by-event likelihood ratio test of 1^{++} and 2^{-+} hypotheses on the full five-dimensional angular distribution [28]. A test statistic was introduced ($t = -2\ln|\frac{\mathcal{L}(2^{-+})}{\mathcal{L}(1^{++})}|$) to distinguish between the two hypotheses. Similar to the Belle analysis [30], the $\alpha = \frac{B_{11}}{B_{11}+B_{12}}$ is used as a comparison between the two hypotheses for the LS combination and the test statistic is maximized with respect to α. Fig. 16 shows the results of the hypotheses testing. The study favors 1^{++} over 2^{-+} by more than eight standard deviations.

With J^{PC} now confirmed to be 1^{++}, the hybrid hypotheses is dismissed. Other interpretations, mentioned above, are still possible.

For a long period of time there was no evidence for existence of the X(3872) in the lattice QCD calculations. Only recently the adoption of appropriate interpolators (both $c\bar{c}$ and DD^* component) into the LQCD calculations showed a bound state consistent with the X(3872)[31]. Due to the strict isospin (I) conservation inherent in the LQCD the state is only seen in $I = 0$ and not in $I = 1$[3]. The results of the lattice calculation do not rule out a possibility of the X(3872) being a radial excitation of the χ_{c1} charmonium state (i.e. $\chi_{c1}(2P)$, see Fig. 2).

3 Decays of the X(3872) were observed to violate the isospin conservation, see 1.3.3 for details.

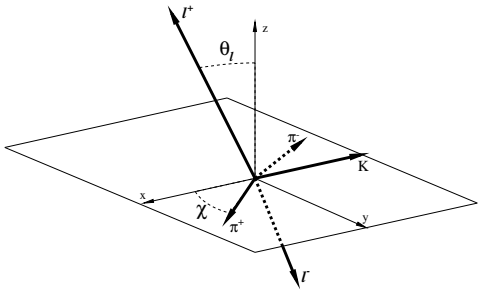

(a) Definition of the angles.

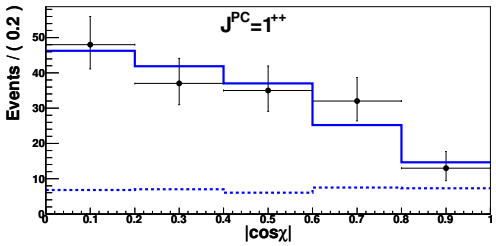

(b) Comparison of the 1^{++} hypothesis applied to $|\cos\chi|$.

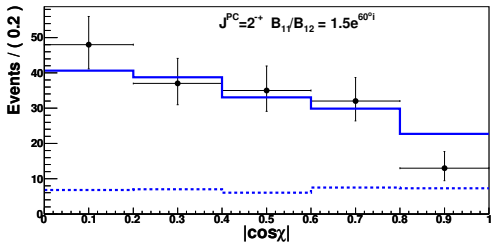

(c) Comparison of the 2^{-+} hypothesis applied to $|\cos\chi|$.

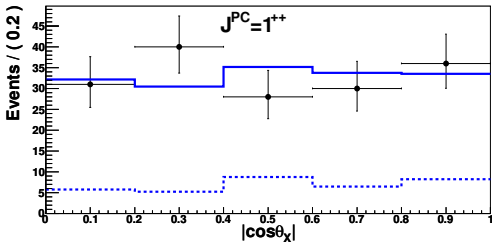

(d) Comparison of the 1^{++} hypothesis applied to $|\cos\theta_X|$.

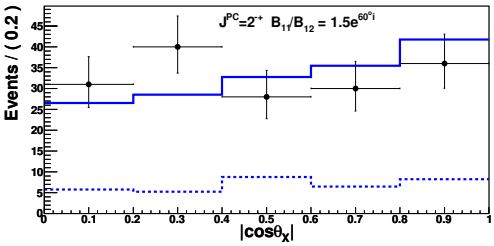

(e) Comparison of the 2^{-+} hypothesis applied to $|\cos\theta_X|$.

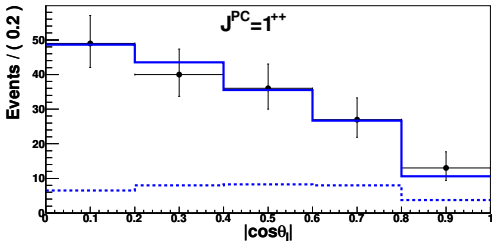

(f) Comparison of the 1^{++} hypothesis applied to $|\cos\theta_l|$.

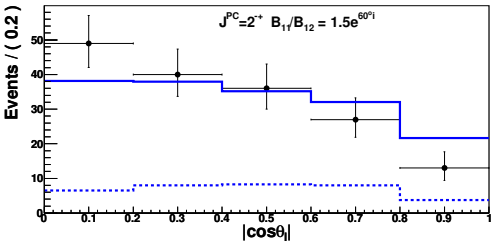

(g) Comparison of the 2^{-+} hypothesis applied to $|\cos\theta_l|$.

Figure 15: The angular correlation studies in [28]. The full lines show hypothesis for either 1^{++} or 2^{-+}, the dashed line the sideband-determined background levels, and the black points show measurements. For the 2^{-+}, the B_{11}/B_{12} is taken as $1.5e^{60^\circ i}$.

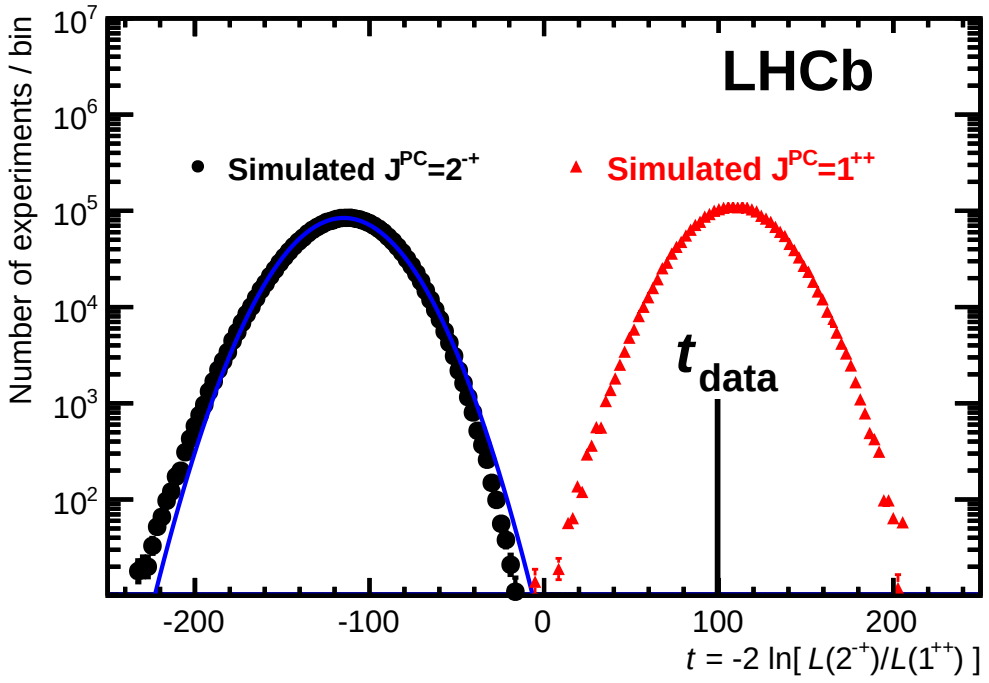

Figure 16: Distribution of the test statistic t for the simulated experiments with $J^{PC} = 2^{-+}$ and $\alpha = \hat{\alpha}$ (maximized value, black circles on the left) and with $J^{PC} = 1^{++}$ (red triangles on the right). The value of the test statistic for the data, t_{data}, is shown by the solid vertical line [28].

1.3 POSSIBLE INTERPRETATIONS

1.3.1 *The molecular hypothesis*

Formation of the nuclear-like bound states has been long speculated about. Proximity of the X(3872) to the $D^{*0}\overline{D}^0$ threshold ($m_{D^{*0}} + m_{\overline{D}^0}$) and expected small binding energy for such molecules immediately drew attention of the theorists and experimentalists alike. Decays to D mesons, an indicator of molecular structure, have been already observed in 2006 (decay channel X(3872)$\rightarrow D^{*0}\overline{D^0}$, reconstructed final state $\pi^0 D^0 \overline{D}^0$ [32]) and later confirmed in a different final state ($\gamma D^0 \overline{D}^0$ [33, 34]). Although the observation of such decays supports the molecular hypothesis, a concern arises from the mass difference when reconstructing X(3872) in the decay channel $J/\psi\pi\pi$ or in the decays to D mesons. Analyses of decays to D mesons usually include the D^* mass constraint, which yields the reconstructed X(3872) mass above the threshold by construction.

1.3.2 *The tetraquark*

In 2005, a model was suggested in which the X(3872) is one of the representatives of the whole class of tetraquarks, particles with four constituent quarks [35]. In the model, the X(3872) is treated as a particle with $J^{PC} = 1^{++}$ with symmetric spin distribution $[cq]_{S=1}[\overline{cq}]_{S=0} + [cq]_{S=0}[\overline{cq}]_{S=1}$. Two possibilities emerge, $X_u = [cu][\overline{cu}]$ and $X_d = [cd][\overline{cd}]$. The model defines low and high state and the mixing angle, θ, between them:

$$\begin{aligned} X_l &= \cos\theta X_u + \sin\theta X_d; \\ X_h &= -\sin\theta X_u + \cos\theta X_d. \end{aligned} \tag{15}$$

The two states should differ by their decays, X_h should decay to $J/\psi\rho$ and X_l to $J/\psi\omega$. The predicted mass difference is related to the difference in the mass of constituent quarks as:

$$M(X_h) - M(X_l) = \frac{2(m_d - m_u)}{\cos 2\theta} = (7 \pm 2)/\cos 2\theta \text{ MeV}. \tag{16}$$

The CDF [36] has set a limit on the mass difference at 3.6 MeV$/c^2$ at 95% C.L. Another test for the model [35] was the mass difference of the X(3872) in decays $B^+ \rightarrow K^+X(3872)$ and $B^0 \rightarrow K^0X(3872)$. The model predicts that decays of charged B mesons should be dominated by the other state than decays of the neutral B mesons (so either X_u or X_d). The latest experimental results [30, 37] give

$$\begin{aligned} \delta M &\equiv M(X|B^+ \rightarrow K^+X) - M(X|B^0 \rightarrow K^0X) \\ &= (+2.7 \pm 1.6 \pm 0.4) \text{ MeV}/c^2 \qquad (BaBar), \\ &= (-0.7 \pm 1.0 \pm 0.2) \text{ MeV}/c^2 \qquad (Belle), \\ &= (+0.2 \pm 0.8) \text{ MeV}/c^2 \qquad (mean). \end{aligned} \tag{17}$$

No significant separation is seen between masses from decays of neutral and charged B mesons so it is assumed that the X(3872) is in fact a single state and the tetraquark hypothesis is set aside.

1.3.3 *Prominent decay modes*

In the overview, Table 3 summarizes branching fractions for some prominent production modes and decay mechanisms. There are two decay modes that should be pointed out:

- X(3872)→ $J/\psi\ \omega$ points to a problem in isospin conservation. The X(3872) decays to $J/\psi\rho$ as well as to the $J/\psi\omega$. As $I_\rho = 1$, $I_\omega = 0$ and $I_{J/\psi} = 0$ it is clear that the isospin of the two final states is different, which constitutes an evidence for the isospin violation in X(3872) decays. The tetraquark hypothesis might be able to explain the existence of decays to $J/\psi\ \omega$, but other searches do not confirm it (see Subsec. 1.3.2);

- X(3872)→ $\gamma\ \psi(2S)$ is important for understanding the structure of the X(3872). The $\gamma\psi(2S)$ decay is expected to be heavily suppressed compared to decays to $\gamma J/\psi$, however some experiments show unexpected results. The latest result, the 2014 measurement by LHCb [38], puts the ratio $B(X(3872) \to \gamma\psi(2S))/B(X(3872) \to \gamma J/\psi)$ to 2.46 ± 0.64 ± 0.29. Discrepancy between different measurements puts the study of radiative decays of the X(3872) to the top of priorities regarding X(3872) at the coming flavor super factories.

To put the numbers in Table 3 into perspective, the Br($B \to J/\psi K$) = $(1.027 \pm 0.031) \times 10^{-3}$, while Br($B \to \psi(2S)K$) = $(6.27 \pm 0.24) \times 10^{-4}$.

B decay mode	X(3872) decay mode	product branching fraction [$\times 10^5$]	reference
$K^{\pm}$X(3872)	$\pi\pi J/\psi$	0.86 ± 0.08 ± 0.05	[30]
K^0X(3872)	$\pi\pi J/\psi$	0.43 ± 0.12 ± 0.04	[30]
KX(3872)	$\pi^0\pi\pi J/\psi$	R = 1.0 ± 0.4†	[26]
K^+X(3872)	$\omega J/\psi$	0.6 ± 0.2 ± 0.1	[39]
$K^{\pm}$X(3872)	$D^{*0}\overline{D}^0$	7.7 ± 1.6 ± 1.0	[34]
K^0X(3872)	$D^{*0}\overline{D}^0$	9.7 ± 4.6 ± 1.3	[34]
K^+X(3872)	$\gamma J/\psi$	0.18 $^{+0.05}_{-0.04}$± 0.01	[40]
K^+X(3872)	$\gamma\psi(2S)$	0.08 $^{+0.20}_{-0.18}$± 0.04	[40]

Table 3: Measured X(3872) product branching fractions, separated by production and decay mechanism for selected decay modes. The result marked with †, denotes the ratio between $\pi\pi\pi^0 J/\psi$ and $\pi\pi J/\psi$ branching fractions. The first error is statistical, the second systematic.

	J/ψ X	$J/\psi\ c\bar{c}$	J/ψ $X_{\text{non-}c\bar{c}}$
σ	1.17 ± 0.02	0.74 ± 0.08	0.43 ± 0.09
σ_{Pet}	1.19 ± 0.01	0.73 ± 0.05	0.48 ± 0.07
ε_{Pet}	0.16 ± 0.01	0.10 ± 0.02	$0.32^{+0.16}_{-0.12}$

Table 4: Cross sections for the processes $e^+e^- \to J/\psi$X,$e^+e^- \to J/\psi c\bar{c}$, and $e^+e^- \to J/\psi\ X_{\text{non-}c\bar{c}}$ with characteristics of the J/ψ spectra, ε_{Pet} [21].

Production of the X(3872) is not limited to decays of B mesons. In 2013, the CMS observed the direct production of X(3872) in the pp collisions [41]. The prompt production in the e^+e^- collisions has not been observed yet. The possibility of such production is discussed in detail in the Subsec. 1.1.5.

1.3.4 *The charmonium production*

In 2009, Belle published a comprehensive article [21] on the subject. In the first part of the article, the production of two bound $c\bar{c}$ states has been measured via the recoil mass technique. To ensure that the reconstructed $c\bar{c}$ states did not originate from decays of B mesons, the CMS momentum of the produced J/ψ, $p^*_{J/\psi}$ had to be larger than 2.0 GeV. The method consists of a reconstruction of a single charmonium state ($(J/\psi, \psi', \chi_{c1(2)})$, called the tagged charmonium state, and a calculation of the recoil mass to the reconstructed charmonium state. The recoil mass is here defined as $M_{\text{recoil}}((c\bar{c})_{\text{tag}}) = \sqrt{(E_{\text{CM}} - E^*_{\text{tag}})^2 - p^{*2}_{\text{tag}}}$. Fig. 18 shows results of the technique confirming the double charmonium production resulting in two bound $c\bar{c}$ states. The same analysis also observed a correlated production of a $c\bar{c}$ state and an additional open charm hadron, another example of the double $c\bar{c}$ production in e^+e^- colliders. Here, D^0, D^+, D^+_S or Λ^+_c were reconstructed alongside J/ψ (see Fig. 17). Measured cross sections for these processes are gathered in Table 4. The measured double charmonium production cross section, $\sigma(e^+e^- \to J/\psi c\bar{c}) = 0.74 \pm 0.08$ pb, is at least an order of magnitude larger than predictions, see Table 2 or [42] for example.
Another important result followed from the same measurement- J/ψ momentum spectrum has been measured both in inclusive production and in processes of type $e^+e^- \to J/\psi\ c\bar{c}$. The momentum spectrum was compared to Peterson fragmentation function (see Fig. 19), defined as

$$z = \frac{p}{p_{\text{max}}},$$
$$\frac{dN}{dz} \propto \frac{1}{z}(1 - \frac{1}{z} - \frac{\varepsilon}{1-z})^{-2}. \tag{18}$$

Discrepancy between theoretical predictions and experimental results makes

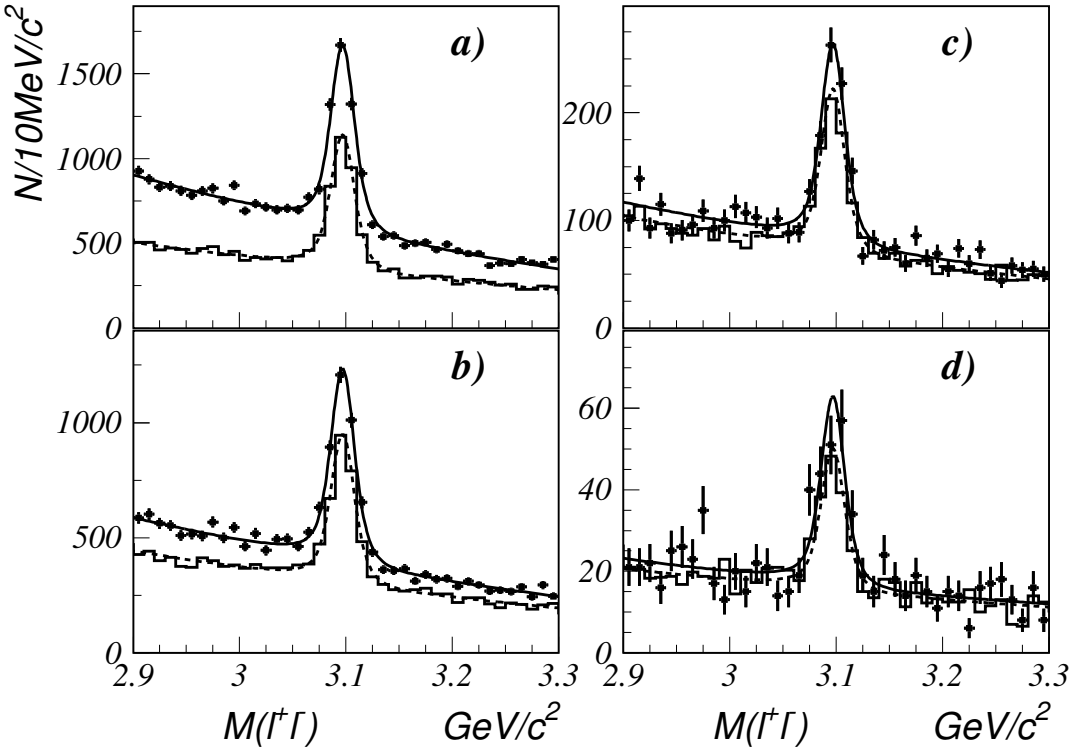

Figure 17: $M_{l^+l^-}$ spectra for H_c signal (points with errors) and scaled H_c sideband windows (histogram). $H_c = (a)D^0, (b)D^+, (c)D_s^+$, and $(d)\Lambda_c^+$. The curves represent the result of the fit - solid in the signal window of H_c and dashed in the H_c sidebands [21].

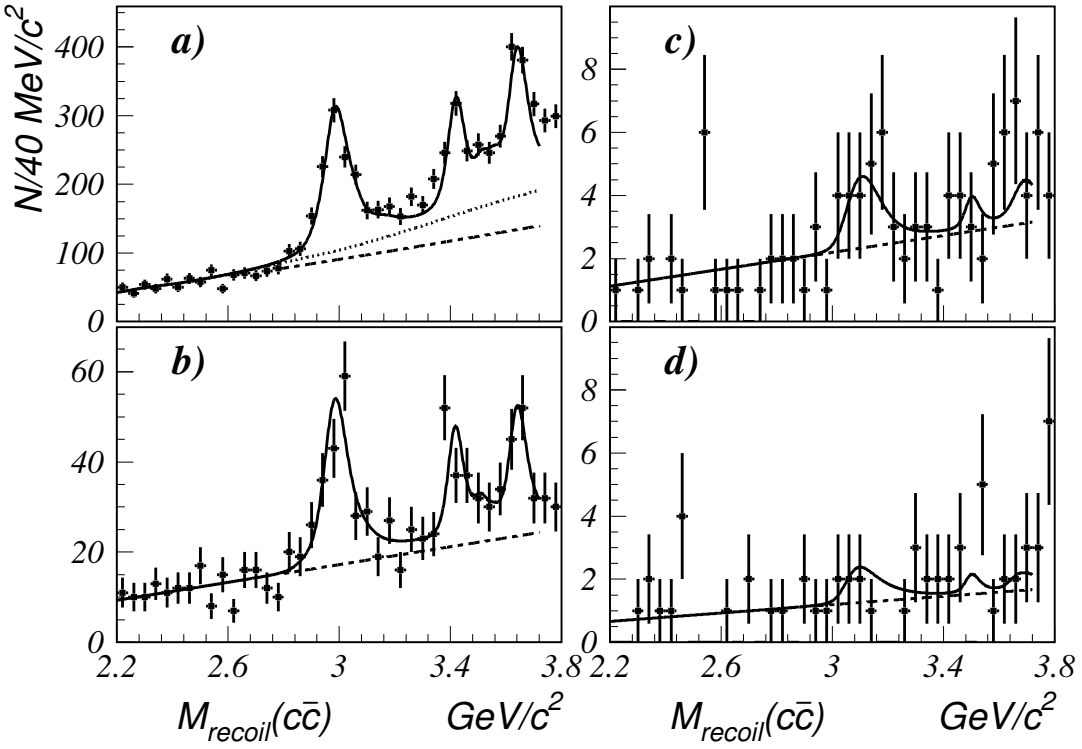

Figure 18: The mass of the system recoiling against the reconstructed a) J/ψ, b) ψ', c) χ_{c1} and d) χ_{c2}. The curves show the fit [21].

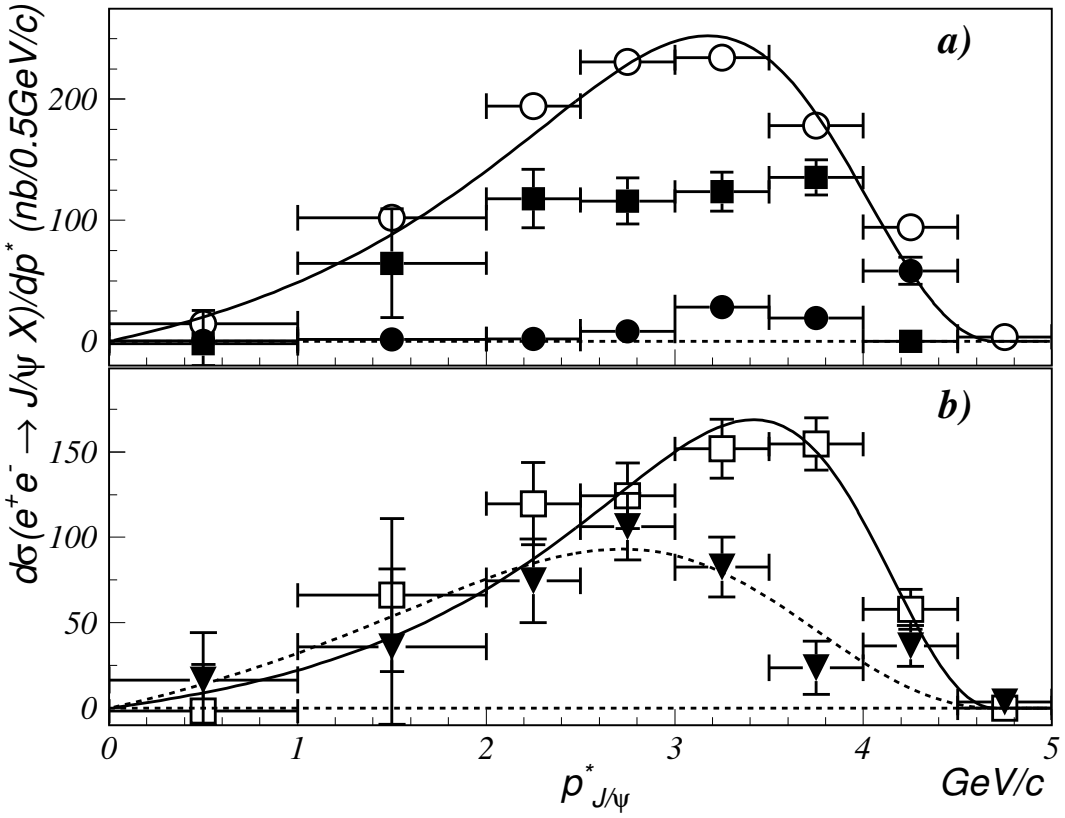

Figure 19: $p^*_{J/\psi}$ spectra: (a) inclusive (open circles), from $e^+e^- \to J/\psi H_c X$ (filled squares) and from double charmonium production (filled circles); (b) the sum of all $e^+e^- \to J/\psi c\bar{c}$ processes (open squares), from the $e^+e^- \to J/\psi X_{\text{non-}c\bar{c}}$ processes (filled triangles). The fit results are shown in (a) for the inclusive spectrum, and in (b) for the processes $e^+e^- \to J/\psi c\bar{c}$ (solid curve) and $e^+e^- \to J/\psi X_{\text{non-}c\bar{c}}$ (dashed curve) [21]. Results of the fit (ε_{Pet}) are gathered in Table 4.

the double charmonium production a very interesting topic both in theoretical and experimental aspect.
The X(3872) is the first, and so far the most widely studied hadron (in the group of hadrons with unusual properties, often referred to as the charmonium-like exotic states) that does not fit into the naive quark picture of mesons and baryons. The nature of its composition is not understood and as such it represents an extremely interesting object in the studies of the the QCD. Following from the observed decays of the type X(3872) $\rightarrow J/\psi$ Y, it is evident that the X(3872) includes a significant component of $c\bar{c}$. Its direct production in e^+e^- annihilation has so far not been observed yet. The production of the X(3872) is thus related to the production of charmonium in e^+e^- collisions. The agreement between experimental measurements and theoretical predictions is far from satisfactory. Hence the study of the prompt production of the X(3872) in e^+e^- annihilation, presented in this work, is hoped to give further answers to these open questions.

2

EXPERIMENTAL SETUP AND SOFTWARE FRAMEWORK

The Belle experiment is one of the world's two experiments operating on B-factories (other being BaBar at the PEPII collider at Stanford Linear Accelerator Laboratory, USA), collider-based experiments, designed to collect copious amount of B mesons. The detector was set at the KEKB accelerator, an asymmetric e^+e^- collider in Tsukuba, Japan. The detector has been collecting data from 1999 to 2010. There are approximately 450 people coming from over 70 different institutions involved in the Belle experiment. This chapter briefly describes the KEKB accelerator and the Belle detector, the experimental setup of this analysis. For a complete description, see [43] for the KEKB collider and [44, 45] for the Belle detector.

2.1 THE KEKB ACCELERATOR

The KEKB accelerator is an asymmetric energy e^+e^- collider, designed to produce a large number of $B\overline{B}$ pairs. Electrons and positrons are first accelerated to their final energies in a linear accelerator (LINAC) and then injected into two separate storage rings. The tunnels have a circumference of ~ 3 km and lie 11 m below the surface. The two rings intersect at the *interaction point* (IP) where bunches of electrons and positrons collide and where the Belle detector is placed (see Fig. 20). There are about 1000 bunches of electrons and positrons in each ring, which corresponds to separation of 3 m between them; the beams collide at an angle of 22 mrad.

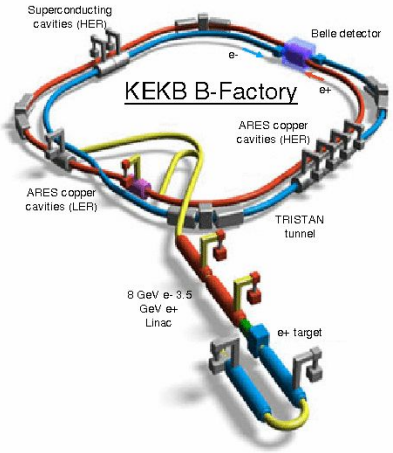

Figure 20: A schematic of the KEKB collider.

The designed energies, 3.5 GeV for positrons and 8 GeV for electrons are selected so that the center-of-mass (CM) energy (10.58 GeV) is at the mass of the $\Upsilon(4S)$ resonance, an excited bound state of $b\overline{b}$. The mass of $\Upsilon(4S)$ is just above the threshold for the production of two B mesons, either charged or neutral. The primary goal of the Belle collaboration was to study the CP violation in the decays

of B mesons and the large cross section for the $e^+e^- \rightarrow \Upsilon(4S) \rightarrow B\overline{B}$ enables such studies. The beam energies are asymmetric so that the produced $\Upsilon(4S)$ resonance is boosted in the laboratory system by:

$$\beta\gamma = \frac{E_{HER} - E_{LER}}{E_{CMS}} = 0.425. \tag{19}$$

The $B\overline{B}$ pairs produced from the $\Upsilon(4S)$ have almost the same boost. This is translated to a separation of the decay vertices of the B mesons - approximately 200 μm apart in the laboratory system. This in turn allows for a measurement of the time-dependent CP violation.
The colliding electrons and positrons do not necessarily produce pairs of B mesons; collisions can result in a muon and the τ pair production, BhaBha scattering, two photon events, or in other quark pair production, except for $t\bar{t}$(a t quark decays before it is able to form bound states). Cross sections for the interactions are listed in Table 5.

interaction type	σ [nb]
$e^+e^- \rightarrow \Upsilon(4S)$	1.1
$e^+e^- \rightarrow \Upsilon(5S)$	0.31
$e^+e^- \rightarrow c\bar{c}$	1.3
$e^+e^- \rightarrow q\bar{q}$	2.1
$e^+e^- \rightarrow \tau^+\tau^-$	0.93
BhaBha, radiative BhaBha	37.8
$\gamma\gamma$	11.1

Table 5: Cross sections for the possible e^+e^- interactions in the KEKB collider.

Performance of an accelerator is described by its luminosity, which relates to the rate of particle collisions as

$$\frac{dN}{dt} = \mathcal{L}\sigma, \tag{20}$$

where $\mathcal{L}$ is the luminosity and σ a cross section for a particular process. The KEKB's design luminosity was $1.0 \times 10^{34}/\text{cm}^2\text{s}$, which was surpassed by the factor of 2 in June 2009, being a current world record for colliders.
The integrated luminosity is defined as

$$L = \int \mathcal{L}dt \tag{21}$$

and represents a measure for the number of collected decays. In its 11 years of operation, the Belle detector had gathered a total of more than 1000 $\text{fb}^{-1}$of data; 711 fb^{-1} at the $\Upsilon(4S)$ resonance and 100 fb^{-1} below the $\Upsilon(4S)$ resonance (see Table 6).

resonance	collected data [fb^{-1}]
$\Upsilon(1S)$	6
$\Upsilon(2S)$	25
$\Upsilon(3S)$	3
60 MeV below $\Upsilon(4S)$	89
$\Upsilon(4S)$	711
$\Upsilon(5S)$	121

Table 6: The amount of data gathered by the Belle detector at various resonances and energies.

2.2 THE BELLE DETECTOR

The Belle detector is positioned around the IP of the KEKB accelerator. It is a large-solid-angle magnetic spectrometer, built for detection of long-lived particles produced in e^+e^- collisions. Both charged and neutral particles can be detected: $e^\pm$, $\mu^\pm$, $\pi^\pm$, $K^\pm$ on the charged side and $p^\pm$ and on the neutral γ and K_L^0.
Typically, heavier hadrons (e.g., X(3872), $\psi(2S)$) decay on a short-time scale and the decay chain has to be reconstructed from the beforementioned long-lived remnants. Therefore, the detector has to be able to perform three basic tasks: to identify the particle, to describe its track and to measure its momentum. The Belle detector consists of several sub-detectors, which perform specific tasks. The sub-detectors are configured around the 1.5 T magnetic field and are placed in symmetrical configuration around the IP with some forward-backward asymmetries, following the topology of e^+e^- collisions. The position of the sub-detectors within Belle detector is illustrated in Fig. 21. In the following paragraph, some basic properties and tasks of the sub-detectors are discussed, while the detailed technical descriptions of each sub-detector follow in the subsequent subsections.
The Belle detector is basically a magnetic spectrometer. A magnetic field of 1.5 T is produced by a large solenoid; when a charged particle enters the magnetic field, its trajectory changes to a helix. By measuring the curvature, the charged particle's transverse momentum is determined. The task of measuring the decay vertices of the B mesons is handled by the *silicon vertex detector* (SVD). which is positioned just outside of the beryllium beam-pipe.The *Central drift chamber (CDC)* detects the particle's trajectory by measuring ionization in the gas. Additionally, the sign of the charge can be determined by orientation of the helix. The CDC can also help with identification of the low momentum particles (< 1 GeV) by measuring their energy loss due to ionization. Moving outwards from the CDC, sub-detectors focus on identification of the particles. Two main principles are used: measuring the velocity of the particle and observation of particle's interaction with matter. Particles can be identified using the relation $p = \gamma mv$: if the velocity and the momentum are determined, the mass of the particle identifies the particle. The *Aerogel Cherenkov counters* (ACC) distinguish between the high

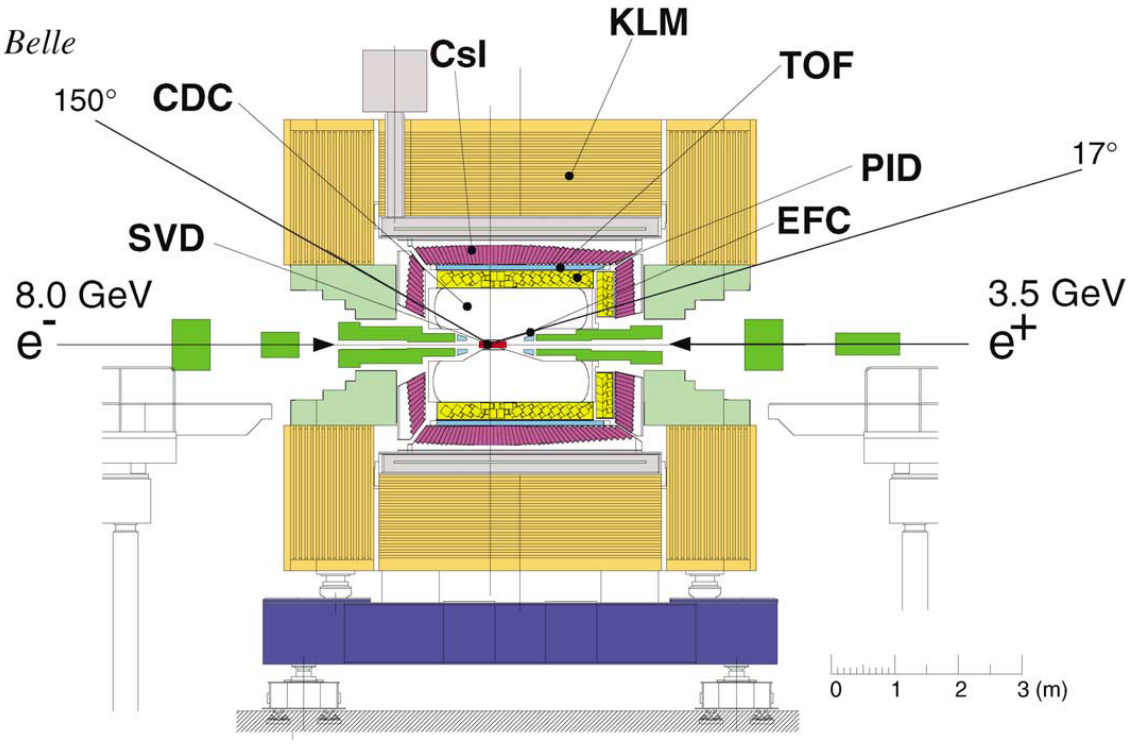

Figure 21: A schematic of the Belle detector [44].

momentum (~ 1.2 - 3.5 GeV) pions and kaons by detecting the photons emitted in the aerogel. The *time of flight* (TOF) identifies the low momentum particles. The two calorimeters (the *electromagnetic calorimeter* (ECL) and the K_L *meson and muon detector* (KLM)) use interaction of the particles with matter to detect the photons and the electrons (ECL) as well as the muons and the neutral kaons (KLM).

2.2.1 *EFC*

The Extreme Forward Calorimeter (EFC) is placed at the front faces of the cryostats of the compensation solenoid magnets of the KEKB accelerator, surrounding the beam pipe (see Fig. 21). It covers the angular range from 6.4° to 11.5° in the forward direction and 163.3° to 171.2° in the backward direction. The EFC was designed in order to improve the experimental sensitivity for certain processes (e.g., $B \to \tau\nu$) that call for extended information in the polar angle outside of ECL coverage ($17° < \theta < 150°$). In addition, the EFC also functions as a beam mask to reduce backgrounds for the CDC, is used as a beam monitor for the KEKB control and as a luminosity monitor for the Belle experiment.
The EFC consists of scintillation detectors made of pure crystals of the BGO (bismuth germanate, $Bi_4Ge_3O_{12}$) and silicon photodiodes. The BGO was chosen because of its radiation hardness; the crystals are segmented into 32 segments in the ϕ and 5 segments in the θ direction for both the forward and the backward cones as shown in Fig. 22.

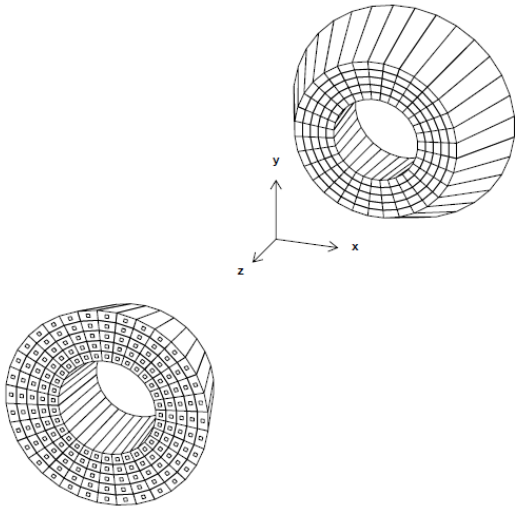

Figure 22: The BGO crystals of the forward and the backward EFC detectors [44].

2.2.2 *SVD*

The Silicon Vertex Detector (SVD) is the most indispensable part of the detector when it comes to measuring the time-dependent CP-violation in decays of B mesons. In order to measure the violation, the decay vertex position of the B mesons has to be pinpointed. The SVD enables the precision of the measurement of $\approx$ 100 μm. Another demand for such detector is a small amount of material inside the detector acceptance area to minimize the effect of multiple scattering of particles. A semi-conductor device is the only possible choice - at Belle, the double-sided silicon strip detectors (DSSD) are used.
The DSSDs are a simple $p-n$ junctions. Pairs of electrons and holes are created when a charged particle passes through the n section. Due to externally applied electrical field, charges separate and are collected at the strip electrodes on the opposite sides of DSSD. Electrodes on the parallel layers are oriented perpendicular to each other - it is possible to determine the position of a particle crossing the DSSD plane.
During the Belle detector operation, two versions of the SVD detector were implemented. The first one (SVD1) was operating from the beginning to 2003 (after 152×10^6 $B\overline{B}$ pairs), while the SVD2 operated till the end of data taking in 2010. In both designs, the DSSD units are placed in cylindrical layers around the beam pipe, as shown in Fig. 23. The SVD1 consisted of three layers of DSSD ladders placed at 30, 45.5 and 60 mm radially from the IP. It covered polar angle of $23°< \theta < 139°$(Fig. 23). The SVD2 had four layers of DSSD ladders added at 20, 43.5, 70 and 80 mm radially from the IP and covered polar angle of $17°< \theta < 150°$(Fig. 23). Because the resolution of the vertex position improves roughly as an inverse of its distance to the IP, placing the innermost layer of the SVD 1 cm closer to the IP was very important.

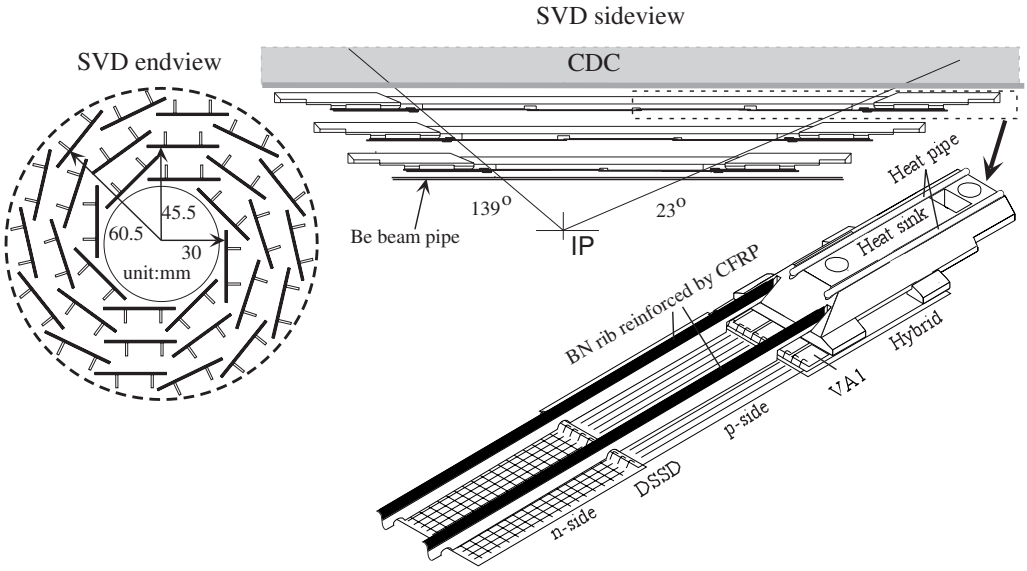

(a) Configuration of the SVD1.

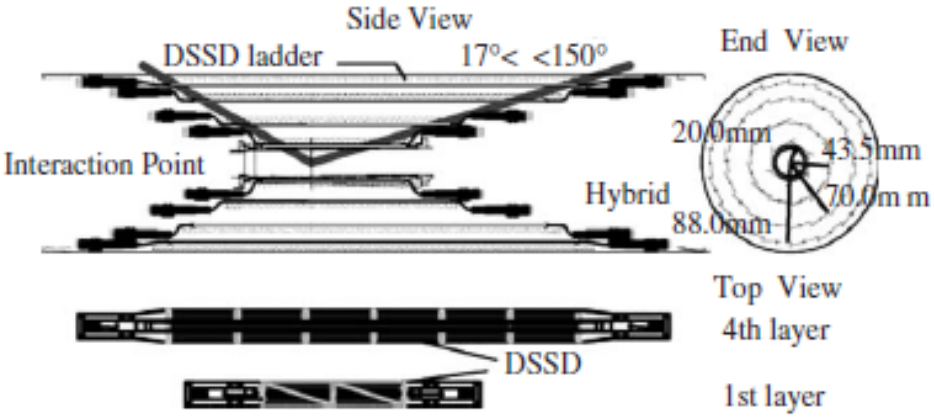

(b) Configuration of the SVD2.

Figure 23: The two configurations of the SVD [44].

Numerically, the performance of the SVD can be described in terms of the resolution on charged tracks hits, which is measured to be

$$\sigma_{xy} = 21.9 \oplus \frac{32.5}{p\beta \sin^{3/2}\theta}\ \mu m, \quad \sigma_z = 27.8 \oplus \frac{31.9}{p\beta \sin^{5/2}\theta}\ \mu m, \tag{22}$$

where p is the particle's momentum in GeV, $\beta = \frac{v}{c}$ and θ its polar angle.

2.2.3 *CDC*

The Central Drift Chamber (CDC) (see Fig. 24) measures particle's momentum by determining its track in the magnetic field. The CDC is a multiwire chamber, filled with a half-half mixture of ethane and helium, which was chosen to reduce the multiple Coulomb scattering contributions to the mo-

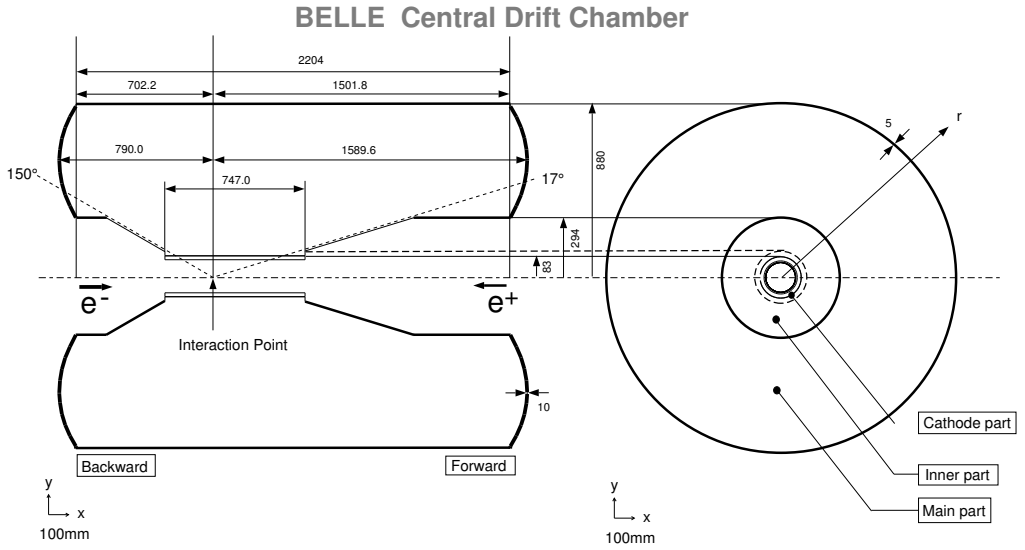

Figure 24: A schematic of the CDC. The side and the front view [44].

mentum resolution. The CDC consists of 8400 cells, where the anode sense wires and the field wires are strung between the cathode planes (see Fig. 25). The negatively biased field wires provide a drift field, whereas the sense wires are positively biased. When a charged particle passes such a cell, it ionizes the gas. The resulting electrons are drawn to the nearest sense wire. The measurement of the drift time can give the distance to the sense wire. The drift time is the time diference between the passing of the particle, determined by a scintillation counter, and the arrival of the pulse in the wire. In the last millimeters from the wire, the electrons gain enough energy to cause the secondary ionization. The cascade of the charge results in a measurable signal.

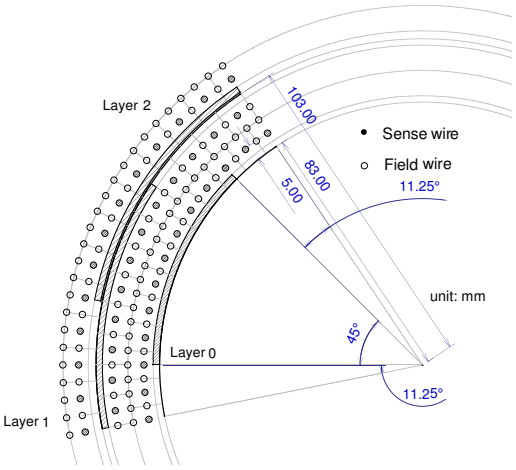

Figure 25: Placement of the field and the sense wires in the CDC [44].

Besides tracking, the CDC can be used for identification of the particle as well. The identity of the particle is related to the energy deposit of the particle per unit length ($\frac{dE}{dx}$) via the Bette-Bloch equation. For a particle with the speed v, the charge z, and the energy E, traveling a distance x into a target of the electron number density n and the mean excitation potential I, the energy loss is

$$-\frac{dE}{dx} = \frac{4\pi}{m_e c^2}\frac{nz^2}{\beta^2}\left(\frac{e^2}{4\pi\varepsilon_0}\right)^2\left[\ln\left(\frac{2m_e c^2\beta^2}{I(1-\beta^2)}\right) - \beta^2\right], \tag{23}$$

where ε_0 is the vacuum permittivity, $\beta = \frac{v}{c}$, e and m_e the electron charge and the rest mass, respectively. Fig. 26 shows energy loss for the different particles as a

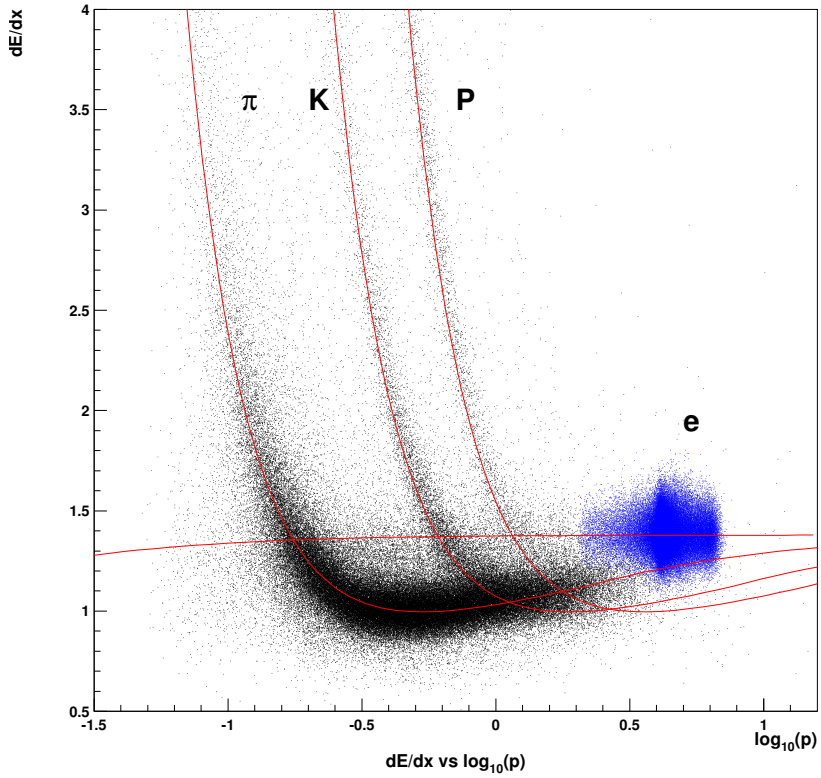

Figure 26: Energy loss of the different particles in the CDC as a function of the particle's momentum [44].

function of their momenta. The CDC can distinguish between kaons, pions and protons sufficiently in the momentum range above 1.5 GeV.

2.2.4 *ACC*

In numerous analyses at Belle, efficient distinguishability between charged kaons and pions at high momenta is of utmost importance. The Aerogel Cherenkov Counter (ACC) provides complementary information to $\frac{dE}{dx}$ measurement of the CDC and time-of-flight information from the TOF in high momentum range (1.2-3.5 GeV/c).
The ACC exploits the Cherenkov effect, the emission of photons when a charged particle passes a dielectric medium with a velocity higher than the velocity of light in that medium. When a particle of mass m and momentum p moves in a medium with refractive index n, Cherenkov photons are emitted if

$$m < p\sqrt{n^2 - 1}. \tag{24}$$

By cleverly selecting n of the radiator, it can be ensured that pions of given momentum are below that threshold, while kaons are not. On that basis, the ACC

distinguishes between the two.
At Belle, the radiator for the Cherenkov light is a silica aerogel, a medium that is suitable because its refractive index can be controlled easily ($\frac{\Delta n}{n} \sim 3\%$). The refractive index ranges from 1.01 to 1.03, depending on the azimuthal angle region. The ACC consists of stacked counter modules - each module comprises 5 aerogel tiles in a thin aluminum box with a side of 12 cm. There are 960 modules in the Φ direction for the barrel part and 228 modules, laid in 5 concentric layers for the forward end-cap region (as shown on Fig. 27).
Emitted Cherenkov light is collected by the fine-mesh photomultiplier tubes

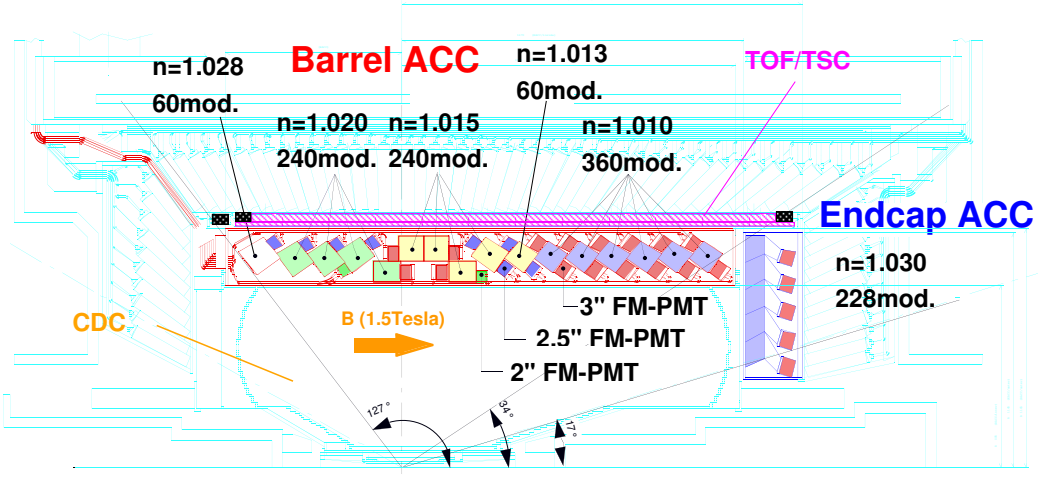

Figure 27: Placement of the ACC [44].

attached directly to the aerogel. Since the ACC is operating in a magnetic field, the fine-mesh photomultipliers were chosen as a photon detector; the photomultipliers are attached directly to the aerogel to collect the emitted Cherenkov light (Fig. 28).

2.2.5 *TOF*

The Time of Flight Counter (TOF) gives particle identification information in order to separate charged pions and kaons with low momenta. Providing information in the momenta range of 0.8-1.2 GeV, it is a complement to measurements from the CDC and the ACC.
The TOF measures the time between a e^+e^- collision at the IP and the passage of the charged particle through the fast plastic scintillators of the TOF. For efficient

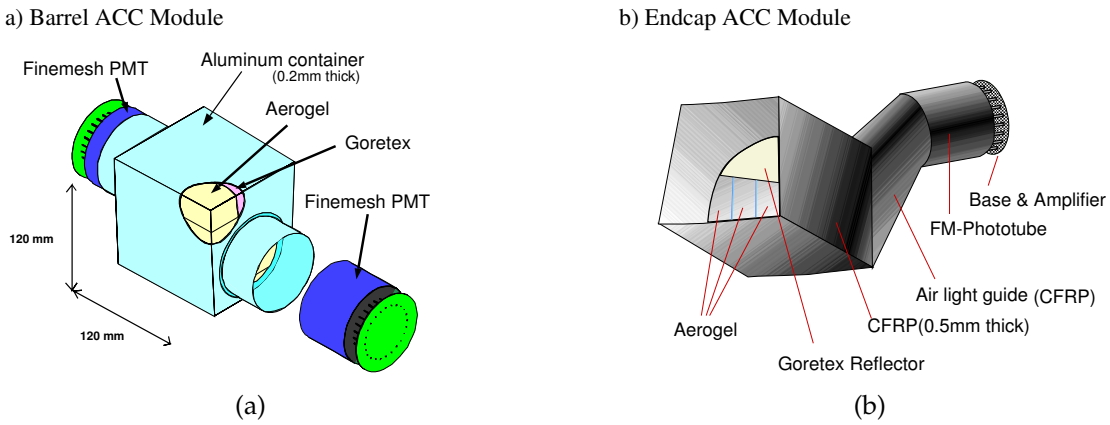

(a) (b)

Figure 28: ACC modules. a): barrel, b): endcap. [44].

separation (3σ) between kaons and pions, timing resolution has to be $\sim$ 100 ps at the distance of 1.2 m. The mass of the passing particle can be calculated as:

$$m = \frac{p}{c}\sqrt{\left(\frac{ct}{l}\right)^2 - 1}, \tag{25}$$

where p is momentum, measured by the CDC, l the length of the helix and t the time, measured by the TOF.
The TOF is built of fast plastic scintillators with an attenuation length longer than 2 m. To avoid pileup in the trigger queue, a thin layer of trigger scintillation counters (TSC) is added to keep the trigger rate below 70 kHz. The whole system comprises 128 TOF counters and 64 TSC, and covers a polar angle of 34°< θ < 120° (Fig. 29, left). Fine-mesh PMTs that collect resulting photons are mounted directly to the scintillators. Fig. 29, right shows time of flight based measurements of particle mass distribution.

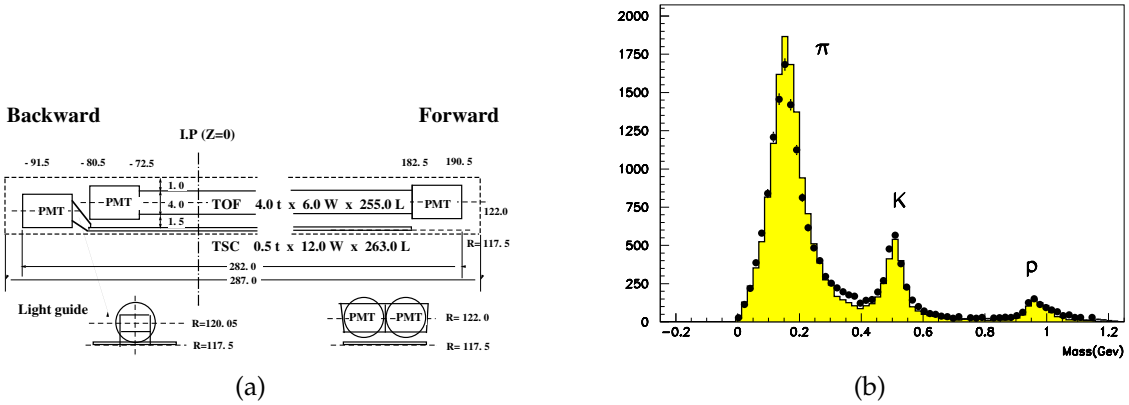

(a) (b)

Figure 29: Left: geometric configuration of the TOF module. All dimensions are in cm [44]. Right: Time of flight based measurements of particle mass distribution. The full yellow area is a results of detector simulation studies and the black points are from experimental data [44].

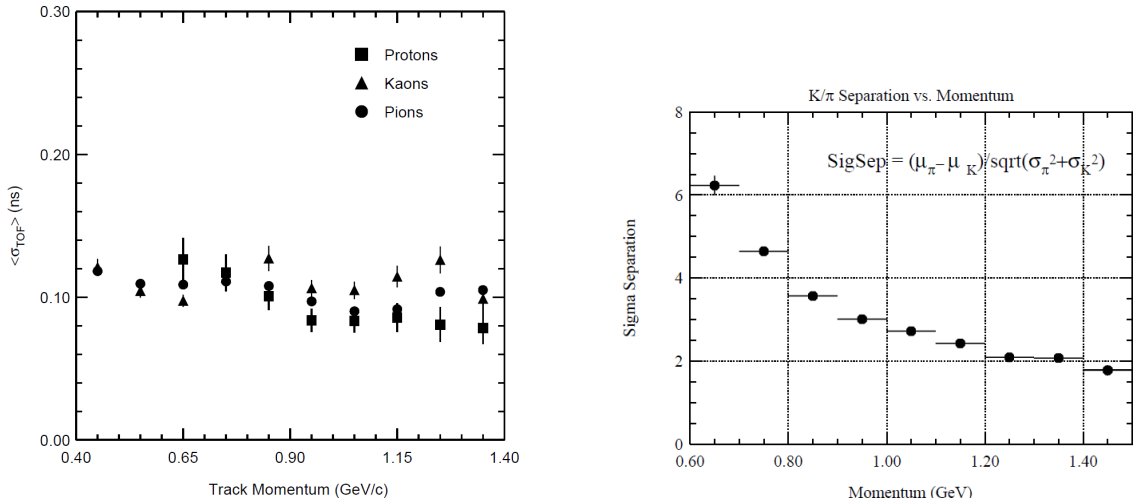

(a) (b)

Figure 30: Left: The averaged time resolution of the TOF over all counters and z, for different particle types [44]. Right: $\pi^{\pm}/K^{\pm}$ separation by the TOF [44].

2.2.6 *ECL*

The Electromagnetic Calorimeter at Belle detects photons with high efficiency and good energy and position resolution. It also provides differentiation between electrons and pions by comparing momenta and the energy deposit of the charged particles.

The ECL is an array of highly segmented thallium doped CsI crystals. The size of a crystal has to provide both good energy and position resolution: in the transverse, the crystals are 6×6 cm^2 and 30 cm in length (16.2 radiation lengths). With such a geometry, 80% of the deposited energy is gathered by the crystals while still obtaining sufficient position resolution.

When an electron or a photon hits a crystal, an electromagnetic shower is produced via bremsstrahlung and a pair creation, which is in turn detected by a photodiode. On the contrary, hadrons and muons do not produce such showers and lose only a small portion of their energy through ionization. The ECL effectively compares the ratio between deposited energy and momenta (E/p) which is close to unity for electrons (photons) and small for other particles (see Fig. 31). Additionally, photons leave no track in the CDC and can therefore be distinguished from electrons.

One of the most important tasks of the ECL is to identify high momenta π^0 through decay to $\gamma\gamma$. An opening angle has to be measured precisely, hence the need for fine segmentation. In total, the ECL consists of 8736 crystals; the configuration is shown in Fig. 32.

Fig. 33 shows photon energy and position resolution for different photon energies.

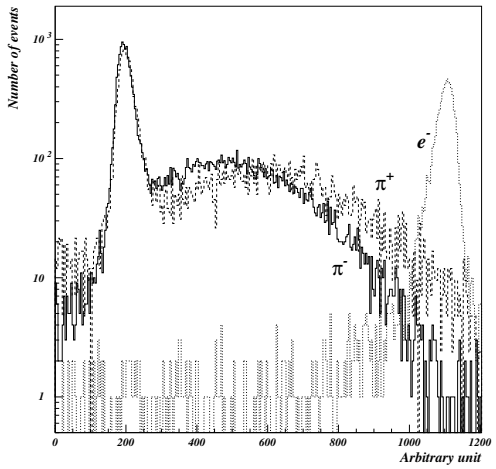

Figure 31: Distribution of the deposited energy in the ECL at the momentum of 1 GeV/c [44].

2.2.7 *KLM*

The K_L^0 and muon detector (KLM) was designed to identify K_L^0 and muons in the wide momentum range ($p_T > 600$ MeV/c, only high energetic particles reach the detector). In our analysis, muon identification is important because it contributes to the efficiency of final particle reconstruction.
The KLM covers a polar angle of $20° < \theta < 155°$ and consists of interchanging RPCs (resistive plate chambers) and 4.7 cm thick iron layers (see Fig. 34). There are 15 detector and 14 iron layers in the octagonal barrel region and 14 iron and detector layers in each endcap (forward and backward).
The RPCs are glass-electrode-resistive counters filled with gas (62 % CH_2FCF_3, 30% Ar and 8% C_4H_{10}). An incoming particle initiates a streamer; the charge is collected by both plates and read out by strips. The two plates are oriented perpendicular in order to gain position information. A K_L^0 interacts with matter in the iron plates and produces a shower of particles which in turn make a signal in the RCPs. A muon can be separated from a K_L^0 due to the absence of a CDC track for the latter. Muons, on the other hand, penetrate much further into the detector than hadrons. Muons are also deflected significantly less then hadrons which are stopped within the first few iron layers. Fig. 35 shows muon detection efficiency and fake rate as a function of momentum.

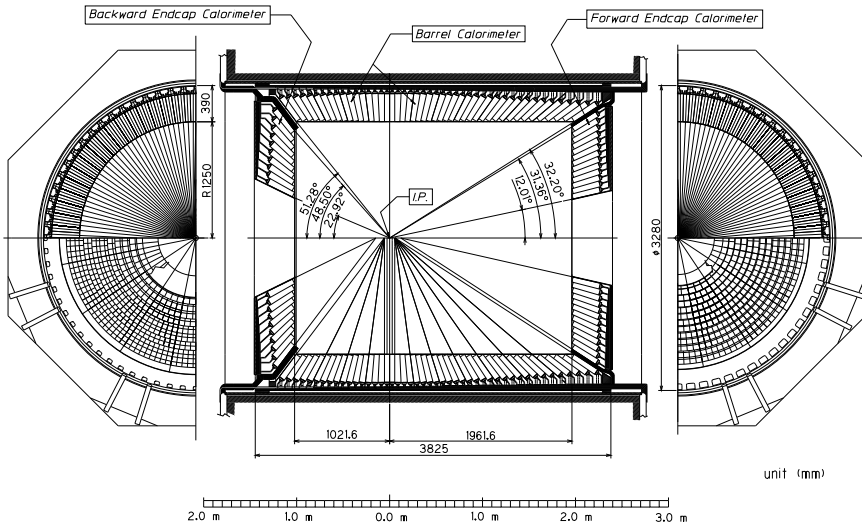

Figure 32: Configuration of ECL [44].

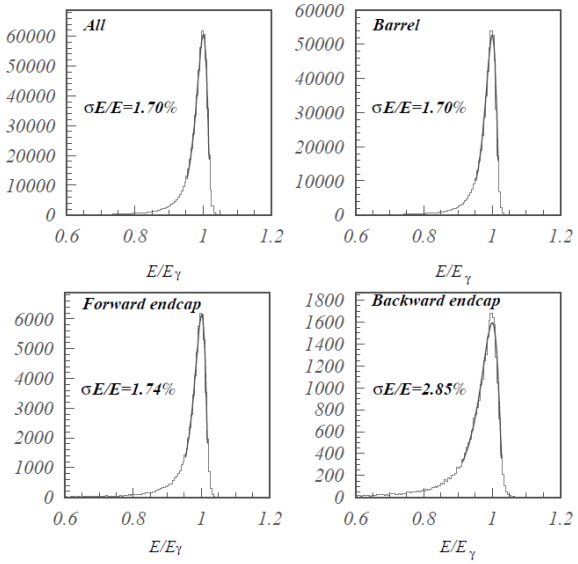

Figure 33: Energy resolutions measured from Bhabha events for overall, barrel, forward and backward end-cap calorimeters [44].

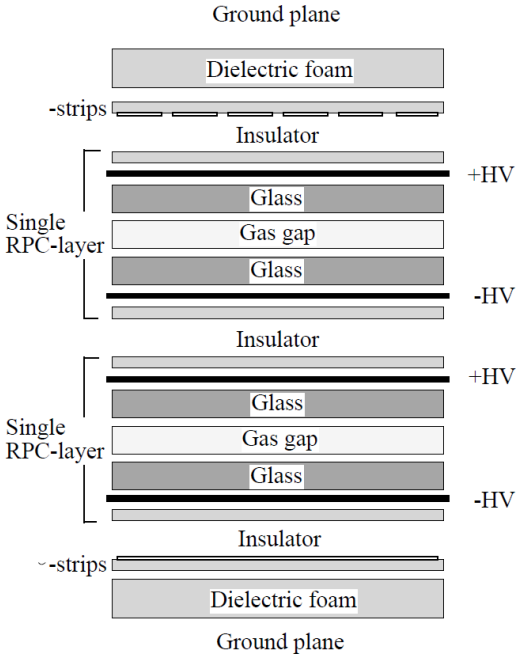

Figure 34: Cross section of the KLM superlayer [44].

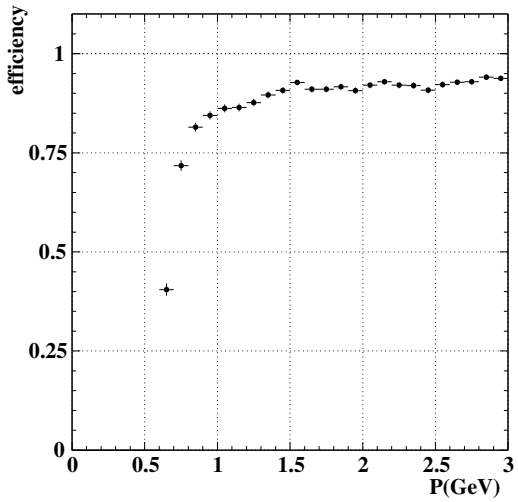

(a) Muon detection efficiency as a function of momentum

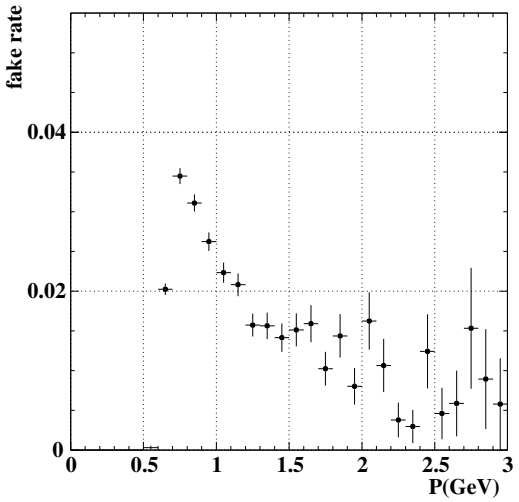

(b) Muon fake rate as a function of momentum.

Figure 35: Muon detection efficiency and fake rate as a function of momentum in the KLM [44].

2.3 OFFLINE DATA

2.3.1 *Trigger and data acquisition*

With an abundance of data flowing into the Belle detector, a system has to distinguish between potentially interesting and throw-away events. At Belle, several stages of triggers have been developed to lower the background rates within the tolerance of the data acquisition system (DAQ, maximum event rate of $\sim$ 500 Hz) while storing as much as possible of events of physics interest. The triggers are a set of selection criteria for an individual event, which allows or denies transfer of the measured data from the detector to the data storage system. The Belle trigger system has three stages - the L_1 is a hardware trigger, the L_3 a software trigger and the L_4 final offline trigger (see Fig. 36). Table 7 lists trigger rates for various physical processes at luminosity of $10^{34}/\text{cm}^2\text{s}$.

In the first step of the DAQ, hardware triggers are used (trigger L_1). The sub-detectors have individual trigger systems which are connected to the central trigger called the Global Decision Logic (GDL). Two types of triggering are used by the sub-detectors - either they check for the tracks or for the energy within the event. The GDL is supposed to collect signals from the sub-detectors within 1.85 μs from an e^+e^- collision and to respond with the final trigger signal 2.2 μs after a collision.
After the GDL triggers the DAQ, a parallel flow of information for sub-detectors is merged into information on a single event. The events are sent to the online computer farm where they are further reduced by the software trigger L_3. The L_3 performs a fast reconstruction of the events and keeps only those where the impact parameter of the tracks satisfies $|z| < 5$ cm. Furthermore, the total deposit of energy in the ECL has to surpass 3 GeV. The L_3 trigger reduces the rate of events by 50%, while keeping 99% of the hadronic events.
The L_4 trigger is the last trigger, already working offline. It decides which events are appropriate for reconstruction and for storage to magnetic tapes. It is crucial in diminishing the required CPU time. Its requirements are:

- at least one track with a transverse momentum > 300 MeV/c,
- impact parameter: r < 1 cm, $|z|$ < 4 cm,
- deposited energy in ECL > 4 GeV.

78% of all triggered events are rejected, but nearly all hadronic events are kept.
A schematic view of triggering and the DAQ systems at Belle is shown in Fig. 36. Events that have passed the L_4 trigger undergo a full reconstruction. The tracks are first reconstructed from the CDC information, then extrapolation to the IP region is done to check for matching SVD hits. The outer detectors mainly provide identification, which is in detail explained in Sec. 3.4.1. An event is formed as a collection of all tracks and neutral showers and is available for analysis.

Physics process	Cross section [nb]	Rate [Hz]
$\Upsilon(4S) \to B\overline{B}$	1.2	12
Hadron production from continuum	2.8	28
$\mu^+\mu^- + \tau^+\tau^-$	1.6	16
Bhabha ($\theta_{lab} < 17°$)	44	4.4[1]
$\gamma\gamma$ ($\theta_{lab} < 17°$)	2.4	0.24[2]
2γ processes ($\theta_{lab} < 17°$), $p_t > 0.1$ GeV	~ 15	~ 35
Total	~ 67	~ 96

[1]Indicates values prescaled by factor 1/100.

[2]Indicates the restricted condition of $p_t > 30$ GeV.

Table 7: Cross sections and trigger rates of physical processes in e^+e^- collisions at the KEKB energies and luminosity. Backgrounds from Bhabha scattering and $\gamma\gamma$ events are large, but they can be significantly reduced due to their distinct signatures. A small fraction is kept and used for luminosity monitoring and detector calibrations.

2.3.1.1 *Monte Carlo simulation*

To have an environment for testing the analysis procedures and detector response to various processes, offline computing provides Monte Carlo (MC) simulation data. MC methods in general belong to a class of computer algorithms that randomly generate outputs from a given probability distribution. At Belle, MC data production is divided into two stages: generation of physical processes and simulation of detector's response. In the first step, physical processes as production and decays of particles are simulated, based on known distributions (e.g., angular distribution of the decay, according to theoretical predictions and branching fraction of various decays according to measured values). For the generation of particles, their decay processes and possible hadronization, two event generators are used: the QQ and the EvtGen [46], both developed by CLEO and BaBar collaborations, but altered to cope with specific Belle requirements. In this specific analysis, Pythia 8 [47] was also used as an event generator. Details about the MC production for this particular analysis can be found in Sec. 3.3.2. In the second stage, generated particles are tracked through the detector in the full detector simulation (GSIM), based on the GEANT [48] platform[1]. Developed at CERN and very commonly used in high energy experimental physics, GEANT is able to simulate interaction of particles with matter. The full Belle detector is implemented in the GSIM, enabling study of response of individual sub-detectors. Output of the simulation is stored in the same event format as the real events from measurements.

1 At the time of the development of the detector response, now widely used GEANT4 has not been available yet.

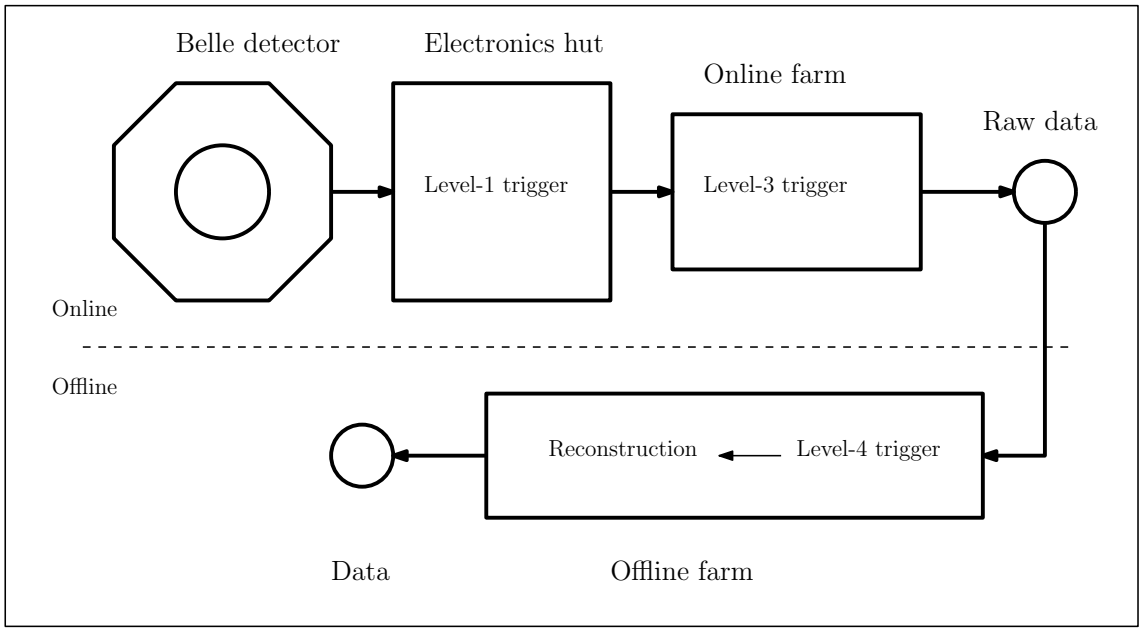

Figure 36: Diagram of the Belle triggering system.

2.3.1.2 *Analysis software*

The first stage of the analysis, event reconstruction, is done completely with tools developed within the Belle collaboration. BASF (Belle AnalysiS Framework) enables reading from the repository of the events on event-by-event basis. Results of the reconstruction are stored in format of ROOT [49] files and all following analysis (e.g., plotting of different variables, fitting procedures, statistical tests, see chapters 3) is done within the ROOT framework.

3

BASICS OF ANALYSIS

3.1 MOTIVATION

Studies of the prompt (double) charmonium production proved to be an interesting field, both experimentally and theoretically. An analysis on the full sample, gathered within 10 years of the Belle's data taking has not been performed yet. The exotic nature of the X(3872) adds to additional interest in such studies. At the time of this analysis, we are not aware of any other study of the prompt production of the X(3872) at e^+e^- colliders. Due to the lack of previous research on the prompt production of the X(3872) and the disagreement between the theory and experiment, a control channel is introduced. The state $\psi(2S)$ is a relatively well understood bound state of the $c\bar{c}$, which shares the J^{PC} assignment and the chosen decay mode with the X(3872).

3.2 SAMPLE SELECTION, VARIABLE ASSIGNMENT, GENERAL PROCEDURE

Three different data types are selected from available Belle measurements: the $\Upsilon(4S)$, the $\Upsilon(5S)$ data and the data, taken 60 MeV under the $\Upsilon(4S)$ resonance (referred to as *continuum*). The integrated luminosity of these samples is 703 fb^{-1}, 121 fb^{-1} and 89 fb^{-1} respectively. Because of the different properties of the X(3872), produced in such samples, the different data types are treated separately. The X(3872) is reconstructed in the decay channel $J/\psi\pi^+\pi^-$. The J/ψ is reconstructed in the leptonic channels, either in the e^+e^- or in the $\mu^+\mu^-$. The final states that the Belle detector is able to track are therefore the two leptons (e^+e^-or $\mu^+\mu^-$), the two pions (π^+ and π^-) and additionally, a photon (γ) for correction of the bremsstralung in the decays of J/ψ to an electron and a positron. The decay channel was chosen due to the relative simplicity of the reconstruction (only four final states) and because the J/ψ has a clear signature in the leptonic decays. The chosen decay was also one of the most studied decays of the X(3872) in general and data exists on the dipion mass properties, as well.
The chosen variable to which the fit is performed is Δm, defined as

$$\Delta m = m_{X(3872)} - m_{J/\psi} - m_{\pi^+} - m_{\pi^-}. \tag{26}$$

The $m_{X(3872)}$ and the $m_{J/\psi}$ are the invariant masses, while masses of pions are the nominal masses presuming that the reconstructed particle is in fact a pion. The

subtraction of the $m_{J/\psi}$ takes care of the spread in the mass due to inaccuracy in the measurement of the lepton momentum. The same procedure is applied for the $\psi(2S)$ reconstruction.
It can be noted that the kinematics of the promptly produced X(3872) differ significantly from the X(3872) produced in decays of B mesons. More specifically, a kinematic cut-off can be determined for the X(3872) in order to distinguish between a promptly produced X(3872) and an X(3872) resulting from the decays of B mesons.
Because of this notion, the p_X^* is binned into 10 bins in the range from 0 - 4 GeV to enable the differentiation between different origins of the X(3872). The procedure above is also applied to the control channel.

3.3 MC GENERATION

3.3.1 *Signal MC*

Generation of the signal MC proved a hard nut to crack. Belle did not have an MC simulation of any process describing prompt production of charmonium. Even worse, the tools available in the older installations of the EvtGen at Belle did not allow such a simulation. The main demands for the simulations were: the simulation had to produce the X(3872) promptly; the momentum of the X(3872) had to cover all available phase space and obey the Peterson fragmentation function; alongside the X(3872), D mesons should be produced.
A simple trick allows us to achieve all the demands. At the desired energy the virtual photon is first decayed into the X(3872) and into another resonance, called here Y. The properties of the Y are as unidentifying as possible - it has a zero spin, its mass is above the open charm threshold and it is made extremely wide (~1 GeV). Such a resonance is in the next step decayed into c and $\bar{c}$, which are in turn hadronized by Pythia. Fig. 37 schematically shows the procedure.
While having fulfilled the first and last demand for the simulation, the shape of

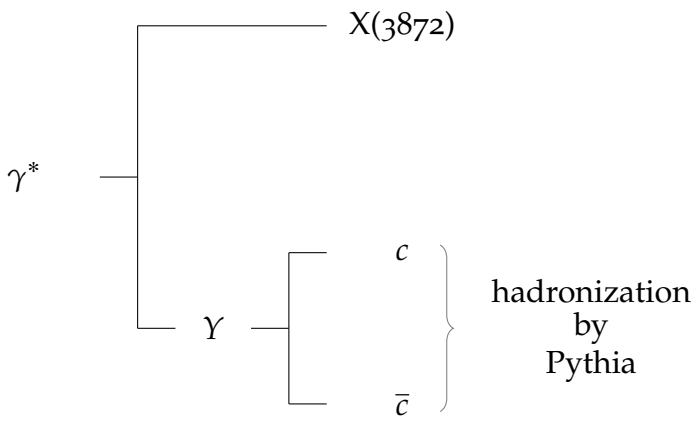

Figure 37: Schematic explanation of the signal MC generation.

	$\Upsilon(4S)$		$\Upsilon(5S)$		continuum	
	1 stream	5 streams	1 stream	5 streams	1 stream	5 streams
X_{ee}	1560	7800	265	1327	195	976
$X_{\mu\mu}$	1547	7735	263	1316	194	968
$\psi(2S)_{ee}$	10748	53740	1829	9146	1345	6727
$\psi(2S)_{\mu\mu}$	10658	53289	1814	9069	1334	6671
J/ψ_{ee}	31200	156001	5310	26549	3905	19527
$J/\psi_{\mu\mu}$	30929	154643	5264	26318	3872	19358

Table 8: Generated nr. of events for all signal-like simulations. All calculations based on the presumption $\sigma_{\text{prod}} == 0.74$ pb^{-1}.

the momentum distribution is not Peterson like. To achieve this, the normalized Peterson distribution for used parameters is compared to the given distribution over momentum. A weight is calculated and again normalized (w). For each event a random number r between 0 and 1 is generated. If the value of the w is larger than the r, the event is accepted, otherwise it is rejected. In such a way, a distribution over momentum that follows the Peterson fragmentation function is obtained (see Fig. 38). The model for the shape of the dipion mass is chosen to be the decay X(3872)$\rightarrow J/\psi\rho$, which is in most accordance with the CDF measurement of the dipion mass.
Three types of signal-like MC were generated: the X(3872)+$c\bar{c}$, the $\psi(2S)$+$c\bar{c}$, and the J/ψ+$c\bar{c}$. The number of generated events was calculated via the equation:

$$N_{\text{signal}} = \mathcal{L} * N_{\text{streams}} * \sigma_{\text{prod}} * BR(X(3872) \rightarrow J/\psi\rho) * BR(J/\psi \rightarrow l^+l^-) \quad (27)$$

for the X(3872) and the $\psi(2S)$ respectively or

$$N_{\text{signal}} = \mathcal{L} * N_{\text{streams}} * \sigma_{\text{prod}} * BR(J/\psi \rightarrow l^+l^-) \quad (28)$$

for the J/ψ.
In all cases, σ_{prod} is taken to be 0.74 pb^{-1}. N_{streams} accounts for the fact that the generic MC contains several *streams* of the simulations, each being equivalent to all gathered Belle data.

3.3.2 *Generic MC simulation*

The main purpose of the generic MC simulation is to describe all possible processes occurring in the detector, which in the analysis represent the background to the searched for signal. As in the signal part, the physical processes are simulated first and the simulation of the detector's response follows.
The generic MC simulation consists of three parts, depending on the beam energy. At the energy of the $\Upsilon(4S)$, four types of MC are produced: charged, mixed, charm, and uds. The former two simulate the production and decay of the $B^{\pm}$

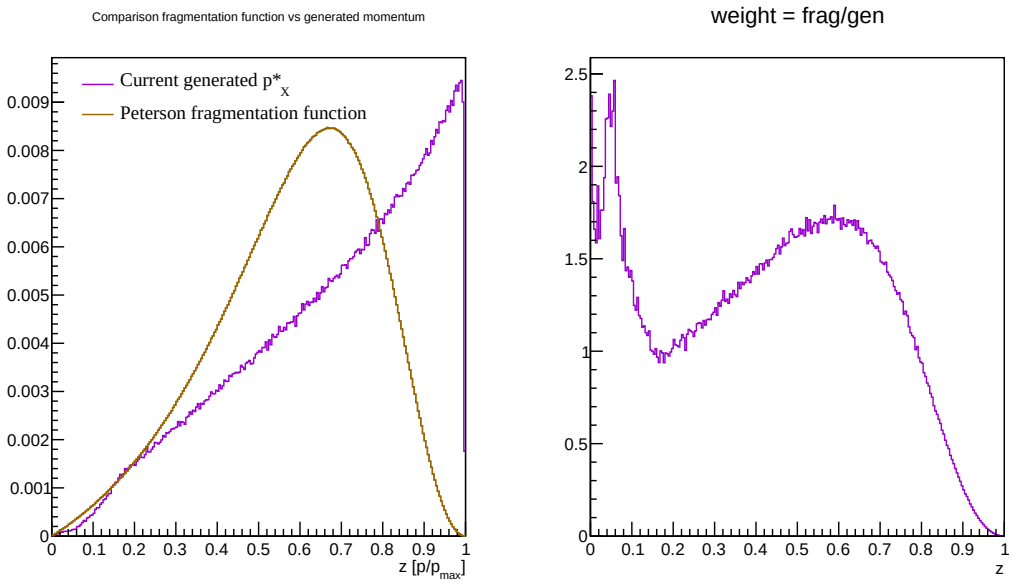

(a)

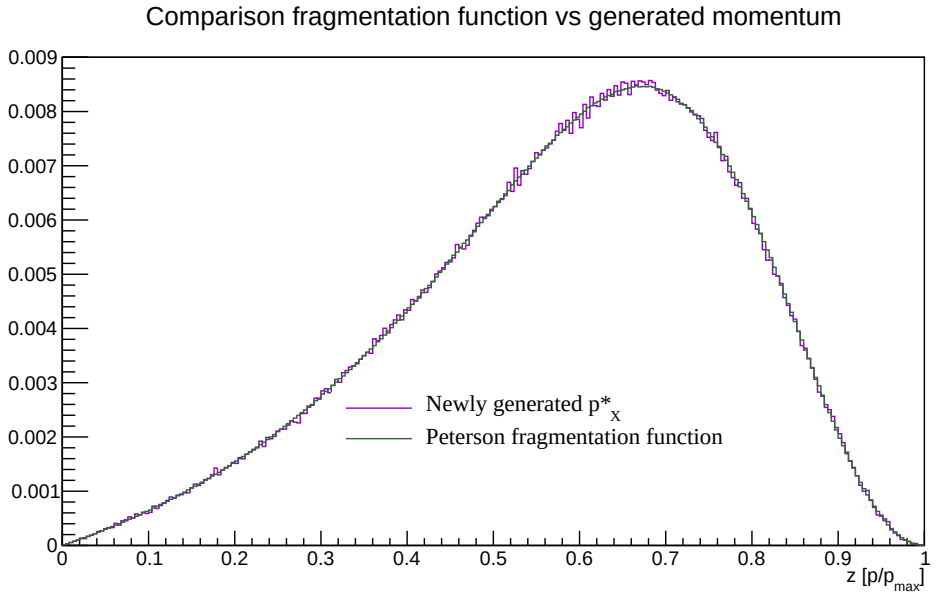

(b)

Figure 38: A schematic representation of the implemmentation of the Peterson fragmentation function. First, a comparison is made between the momentum, initially generated in the MC simulation and the desired Peterson fragmentation function; a weight is calculated. In the second step, a comparison is made between normalized weight and randomly assigned value between 0 and 1 to obtain the desired fragmentation shape.

or $B^0/\overline{B}^0$ mesons, the latter two the production and hadronization of the pair of quarks (either c and $\overline{c}$ in the case of the charm, and all three light quarks in the case of the uds). At 60 MeV under the $\Upsilon(4S)$, B mesons cannot form and the simulation contains only charm and uds types of MC. At the energy of the $\Upsilon(5S)$,

Decay channel	Belle MC assigned Br	current PDG value
$B^+ \rightarrow$X(3872)K^+	4×10^{-4}	$< 3.2 \times 10^{-4}$(90% CL)
$B^0 \rightarrow$X(3872)K^0	4×10^{-4}	/
$B^+ \rightarrow \psi(2S)$+ anything	29.67×10^{-4}	/
$B^0 \rightarrow \psi(2S)$+ anything	31.52×10^{-4}	/
X(3872)$\rightarrow J/\psi\rho$	0.366	> 0.026
X(3872)$\rightarrow J/\psi\omega$	0.402	> 0.019
$\psi(2S) \rightarrow J/\psi\pi^+\pi^-$	0.3170	0.3445 ± 0.0030
$\psi(2S) \rightarrow J/\psi\pi^0\pi^0$	0.1860	0.1813 ± 0.0031
$J/\psi \rightarrow e^+e^-$	0.0539	0.05971 ± 0.00032
$J/\psi \rightarrow \mu^+\mu^-$	0.0588	0.05961 ± 0.00033

Table 9: Comparison of values of the Belle generic MC simulation and the current PDG values [11] for the decays, used in the analysis. Quoted branching fractions for the B^+ and B^0 are also the values for the decays of the charge-conjugated counterparts, e.g. B^- and $\overline{B}^0$.

four types of MC are generated: the charm and the uds sample (describing the same processes as in the $\Upsilon(4S)$), the BsBs sample and the non-BsBs sample. As readily seen from the name, the BsBs is a sample in which the $\Upsilon(5S)$ decays to B_S and $\overline{B}_S$ mesons while in the non-BsBs sample the $\Upsilon(5S)$ immediately decays to a pair of B mesons with or without additional pion.
The generic MC, used in this analysis, has been produced by Belle in 2009. At the time, several properties of the X(3872) were not determined and the simulation is therefore somewhat limited. Of all the given samples, only three contain the decays to the X(3872): the charged and mixed sample at the $\Upsilon(4S)$ and the non-BsBs at the $\Upsilon(5S)$, all in the decay of B mesons to the X(3872) and a kaon. The charm samples do not include the X(3872); in fact, they do not include any charmonium state despite the possibility of prompt production, as discussed in Subsec.1.1.5. The mass of the X(3872) is set to 3.8714 GeV and the spin to 1. Since the mass of the X(3872) is being set under the open charm threshold, the decays of the X(3872) to D mesons are not included in the simulation. Table 9 summarizes the decay modes of the X(3872) in the generic part of the MC simulation. In [50], the lower limit for the BR(X(3872)$\rightarrow J/\psi\pi\pi$) is only 5×10^{-2}. The pessimistic scenario - BR(X(3872)$\rightarrow J/\psi\rho$) $= 5 \times 10^{-2}$ - is used in this analysis. In the Belle generic MC, the branching fraction for the process X(3872)$\rightarrow J/\psi\rho$ is set to 0.366. This means that all events of such type in the generic MC should be scaled down for the discrepancy for a factor of 7.322.

3.4 OPTIMIZATION OF SELECTION CRITERIA

3.4.1 *Reconstruction of the final particles*

Four types of final particles are reconstructed for each event: two leptons from the J/ψ (e^+e^- or $\mu^+\mu^-$) and two pions. Additionally, a photon has to be reconstructed to account for the bremsstralung in the $J/\psi \rightarrow e^+e^-$decays.
The identification of hadrons takes information from the $\frac{dE}{dx}$ measurements in the CDC, from the TOF detector and from the count of photoelectrons in the ACC. For the CDC measurements, the probability for the measured particle to be of type f can be expressed as

$$P_f^{dE/dx} = \frac{e^{-\frac{\chi^2}{2}}}{\sqrt{2\pi}\sigma_{dE/dx}}, \chi^2 = \left(\frac{(dE/dx)_{measured} - (dE/dx)_{f,expected}}{\sigma_{dE/dx}} \right)^2 . \tag{29}$$

Here, $\sigma_{dE/dx}$ is the expected resolution of dE/dx in the CDC.
The TOF probability exploits the difference between the measured and expected times for each photo-tube. The Eq. 30 shows how the probability is constructed.

$$\begin{aligned} &\Delta^i = t_o^i - t_p^i; \quad i = 0, 1; \\ &\chi^2 = \sum_j \vec{\Delta}_j E_j^{-1} \vec{\Delta}_j \end{aligned} \tag{30}$$

Δ^i is the difference between the observed and predicted time for individual photo-tube. E_j is the 2×2 error matrix for the j-th TOF hit vector $\vec{\Delta}_j$. The probability is finally constructed as a Gaussian distribution:

$$P_f^{TOF} = \frac{e^{\frac{-\chi^2}{2}}}{\sqrt{2\pi}\prod_j \sigma_j}, \tag{31}$$

where σ_j is the expected timing resolution.
The ACC is a threshold counter, meaning that the output of identification is a Heaviside function, defined as

$$P_f^{ACC} = \begin{cases} \varepsilon_f, & N_{pe} \geqslant N_{pe,f}^{th}, \\ 1 - \varepsilon_f, & N_{pe} \leqslant N_{pe,f}^{th}; \end{cases} \tag{32}$$

where ε_f is the expected efficiency for the hypothesis that a particle is in fact of type f.
The final probability for the reconstructed particle to match the identification hypothesis is simply a product of probabilities from the sub-detectors:

$$P_f = P_f^{dE/dx} \times P_f^{ACC} \times P_f^{TOF} \tag{33}$$

For the differentiation between the two types of hadrons a so called normalized probability is defined as

$$R_{f/f'} = \frac{P_f}{P_f + P_{f'}}. \tag{34}$$

The differentiation between kaons and pions, the R(K/π) is a typical example: in an ideal detector, the kaon probability would be a δ function at 1, and the pion probability a δ function at 0. In a realistic detector, the probability function smears as seen from the Fig. 39.

Identification of electrons is also done with combining information from three

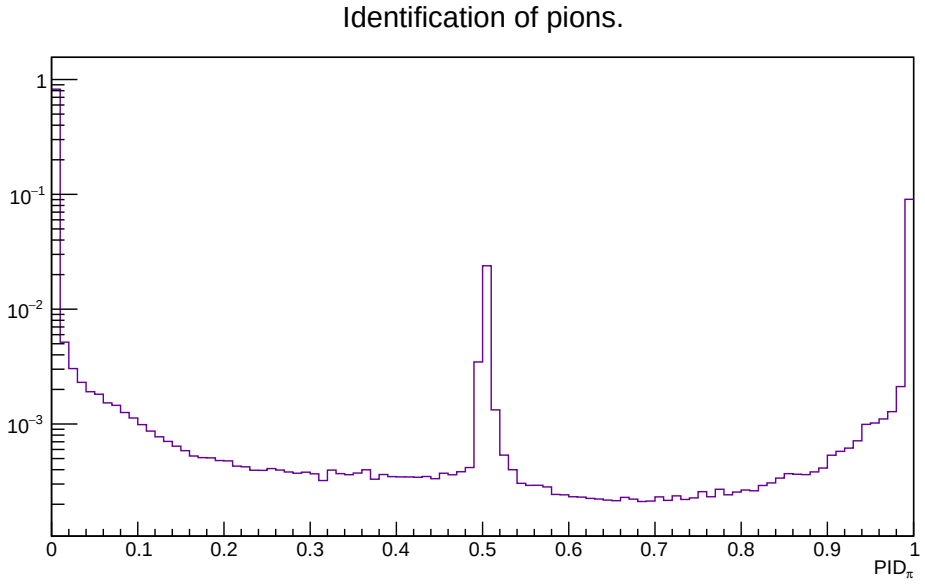

Figure 39: Example of the function for hadrons, differentiation K/π.

sub-detectors: the shape and the position of the shower in the ECL, the measurement of ionization loss dE/dx and the comparison of the track in the CDC, and the number of photoelectrons in the ACC. From all the listed properties, Belle has devised a function L_{eid} defined as:

$$L_{eid} = \frac{\Pi_{i=1}^{n} L_e(i)}{\Pi_{i=1}^{n} L_e(i) + \Pi_{i=1}^{n} L_{\bar{e}}(i)}, \tag{35}$$

where $L_e(i)$ is a function, describing probability that in the i-th subdetector, the reconstructed particle is in fact an electron. Contrary, $L_{\bar{e}}(i)$ is a similar function, describing probability that the particle is not an electron. The L_{eid} is not a simple probability because the different methods of the identification are correlated; however, it suffices for effective separation of electrons from other particles.

Muons are identified similarly as electrons. Additional information is gathered from the extrapolation of the track, obtained in the CDC, to the outer KLM detector. If the momentum is known from the tracking of the CDC, the approximate range in the KLM can be estimated. When the hypothesized and measured position in the KLM differ, the reconstructed particle is probably a hadron, not a muon. The identification function is again defined between 0 and 1 as a comparison between probabilities for a muon, pion, and kaon:

$$L_\mu = \frac{P_\mu}{P_\mu + P_\pi + P_K}. \tag{36}$$

An example of the described probability can be seen on Fig. 40.

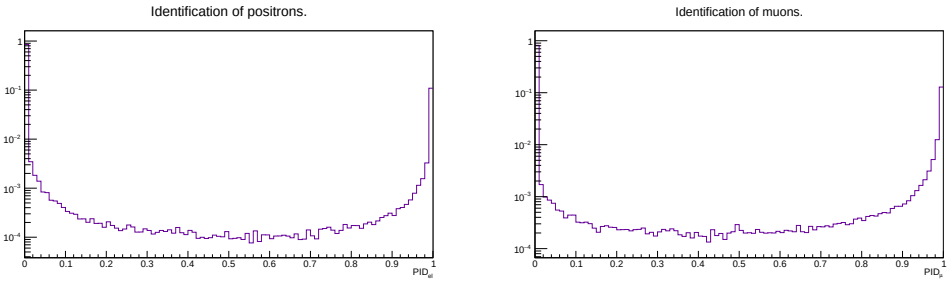

(a) PID for electrons. (b) PID for muons.

Figure 40: General example of the lepton identification.

3.4.2 *FOM*

The idea of the figure-of-merit (FOM) optimization is determination of selection criteria for the selected decay modes. Of all the possible events gathered by the detector, the combination of selection criteria should most efficiently separate the chosen decays from the remaining processes, which represent the background. For this purpose, the FOM, defined as

$$\mathrm{FOM} = \frac{N_{\mathrm{sig}}}{\sqrt{N_{\mathrm{sig}} + N_{\mathrm{bkg}}}} \tag{37}$$

should be maximized. The FOM is not calculated on the entire range, later used for fitting. It is customary to choose the signal window in width of $\pm 3\sigma$ where σ denotes the width of the true signal. For this analysis, it means the interval of $[0.489, 0.503]$ GeV for the Δm of X(3872) and $[0.303, 0.317]$ GeV for the Δm of $\psi(2S)$.

3.4.2.1 *Preselection*

The preselection, called HadronB was used as the first step in the FOM optimization. The HadronB preselection is used by the Belle collaboration as a first step of rejecting background to a signal. In this case, the background are the processes that are not experimentally interesting (e.g., $\tau\tau$, $\gamma\gamma$) and the signal processes are the $B\overline{B}$ and $q\overline{q}$ processes. The preselection requires the following:

- *number of charged tracks*; the QED background and the two-photon processes rarely exhibit more than three charged tracks. To remove background from such events, each event has to contain at least three charged tracks.
- *energy loss in the detector*; the measured energy in the ECL should be larger than $0.2\sqrt{s}$.
- *sum of momenta in the z-direction*; the sum of momenta of all produced particles from the $\Upsilon(4S)$resonance is close to 0 in the z-direction. This enables differentiation of such events with events that are a consequence

process	efficiency (ε_{Had})
$B\overline{B}$	0.991
$q\bar{q}$	0.795
$\tau^+\tau^-$	0.049
QED	0.00002
$\gamma\gamma$	0.004

Table 10: Efficiencies for different processes for the HadronB preselection [51]. The $q\bar{q}$ process contains processes with quarks u, d, s, and c.

of a scattering in the vacuum tube where the sum of momenta in the z-direction does not equal 0.

- *position of the primary interaction*; to further exclude all events that originate in the scattering of particles of the walls of the vacuum tube or on the remains of the gas in the tube, the point of primary interaction is within measuring accuracy limited to the interaction point of the positron and electron.

The efficiencies of the HadronB procedure are listed in Table 10.

3.4.2.2 *Resulting cuts*

Optimization of the FOM is performed with respect to several quantities.
First, the goodness of the identification of the final particles is taken into account. The resulting values are rounded up to the values for which an estimation of the systematic error exists.

- $\text{PID}_{leptons} > 0.8$
- $\text{PID}_{pions} < 0.3$

Secondly, moving on to the reconstructed particles, the χ^2 of the vertex fit has to be smaller than 20.
With the reconstructed particles, two other quantities are taken into account: the cut around the expected mass of the $J/\psi$and the cut on the dipion mass. The cut around the expected mass of the J/ψ ensures better identification of the true J/ψ; the cut around the dipion mass dicards the low-lying contributions, which are less likely for the signal. The dipion cut is performed only in the reconstruction of the X(3872), which proved unuseful for the $\psi(2S)$.
The values of the cuts are presented in Table 11 . In each item, the sample ($\Upsilon(4S)$, $\Upsilon(5S)$, or continuum) is marked, alongside with the reconstructed channel (X_{ee} or $X_{\mu\mu}$ for the decays of X(3872), where the resulting J/ψ decays to e^+e^-or $\mu^+\mu^-$, respectively; similar for the $\psi(2S)$).

Another measure is taken into account - if even after applying all the cuts, there are still multiple candidates in the event, the candidate with the smallest χ^2 is chosen.

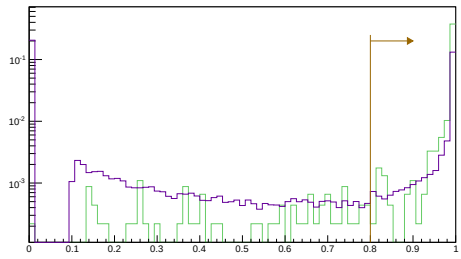

(a) Cut on the PID of the electrons.

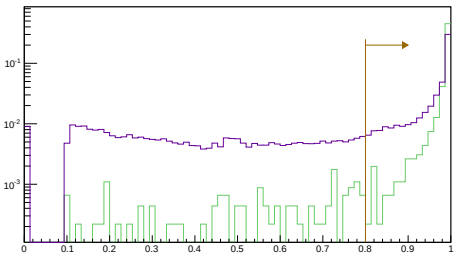

(b) Cut on the PID of the muons.

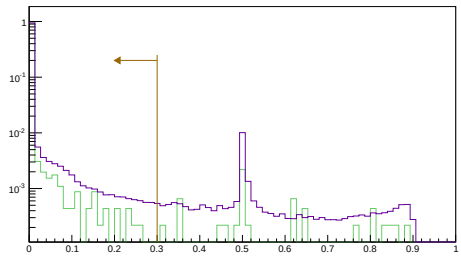

(c) Cut on the PID of the pions.

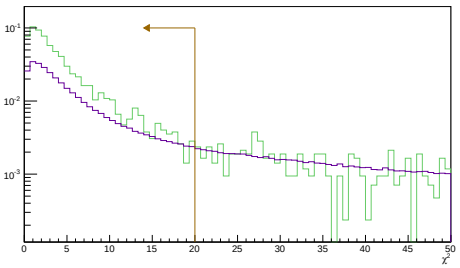

(d) Cut on the χ^2 of the vertex fit.

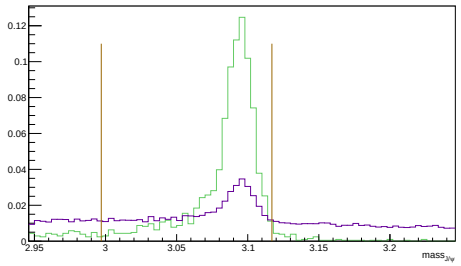

(e) Cut around nominal value of the J/ψ_{ee} (mass$_{J/\psi}$ in units GeV).

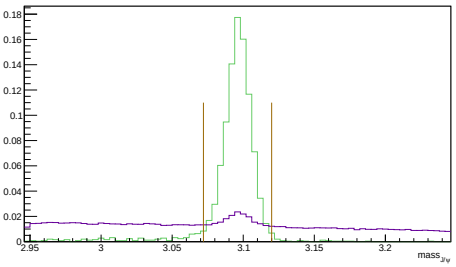

(f) Cut around nominal value of the $J/\psi_{\mu\mu}$ (mass$_{J/\psi}$ in units GeV).

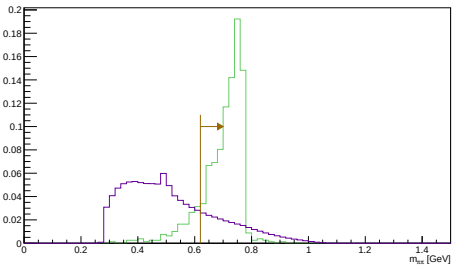

(g) Cut on the dipion mass.

Figure 41: Examples of the cuts applied for the optimization of the FOM. All examples are taken from the reconstruction in the continuum sample; for the dipion mass in the reconstruction of the X(3872) and for all the rest in the reconstruction of the $\psi(2S)$. The green color depicts the signal and the violet the background distributions. All plots are normalized to enable comparison between the two. The orange arrow shows the applied cut.

sample	variable	$X(3872)_{ee}$	$X(3872)_{\mu\mu}$	$\psi(2S)_{ee}$	$\psi(2S)_{\mu\mu}$
$\Upsilon(4S)$	$\Delta m_{J/\psi}$	[-0.102,0.018]	[-0.021,0.021]	[-0.1,0.03]	[-0.03,0.03]
	$m_{\pi\pi}$	> 0.72	> 0.68	/	/
continuum	$\Delta m_{J/\psi}$	[-0.069,0.027]	[-0.015,0.015]	[-0.099,0.021]	[-0.024,0.024]
	$m_{\pi\pi}$	>0.62	>0.66	/	/
$\Upsilon(5S)$	$\Delta m_{J/\psi}$	[-0.132,0.03]	[-0.054,0.054]	[-0.12,0.056]	[-0.052,0.052]
	$m_{\pi\pi}$	>0.68	>0.68	/	/

Table 11: Cuts for all reconstructed modes and samples as obtained with the FOM procedure. All values have units of GeV.

bin nr	p^* region in [GeV]
0	[0.0, 0.4]
1	[0.4, 0.8]
2	[0.8, 1.2]
3	[1.2, 1.6]
4	[1.6, 2.0]
5	[2.0, 2.4]
6	[2.4, 2.8]
7	[2.8, 3.2]
8	[3.2, 3.6]
9	[3.6, 4.0]

Table 12: Connection between bin number and region in p^*.

3.4.2.3 *Efficiencies*

For all the samples and modes of the reconstruction, the efficiency is calculated. The efficiency indicates how many events can be correctly reconstructed in the given sample:

$$\varepsilon = \frac{N_{\text{correctly reconstructed}}}{N_{\text{generated}}}. \tag{38}$$

Table 12 connects the bin number with the range in the p^*.

Tables 13-18 give efficiencies in the individual bins of different samples. The results of the efficiency calculation are also given in Fig. 42.

bin nr	ε_{ee}	$\sigma_{\varepsilon_{ee}}$	$\varepsilon_{\mu\mu}$	$\sigma_{\varepsilon_{\mu\mu}}$
0	0.167	0.104	0.115	0.070
1	0.049	0.022	0.250	0.055
2	0.085	0.018	0.214	0.029
3	0.099	0.015	0.196	0.021
4	0.097	0.012	0.171	0.016
5	0.091	0.010	0.186	0.015
6	0.098	0.009	0.195	0.014
7	0.101	0.009	0.188	0.013
8	0.095	0.008	0.188	0.012
9	0.088	0.010	0.239	0.022

Table 13: Reconstruction efficiency of the X(3872) as a function of $p*_X$ in the $\Upsilon(4S)$ sample.

bin nr	ε_{ee}	$\sigma\varepsilon_{ee}$	$\varepsilon_{\mu\mu}$	$\sigma_{\varepsilon_{\mu\mu}}$
0	0.204	0.071	0.114	0.054
1	0.095	0.019	0.189	0.029
2	0.112	0.014	0.133	0.0147
3	0.101	0.009	0.155	0.012
4	0.128	0.009	0.196	0.011
5	0.135	0.007	0.167	0.008
6	0.154	0.007	0.205	0.009
7	0.143	0.006	0.226	0.008
8	0.161	0.006	0.227	0.007
9	0.190	0.008	0.267	0.011

Table 14: Reconstruction efficiency of the $\psi(2S)$ as a function of $p*_{\psi(2S)}$ in the $\Upsilon(4S)$ sample.

bin nr	ε_{ee}	$\sigma_{\varepsilon_{ee}}$	$\varepsilon_{\mu\mu}$	$\sigma_{\varepsilon_{\mu\mu}}$
0	0.107	0.009	0.205	0.013
1	0.103	0.005	0.207	0.007
2	0.099	0.004	0.205	0.005
3	0.101	0.003	0.204	0.004
4	0.101	0.002	0.203	0.003
5	0.104	0.002	0.200	0.003
6	0.108	0.002	0.201	0.003
7	0.110	0.002	0.202	0.003
8	0.114	0.003	0.205	0.004
9	0.130	0.011	0.209	0.014

Table 15: Reconstruction efficiency of the X(3872) as a function of $p*_X$ in the $\Upsilon(5S)$ sample.

bin nr	ε_{ee}	$\sigma_{\varepsilon_{ee}}$	$\varepsilon_{\mu\mu}$	$\sigma_{\varepsilon_{\mu\mu}}$
0	0.101	0.016	0.219	0.025
1	0.110	0.009	0.179	0.012
2	0.107	0.006	0.162	0.008
3	0.111	0.005	0.166	0.006
4	0.123	0.005	0.176	0.005
5	0.127	0.004	0.185	0.005
6	0.144	0.004	0.205	0.005
7	0.161	0.004	0.223	0.005
8	0.161	0.006	0.233	0.007
9	0.178	0.014	0.240	0.017

Table 16: Reconstruction efficiency of the $\psi(2S)$ as a function of $p*_{\psi(2S)}$ in the $\Upsilon(5S)$ sample.

bin nr	ε_{ee}	$\sigma_{\varepsilon_{ee}}$	$\varepsilon_{\mu\mu}$	$\sigma_{\varepsilon_{\mu\mu}}$
0	0.130	0.008	0.192	0.010
1	0.133	0.005	0.187	0.006
2	0.138	0.004	0.183	0.004
3	0.142	0.004	0.178	0.005
4	0.143	0.003	0.169	0.003
5	0.144	0.002	0.169	0.003
6	0.148	0.002	0.168	0.002
7	0.155	0.002	0.169	0.002
8	0.158	0.002	0.171	0.002
9	0.159	0.002	0.175	0.002

Table 17: Reconstruction efficiency of the X(3872) as a function of $p*_X$ in the continuum sample.

bin nr	ε_{ee}	$\sigma_{\varepsilon_{ee}}$	$\varepsilon_{\mu\mu}$	$\sigma_{\varepsilon_{\mu\mu}}$
0	0.068	0.035	0.159	0.065
1	0.093	0.022	0.106	0.025
2	0.099	0.016	0.120	0.018
3	0.111	0.014	0.159	0.016
4	0.115	0.011	0.178	0.014
5	0.126	0.011	0.184	0.013
6	0.138	0.011	0.193	0.013
7	0.127	0.013	0.195	0.016
8	0.179	0.027	0.180	0.027
9	0.273	0.178	0.256	0.019

Table 18: Reconstruction efficiency of the $\psi(2S)$ as a function of $p*_{\psi(2S)}$ in the continuum sample.

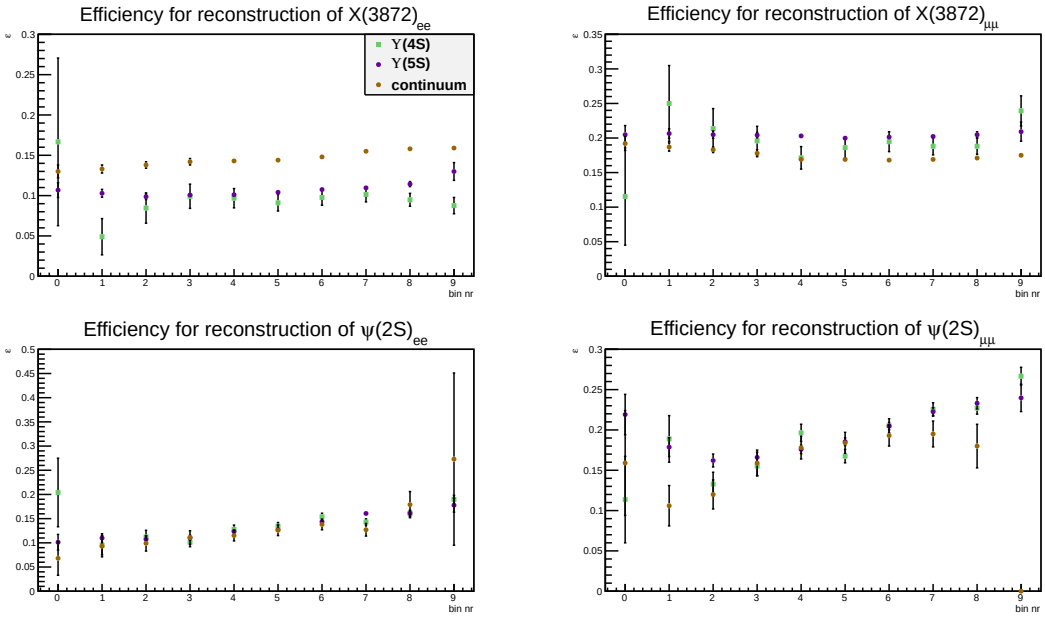

Figure 42: Reconstruction efficiencies for different samples and modes of reconstruction.

3.5 RESULTS OF RECONSTRUCTION ON MC

3.5.1 *Measurement of σBr*

Fig. 43 to Fig. 48 show the results of the reconstruction on the MC.
Expected values for the peak of the Δm distribution for the X(3872) and the $\psi(2S)$ are 0.495 GeV and 0.31 GeV, respectively. An interval of ± 100 MeV is chosen for the representation of the distribution. The distribution is binned in 150 bins for the $\Upsilon(4S)$ (75 bins for the $\Upsilon(5S)$, continuum).
As already explained in Subsec. 3.3.2, the contribution of $B \rightarrow$X(3872) + anything is overrated by a factor of 7.3 and all the events of this type are scaled for the discrepancy.
All the graphs exhibit similar behavior: a more or less dominant peak from the correctly reconstructed X(3872) ($\psi(2S)$) on the smooth background. No peaking background is detected. A clear pattern emerges especially in the case of the $\psi(2S)$ reconstruction: in the first four bins, the contribution from B mesons is pronounced and in the last 5 bins, the contribution from the promptly produced $\psi(2S)$ is prominent; all this is due to the kinematic cut-off for the production of the $\psi(2S)$ (X(3872)) from the B mesons, compared to the kinematic range of the X(3872)($\psi(2S)$) in the prompt production. A simple shape of the mass difference distribution allows for a simple fit function.
Fig. 49 shows the sources of the background for the $\psi(2S)$. The majority of background comes from the correctly reconstructed J/ψ, originating from the decays of the B mesons. This can be clearly seen as a predominant contribution from the charged and mixed type of MC in the $\Upsilon(4S)$sample; the charged and mixed type of MC describe the decays of the B mesons, produced at the $\Upsilon(4S)$. No such contribution is seen for the uds and the charm type of MC, since these types of MC do not contain the J/ψ. The correctly reconstructed J/ψ is combined with two (random) pions to result in a smooth combinatorial background. Similar can be seen in the case of the $\Upsilon(5S)$. In this case, the non-BsBs is the predominant source of the background, again due to the presence of the J/ψ. The continuum sample differs from the two previous ones because it does not contain the J/ψ in the generic part of the simulation; no prevalent pattern emerges in the origin of the combinatorial background.

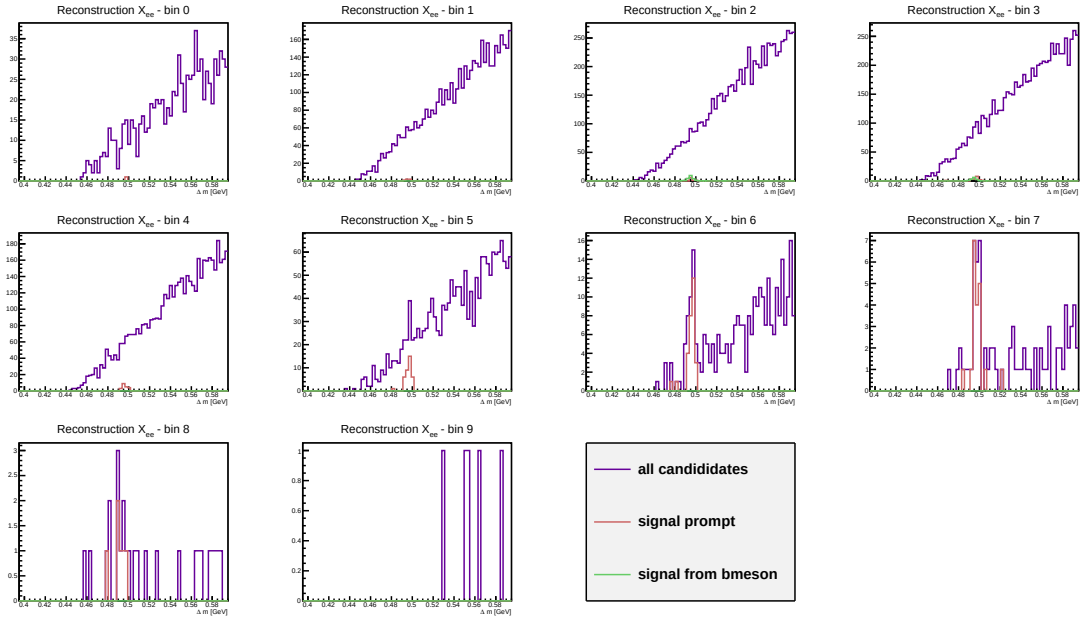

(a) Reconstruction of the X(3872)$_{ee}$

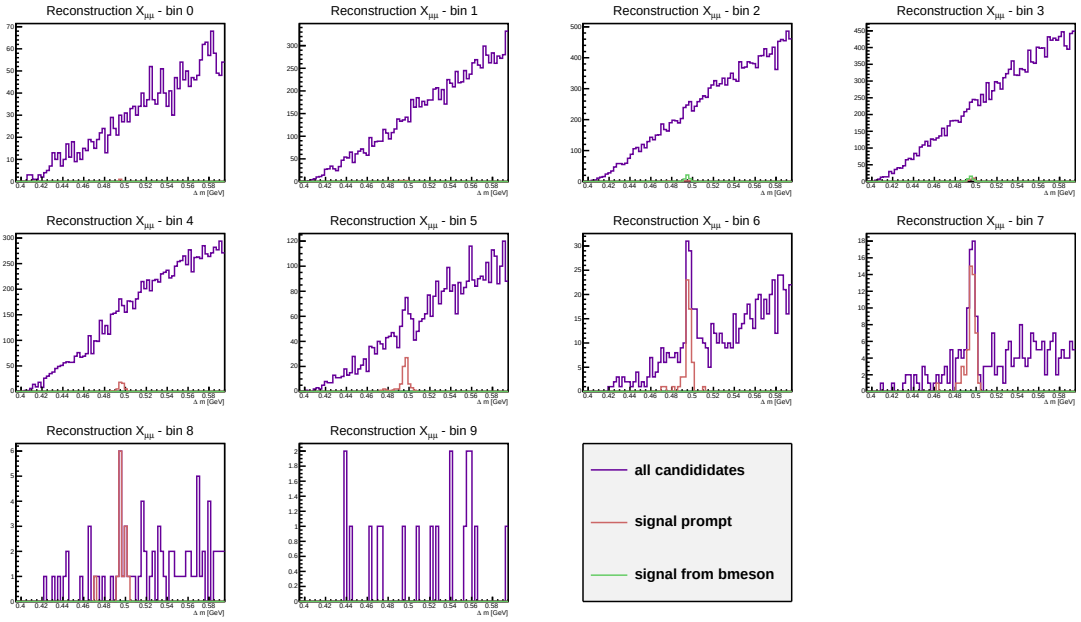

(b) Reconstruction of the X(3872)$_{\mu\mu}$.

Figure 43: Example of a reconstruction of the X(3872) on the $\Upsilon(4S)$ sample (1 stream). The green denotes the promptly produced X(3872), the red the X(3872), originating from the decays of the B mesons. MC simulation.

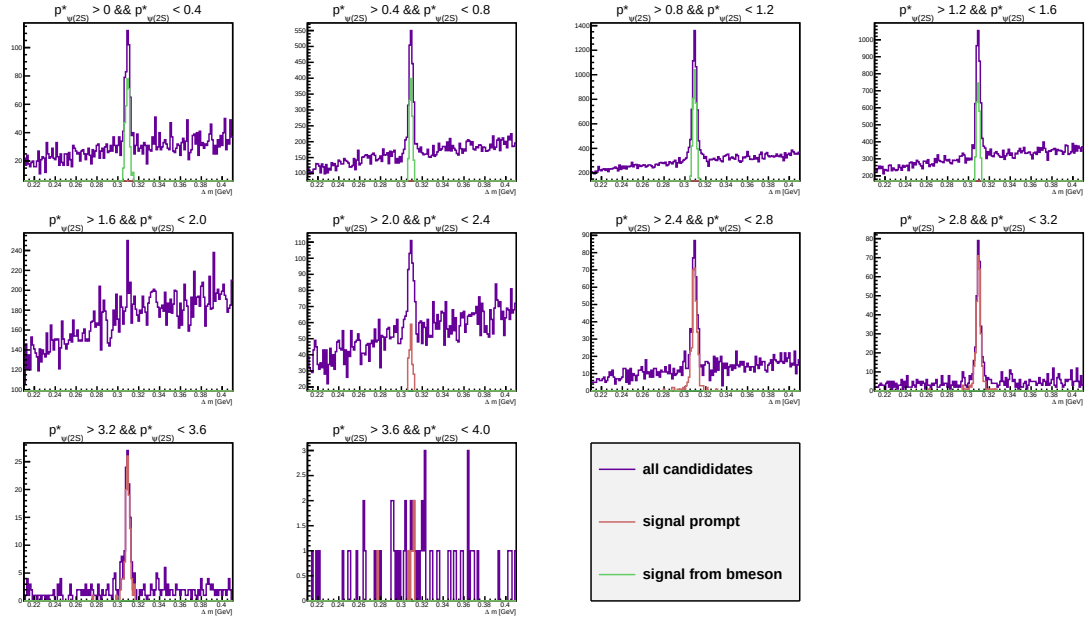

(a) Reconstruction of $\psi\,(2S)_{ee}$

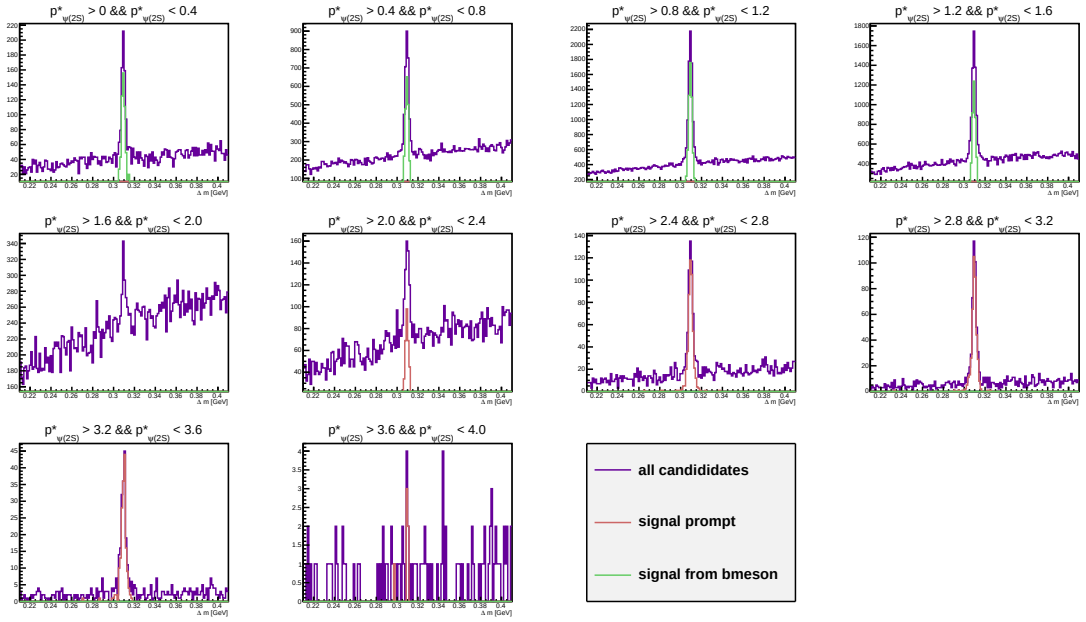

(b) Reconstruction of $\psi\,(2S)_{\mu\mu}$.

Figure 44: Example of a reconstruction of the $\psi\,(2S)$ on the $\Upsilon\,(4S)$ sample (1 stream). The green denotes the promptly produced $\psi\,(2S)$, the red the $\psi\,(2S)$, originating from the decays of the B mesons. MC simulation.

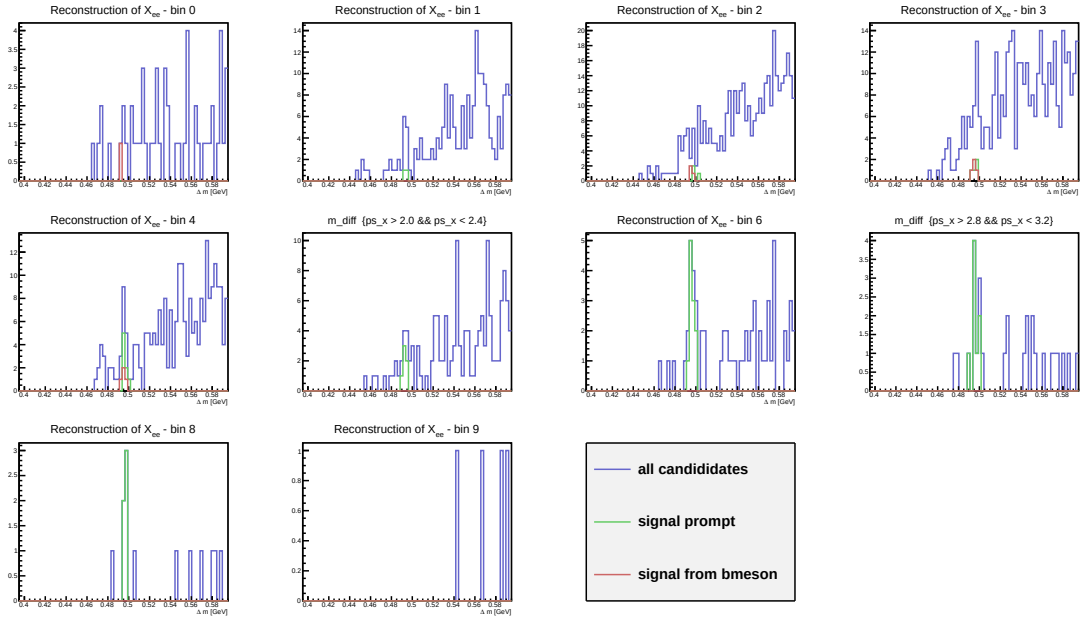

(a) Reconstruction of the X(3872)$_{ee}$

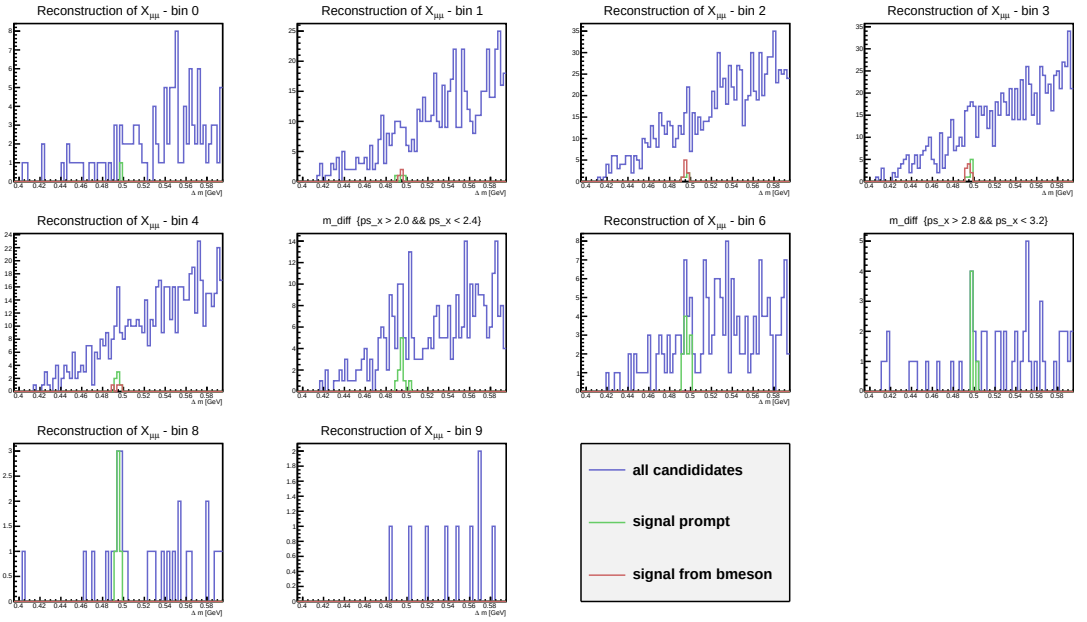

(b) Reconstruction of the X(3872)$_{\mu\mu}$.

Figure 45: Example of a reconstruction of the X(3872) on the Υ (5S) sample (1 stream). The green denotes the promptly produced X(3872), the red the X(3872), originating from the decays of the B mesons. MC simulation.

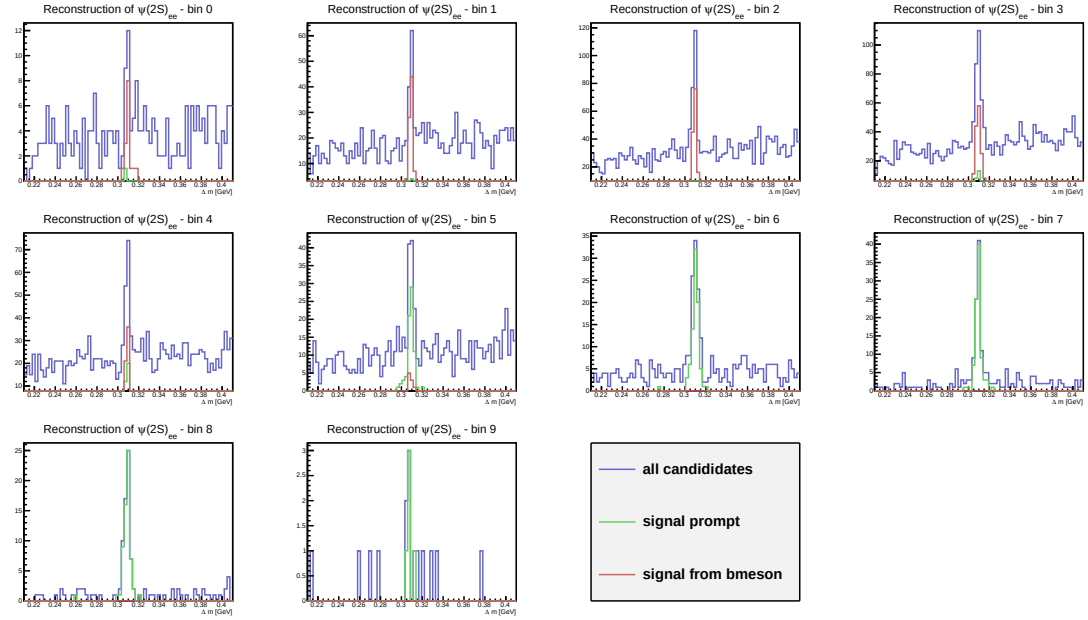

(a) Reconstruction of $\psi(2S)_{ee}$

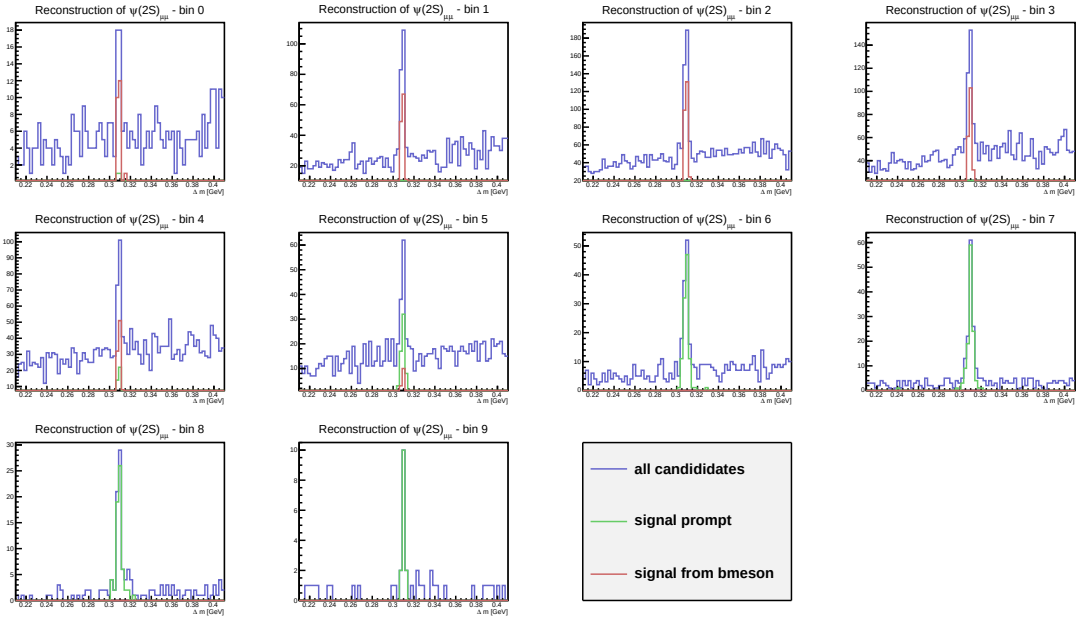

(b) Reconstruction of $\psi(2S)_{\mu\mu}$.

Figure 46: Example of a reconstruction of the $\psi(2S)$ on the $\Upsilon(5S)$ sample (1 stream). The green denotes promptly produced $\psi(2S)$, the red $\psi(2S)$, originating from the decays of the B mesons. MC simulation.

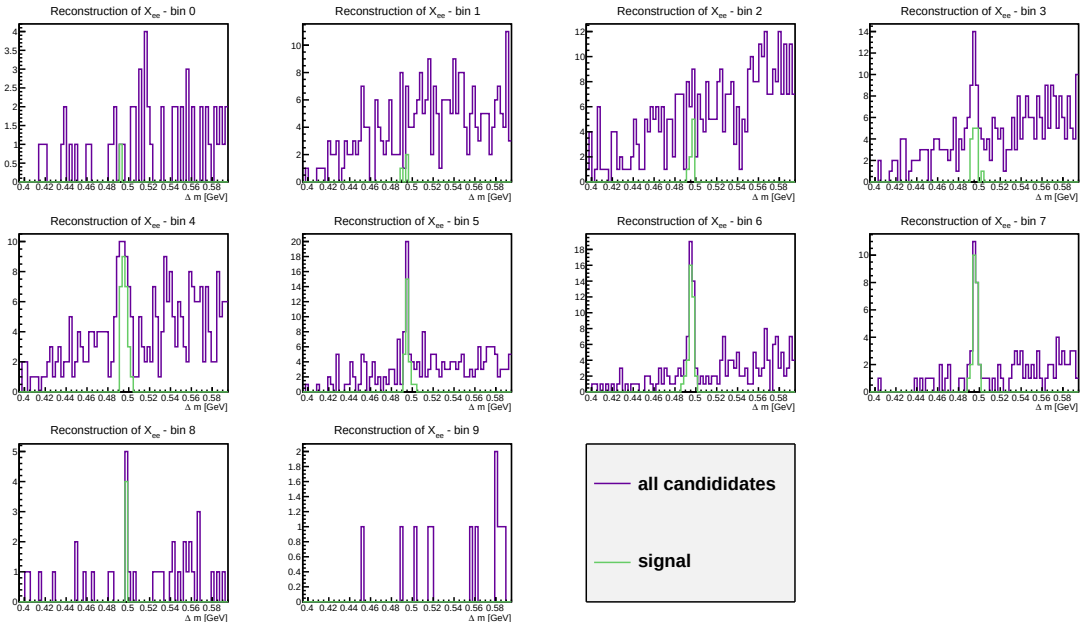

(a) Reconstruction of the X(3872)$_{ee}$

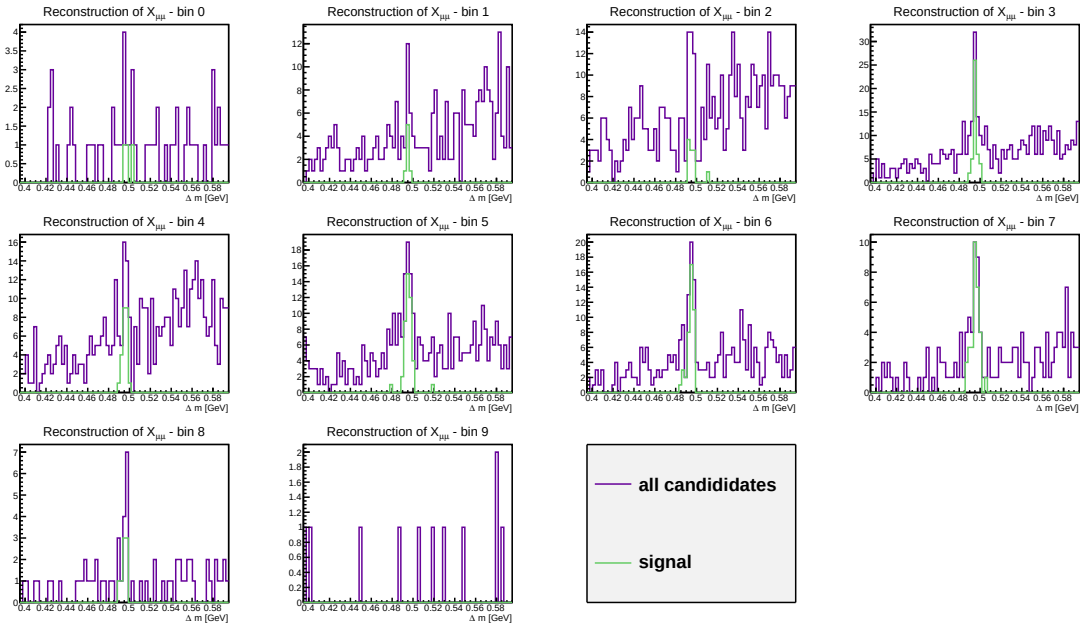

(b) Reconstruction of the X(3872)$_{\mu\mu}$.

Figure 47: Example of a reconstruction of the X(3872) on the continuum sample (5 streams). The green denotes the promptly produced X(3872). MC simulation.

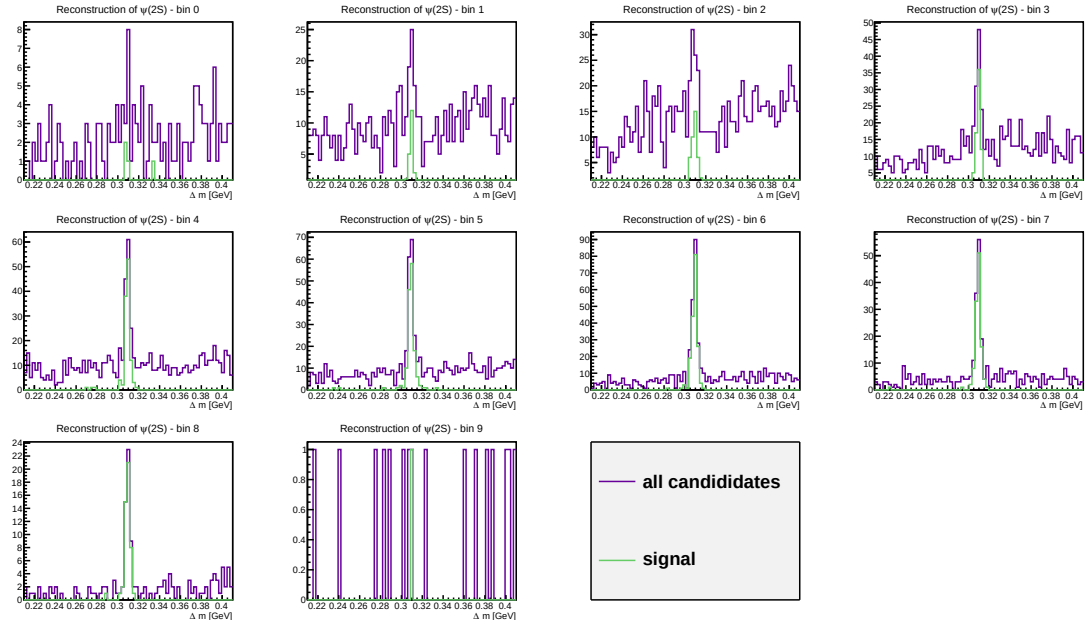

(a) Reconstruction of $\psi(2S)_{ee}$

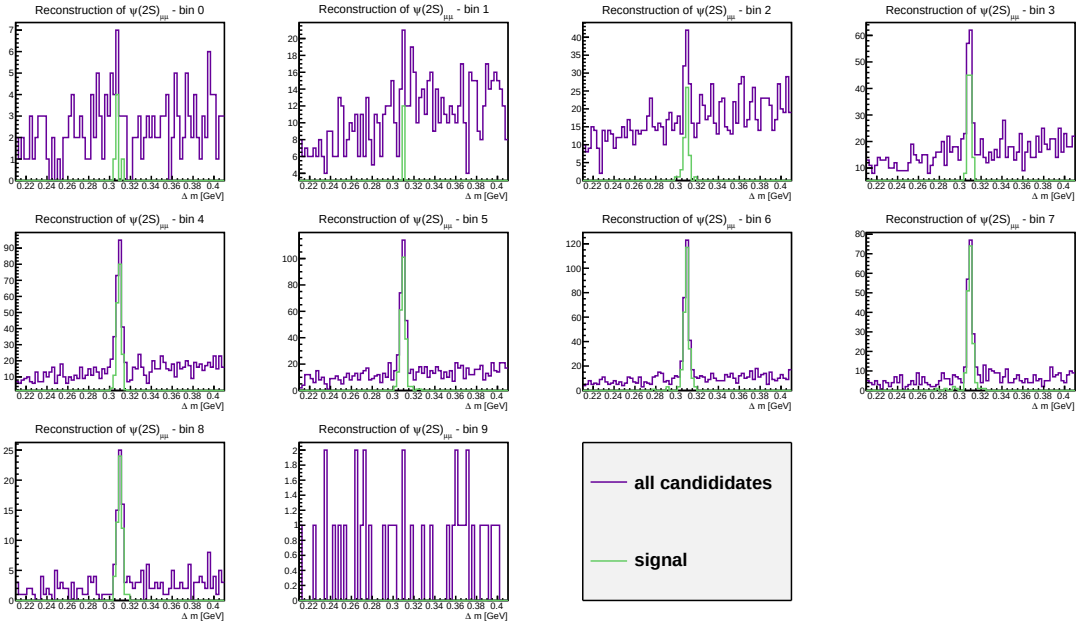

(b) Reconstruction of $\psi(2S)_{\mu\mu}$.

Figure 48: Example of a reconstruction of the $\psi(2S)$ on the continuum sample (5 streams). The green denotes the promptly produced $\psi(2S)$. MC simulation.

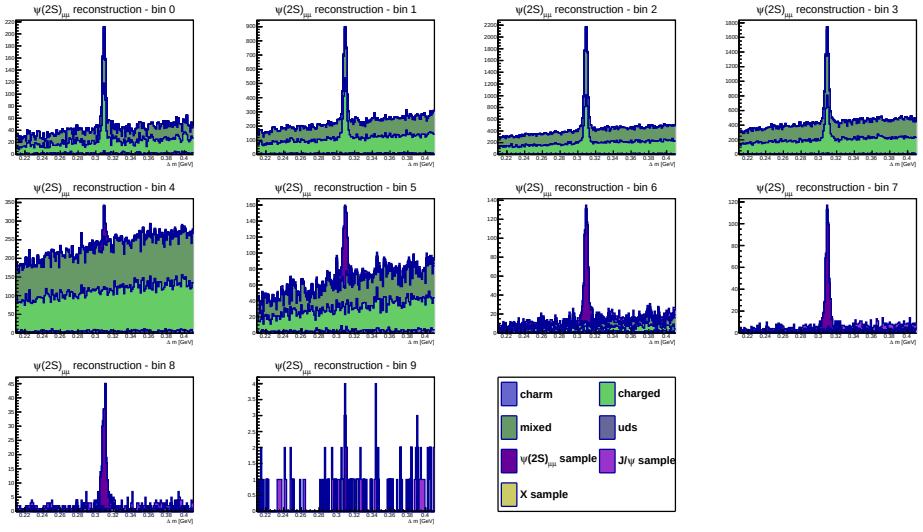

(a) Reconstruction of $\psi(2S)_{\mu\mu}$ - 1 stream of $\Upsilon(4S)$ MC.

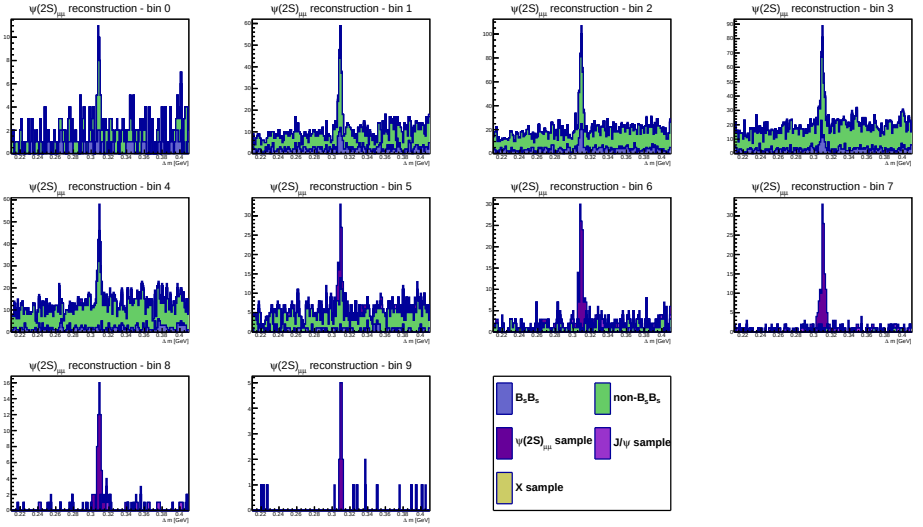

(b) Reconstruction of $\psi(2S)_{\mu\mu}$ - 1 stream of $\Upsilon(5S)$ MC.

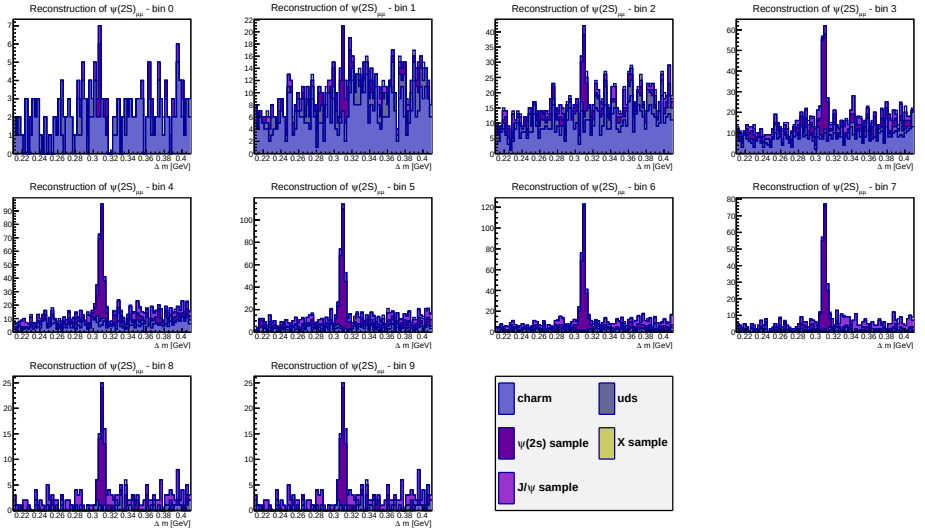

(c) Reconstruction of $\psi(2S)_{\mu\mu}$ - 5 streams of the continuum MC.

Figure 49: Origins of background for reconstructed $\psi(2S)_{\mu\mu}$ for different MC samples.

4

FITS TO THE RECONSTRUCTION ON THE MC

The fitting procedure, described in this chapter, was done in the RooFit environment [52]. RooFit is a framework for fitting, plotting and toy Monte Carlo generation. It introduces the concept of the PDF (probability density function) $F(\vec{x};\vec{p},\vec{q})$ that is normalized over the allowed range of the observables $\vec{x}$ with respect to the parameters $\vec{p}$ and $\vec{q}$. Fitting in RooFit is based on the maximum likelihood fit. Let $P(X|\alpha)$ be a probability of measuring X on a given event. Here, α is a parameter (or a set of parameters) on which the P depends. Generally, a series of measurements is performed in the experiment and a set of X_i is obtained. The likelihood function is then defined as

$$L = \prod_{i=1}^{N} P(X_i|\alpha). \tag{39}$$

The aim of the fitting is to obtain the value of α that maximizes the L. Often, the $\ln L$ is used to determine the maximum likelihood.
The aim of this analysis is to give value of $\sigma_{\text{prod}}\ \text{Br}(X(3872) \to J/\psi\pi^+\pi^-)$ for which the distribution over Δm is chosen as the fitted variable. A simple relation between the number of signal events, efficiency, luminosity[1], and the σBr is

$$\begin{aligned} N_{ee} &= N_{\text{stream}}\ \mathcal{L}\ \sigma_{\text{prod}}\ \text{Br}(X(3872) \to J/\psi\pi^+\pi^-)\ \text{Br}(J/\psi \to e^+e^-)\ \varepsilon_{ee}; \\ N_{\mu\mu} &= N_{\text{stream}}\ \mathcal{L}\ \sigma_{\text{prod}}\ \text{Br}(X(3872) \to J/\psi\pi^+\pi^-)\ \text{Br}(J/\psi \to \mu^+\mu^-)\ \varepsilon_{\mu\mu}. \end{aligned} \tag{40}$$

σBr can be expressed for both reconstruction channels (electronic and muonic) as

$$\sigma_{\text{prod}}\ \text{Br}(X(3872) \to J/\psi\pi^+\pi^-) = \frac{N_{ee}}{\mathcal{L}\ \text{Br}(J/\psi \to e^+e^-)\ \varepsilon_{ee}} = \frac{N_{\mu\mu}}{\mathcal{L}\ \text{Br}(J/\psi \to \mu^+\mu^-)\ \varepsilon_{\mu\mu}}. \tag{41}$$

This leads to a decision for a simultaneous fit. Instead of fitting the individual channels and then merging the results, both channels are treated simultaneously. As shown in Ch. 3, the reconstructed distribution over Δm exhibits a simple pattern - a smooth (combinatorial) background and a peak for the signal.
The signal part is described with three Gaussians as

$$\text{S} = \text{N}_{\text{sig}}\left(\text{f}_1\ \text{G}_1(\Delta\text{m}_{01},\sigma_1) + \text{f}_2\ \text{G}_2(\Delta\text{m}_{02},\sigma_2) + (1-\text{f}_1-\text{f}_2)\ \text{G}_3(\Delta\text{m}_{03},\sigma_3)\right). \tag{42}$$

1 The N_{streams} is added because the fit is done on the MC where several streams of MC can be used.

	X_{ee}	$X_{\mu\mu}$	$\psi(2S)_{ee}$	$\psi(2S)_{\mu\mu}$
Δm_{01} [GeV]	0.4957	0.4956	0.3092	0.3095
Δm_{02} [GeV]	0.4943	0.4820	0.2861	0.2951
Δm_{03} [GeV]	0.4840	0.4950	0.3093	0.3091
σ_1 [GeV]	0.0024	0.0022	0.0017	0.0020
σ_2 [GeV]	0.0066	0.0329	0.0382	0.0301
σ_3 [GeV]	0.0460	0.0066	0.0040	0.0048
f_1	0.822	0.767	0.770	0.765
f_2	0.155	0.013	0.020	0.037

Table 19: Results of the fit to a signal-only sample.

Here, the Gaussians are defined as

$$G_i = \frac{1}{\sqrt{2\pi}\sigma_i} \exp\left[-\frac{(\Delta m - m_{i0})^2}{2\sigma_i^2}\right] \tag{43}$$

m_{0i} describe the central value and the σ_i the variance of the individual Gaussians. f_i represent the fractions of the individual Gaussians for the total yield.
A smooth background calls for use of polynomials to fit the distribution. Due to their numerical stability, Chebyshev polynomials are chosen for fits of the background. The RooFit framework uses Chebyshev polynomials of the first kind; the first six polynomials are given below.

$$\begin{aligned}
T_0(x) &= 1 \\
T_1(x) &= 2x \\
T_2(x) &= 4x^2 - 1 \\
T_3(x) &= 8x^3 - 4x \\
T_4(x) &= 16x^4 - 12x^2 + 1 \\
T_5(x) &= 32x^5 - 32x^3 + 6x
\end{aligned}$$

RooFit assigns a coefficient to each polynomial, so that function describing background reads as $N_{bkg} = \sum_i \alpha_i T_i$. The coefficients α_i are defined in the range of [-1,1]. Usage of Chebyshev polynomials up to the third order suffices for the fit of the background.
The fit is first tested on a signal-only sample in order to get the parameters, describing Gaussians. For all the following fits, the central values, variances, and the fractions of yields are fixed to the results from the signal-only fit. The fixed parameters are given in Table 19 and the shape of the Gaussians is given in Fig. 50.

After obtaining fixed fit parameters from the signal-only sample, the fitting procedure can be performed on the generic MC, too. The free parameters of the

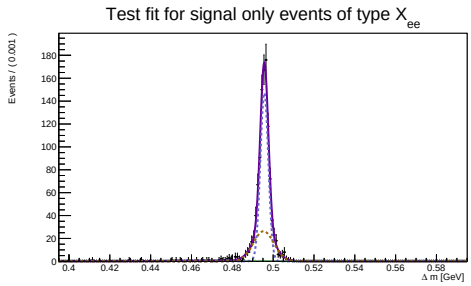

(a) X_{ee} reconstruction.

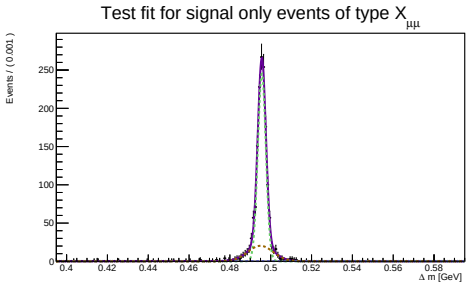

(b) $X_{\mu\mu}$ reconstruction.

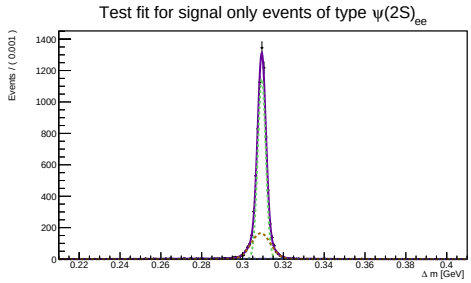

(c) $\psi\,(2S)_{ee}$ reconstruction.

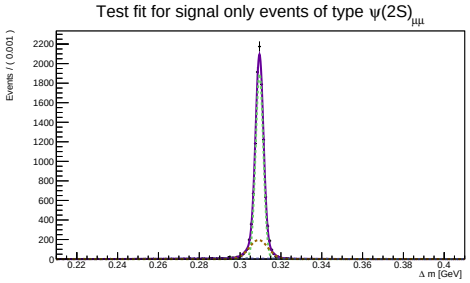

(d) $\psi\,(2S)_{\mu\mu}$ reconstruction.

Figure 50: Example of a fit on the signal only sample to obtain the fixed parameters.

fit are the number of background events in the muonic and electronic channel (separately), the parameters, describing the shape of the background (the α_i of the Chebychev polynomials), and the product of the production cross section and the branching fraction for the decay to $J/\psi\pi\pi$ ($\sigma_{prod}\mathrm{BR}(X(3872) \to J/\psi\pi\pi)$). An example of such a fit is given on Fig. 51. The fits are presented in Fig. 52 to Fig. 56.

The results of the fit on the generic MC for the X(3872) are given in Fig. 58-Fig. 56. The comparison between the counted (i.e., MC truth checked events) and the results of the fit are given together with the fit result for the product of production cross section and the branching fraction for decay to the $J/\psi\pi\pi$. The comparison shows that the fit describes the observed distributions well - number of counted and fitted events match within 1σ uncertainties.

Because of low expected number of events in the continuum sample, the fit is performed on the complete region of p_X^* (Fig. 57). An simple justification is that the continuum sample does not contain the X(3872) from the B mesons and as such lacks their contribution in the lower region of p_X^*. Again, the number of counted signal events corresponds to the fitted number of events within 1σ uncertainty.

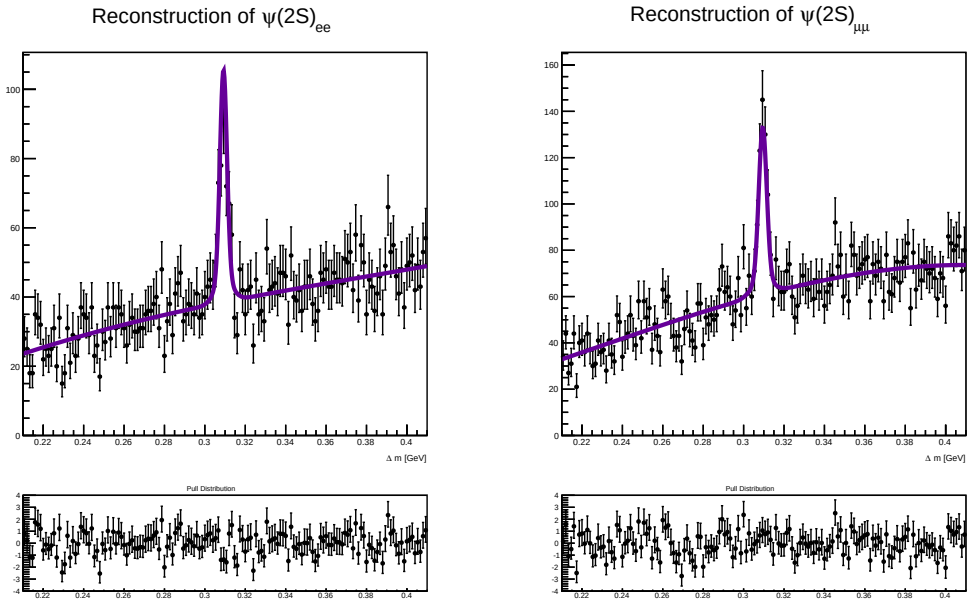

Figure 51: Example of a fit on the generic MC. $\psi(2S)$ reconstruction, bin 5 in the $\Upsilon(4S)$ sample. Dots - results of reconstruction, violet line - result of the fit. The bottom two plots present the pull of these fits.

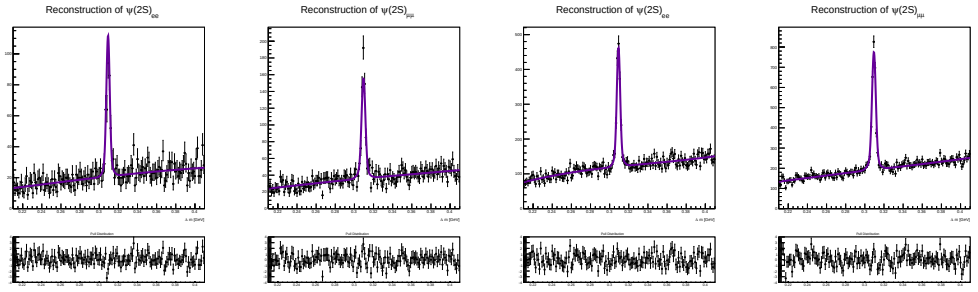

(a) Bin 0 (b) Bin 1

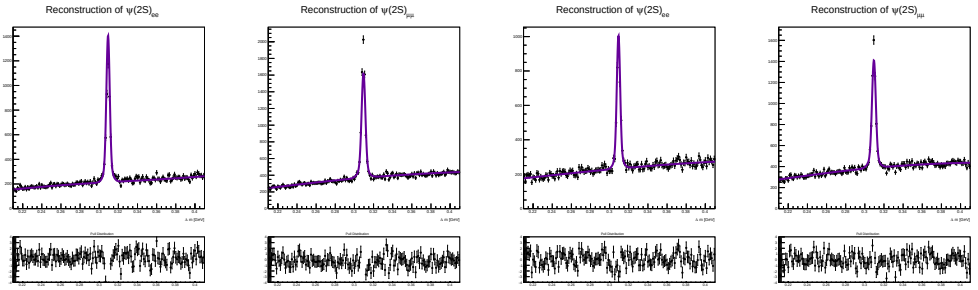

(c) Bin 2 (d) Bin 3

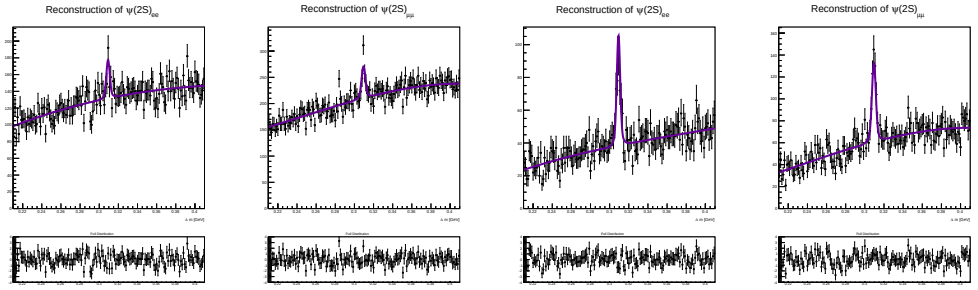

(e) Bin 4 (f) Bin 5

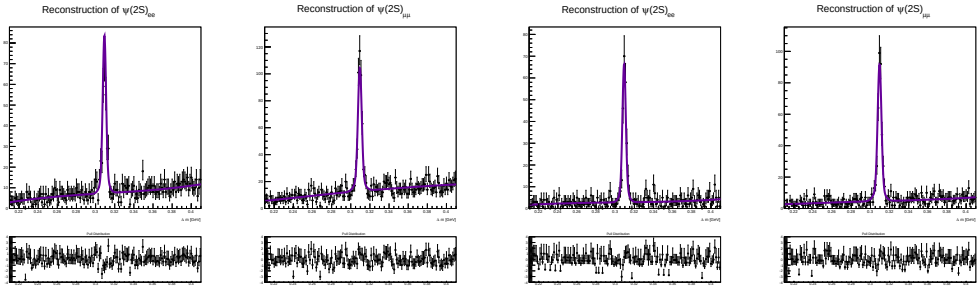

(g) Bin 6 (h) Bin 7

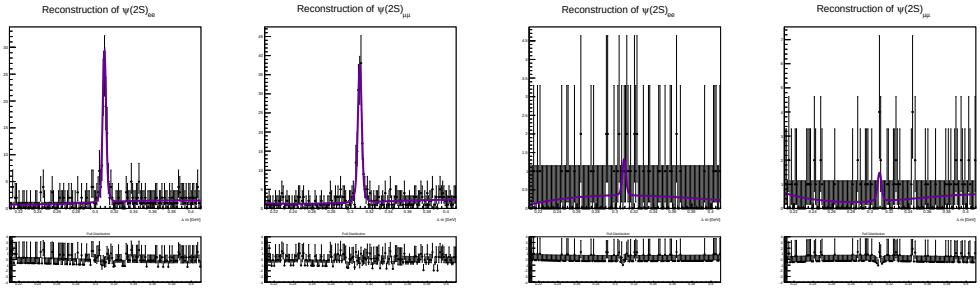

(i) Bin 8 (j) Bin 9

Figure 52: Fits to reconstructed $\psi(2S)$ in the $\Upsilon(4S)$ sample. In each subfigure, the plot on the left is reconstructed $\psi(2S)_{ee}$, and on the right, reconstructed $\psi(2S)_{\mu\mu}$. Number of the bin is marked below the subfigure.

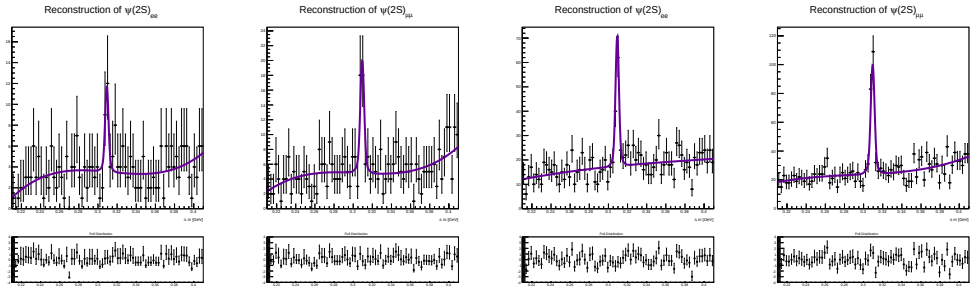

(a) Bin 0 (b) Bin 1

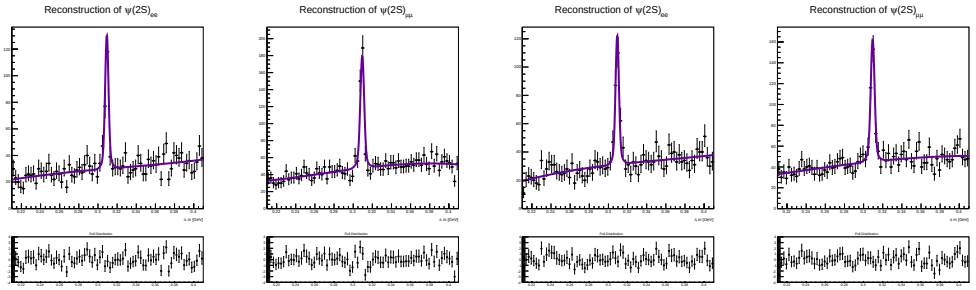

(c) Bin 2 (d) Bin 3

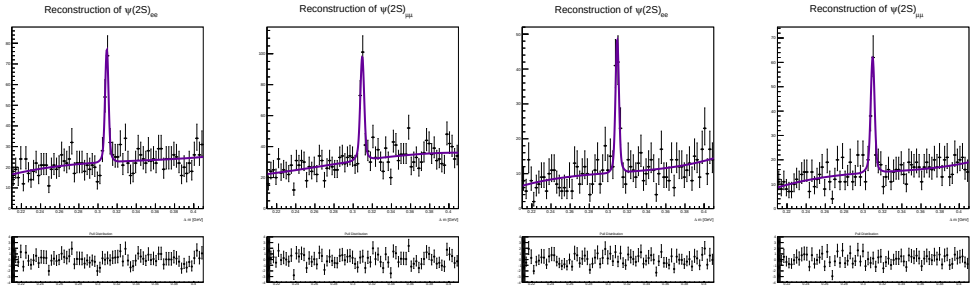

(e) Bin 4 (f) Bin 5

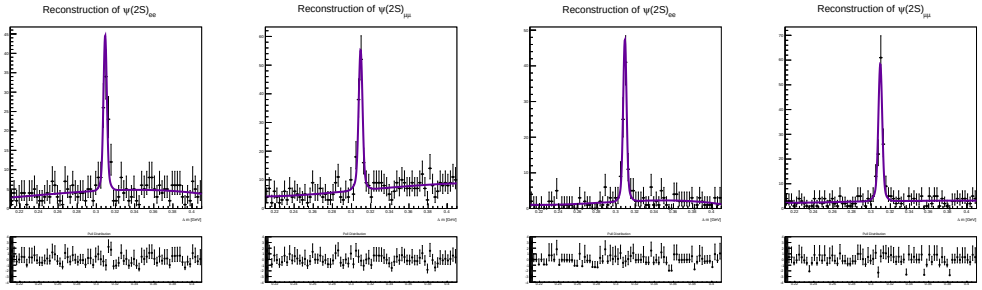

(g) Bin 6 (h) Bin 7

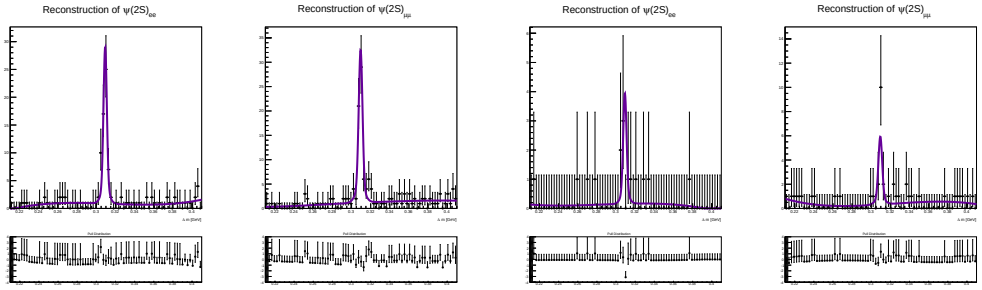

(i) Bin 8 (j) Bin 9

Figure 53: Fits to reconstructed $\psi(2S)$ in the $\Upsilon(5S)$ sample. In each subfigure, the plot on the left is reconstructed $\psi(2S)_{ee}$, and on the right, reconstructed $\psi(2S)_{\mu\mu}$. Number of the bin is marked below the subfigure.

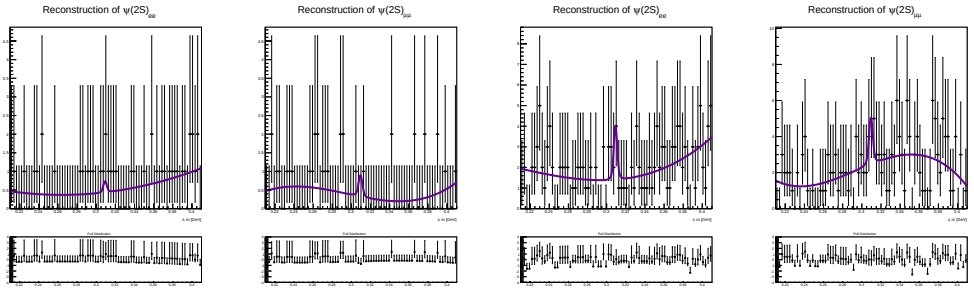

(a) Bin 0

(b) Bin 1

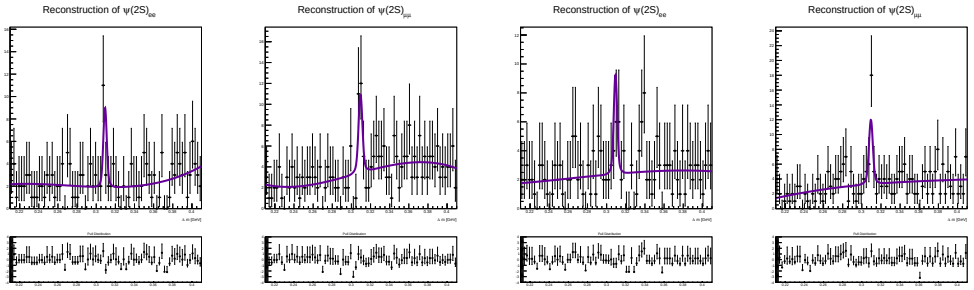

(c) Bin 2

(d) Bin 3

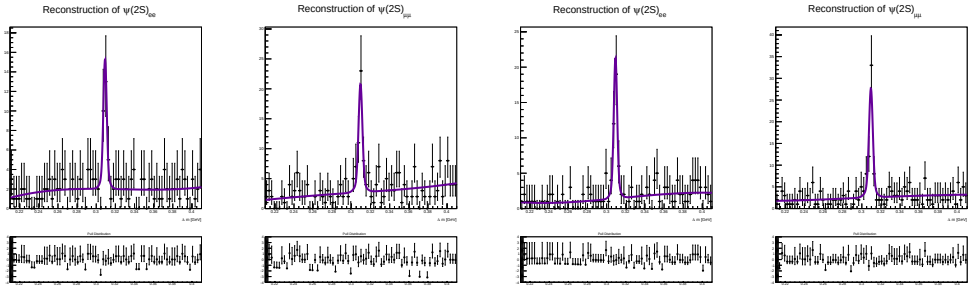

(e) Bin 4

(f) Bin 5

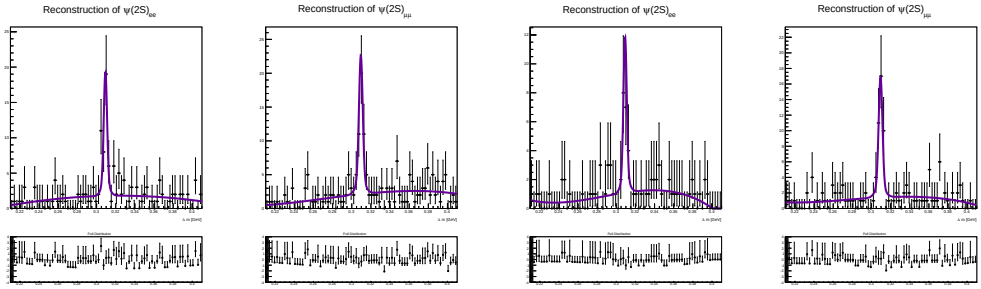

(g) Bin 6

(h) Bin 7

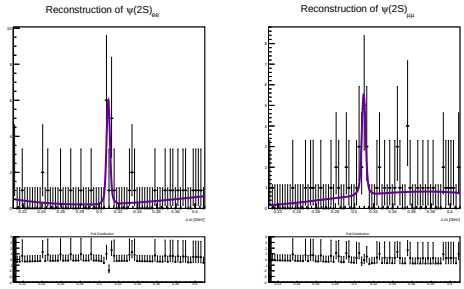

(i) Bin 8

Figure 54: Fits to reconstructed $\psi(2S)$ in the continuum sample. In each subfigure, the plot on the left is reconstructed $\psi(2S)_{ee}$, and on the right, reconstructed $\psi(2S)_{\mu\mu}$. Number of the bin is marked below the subfigure.

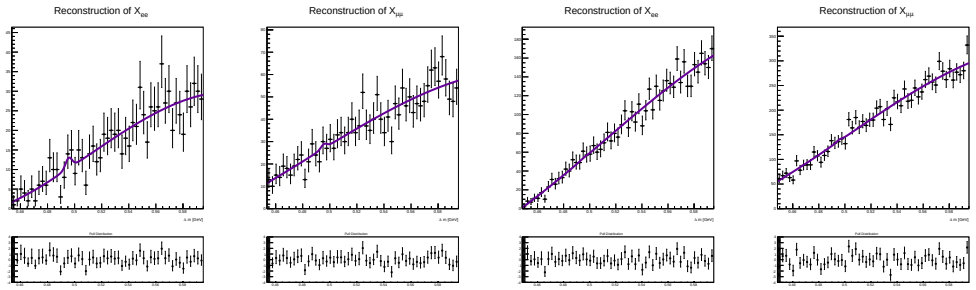

(a) Bin 0 (b) Bin 1

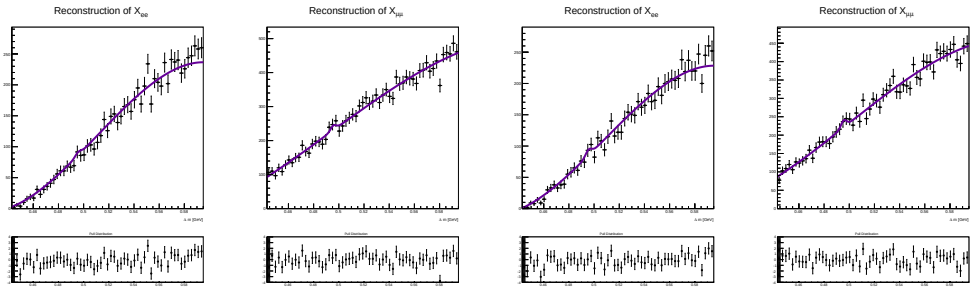

(c) Bin 2 (d) Bin 3

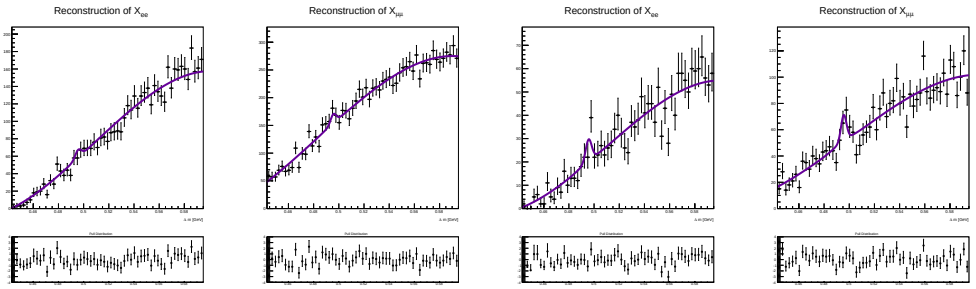

(e) Bin 4 (f) Bin 5

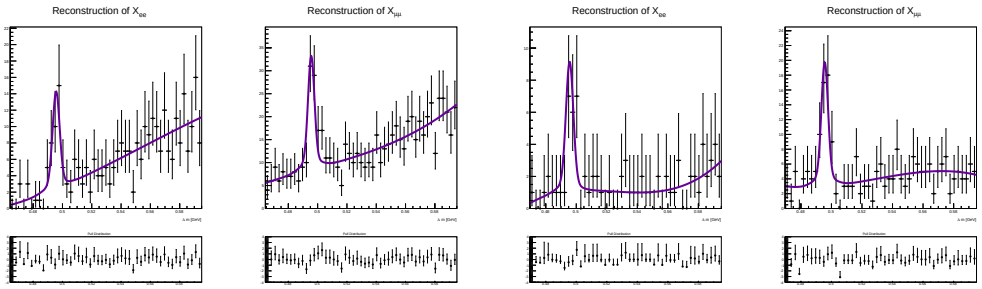

(g) Bin 6 (h) Bin 7

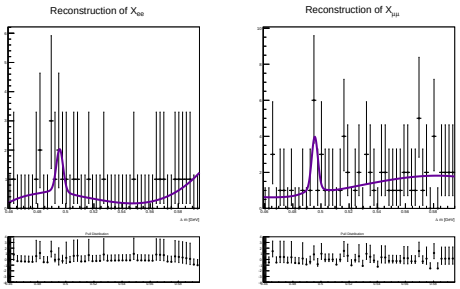

(i) Bin 8

Figure 55: Fits to reconstructed X(3872) in the $\Upsilon(4S)$ sample. In each subfigure, the plot on the left is reconstructed X(3872)$_{ee}$, and on the right, reconstructed X(3872)$_{\mu\mu}$. Number of the bin is marked below the subfigure.

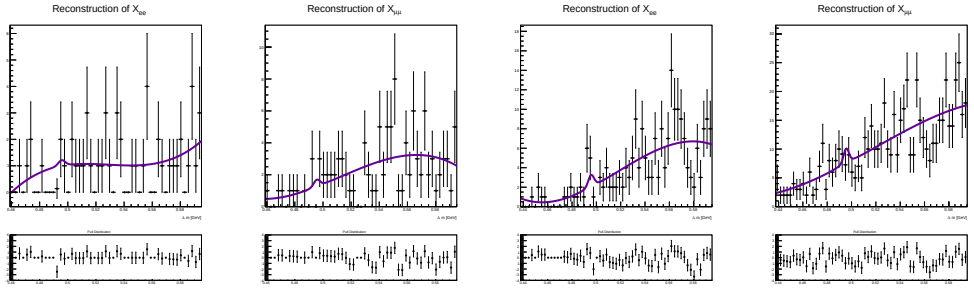

(a) Bin 0 (b) Bin 1

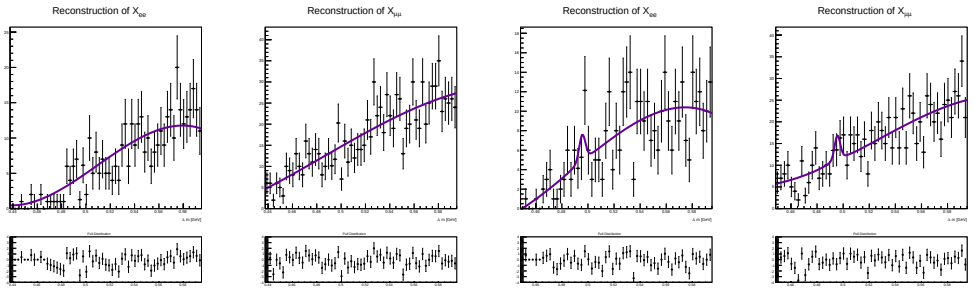

(c) Bin 2 (d) Bin 3

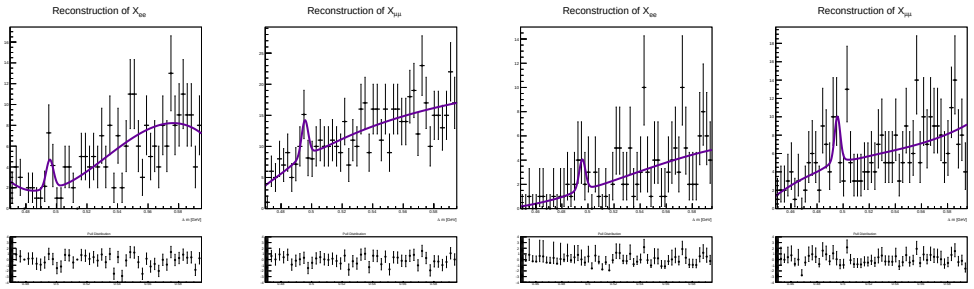

(e) Bin 4 (f) Bin 5

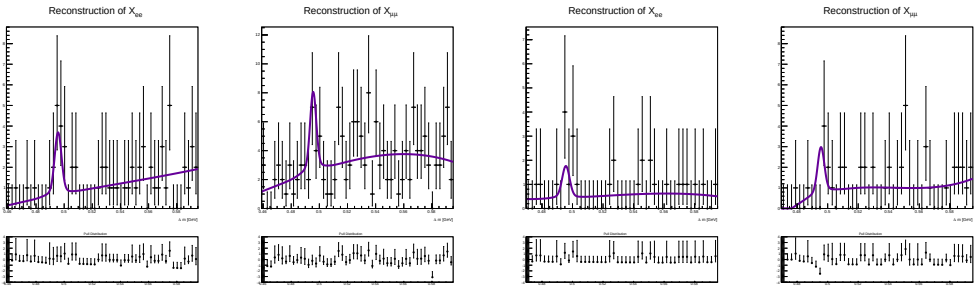

(g) Bin 6 (h) Bin 7

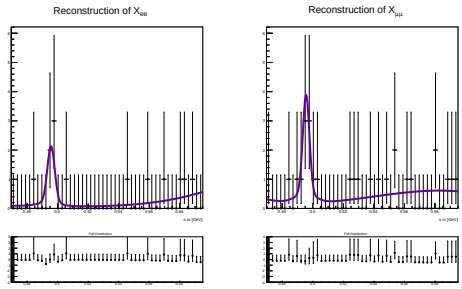

(i) Bin 8

Figure 56: Fits to reconstructed X(3872) in the $\Upsilon(5S)$ sample. In each subfigure, the plot on the left is reconstructed $X(3872)_{ee}$, and on the right, reconstructed $X(3872)_{\mu\mu}$. Number of the bin is marked below the subfigure.

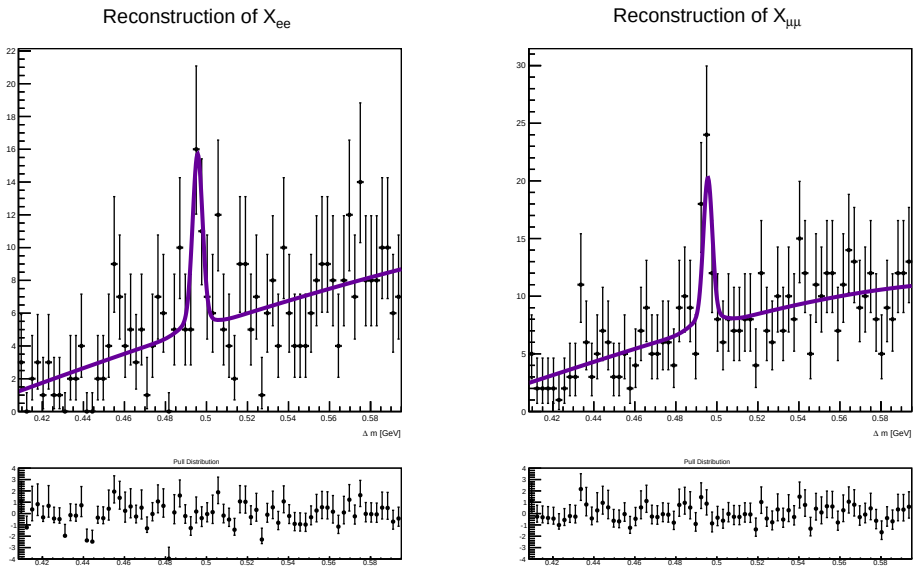

Figure 57: Fit to reconstructed X(3872) in the continuum sample (region $0 < p^*_{X(3872)} < 4.0$ GeV).

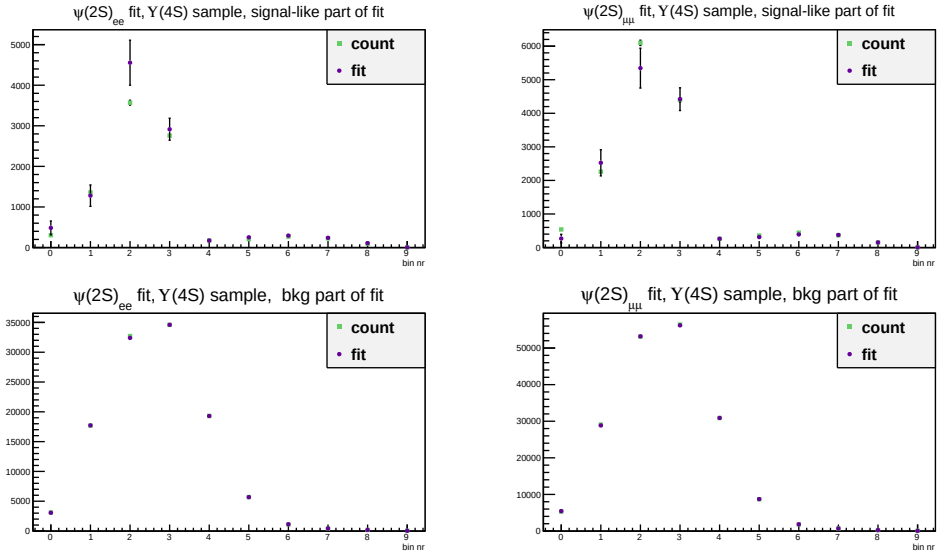

(a) Comparison of the fitted nr of events to the counted nr of events.

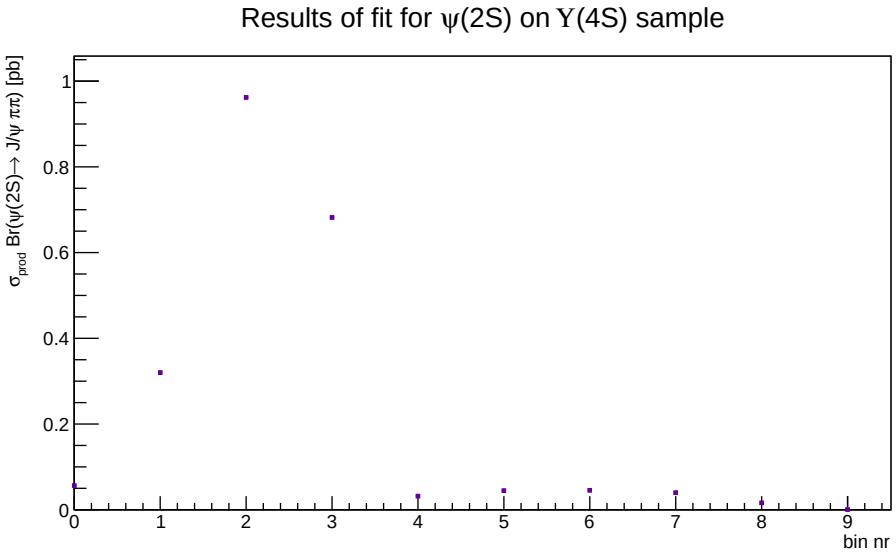

(b) Fitted σ Br (in pb).

Figure 58: Results of the fit of the $\psi(2S)$ reconstruction for the $\Upsilon(4S)$ sample [MC].

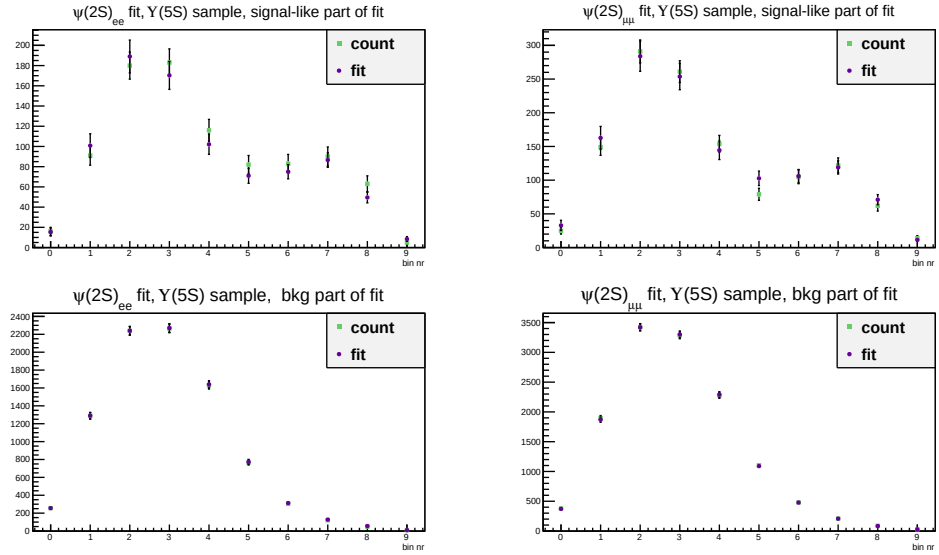

(a) Comparison of the fitted nr of events to the counted nr of events.

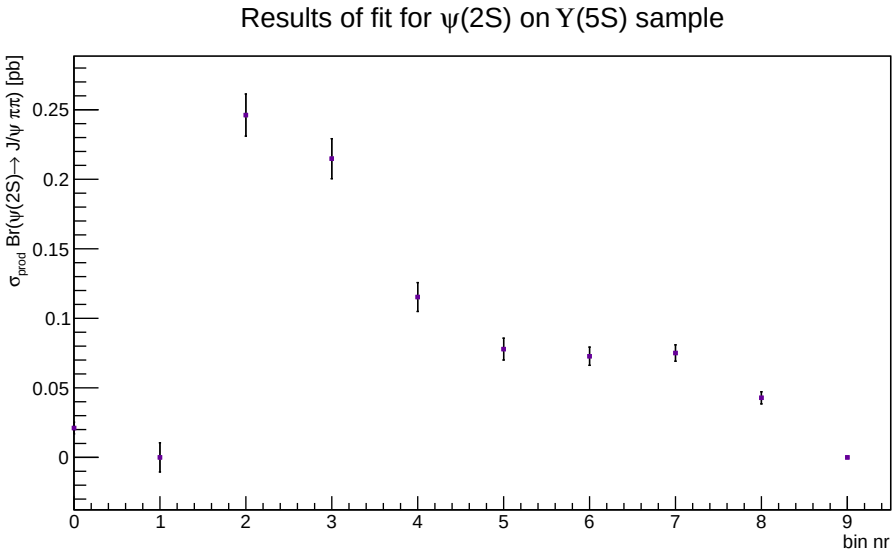

(b) Fitted σ Br (in pb).

Figure 59: Results of fit of the $\psi(2S)$ reconstruction for the $\Upsilon(5S)$ sample [MC].

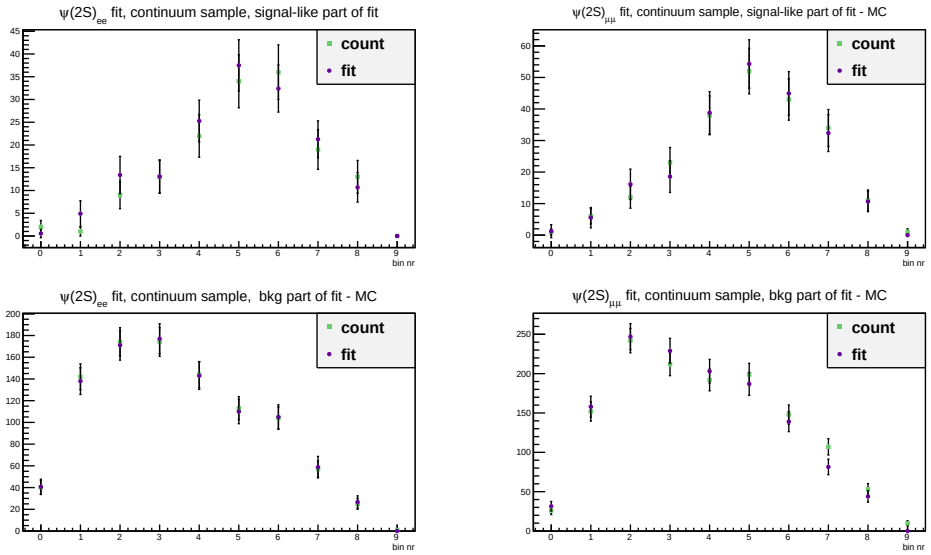

(a) Comparison of the fitted nr of events to the counted nr of events.

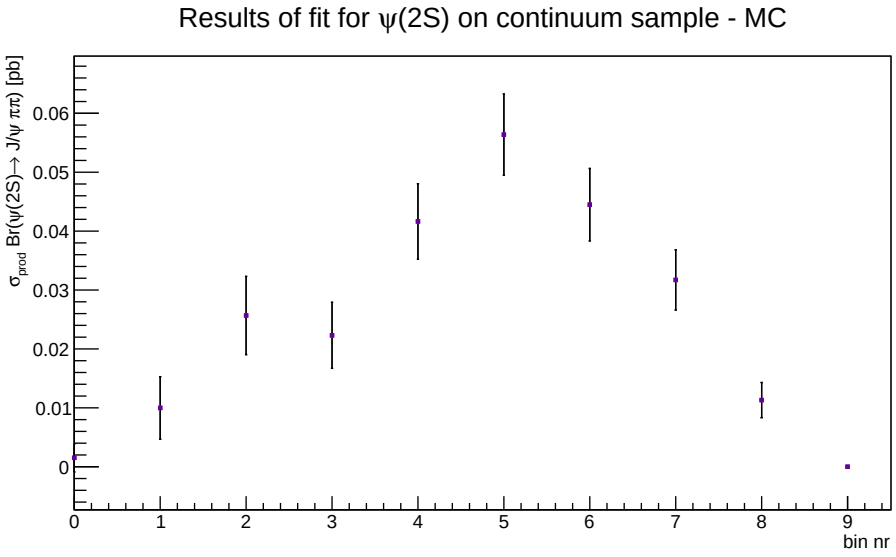

(b) Fitted σ Br (in pb).

Figure 60: Results of the fit of the $\psi\,(2S)$ reconstruction for the continuum sample [MC].

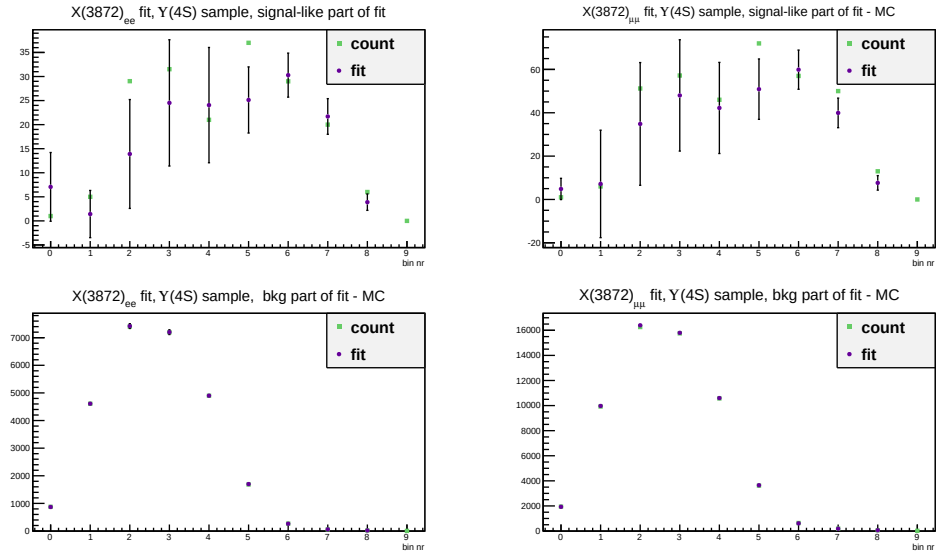

(a) Comparison of fitted nr of events to the counted nr of events.

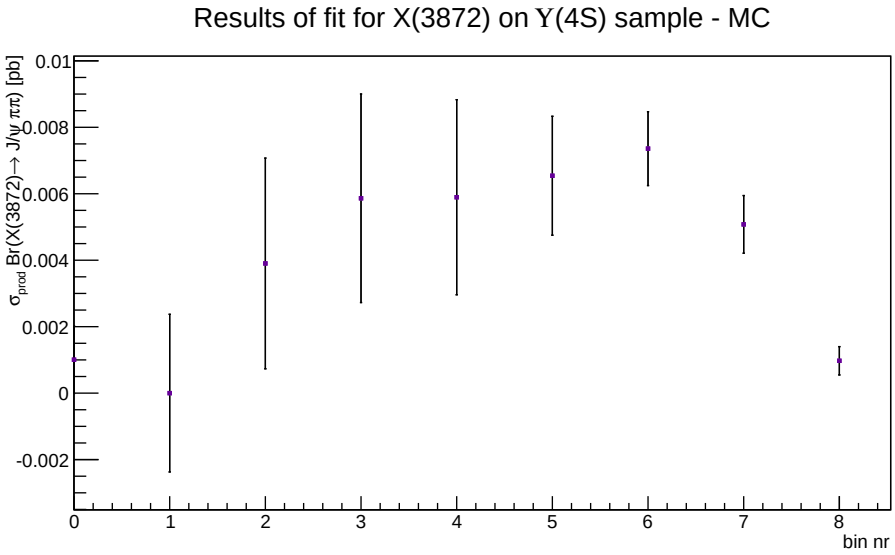

(b) Fitted σ Br (in pb).

Figure 61: Results of the fit of the X(3872) reconstruction for the $\Upsilon(4S)$ sample [MC].

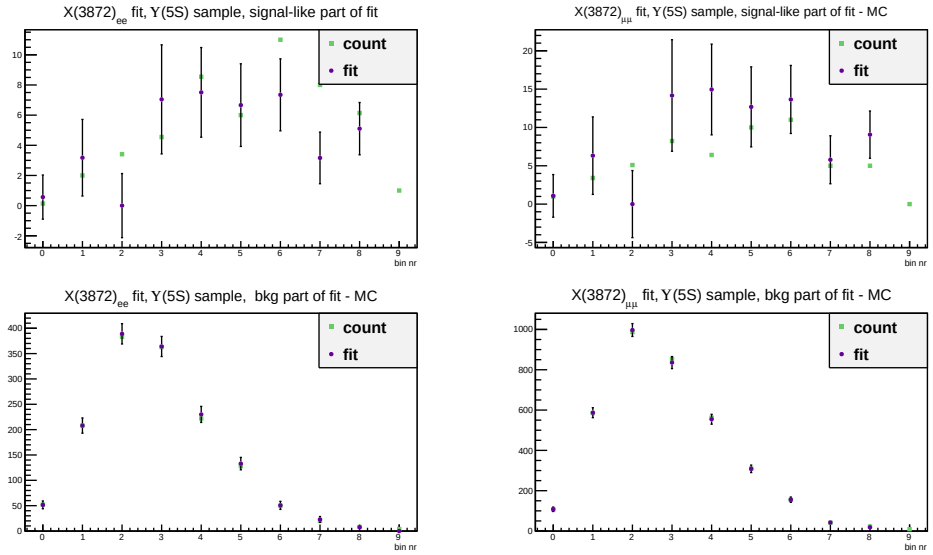

(a) Comparison of fitted nr of events to the counted nr of events.

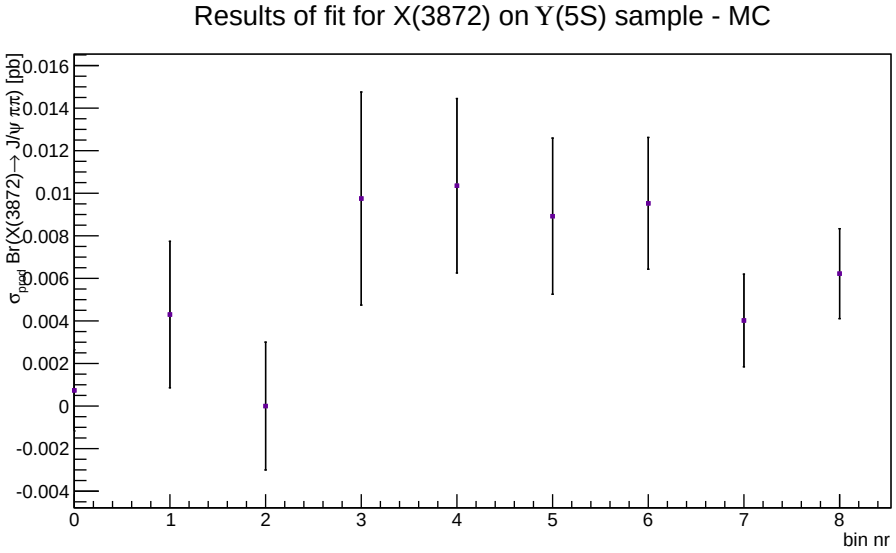

(b) Fitted σ Br (in pb).

Figure 62: Results of the the fit of the X(3872) reconstruction for the $\Upsilon(5S)$ sample [MC].

5

ANALYSIS ON THE REAL DATA

5.1 MEASUREMENT OF σ_{PROD} BR$(\psi(2s) \to J/\psi\pi\pi)$

The reconstruction procedure is now run on the real data. All the cuts are kept the same as on the MC, the best candidate selection is also performed in the same way as on the MC. Fig. 63, Fig. 64, Fig. 65 show comparison between the MC simulation and the data. Although very similar in shape, the distributions differ in the amount of events. A similar pattern emerges in all the samples - in the first three bins, the amount of background in the data exceeds the background in the MC, but up to bin 4, the amount of the background from the MC is equal or larger than the background from the data. The origin of such behavior is suspected to be incorrect description of the J/ψ momentum in the MC. To check the explanation, Δm is plotted in the sideband region of the J/ψ (see Fig. 66). The two distributions now match much better.
The exact same procedure as in Chapter 4 is used to fit the data. The fits themselves are plotted in Fig. 67, Fig. 68, and Fig. 69. The results of the fits are given in Fig. 70.
The dominant contribution in the first four bins comes from the $\psi(2S)$, which originate in the decays of the B mesons. The contribution of $B \to \psi(2S)$ + anything decays to the total production cross-section can be written as

$$\sigma_{e^+e^-\to\psi(2S)}\text{Br}(\psi(2S) \to J/\psi\pi\pi) \sim \sigma_{e^+e^-\to\Upsilon(4S)}\text{Br}(\Upsilon(4S) \to B\overline{B}) \quad (44)$$
$$\text{Br}(B \to \psi(2S)\text{ anything})\text{Br}(\psi(2S) \to J/\psi\pi\pi)$$

for the $\Upsilon(4S)$ sample. Similarly, for the $\Upsilon(5S)$ sample, the σBr can be rewritten as

$$\sigma_{e^+e^-\to\psi(2S)}\text{Br}(\psi(2S) \to J/\psi\pi\pi) \sim \sigma_{e^+e^-\to\Upsilon(5S)}\text{Br}(\Upsilon(5S) \to B\overline{B}\text{ anything}) \quad (45)$$
$$\text{Br}(B \to \psi(2S)\text{ anything})\text{Br}(\psi(2S) \to J/\psi\pi\pi).$$

The difference in the σBr between the $\Upsilon(4S)$ sample and the $\Upsilon(5S)$ sample therefore arises from the different cross section for the production of the resonance and from the different branching fraction for the decays to B mesons, which in turn decay to the $\psi(2S)$. The $\sigma_{e^+e^-\to\Upsilon(5S)} = 0.3$ nb, while the $\sigma_{e^+e^-\to\Upsilon(4S)} = 1.1$ nb. The Br$(\Upsilon(5S) \to B\overline{B}$ anything$) = 76.2^{+2.7}_{-4.0}\%$[11] while the Br$(\Upsilon(4S) \to B\overline{B}) > 96\%$[11]. The σBr for the $\Upsilon(4S)$ is expected to be ≈ 4 times larger than for the

bin	comb.						B meson			
nr	$\Upsilon(4S)$		$\Upsilon(5S)$		cont.		$\Upsilon(4S)$		$\Upsilon(5S)$	
	σBr	$\sigma_{\sigma\text{Br}}$	σBr	$\sigma_{\sigma\text{Br}}$	σBr	$\sigma_{\sigma\text{Br}}$	σBr	$\sigma_{\sigma\text{Br}}$	σBr	$\sigma_{\sigma\text{Br}}$
0	1.31E-1	4.75E-3	2.16E-2	4.68E-3	3.42E-5	1.89E-3	1.31E-2	5.12E-3	2.16E-2	5.05E-3
1	4.55E-1	8.51E-3	1.21E-1	1.12E-2	6.91E-3	5.15E-3	4.48E-1	9.95E-3	1.14E-1	1.23E-2
2	7.30E-1	1.14E-2	2.31E-1	1.55E-2	1.91E-2	6.31E-3	7.11E-1	1.30E-2	2.12E-1	1.68E-2
3	5.21E-1	9.69E-3	1.38E-1	1.29E-2	1.41E-2	5.01E-3	5.07E-1	1.09E-2	1.24E-1	1.38E-2
4	1.73E-2	3.76E-3	7.98E-2	9.22E-3	1.52E-2	4.57E-3	2.14E-3	5.91E-3	6.47E-2	1.03E-2
5	1.86E-2	2.51E-3	2.88E-2	5.87E-3	2.14E-2	4.84E-3				
6	2.47E-2	1.69E-3	2.70E-2	4.46E-3	4.00E-2	5.67E-3				
7	3.09E-2	1.64E-3	3.08E-2	4.03E-3	3.87E-2	5.74E-3				
8	3.68E-2	1.68E-3	3.54E-2	4.17E-3	4.63E-2	5.69E-3				
9	3.86E-2	1.54E-3	3.86E-2	4.10E-3	3.77E-2	4.54E-3				

Table 20: The results of the fit for data, reconstruction of the $\psi(2S)$. All the σBr and the $\sigma_{\sigma\text{Br}}$ are in pb. The error is statistical only. The *comb.* marks the σBr for combined sample (from the B mesons and from the prompt production). The production in the continuum sample is assumed to be prompt. The *B meson* marks the σBr, obtained with subtraction of results for the continuum from the $\Upsilon(4S)/\Upsilon(5S)$ results.

$\Upsilon(5S)$(compare Fig. 70).
Although both promptly produced $\psi(2S)$ and the $\psi(2S)$ from the decays of the B mesons contribute to the σBr in the first four bins, additional information can be extracted due to the analysis on the continuum sample. Since there are no B mesons in the continuum sample, the σBr can be attributed to the prompt production only. Disregarding the effect of the $p*$ of the used samples, the σBr for the $\psi(2S)$ from the B mesons is simply the difference between the total obtained value for the σBr and the value of σBr for the prompt production. Table 20 summarizes the results for the $\psi(2S)$ reconstruction.

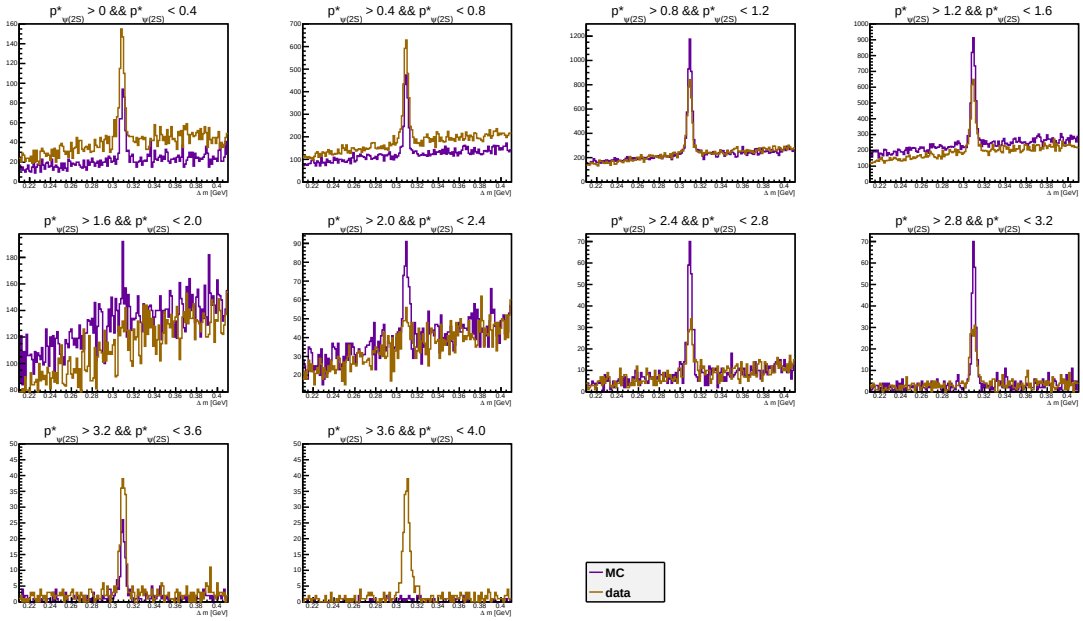

(a) $\psi(2S)_{ee}$.

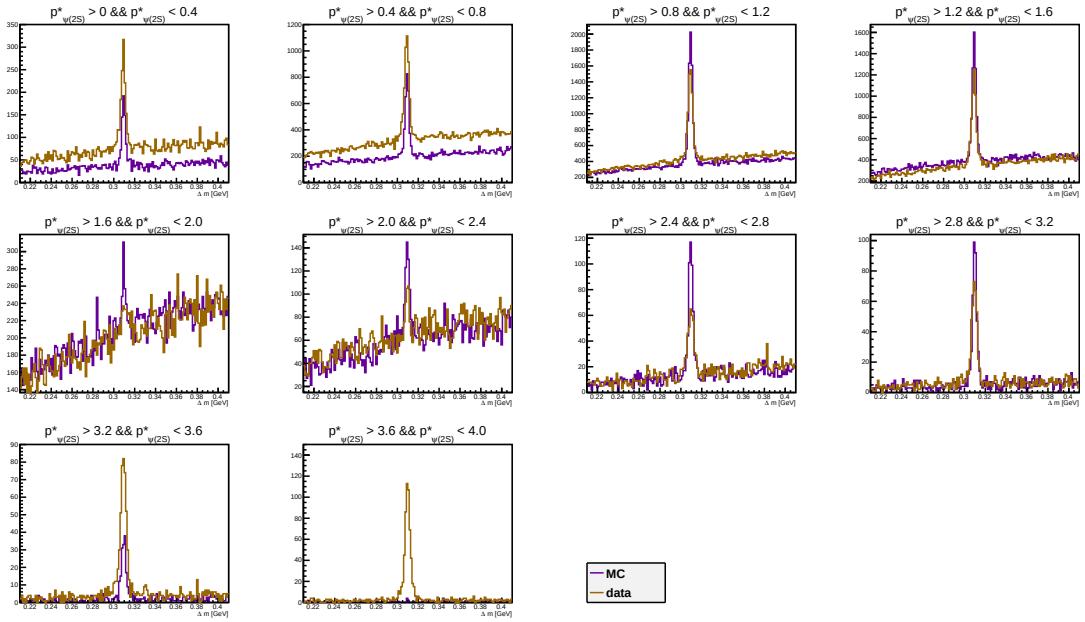

(b) $\psi(2S)_{\mu\mu}$.

Figure 63: Comparison of the MC sample and the real data for the $\psi(2S)$ reconstruction on the $\Upsilon(4S)$ sample. Violet - MC, golden - data.

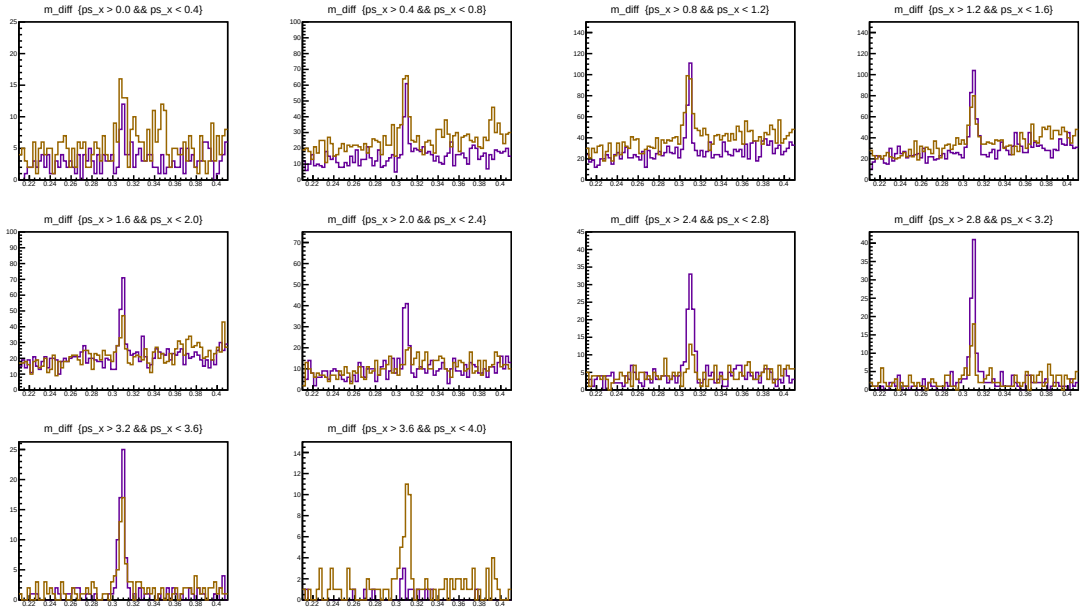

(a) $\psi(2S)_{ee}$.

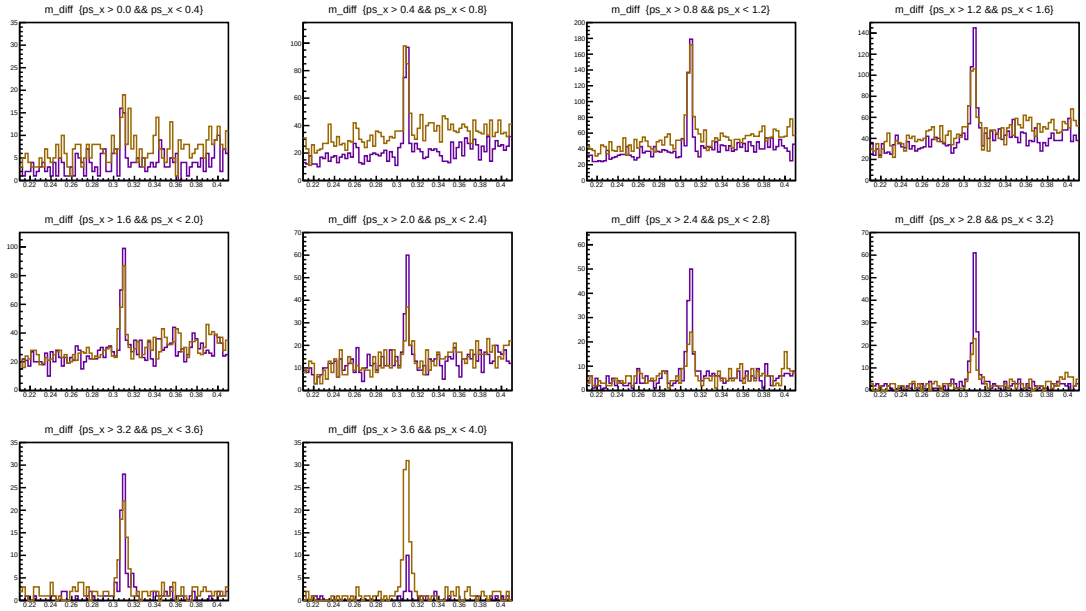

(b) $\psi(2S)_{\mu\mu}$.

Figure 64: Comparison of the MC sample and the real data for $\psi(2S)$ reconstruction on the $\Upsilon(5S)$ sample. Violet - MC, golden - data.

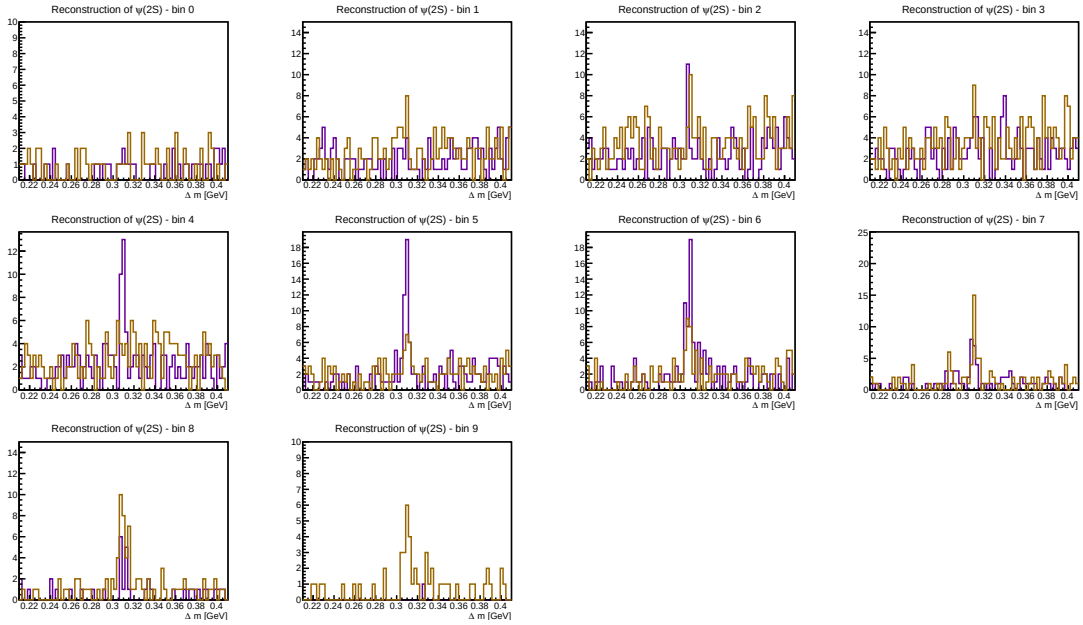

(a) $\psi(2S)_{ee}$.

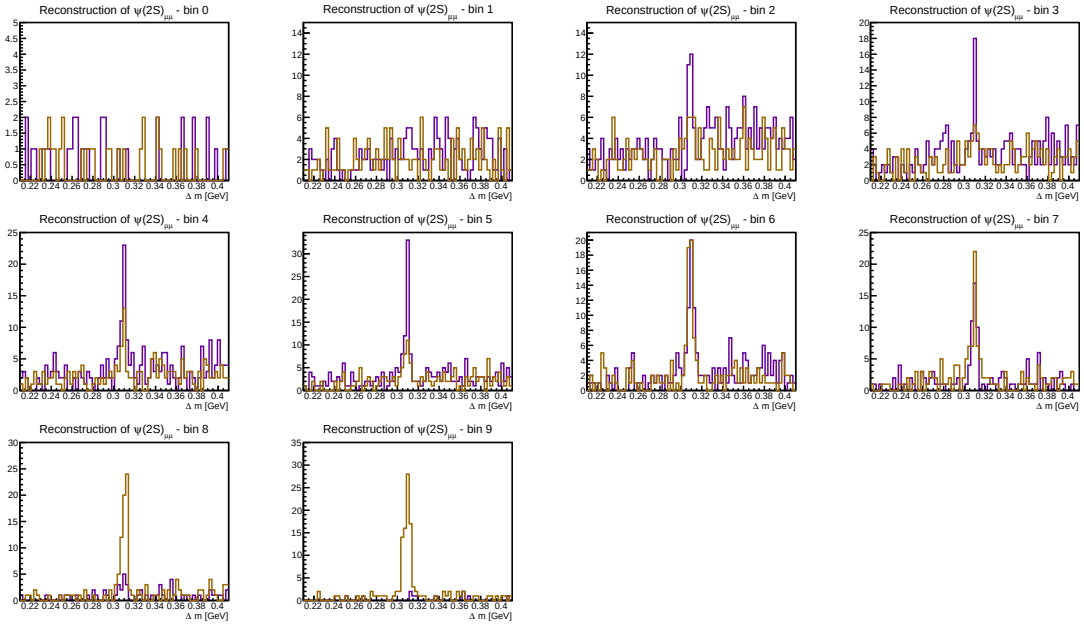

(b) $\psi(2S)_{\mu\mu}$.

Figure 65: Comparison of MC sample and real data for $\psi(2S)$ reconstruction on the continuum sample. Violet - MC, golden - data.

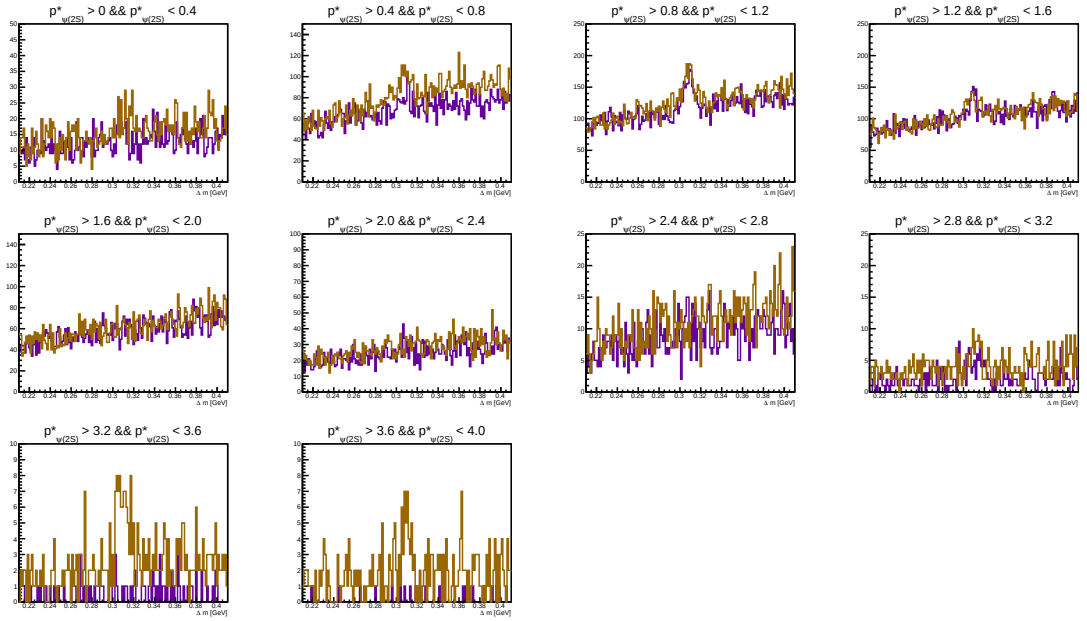

(a) $\psi(2S)_{ee}$.

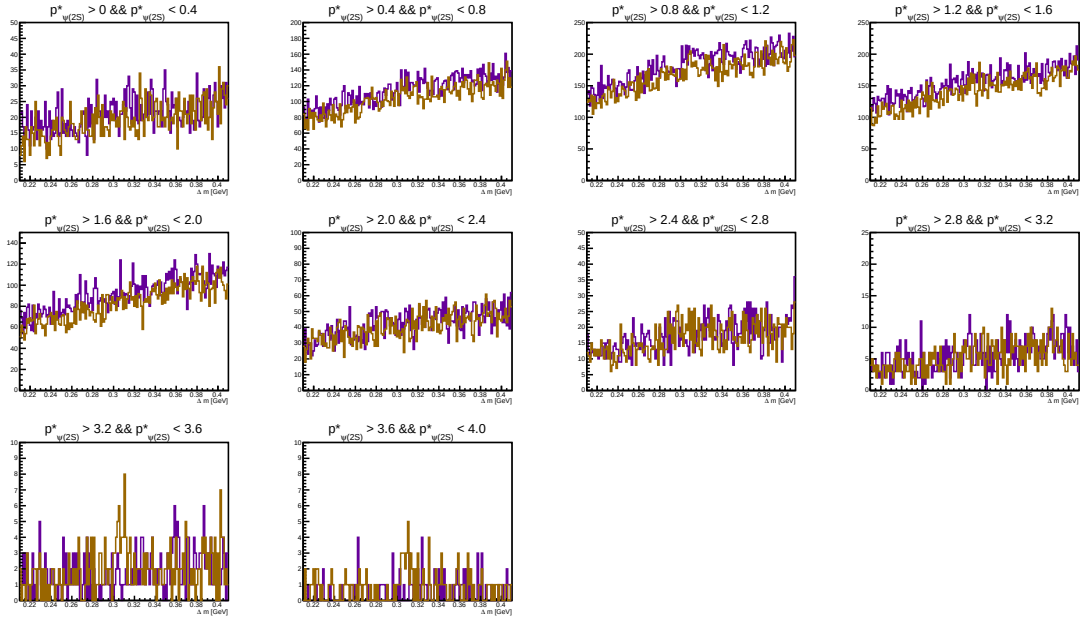

(b) $\psi(2S)_{\mu\mu}$.

Figure 66: Comparison of the MC sample and the real data for $\psi(2S)$ reconstruction on the $\Upsilon(4S)$ sample - J/ψ sideband. Violet - MC, golden - data.

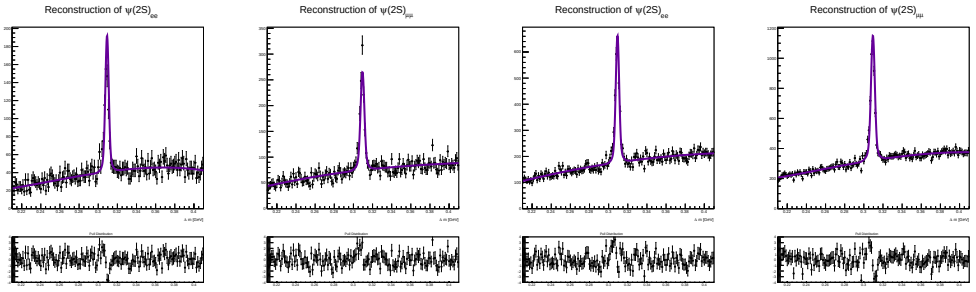

(a) Bin 0 (b) Bin 1

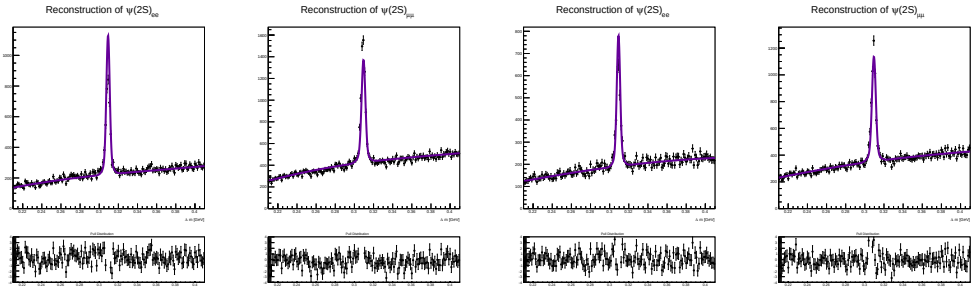

(c) Bin 2 (d) Bin 3

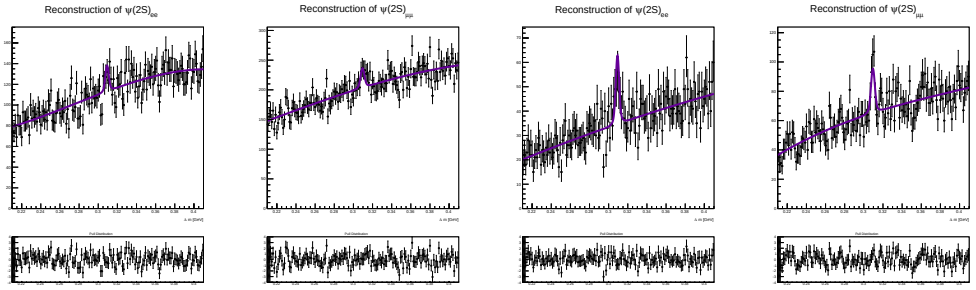

(e) Bin 4 (f) Bin 5

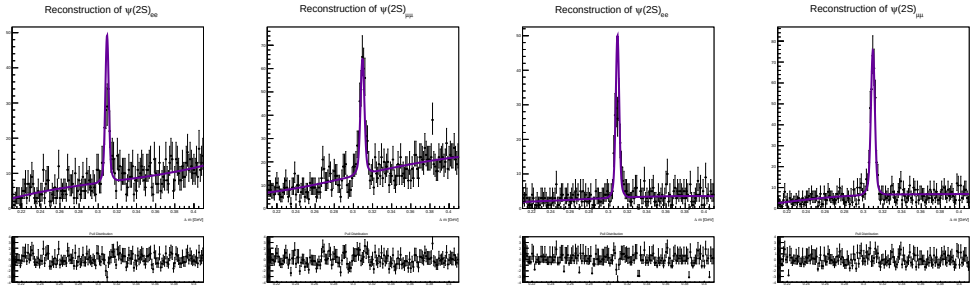

(g) Bin 6 (h) Bin 7

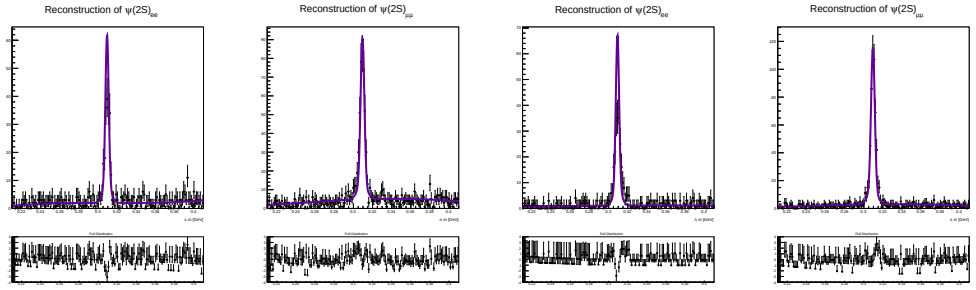

(i) Bin 8 (j) Bin 9

Figure 67: Fits to the reconstructed $\psi(2S)$ in the $\Upsilon(4S)$ sample. In each subfigure, the plot on the left are the reconstructed $\psi(2S)_{ee}$, and on the right, a reconstructed $\psi(2S)_{\mu\mu}$. Number of the bin is marked below the subfigure.

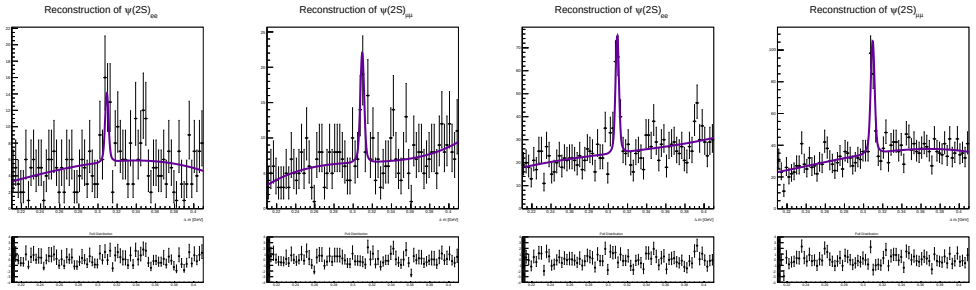

(a) Bin 0 (b) Bin 1

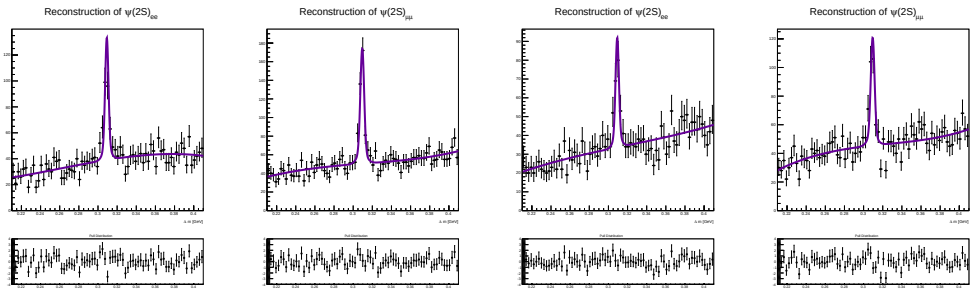

(c) Bin 2 (d) Bin 3

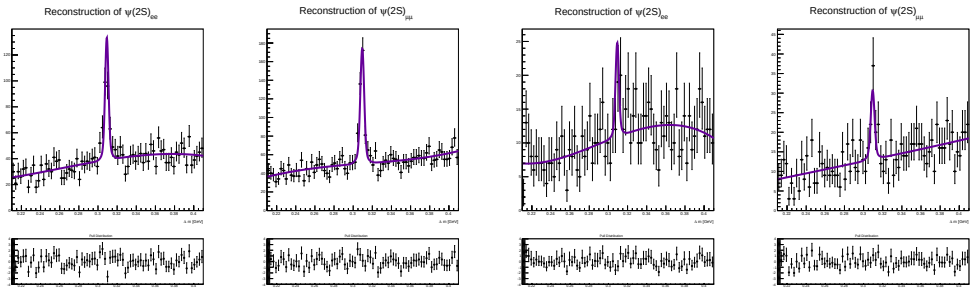

(e) Bin 4 (f) Bin 5

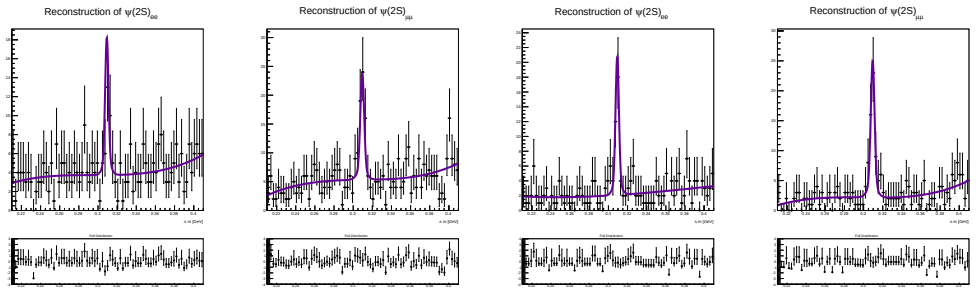

(g) Bin 6 (h) Bin 7

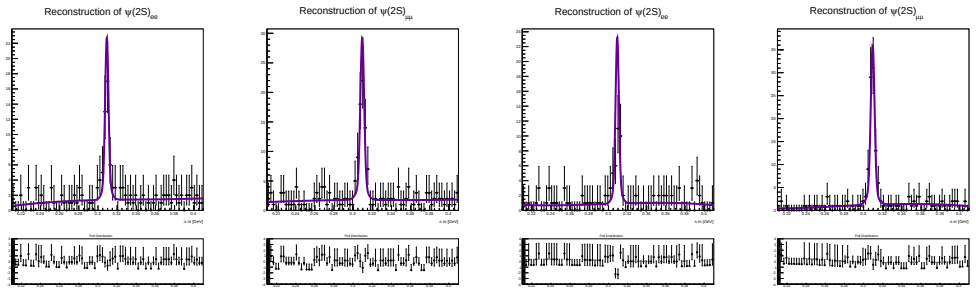

(i) Bin 8 (j) Bin 9

Figure 68: Fits to the reconstructed $\psi(2S)$ in the $\Upsilon(5S)$ sample. In each subfigure, the plot on the left are the reconstructed $\psi(2S)_{ee}$, and on the right, the reconstructed $\psi(2S)_{\mu\mu}$. Number of the bin is marked below the subfigure.

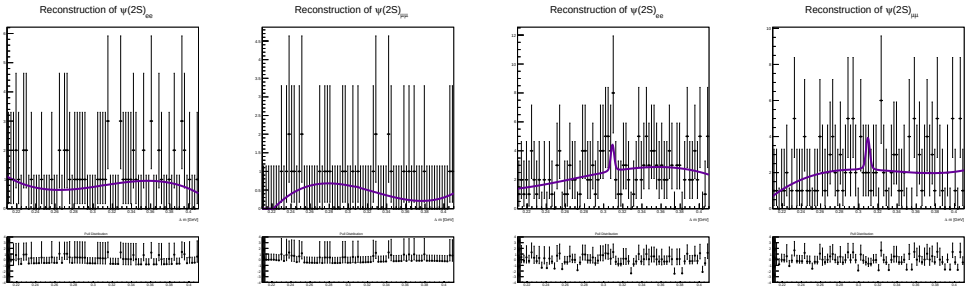

(a) Bin 0 (b) Bin 1

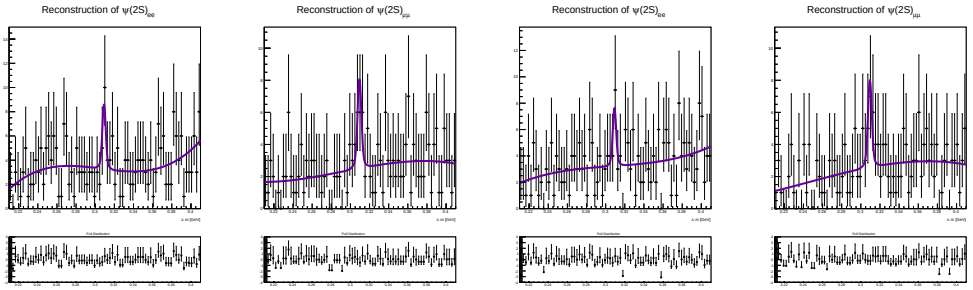

(c) Bin 2 (d) Bin 3

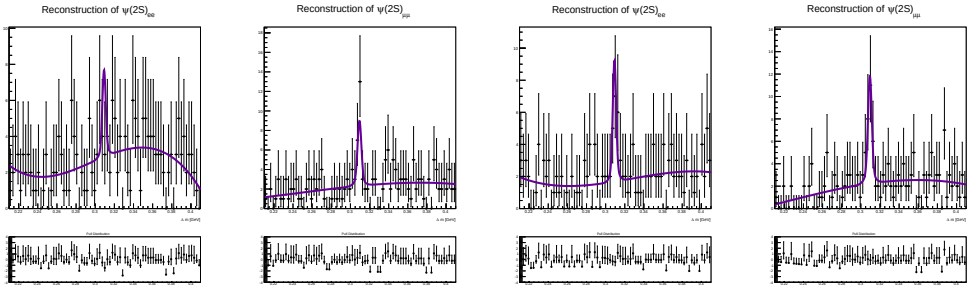

(e) Bin 4 (f) Bin 5

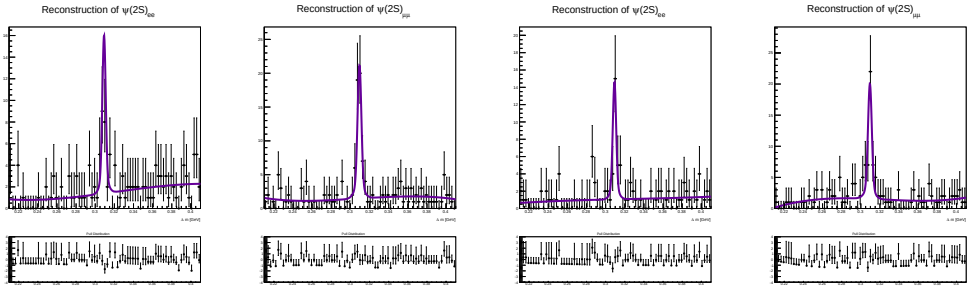

(g) Bin 6 (h) Bin 7

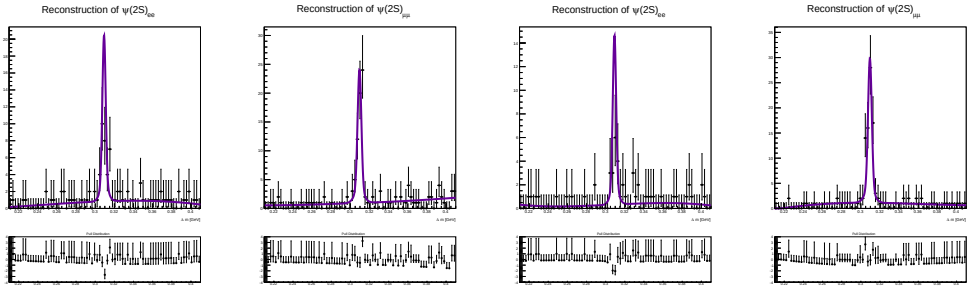

(i) Bin 8 (j) Bin 9

Figure 69: Fits to the reconstructed $\psi(2S)$ in the continuum sample. In each subfigure, the plot on the left are the reconstructed $\psi(2S)_{ee}$, and on the right, the reconstructed $\psi(2S)_{\mu\mu}$. Number of the bin is marked below the subfigure.

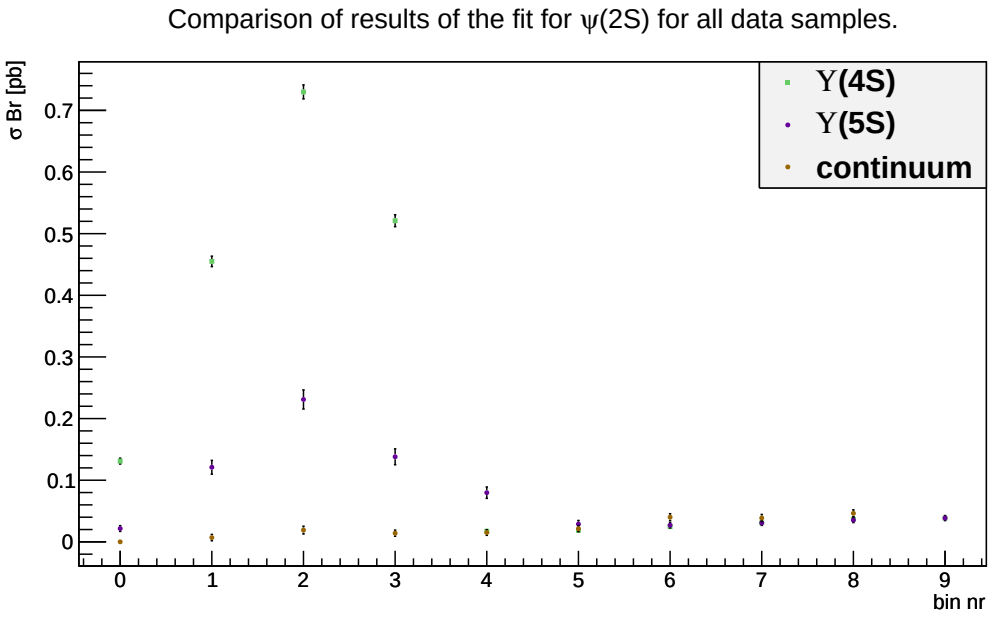

(a) Entire momentum range.

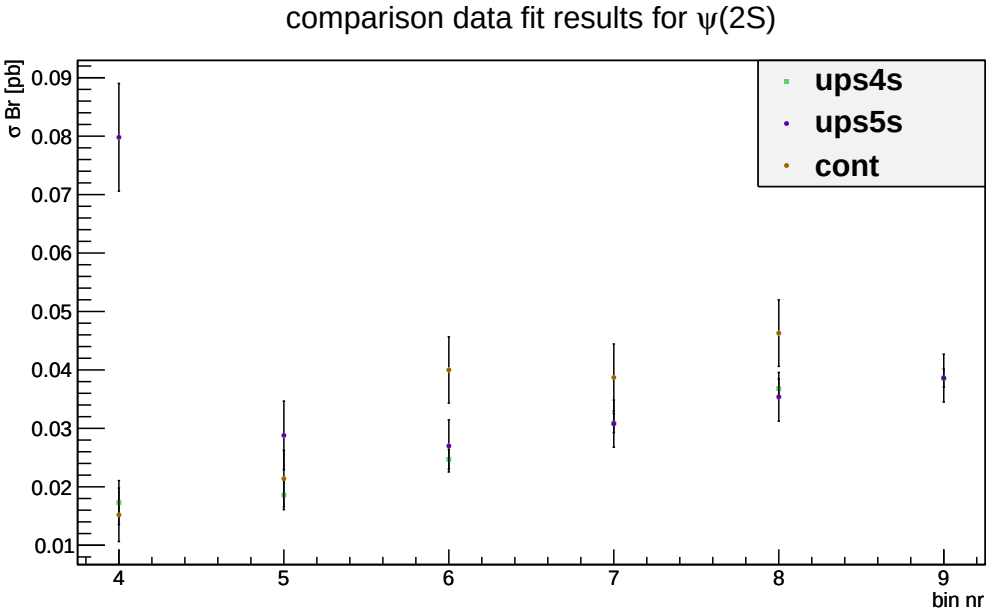

(b) The prompt production region.

Figure 70: Results of fits to data for reconstruction of the $\psi\,(2S)$.

5.2 RECONSTRUCTION OF THE X(3872)

The distributions of Δm show the same discrepancy in the amount of the data as the $\psi(2S)$ sample (see Fig. 71 and Fig. 72 for the comparison between the MC and the data). Again, the incorrect description of the momentum of the J/ψ in the generic MC is the cause.
Contrary to the $\psi(2S)$, the signal in the prompt area is consistent with 0 (see Fig. 77) and an upper limit will be determined. A significant signal can be seen in the region where the X(3872) originate from decays of B mesons. The results of the fits for the first three bins are gathered in Table 21.
The reconstruction on the continuum sample and comparison between the data and MC can be seen in Fig. 73. Again, the fit results are consistent with zero (see Fig. 76) and an upper limit is determined.

bin nr	σBr	$\sigma_{\sigma\text{Br}}$
0	5.63E-3	1.70E-3
1	1.93E-2	3.47E-3
2	2.53E-2	3.70E-3

Table 21: The results of the fit for the data, reconstruction of the X(3872). All the σBr and the $\sigma_{\sigma\text{Br}}$ are in pb. The error is statistical only.

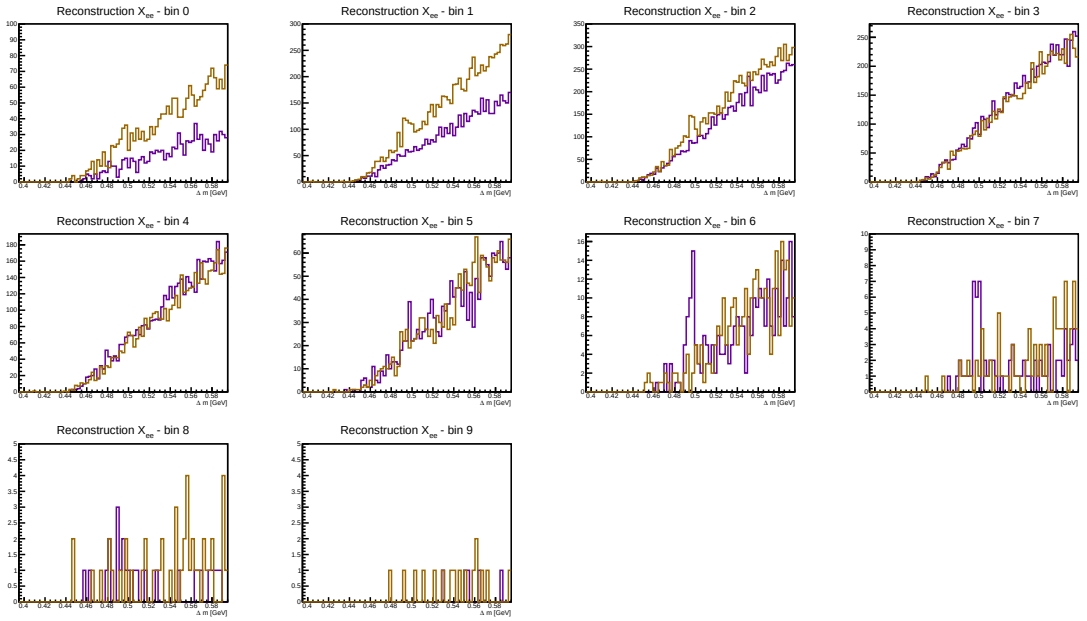

(a) $X(3872)_{ee}$.

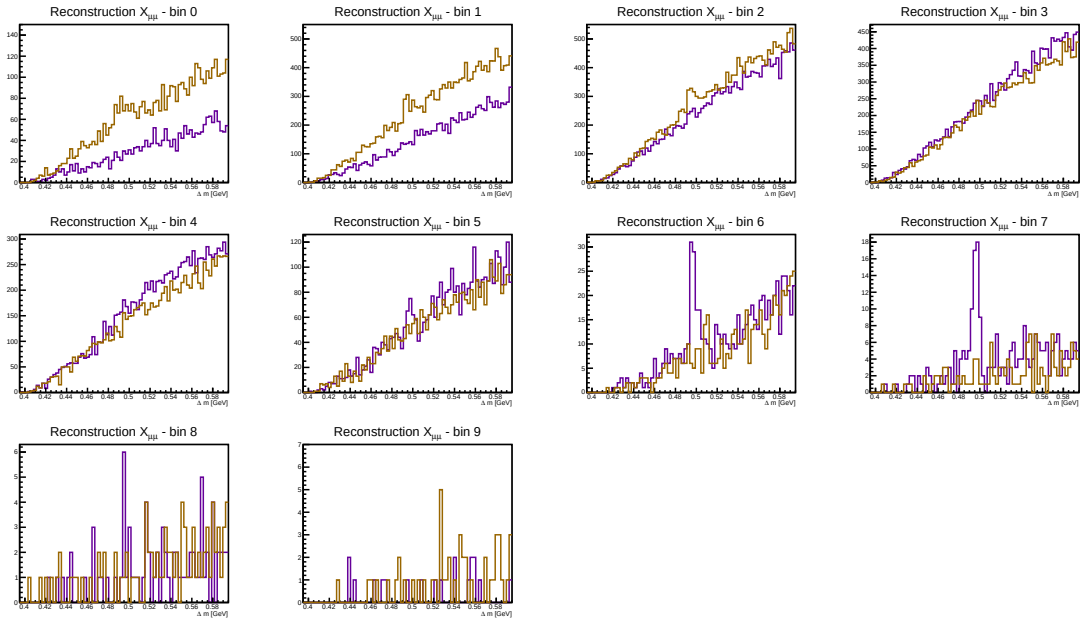

(b) $X(3872)_{\mu\mu}$.

Figure 71: Comparison of the MC sample and the real data for the X(3872) reconstruction on the $\Upsilon(4S)$ sample. Violet - MC, golden - data.

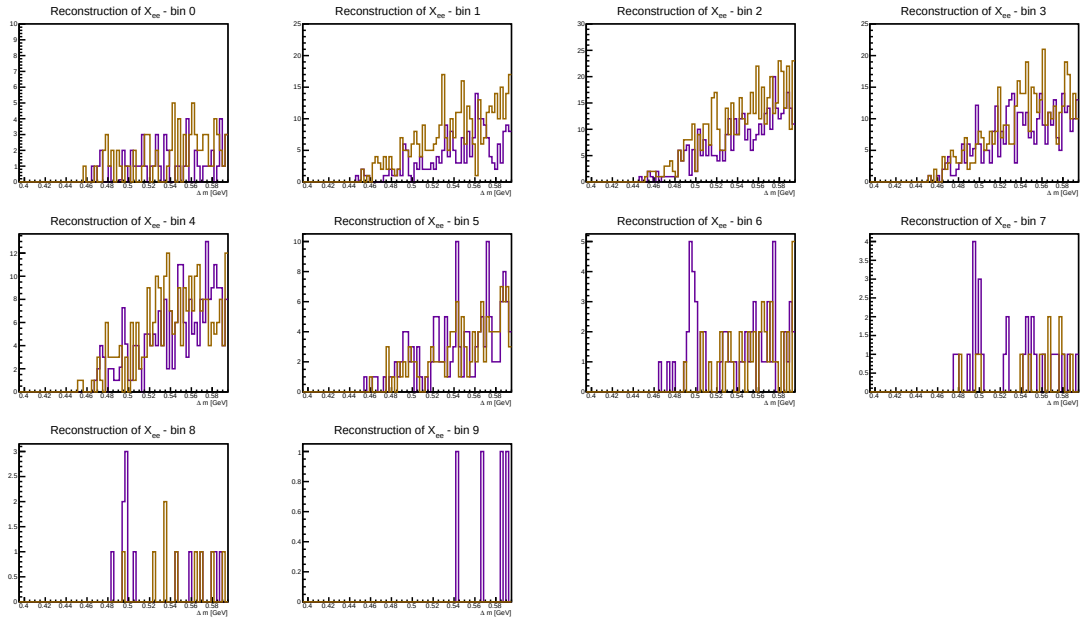

(a) X(3872)$_{ee}$.

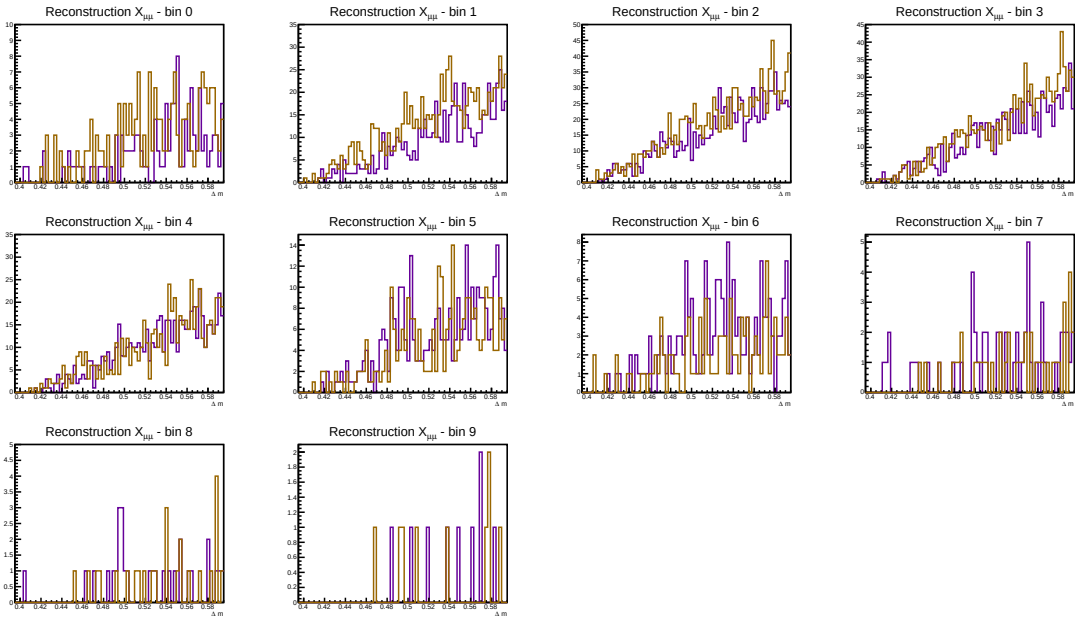

(b) X(3872)$_{\mu\mu}$.

Figure 72: Comparison of the MC sample and the real data for the X(3872) reconstruction on the $\Upsilon(5S)$ sample. Violet - MC, golden - data.

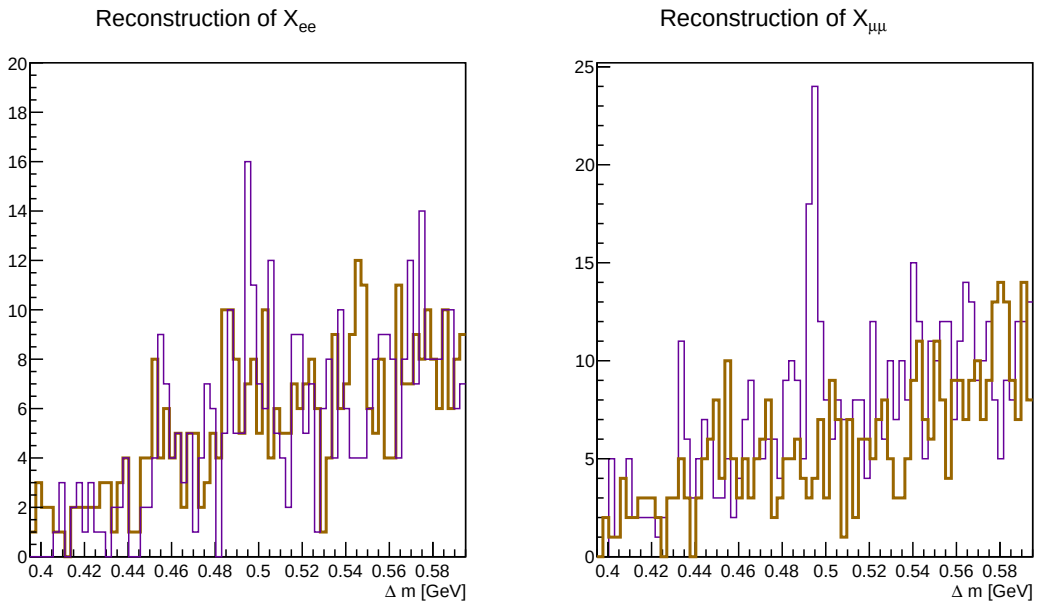

Figure 73: Comparison of the MC sample and the real data for the X(3872) reconstruction on the continuum sample. Violet - MC, golden - data.

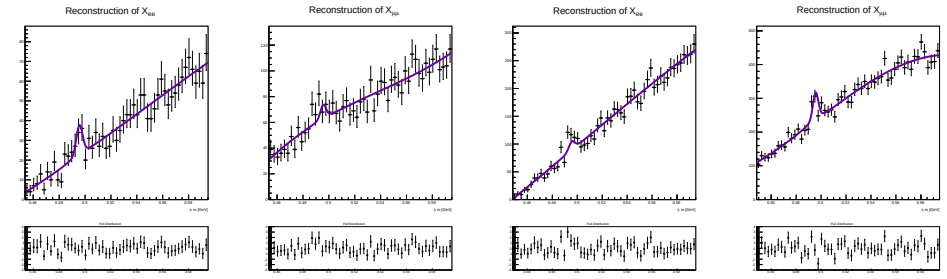

(a) Bin 0 (b) Bin 1

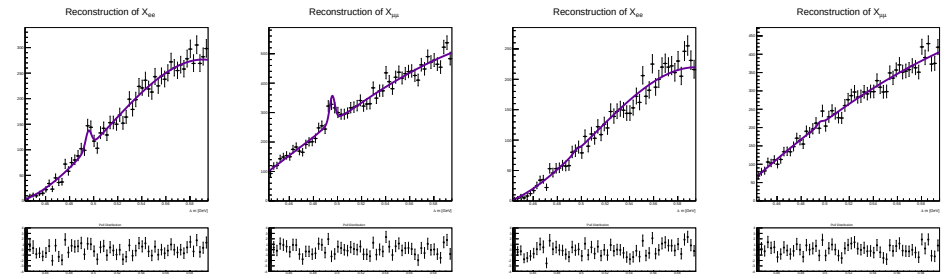

(c) Bin 2 (d) Bin 3

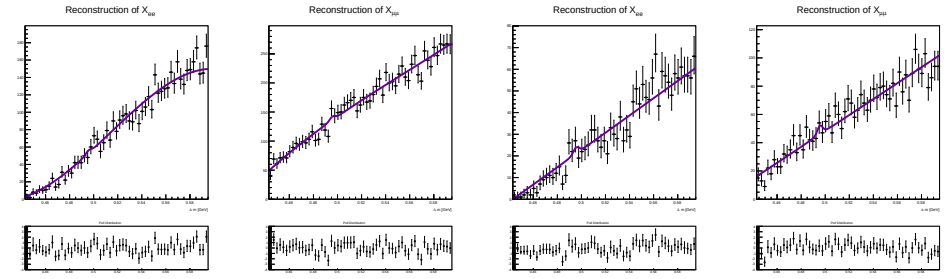

(e) Bin 4 (f) Bin 5

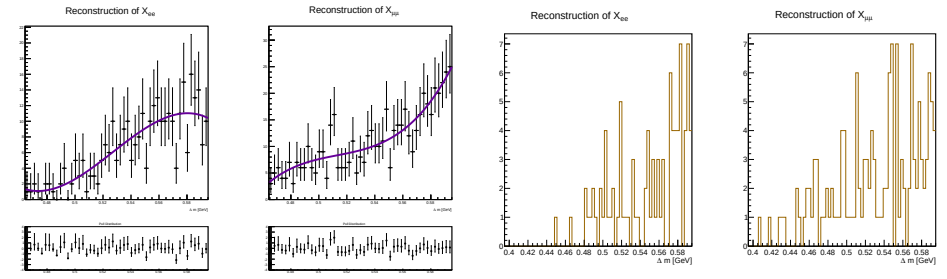

(g) Bin 6 (h) Bin 7

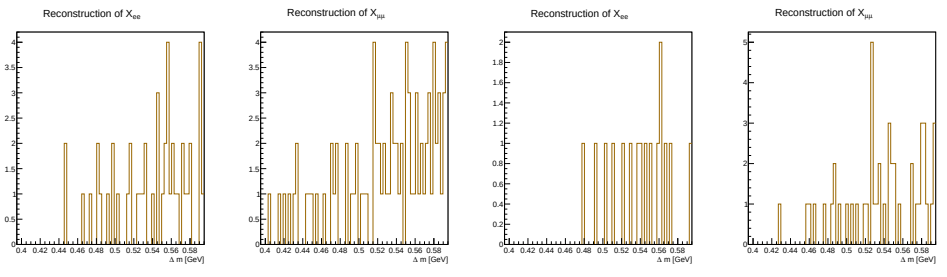

(i) Bin 8 (j) Bin 9

Figure 74: Fits to the reconstructed X(3872) in the $\Upsilon(4S)$ sample. In each subfigure, the plot on the left are the reconstructed $X(3872)_{ee}$, and on the right, the reconstructed $X(3872)_{\mu\mu}$. Number of the bin is marked below the subfigure. The chosen area for fitting had to be changed in order to avoid fitting of empty bins. Considering a very low number of events in the last three bins, the fit could not be performed.

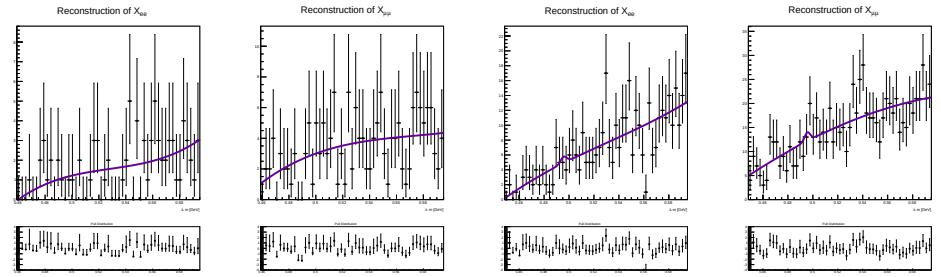

(a) Bin 0 (b) Bin 1

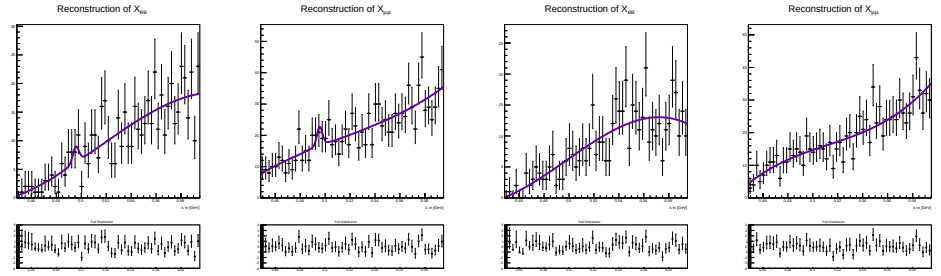

(c) Bin 2 (d) Bin 3

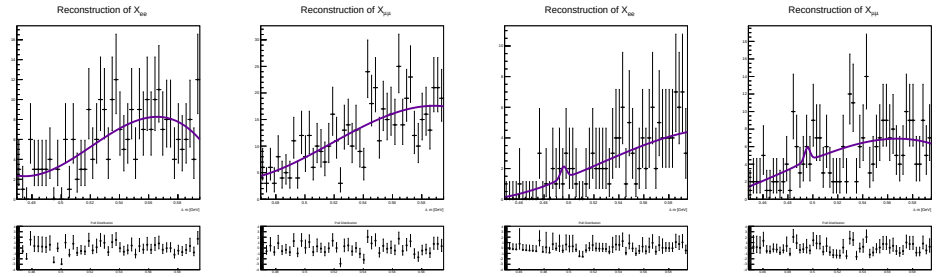

(e) Bin 4 (f) Bin 5

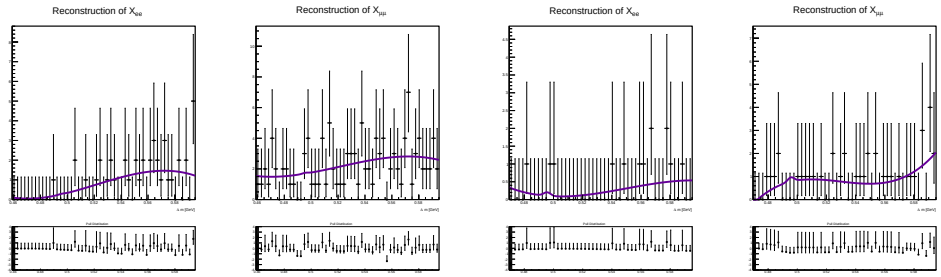

(g) Bin 6 (h) Bin 7

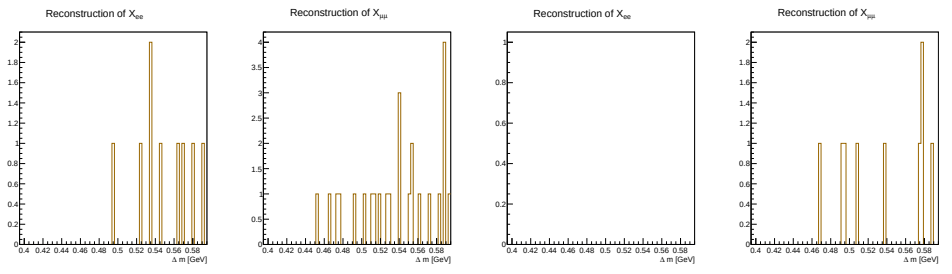

(i) Bin 8 (j) Bin 9

Figure 75: Fits to the reconstructed X(3872) in the $\Upsilon(5S)$ sample. In each subfigure, the plot on the left are the reconstructed X(3872)$_{ee}$, and on the right, the reconstructed X(3872)$_{\mu\mu}$. Number of the bin is marked below the subfigure. The chosen area for fitting had to be changed in order to avoid fitting of empty bins. Considering a very low number of events in the last two bins, the fit could not be performed.

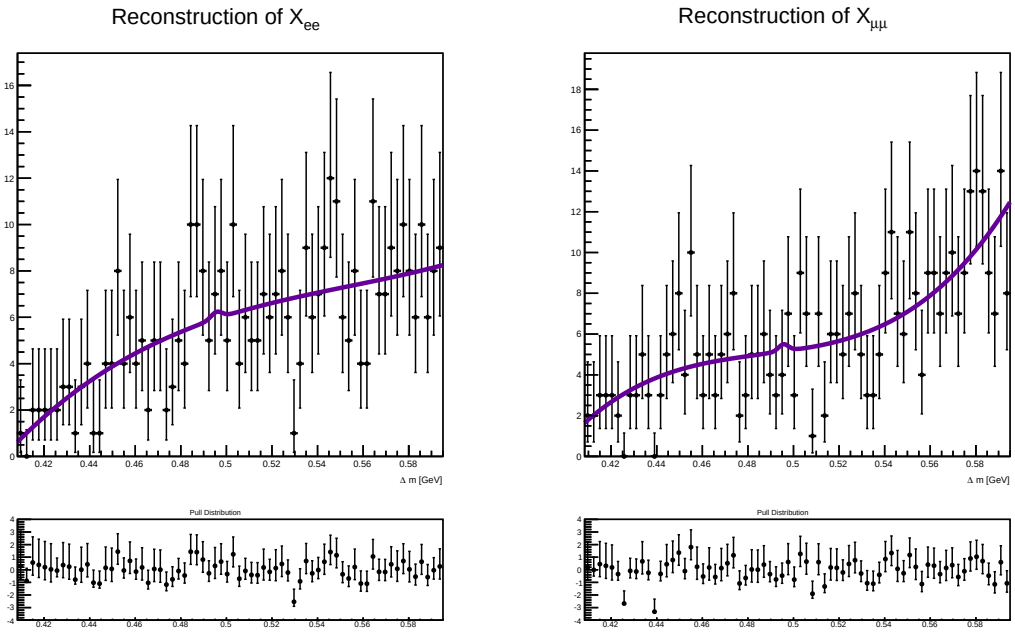

Figure 76: Fit to the reconstructed X(3872) in the continuum sample. Region of $0 < p_{X(3872)*} < 4.0$ GeV is used. Result of the fit is consistent with zero and an upper limit is determined.

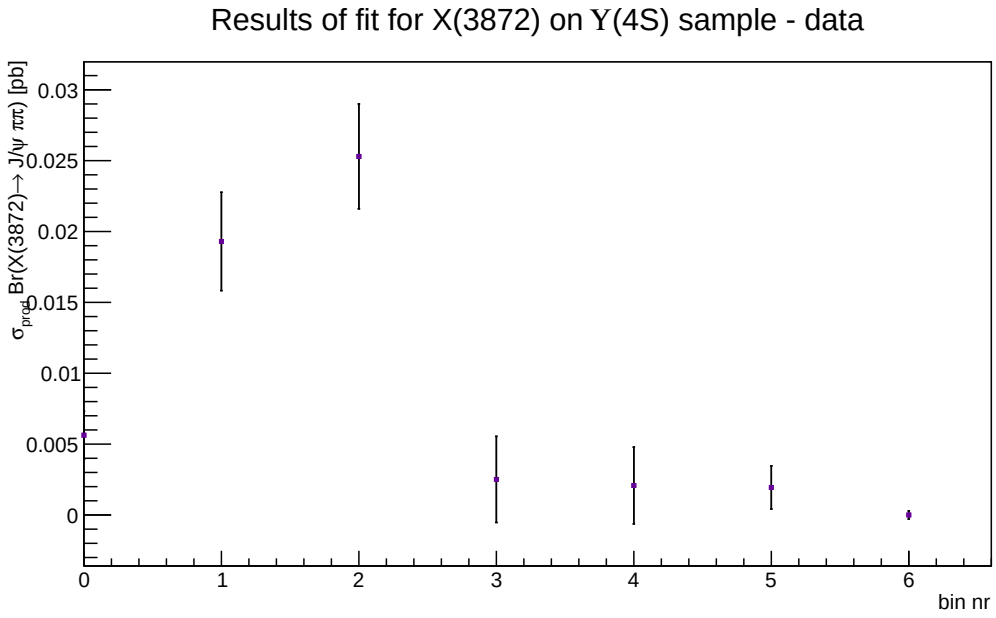

(a) $\Upsilon(4S)$ sample.

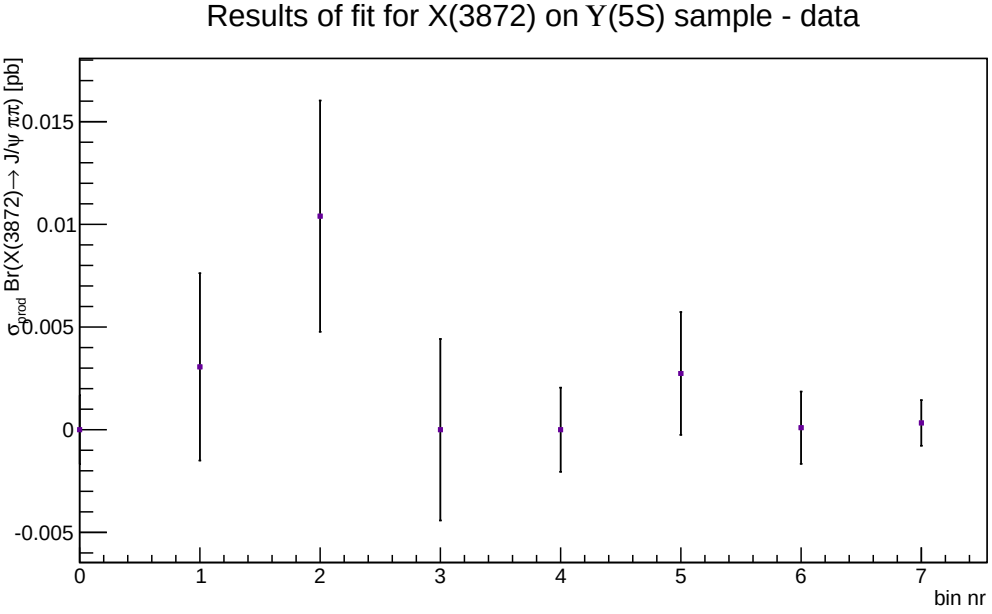

(b) $\Upsilon(5S)$ sample

Figure 77: Results of the fit for the reconstruction of X(3872).

5.3 MEASUREMENT OF BR(B → ψ(2s) + ANYTHING)

Having the data from both the $\Upsilon(4S)$ sample and the continuum sample, a determination of $Br(B \to \psi(2S)$ anything) is possible.
First, a kinematic limit is established for the $\psi(2S)$, originating in decays of B mesons. In case of the dominant decay mode - $B^+ \to \psi(2S)K^+$ - the $p^*_{\text{max}} < 1.6$ GeV. Δm is plotted for both the $\Upsilon(4S)$ and the continuum sample in a region between [0,1.6] GeV. The $\Upsilon(4S)$ sample contains $\psi(2S)$, originating from B decays and from prompt production, whereas the continuum sample contains only the promptly produced $\psi(2S)$. The branching fraction for $B \to \psi(2S)$ anything can be written as:

$$\text{Br}(B \to \psi(2S) \text{ anything}) = \frac{N_{ee,\,\Upsilon(4S)} - \frac{\mathcal{L}_{\Upsilon(4S)}}{\mathcal{L}_{cont}} N_{ee,\,\text{continuum}}}{2\; N_{B\overline{B}}\; \varepsilon_{ee}\; \text{Br}(\psi(2S) \to J/\psi\pi^+\pi^-)\; \text{Br}(J/\psi \to e^+e^-)} \tag{46}$$

or

$$\text{Br}(B \to \psi(2S) \text{ anything}) = \frac{N_{\mu\mu,\,\Upsilon(4S)} - \frac{\mathcal{L}_{\Upsilon(4S)}}{\mathcal{L}_{cont}} N_{\mu\mu,\,\text{continuum}}}{2\; N_{B\overline{B}}\; \varepsilon_{\mu\mu}\; \text{Br}(\psi(2S) \to J/\psi\pi^+\pi^-)\; \text{Br}(J/\psi \to \mu^+\mu^-)}, \tag{47}$$

respectively.
Two corrections have to be made in the process of extracting the Br. First, the correction factor has to be added because of the difference in the efficiency for the MC and data for leptons [53]. The correction factor for pions is 1.00 ± 0.012, for the leptons 0.97 ± 0.017. In Eq. 47, the ε has to be multiplied with these factors. The second correction is the parametrization of the fitting function. Not unexpectedly, the resolution of the signal part in the data does not match the one, determined in the MC. The widest Gaussian remains fixed to the parameters from the signal MC (G_2); the mean of the remaining two Gaussians is set to be the same for both and allowed to float for δm around the central value; and finally, the σ_1 and σ_3 are multiplied with a factor s to allow for scaling of the resolution. The new parametrization is run on the $\Upsilon(4S)$ sample and the fit returns the s, δm and the signal yield. Contrary to the previous procedures, the channels are fitted individually to obtain the number of signal events. Results for s and δm are gathered in Table 22; the yields of the fits are given int Table 23 and fits themselves at Fig. 78.

The calculation via Eq. 47 give

$$\begin{aligned} BR_{\text{elec}} &= (2.683 \pm 0.052)\; 10^{-3} \\ BR_{\text{muon}} &= (2.954 \pm 0.041)\; 10^{-3}, \end{aligned} \tag{48}$$

where the uncertainty is statistical only. The estimation of the systematic uncertainty and the comparison to the previous measurements is given in Chapter 6 and in Section 7.1.

	electronic channel	muonic channel
s	1.2677 ± 0.0257	1.0558 ± 0.0162
δm	$(-3.2583 \pm 0.4425)\ 10^{-4}$ GeV	$(-4.6269 \pm 0.3213)\ 10^{-4}$ GeV

Table 22: Results of changed parametrization.

	$\psi\,(2S)_{ee}$	$\psi\,(2S)_{\mu\mu}$
$\Upsilon\,(4S)$	8849.0 ± 151.4	13781.1 ± 179.8
continuum	30.3 ± 8.6	21.1 ± 7.7

Table 23: Signal yields from the fit. The uncertainty is statistical only.

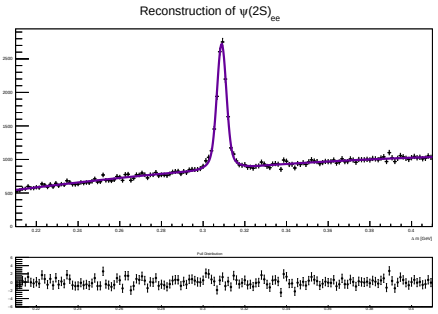

(a) $\psi\,(2S)_{ee}$, $\Upsilon\,(4S)$ sample.

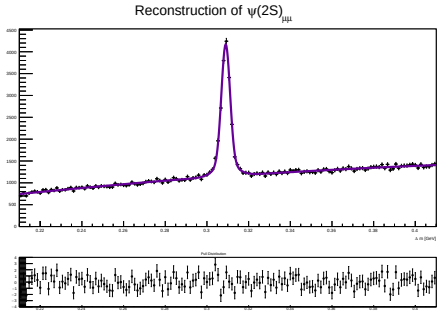

(b) $\psi\,(2S)_{\mu\mu}$, $\Upsilon\,(4S)$ sample.

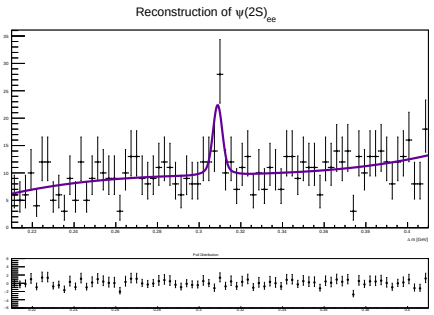

(c) $\psi\,(2S)_{ee}$, continuum sample.

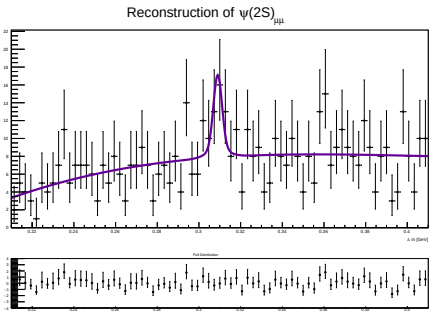

(d) $\psi\,(2S)_{\mu\mu}$, continuum sample.

Figure 78: Results of the fit in the $p^*_{\psi(2S)} < 1.6$ GeV region.

5.4 MEASUREMENT OF BR$(B \to X(3872)$ + ANYTHING$)\times$ BR$(X(3872) \to J\psi\pi^+\pi^-)$

In a similar manner as described in $\psi\,(2S)$ sample, the Br$(B \to X(3872)$ + anything$)\times$ Br$(X(3872) \to J\psi\pi^+\pi^-)$ is measured. Since only the upper limit is set to Br$(X(3872) \to J\psi\pi^+\pi^-)$, the product of both branching fractions is given.
The kinematic limit for the X(3872), originating in the decays of the B mesons is set to 1.45 GeV. As in $\psi\,(2S)$ case, the Δm is plotted for both $\Upsilon\,(4S)$ and continuum sample in region between [0,1.45] GeV.

	$X(3872)_{ee}$	$X(3872)_{\mu\mu}$
$\Upsilon(4S)$	298.7 ± 45.1	511.1 ± 72.0
continuum	3.0 ± 5.4	1.9 ± 4.3

Table 24: Signal yields from the fit. The uncertainty is statistical only.

The correction of the parametrization is done in a same way as for $\psi(2S)$ and the correction factors for the fit (δm, s) are taken from the $\psi(2S)$ results. The correction factors for the difference in the efficiency for the MC and the data are also applied.
The fit procedure is done on the individual channels and designed to return the yield of the signal. For the continuum sample, the result is consistent with 0.
The yields from the fit are gathered in the Table 24 and the fit is shown in Fig. 79.

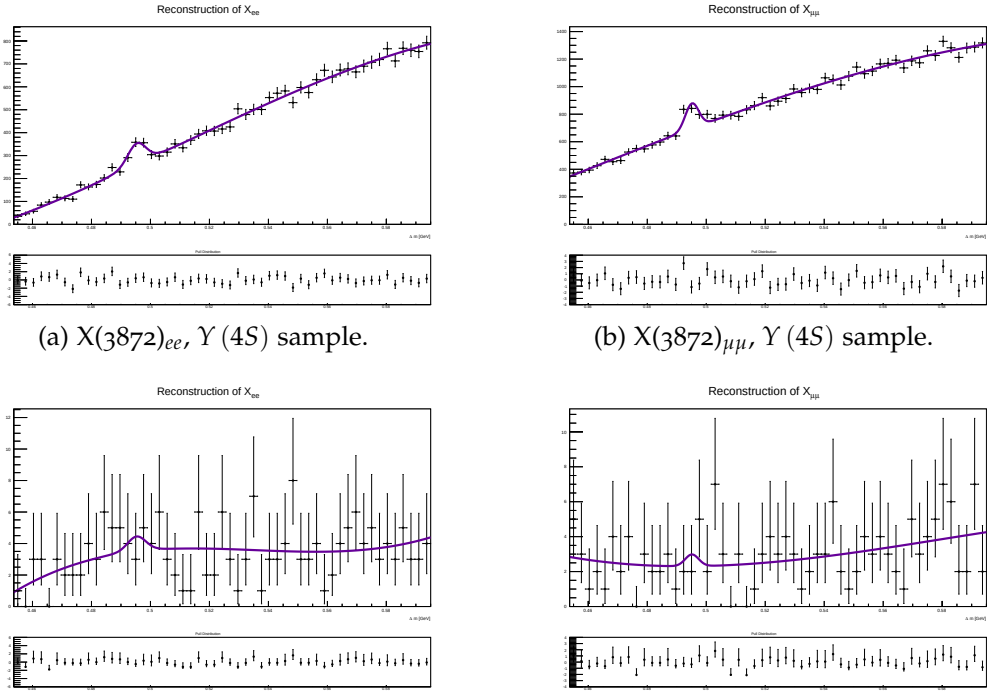

(a) $X(3872)_{ee}$, $\Upsilon(4S)$ sample.
(b) $X(3872)_{\mu\mu}$, $\Upsilon(4S)$ sample.
(c) $X(3872)_{ee}$, continuum sample.
(d) $X(3872)_{\mu\mu}$, continuum sample.

Figure 79: Results of the fit in the $p^*_{X(3872))} < 1.45$ GeV region.

Results for the Br($B \to X(3872)$ + anything)× Br($X(3872) \to J\psi\pi^+\pi^-$) are given in Eq. 49. The uncertainty is statistical only; the systematic error is calculated in Chapter 6 and the discussion follows in Chapter 7.

$$\begin{aligned} BR_{\text{elec}} &= (2.629 \pm 0.595)\ 10^{-5} \\ BR_{\text{muon}} &= (2.865 \pm 0.460)\ 10^{-5} \end{aligned} \tag{49}$$

6

SYSTEMATIC UNCERTAINTY

In this chapter, the systematic uncertainty of the result is evaluated. In present analysis, several sources of systematic uncertainty were identified:

- the difference in the PID efficiency between the real data and the MC simulation introduces an uncertainty for each charged track used in the reconstruction of the X(3872) or $\psi(2S)$, respectively,
- the tracking uncertainty,
- the uncertainty due to the limited size of the MC sample used to determine the reconstruction efficiency,
- the uncertainties in the branching fractions, used in the various calculations,
- the uncertainty in number of B mesons.

6.1 TRACKING UNCERTAINTY

In general, all charged tracks carry a systematic uncertainty of 0.35%. Having used four charged tracks in the reconstruction procedure, the uncertainty because of the tracking amounts to 1.4%.

6.2 PID EFFICIENCY UNCERTAINTY

The PID efficiency systematic error stems from comparison between the efficiency as estimated from the MC events and the efficiency for the real data. While the former is estimated on the provided MC events, the latter has to be estimated from particular decay modes. For kaons and pions, the difference is measured using partially reconstructed D^* decays. For electrons and muons, the estimate is done on the reconstruction of the J/ψ.
For estimation of the PID efficiency uncertainty, we rely on the recent Belle analysis [53] where both the X(3872) and the $\psi(2S)$ are reconstructed in the decay channel $J/\psi\pi\pi$ in a similar manner as in this analysis. The correction factors are defined as $\mathrm{CF} = \frac{\varepsilon_{\mathrm{DATA}}}{\varepsilon_{\mathrm{MC}}}$. For the charged pions, the CF reads

$$CF = 1.00 \pm 0.012 \tag{50}$$

and for the leptons

$$CF = 0.973 \pm 0.017. \tag{51}$$

The error on the correction factor is assumed to be the uncertainty due to the PID efficiency, so the error for the pion track is 1.2% and for the lepton track 1.7%.

6.3 SYSTEMATIC UNCERTAINTY DUE TO BRANCHING FRACTION UNCERTAINTY

The latest PDG [11] values give the following for the used branching fractions:

$$\mathrm{Br}(J/\psi \to e^+e^-) = (5.971 \pm 0.032)\%,$$

$$\mathrm{Br}(J/\psi \to \mu^+\mu^-) = (5.961 \pm 0.033)\%,$$

$$\mathrm{Br}(\psi(2S) \to J/\psi\pi^+\pi^-) = (34.45 \pm 0.30)\%.$$

In terms of relative errors, this amounts to 0.54%, 0.55% and 0.87%, respectively.

6.4 SYSTEMATIC UNCERTAINTY DUE TO NUMBER OF B MESONS

The systematic uncertainty in the number of B mesons is reported as 1.4% [54].

6.5 UNCERTAINTY OF THE RECONSTRUCTION EFFICIENCY

6.5.1 *Systematic error due to uncertainty in the efficiency*

Systematic error due to uncertainty in the efficiency for $\psi(2S)$ is given in Table 25. The combined uncertainty is calculated as $\frac{1}{\sigma^2_{comb.}} = \frac{1}{\sigma^2_{ee}} + \frac{1}{\sigma^2_{\mu\mu}}$ and used for estimation of systematic uncertainty of results, obtained with simultaneous fitting.

Systematic error due to uncertainty in the efficiency for the X(3872) is given in Table 26. Again, the combined uncertainty is calculated as $\frac{1}{\sigma^2_{comb.}} = \frac{1}{\sigma^2_{ee}} + \frac{1}{\sigma^2_{\mu\mu}}$ and used for estimation of the systematic uncertainty of results, obtained with simultaneous fitting.

6.5.2 *In calculation of the inclusive branching fractions*

For the calculation of the inclusive branching fractions, the uncertainty for the efficiency is calculated from averaging over bins in which the $\psi(2S)$ or X(3872) are expected to originate from B mesons. For the X(3872), this amounts to 1.3% for the electronic channel and 1.0% for the muonic channel; for $\psi(2S)$ the values are 2.7% and 2.3%, respectively.

	$\Upsilon(4S)$			$\Upsilon(5S)$			cont		
bin nr	ee	$\mu\mu$	comb.	ee	$\mu\mu$	comb.	ee	$\mu\mu$	comb.
0	0.067	0.060	0.045	0.158	0.114	0.093	0.515	0.409	0.320
1	0.200	0.153	0.122	0.082	0.067	0.052	0.237	0.236	0.167
2	0.125	0.111	0.083	0.056	0.049	0.037	0.162	0.150	0.110
3	0.089	0.077	0.058	0.045	0.036	0.028	0.126	0.101	0.079
4	0.070	0.056	0.044	0.041	0.028	0.023	0.096	0.079	0.061
5	0.052	0.048	0.035	0.031	0.027	0.021	0.087	0.071	0.055
6	0.045	0.044	0.032	0.026	0.024	0.018	0.080	0.067	0.051
7	0.042	0.035	0.027	0.025	0.022	0.017	0.102	0.082	0.064
8	0.037	0.031	0.024	0.037	0.030	0.023	0.151	0.150	0.106
9	0.042	0.041	0.029	0.079	0.071	0.053	0.652	0.117	0.115

Table 25: Relative uncertainty of efficiency for bins in p^* for $\psi(2S)$ reconstruction in different samples. *ee* marks electronic channel, $\mu\mu$ muonic channel. The combined result is used in determination of σBr when a simultaneous fit is used.

	$\Upsilon(4S)$			$\Upsilon(5S)$		
	ee	$\mu\mu$	comb.	ee	$\mu\mu$	comb.
0	0.623	0.609	0.435	0.084	0.063	0.051
1	0.449	0.220	0.198	0.049	0.034	0.028
2	0.212	0.136	0.114	0.040	0.024	0.021
3	0.152	0.107	0.087	0.030	0.020	0.016
4	0.124	0.094	0.075	0.020	0.015	0.012
5	0.110	0.081	0.065	0.019	0.015	0.012
6	0.092	0.072	0.057	0.019	0.015	0.012
7	0.089	0.069	0.055	0.018	0.015	0.012
8	0.084	0.064	0.051	0.026	0.020	0.016
9	0.114	0.092	0.072	0.085	0.067	0.053

Table 26: Relative uncertainty of efficiency for bins in p^* for X(3872) reconstruction in different samples. *ee* marks electronic channel, $\mu\mu$ muonic channel. The combined result is used in determination of σBr when a simultaneous fit is used.

6.6 SUMMARY OF SYSTEMATIC UNCERTAINTIES

All sources of the systematic uncertainty are summarized in Table 27. The total systematic uncertainty is obtained by adding the individual sources of uncertainty in quadrature.

Identification	muons	3.4%
	electrons	3.4%
	pions	2.4%
Tracking efficiency		1.4 %
Secondary BR	$J/\psi \to e^+e^-$	0.54 %
	$J/\psi \to \mu^+\mu^-$	0.55 %
	$\psi(2S) \to J/\psi\pi\pi$	0.87 %
Number of B meson pairs		1.4%
Efficiency		see Table 25, Table 26

Table 27: Systematic uncertainties.

7

RESULTS AND DISCUSSION

7.1 BR(B → $\psi(2s)$ + ANYTHING)

After merging the both channels and accounting for propagation of uncertainties, the result is:

$$\mathrm{Br}(\mathrm{B} \to \psi(2S) + \text{anything}) = (2.817 \pm 0.032 \pm 0.104)\ 10^{-3},$$

which is in accordance with the latest PDG value [11]: $(3.07 \pm 0.21)\ 10^{-3}$. This result presents an important proof of validity for all the procedures and futher results.

7.2 BR($B \to X(3872)$ + ANYTHING)× BR($X(3872) \to J\psi\pi^+\pi^-$)

After merging the both channels and accounting for propagation of uncertainties, the result is:

$$\mathrm{Br}(B \to X(3872) + \text{anything}) \times \mathrm{Br}(X(3872) \to J\psi\pi^+\pi^-) = (2.79 \pm 0.37 \pm 0.11)\ 10^{-5}.$$

A comparison between the previous measurements for the inclusive cross section for decays of B mesons to charmonium is given in Table 28. The last item in the table is the result from above, obtained with using $Br(X(3872) \to J/\psi\pi\pi) = (5.5 \pm 2.0)\%$ [55]. Although most measurements put the inclusive cross section for $B \to$ charmonium + anything at the order 10^{-3}, a very recent Belle preliminary result also quotes an order smaller magnitude for the decays $B \to \chi_{c2}$ + anything. Another interesting result is a comparison of ratio between $\mathrm{Br}(B \to (c\bar{c})K)$ and $\mathrm{Br}(B \to (c\bar{c})$+ anyhing). Table 29 gives the charmonium of interest and the above-mentioned ratio (without errors).

decay mode	latest PDG [11]	Belle preliminary
$B \to J/\psi$+ anything	$(7.8 \pm 0.4)\ 10^{-3}$	
$B \to \psi(2S)$ + anything	$(3.07 \pm 0.21)\ 10^{-3}$	
$B \to \chi_{c1}(1P)$ + anything	$(3.24 \pm 0.25)\ 10^{-3}$	$(3.03 \pm 0.04 \pm 0.22)\ 10^{-3}$
$B \to \chi_{c2}(1P)$ + anything	$(1.65 \pm 0.31)\ 10^{-3}$	$(0.70 \pm 0.05 \pm 0.07)\ 10^{-3}$
$B \to X(3872)$ + anything	$(5.1 \pm 2.0)\ 10^{-4}$	$(0.51 \pm 0.2)\ 10^{-3}$

Table 28: Comparison of branching fractions for inclusive decay modes of B mesons to charmonium.

$(c\bar{c})$ state	ratio
$\psi\,(2S)$	$\approx$ 20%
J/ψ	$\approx$ 12%
X(3872)	$\approx$ 30%
χ_{c1}	$\approx$ 16%
χ_{c2}	$\approx$ 2%

Table 29: Ratio of Br$(B \to (c\bar{c})K)$ and Br$(B \to (c\bar{c})$+ anyhing). The first two values are calculated from the PDG data [11], the third is partially a result of this analysis and the last two items come from the Belle preliminary results.

7.3 RESULTS FOR THE PRODUCTION OF $\psi(2s)$

Tables 30 - 32 give results of the measurement of $\sigma_{e^+e^-\to\psi(2S)}\mathrm{Br}(\psi(2S)\to J/\psi\pi\pi)$ in bins of $p^*_{\psi(2S)}$ for various data samples.

bin nr	σBr [pb]	$\sigma_{\text{stat.}}$ [pb]	$\sigma_{\text{syst.}}$[pb]
0	1.31E-001	4.75E-003	7.90E-003
1	4.55E-001	8.51E-003	5.84E-002
2	7.30E-001	1.14E-002	6.73E-002
3	5.21E-001	9.69E-003	3.70E-002
4	1.73E-002	3.76E-003	1.03E-003
5	1.86E-002	2.51E-003	9.96E-004
6	2.47E-002	1.69E-003	1.27E-003
7	3.09E-002	1.64E-003	1.50E-003
8	3.68E-002	1.68E-003	1.72E-003
9	3.86E-002	1.54E-003	1.93E-003

Table 30: Results for the production of $\psi(2S)$ in the $\Upsilon(4S)$ sample. σBr marks $\sigma_{e^+e^-\to\psi(2S)\text{ any.}}\mathrm{Br}(\psi(2S)\to J/\psi\pi\pi)$. All quantities are in units of pb.

bin nr	σBr [pb]	$\sigma_{\text{stat.}}$ [pb]	$\sigma_{\text{syst.}}$[pb]
0	2.16E-002	4.68E-003	2.18E-003
1	1.21E-001	1.12E-002	7.95E-003
2	2.31E-001	1.55E-002	1.27E-002
3	1.38E-001	1.29E-002	6.80E-003
4	7.98E-002	9.22E-003	3.72E-003
5	2.88E-002	5.87E-003	1.30E-003
6	2.70E-002	4.46E-003	1.20E-003
7	3.08E-002	4.03E-003	1.35E-003
8	3.54E-002	4.17E-003	1.65E-003
9	3.86E-002	4.10E-003	2.56E-003

Table 31: Results for the production of $\psi(2S)$ in the $\Upsilon(5S)$ sample. σBr marks $\sigma_{e^+e^-\to\psi(2S)\text{ any.}}\mathrm{Br}(\psi(2S)\to J/\psi\pi\pi)$. All quantities are in units of pb.

bin nr	σBr [pb]	$\sigma_{\text{stat.}}$ [pb]	$\sigma_{\text{syst.}}$[pb]
0	3.42E-005	1.89E-003	2.25E-005
1	6.91E-003	5.15E-003	2.34E-003
2	1.91E-002	6.31E-003	4.32E-003
3	1.41E-002	5.01E-003	2.39E-003
4	1.52E-002	4.57E-003	2.04E-003
5	2.14E-002	4.84E-003	2.64E-003
6	4.00E-002	5.67E-003	4.65E-003
7	3.87E-002	5.74E-003	5.45E-003
8	4.63E-002	5.69E-003	1.01E-002
9	3.77E-002	4.54E-003	2.51E-002

Table 32: Results for the production of $\psi(2S)$ in the continuum sample. σBr marks $\sigma_{e^+e^-\to\psi(2S)\text{ any.}}\text{Br}(\psi(2S)\to J/\psi\pi\pi)$. All quantities are in units of pb.

From the continuum sample, the result for $\sigma_{e^+e^-\to\psi(2S)+anything}$ can be extracted, using 0.3445 for the $\text{Br}(\psi(2S)\to J/\psi\pi\pi)$:

$$\sigma_{e^+e^-\to\psi(2S)+anything} = (0.694 \pm 0.046 \pm 0.083)\text{ pb}$$

7.4 PRODUCTION OF X(3872)

Tables 33 - 35 give results of the measurement of $\sigma_{e^+e^-\to X(3872)}\text{Br}(X(3872)\to J/\psi\pi\pi)$ in bins of p^*_X for various data samples.
The results for the upper limit use the 90% confidence level. RooStats, a framework within ROOT [49] is used for the determination of the upper limit.

bin nr	σBr [pb]	$\sigma_{\text{stat.}}$ [pb]	$\sigma_{\text{syst.}}$[pb]	upper limit (stat. only)
0	5.63E-003	1.70E-003	2.46E-003	
1	1.93E-002	3.47E-003	3.89E-003	
2	2.53E-002	3.70E-003	3.06E-003	
3	2.51E-003	3.04E-003		7.12E-003
4	2.08E-003	2.71E-003		6.12E-003
5	1.94E-003	1.52E-003		3.71E-003
6	3.88E-022	2.82E-004		8.74E-004

Table 33: Results for the production of the X(3872) in the $\Upsilon(4S)$ sample. σBr marks $\sigma_{e^+e^-\to X(3872)\text{ any.}}\text{Br}(X(3872)\to J/\psi\pi\pi)$. All quantities are in units of pb. For the bins 3-6, the result is consistent with 0 and un upper limit has been set.

bin nr	σBr [pb]	$\sigma_{\text{stat.}}$ [pb]	$\sigma_{\text{syst.}}$[pb]	upper limit (stat. only)
0	1.28E-007	1.68E-003		3.51E-003
1	3.06E-003	4.56E-003	1.48E-004	
2	1.04E-002	5.63E-003	4.64E-004	
3	3.17E-007	4.42E-003		7.93E-003
4	1.00E-007	2.05E-003		5.37E-003
5	2.74E-003	2.99E-003		7.45E-003
6	9.83E-005	1.76E-003		3.29E-003
7	3.31E-004	1.11E-003		2.22E-003

Table 34: Results for the production of the X(3872) in the $\Upsilon(5S)$ sample. σBr marks $\sigma_{e^+e^-\to X(3872)\text{ any.}}\text{Br}(X(3872) \to J/\psi\pi\pi)$. All quantities are in units of pb. In bins where the result is consistent with 0, un upper limit has been set.

bin nr	σBr [pb]	$\sigma_{\text{stat.}}$ [pb]	$\sigma_{\text{syst.}}$[pb]	upper limit (stat. only)
0	9.67E-004	4.45-003		8.52E-003

Table 35: Results for the production of the X(3872)in the continuum sample (kinematic range $0 < p^*_{X(3872)} < 4.0$ GeV). σBr marks $\sigma_{e^+e^-\to X(3872)\text{ any.}}\text{Br}(X(3872) \to J/\psi\pi\pi)$. All quantities are in units of pb.

8

POVZETEK V SLOVENŠČINI

8.1 TEORETIČNI UVOD

Delec X(3872) je bil odkrit l. 2003, ko je raziskovalna skupina Belle preučevala razpade $B^{\pm} \to K^{\pm}\pi^{+}\pi^{-}J/\psi$. V porazdelitvi invariantne mase $J/\psi\pi^{+}\pi^{-}$ so opazili nepričakovan vrh, ki je pripadal prej nepoznanemu delcu. Po njegovi invariantni masi, 3.872 GeV, so ga poimenovali X(3872). Odkritje je takoj sprožilo zanimanje mednarodne fizikalne skupnosti in skupine BaBar [2], CDF [3] in Do [4] so odkritje potrdile v nekaj mesecih. Delca X(3872) ni bilo moč uvrstiti v znane kvarkovske modele, ravno tako je bila nenavadna njegova razpadna širina, 2.3 MeV.
Hitro so se oblikovale štiri hipoteze o dejanski naravi X(3872):

- še neuvrščeno vezano stanje $c\bar{c}$,
- hibrid, vezano stanje kvarkov c, $\bar{c}$ in gluona,
- mezonska molekula, vezano stanje dveh mezonov D in
- tetrakvark, vezano stanje štirih kvarkov.

Za lažjo obravnavo hipotez je bilo najprej potrebno ugotoviti, kakšno je kvantno število J^{PC} za X(3872).
J^{PC} je kvantno število, pri katerem J predstavlja celotno vrtilno količino delca, P lastno vrednost operatorja parnosti (zrcaljenja preko izhodišča koordinatnega sistema) in C lastno vrednost operatorja konjugacije naboja (zamenjave pozitivnega z negativnim električnim nabojem in nasprotno); za P in C sta možni lastni vrednosti ± 1. Pri vezanih stanjih kvarka c in $\bar{c}$, ti. čarmoniju, je J^{PC} preprosto povezati s tirno vrtilno količino l in spinskim delom vrtilne količine, s. Lastne vrednosti operatorjev parnosti in konjugacije naboja zapišemo kot

$$\begin{aligned} P &= (-1)^{l+1}; \\ C &= (-1)^{l+s}. \end{aligned} \tag{52}$$

Vrednost operatorja C je bila nedvoumno določena zelo hitro, že dve leti po odkritju [26, 27]. C je multiplikativno kvantno število, kar pomeni, da lahko na C X(3872) sklepamo glede na C njegovih razpadnih produktov. V primeru radiativnih razpadov X(3872)$\to J/\psi\gamma$ je C tako za J/ψ kot tudi za γ -1, kar pomeni,

da ima X(3872) pozitiven C. Določitev C je omejila možnost uvrstitve X(3872) v sistem čarmonija, ni pa postavila omejitev glede ostalih hipotez.
Kar 12 let je minilo od odkritja X(3872) do končne določitve J^P. Tako pri analizi dipionske mase kot tudi pri analizi kotne porazdelitve nista bili izločeni zgolj dve moznosti - 1^+ ali 2^-. Oba postopka sta bila izvedena na vzorcih, kjer X(3872) razpada na končna stanja $J/\psi\pi^+\pi^-$.
L. 2006 je CDF [29] preučeval omenjeni razpad, primer razpada preko močne interakcije. Taki razpadi ohranjajo parnost (P) ter tirno vrtilno količino (L), parnost X(3872) pa je določena s parnostmi razpadnih produktov in tirne vrtilne količine kot $P_X = P_{J/\psi}\ P_\rho\ (-1)^L$. Analiza je sicer nedvoumno pokazala, da ima dipionska masa vrh pri vrednostih blizu mase mezona ρ, katerega parnost je negativna. Raziskovalna skupina je zaključila, da je najbolj verjetna vrednost za L 0, a ni mogla izključiti možnosti $L = 1$ in s tem negativne parnosti X(3872).
Kotna analiza zahteva opis petdimenzionalnega problema, torej iskanje porazdelitve po petih izbranih spremenljivkah: treh kotih vijačnosti (θ_X, $\theta_{\pi\pi}$, $\theta_{J/\psi}$) ter dveh kotih med razpadnimi ravninami ($\Delta\phi_{X,\pi\pi}$, $\Delta\phi_{X,J/\psi}$). Analiza LHCb [28] je bila prva, ki je upoštevala vseh pet količin; prejšnji analizi skupin CDF [29] in Belle [30] sta zaradi premajhnega števila podatkov, ki je bilo na voljo ob času analize, problem poenostavili z obravnavo v treh dimenzijah. Raziskava LHCb postavlja verjetnost za $J^P = 1^+$ kar za osem standardnih odklonov višje kot za $J^P = 2^-$.
J^{PC} za X(3872) je tako nedvoumno 1^{++}. S tem se skrči nabor možnosti za uvrstitev X(3872) v sistem čarmonija in izključi hipotezo, da je X(3872) hibridno stanje. V slednjem primeru bi bila kvantna števila eksotična, npr. 1^{-+}.
L. 2005 se je pojavila hipoteza, da je X(3872) eno od stanj predlaganega tetrakvarka - hadrona, sestavljenega iz dveh kvarkov in dveh antikvarkov [35]. Model napoveduje obstoj dveh stanj, X_l in X_h, ki se razlikujeta tako po masi kot po razpadnih načinih. Ker masna razlika ni bila opažena [30, 37], je bila hipoteza o tetrakvarkovski naravi opuščena.
Zaradi bližine mase X(3872) pragu za tvorbo mezonov $D^{*0}\overline{D}^0$ je nastala ideja o ti. mezonski molekuli, vezanem stanju dveh mezonov D. Razpad X(3872) v dva mezona D je bil opažen že l. 2006 [33, 34]. Kljub temu, da je tak razpad indikator mogoče molekulske narave X(3872), skrb vzbuja razlika izmerjenih mas X(3872) glede na razpadni kanal - masa X(3872) v razpadih na mezone D je tako višja kot masa X(3872) v razpadih na $J/\psi\pi^+\pi^-$.

Takojšnja produkcija X(3872) je precej neraziskano podrocje. Kot bolj splošni primer lahko takojšnjo produkcijo čarmonija razdelimo na produkcijo, kjer nastane eno vezano stanje $c\bar{c}$ in produkcijo, kjer poleg tega stanja nastane bodisi še en čarmonij bodisi par mezonov D.
Produkcija zgolj enega čarmonija se lahko zgodi v ti. barvno singletnem ali oktetnem načinu. Pri prvem sta nastala kvarka c in $\bar{c}$ že v singletnem stanju, ki je

kar enako kot stanje po hadronizaciji. Pri drugem primeru sta nastala kvarka v oktetnem stanju in morata za prehod v singletno stanje izsevati en gluon. Teoretčne napovedi [22, 23] za produkcijo $e^+e^- \to J/\psi X_{non-c\bar{c}}$ postavljajo za presek vrednosti ~1 pb, a so zaradi nizkih energij, ki so na voljo v trkalnikih elektronov in pozitronov, precej nezanesljive.
Pri ti. dvojni produkciji čarmonija lahko nastala kvarka c in $\bar{c}$ iz vakuuma potegneta dodaten par $c - \bar{c}$ in hadronizirata v dva čarmonija, denimo J/ψ in η_C. Lahko pa iz vakuuma potegneta tudi dva para kvarkov, denimo $c - \bar{c}$ in $u - \overline{u}$; v tem primeru so končna stanja en čarmonij in dva mezona D. Teoretične napovedi, ki izhajajo iz barvno singletnega modela [25], postavljajo za produkcijo $e^+e^- \to J/\psi\eta_C$ vrednost ~4 fb.
Vse štiri načine opisuje slika 80.

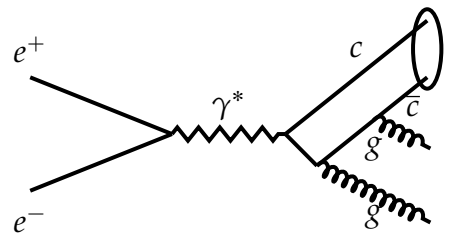

(a) Barvno singletna produkcija, nastanek vezanega stanja $c\bar{c}$ v singletnem stanju.

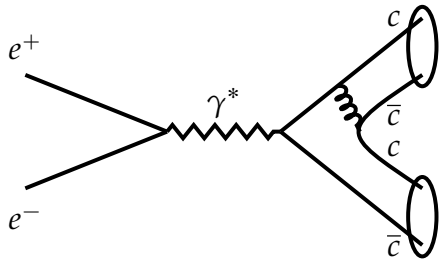

(b) Primer dvojne produkcije čarmonija z dvema vezanima $c\bar{c}$ stanjema.

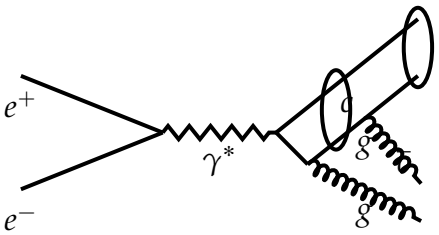

(c) Barvno oktetna produkcija, nastanek vezanega stanja $c\bar{c}$ v oktetnem stanju, izsevanje gluona in prehod mezona v barvno singletno stanje

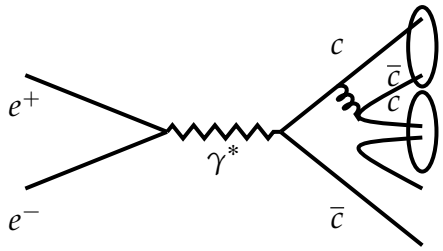

(d) Primer dvojne produkcije čarmonija z enim vezanim $c\bar{c}$ stanjem in dvema mezonoma D v končnem stanju.

Slika 80: Primeri mehanizmov takojšnje produkcije čarmonija.

L. 2009 je raziskovalna skupina Belle [21] objavila obsežen članek, kjer je bila obravnavana večina navedenih procesov. Nastanek dveh čarmonija je bil izmerjen s pomočjo rekonstrukcije odrivne mase, ki poleg neposredno rekonstruiranega čarmonija identificira tudi dodatni čarmonij preko relacije $M_{\text{odrivna}}((c\bar{c})_{\text{tag}}) = \sqrt{(E_{\text{CM}} - E^*_{\text{tag}})^2 - p^{*2}_{\text{tag}}}$. Ravno tako so bili obravnavani dogodki, kjer poleg čarmonija (J/ψ) nastane hadron s kvarkom c, denimo mezoni D. Za navedene procese je bila izmerjena tudi fragmentacijska funkcija, opis porazdelitve nastalih

	J/ψ X	$J/\psi\ c\bar{c}$	J/ψ $X_{\text{non-}c\bar{c}}$
σ	1.17 ± 0.02	0.74 ± 0.08	0.43 ± 0.09
σ_{Pet}	1.19 ± 0.01	0.73 ± 0.05	0.48 ± 0.07
ε_{Pet}	0.16 ± 0.01	0.10 ± 0.02	$0.32^{+0.16}_{-0.12}$

Tabela 36: Preseki za procese $e^+e^- \to J/\psi$ X,$e^+e^- \to J/\psi\ c\bar{c}$in $e^+e^- \to J/\psi\ X_{\text{non-}c\bar{c}}$ s parametri spektra J/ψ, ε_{Pet} [21].

delcev po gibalni količini. Za prilagajanje podatkom je bila izbrana Petersonova fragmentacijska funkcija, definirana kot

$$z = \frac{p}{p_{\max}},$$
$$\frac{dN}{dz} \propto \frac{1}{z}(1 - \frac{1}{z} - \frac{\varepsilon}{1-z})^{-2}. \tag{53}$$

Rezultati za preseke posameznih procesov in vrednosti parametrov fragmentacijske funkcije so zbrani v tabeli 36.
X(3872) ostaja najbolj preučevano stanje v skupini ti. eksotičnih čarmoniju podobnih hadronov. Ker kvarkovska sestava še vedno ni določena, X(3872) ostaja izjemno zanimiv problem v kvantni kromodinamiki. Takojšnja produkcija X(3872) še ni bila opažena; ker pa X(3872) vsebuje prispevek komponente $c\bar{c}$, je taka produkcija sorodna takojšnji produkciji čarmonija v trkih elektronov in pozitronov. Neujemanje med teoretičnimi napovedmi in eksperimentalnimi rezultati predstavlja dodatno motivacijo za študije takojšnje produkcije X(3872) v trkih elektronov in pozitronov.

8.2 POSTAVITEV POSKUSA IN PROGRAMSKO OKOLJE

8.2.1 *Pospeševalnik KEKB in detektor Belle*

Podatki, ki so bili uporabljeni za namene doktorskega dela, so bili zajeti z detektorjem Belle na pospeševalniku KEKB v Tsukubi na Japonskem.
Pospeševalnik KEKB je energijsko asimetrični trkalnik elektronov in pozitronov z obsegom okoli 3 km. Sestavljata ga dva enako velika pospeševalna obroča; v obroču HER (High Energy Ring) krožijo gruče elektronov z energijo okoli 8 GeV, v obroču LER (Low Energy Ring) pa gruče pozitronov z energijo 3,5 GeV. Do trkov gruč elektronov in pozitronov prihaja v interakcijski točki, kjer se križata obe pospeševalni cevi in kjer stoji tudi detektor Belle. Energiji elektronov in pozitronov sta izbrani tako, da je celotna razpoložljiva energija pri trkih enaka 10,58 GeV, kar ustreza lastni energiji resonance $\Upsilon(4S)$. Resonanca $\Upsilon(4S)$, ki nastane ob trkih, je najlažje vezano stanje kvarkov $b\bar{b}$, katere masa je nad pragom za razpad v par mezonov $B\overline{B}$. Glavni namen gradnje detektorja Belle je bil preučevanje časovno odvisne asimetrije CP v sistemu mezonov B; zaradi razlike

v energiji elektronov in pozitronov imajo razpadni produkti Lorentzov potisk $\beta\gamma = 0,425$, tako da nastali B mezoni v svojem življenjskem času preletijo tipično ~200 μm. Pri težiščni energiji pa potekajo tudi številni drugi procesi: elektromagnetne interakcije (npr. sipanje BhaBha), procesi $e^+e^+ \rightarrow \tau\tau$, predvsem pa procesi, kjer ob anihilaciji e^+e^- nastane virtualni foton, ki razpade v enega lažjih parov kvark-antikvark ($u\bar{u}$, $d\bar{d}$, $s\bar{s}$ in za to analizo ključen $c\bar{c}$). Delovanje pospeševalnika opisuje luminoznost $\mathcal{L}$, ki jo lahko povežemo s številom trkov delcev kot $\frac{dN}{dt} = \mathcal{L}\sigma$, kjer je σ presek za specifičen proces. Načrtovana luminoznost KEKB je bila $1.0 \times 10^{34}/\text{cm}^2\text{s}$; trkalnik je to mejo presegel za dvakrat že l. 2009. Integrirana luminoznost, $L = \int \mathcal{L}dt$, je merilo za število zbranih dogodkov. V 11 letih delovanja je detektor Belle zbral več kot 1000 fb^{-1} podatkov, 711 fb^{-1} pri resonanci $\Upsilon(4S)$ in 100 fb^{-1} pod energijo resonance $\Upsilon(4S)$.

Detektor Belle je postavljen okoli interakcijske točke pospeševalnika KEKB. Je cilindrično simetrični magnetni spektrometer, namenjen detekciji dolgoživih delcev, ki nastanejo ob trkih elektronov in pozitronov. Omogoča detekcijo tako nabitih (elektronov, mionov, pionov, kaonov in protonov) kot nevtralnih delcev (fotonov in nevtralnih kaonov). Težji hadroni, kot sta X(3872) in $\psi(2S)$, razpadejo prehitro, da bi jih lahko detektirali neposredno. Tako je njihova razpadna veriga rekonstruirana preko dolgoživih razpadnih produktov. Detektor Belle mora zaradi rekonstrukcije razpadne verige opravljati tri različne naloge: identifikacijo delcev, opis njihove sledi v detektorju in meritev njihove gibalne količine. Detektor Belle tako sestavljajo različni poddetektorji, namenjeni specifičnim nalogam. Poddetektorje obdaja magnetno polje gostote 1,5 T; postavljeni so simetrično okoli interakcijske točke z nekaj asimetrijami naprej - nazaj, ki sledijo topologiji trkov elektronov in pozitronov. Detektor Belle je predstavljen na sliki 81.

Detektor Belle je magnetni spektrometer - ko nabit delec vstopi v magnetno polje, ki obdaja detektor, se njegova trajektorija spremeni v vijačnico. Z meritvijo ukrivljenosti se določi gibalna količina tega delca.

Detektor SVD (detektor sledi), ki leži takoj za cevjo, kjer krožijo elektroni in pozitroni, je namenjen meritvi trajektorij delcev zelo blizu interakcijske točke. SVD je sestavljen iz večih slojev koncentričnih silicijevih mikropasovnih detektorjev in je odločilnega pomena za rekonstrukcijo razpadne točke mezonov B, s tem pa za meritev časovno odvisne asimetrije CP.

Detektor CDC (osrednja potovalna komora) je osrednji del detektorja; meri sledi nabitih delcev in iz njihove ukrivljenosti v magnetnem polju določi gibalno količino. Ob preletu komore nabiti delci ionizirajo plin, ioni pa nato na žicah za zaznavo povzročijo merljiv sunek. CDC prispeva tudi k identifikaciji delcev z nizko gibalno količino (p < 1 GeV) preko meritve izgube energije zaradi identifikacije.

Detektorji, nameščeni za osrednjo potovalno komoro, skrbijo za identifikacijo delcev bodisi preko meritve hitrosti delca bodisi preko opazovanja interakcije delca z materijo. Delce identificiramo preko povezave $p = \gamma mv$: če poznamo hitrost in gibalno količino delca, potem masa nedvoumno določi tip delca.

Detektor ACC (števec Čerenkovega sevanja na osnovi aerogela) razlikuje med kaoni in pioni z gibalno količino ~1,2 - 3,5 GeV preko zaznave fotonov, ki jih

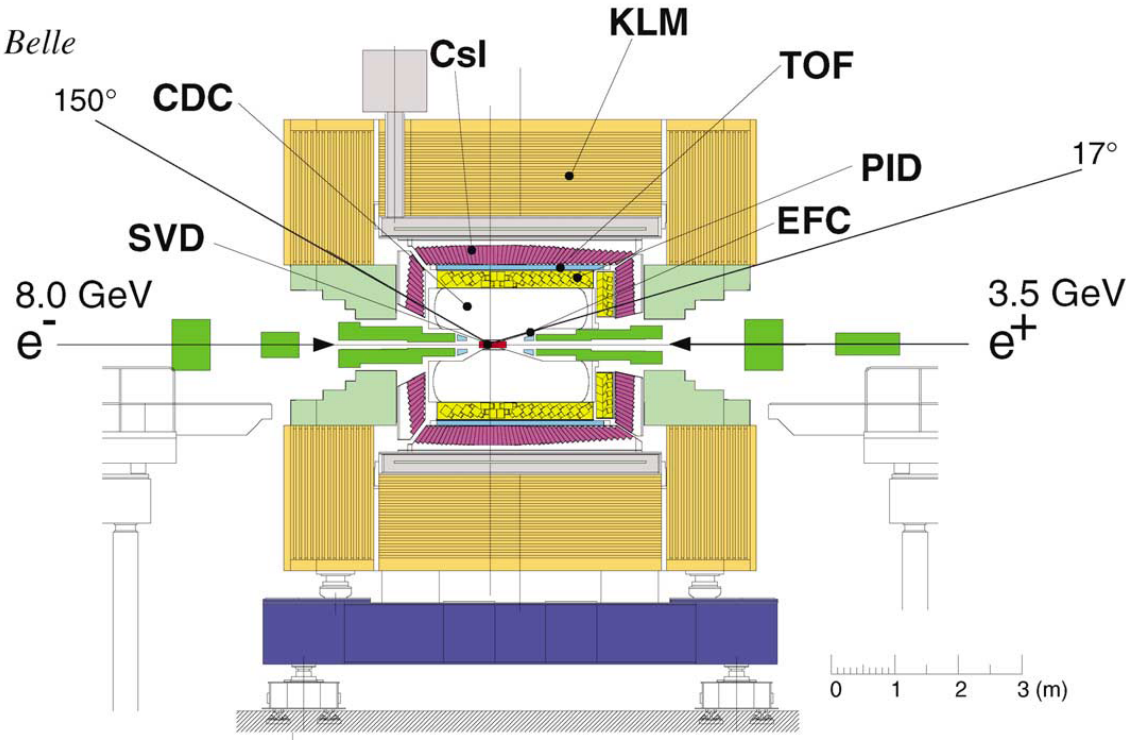

Slika 81: Shematski prerez detektorja Belle z oznakami komponent, razloženimi v besedilu. Magnetno polje v središčnem delu detektorja znaša 1,5 T [44].

kot posledico sevanja Čerenkova emitira aerogel. V spektrometru Belle je ACC pragovni števec, kar pomeni, da glede na pričakovane gibalne količine pionov, mionov in elektronov nastajajo Čerenkovi fotoni, kaoni in protoni pa teh fotonov ne producirajo. Fotone Čerenkova zaznava nabor fotopomnoževalk, ki dobro delujejo tudi v magnetnem polju detektorja.
TOF (merilec časa preleta) je plastični scintilator. Začetek meritve časa določi prehod gruč elektronov in pozitronov skozi interakcijsko točko, komec pa sprožijo fotopomnoževalke ob robu scintilatorja, ki zaznavajo scintilacijske bliske ob preletu delca. TOF skrbi za identifikacijo delcev v območju ~0,8-1,2 GeV.
Na zunanjem robu sledita še dva kalorimetra, ECL (elektromagnetni kalorimeter) in KLM (detektor dolgoživih nevtralnih kaonov in mionov).
ECL je namenjen meritvi energije in položaja fotonov in elektronov. Fotoni v ECl povzročijo nastanek parov e^+e^-, nastali elektroni in pozitroni pa preko zavornega sevanja ponovno sevajo visokoenergijske fotone. Tako po več korakih na koncu nastane plaz nizkoenergijskih elektronov, pozitronov in fotonov, ki jih zaznajo scintilatorji. Celotna energija delcev v plazu je sorazmerna z energijo začetnega visokoenergijskega fotona ali elektrona, ki se na ta način ustaviv v elektromagnetnem kalorimetru. Hkrati ECL zaradi značilne oblike pljuskov, ki nastajajo ob zavornem sevanju, prispeva k ločevanju elektronov od mionov in nabitih hadronov.
KLM je nameščen na zunanji strani detektorja. Sestavljen je iz izmenjajočih se plasti plinskih detektorjev nabitih delcev in plasti železa, ki služijo kot absorpcijski material. S KLM ločimo mione od pionov in kaonov, ki še priletijo do zunanjih

plasti detektorja. Pri ločevanju izkoriščamo dejstvo, da mioni ne interagirajo preko močne interakcije - tako preletijo velik del detektorja, medtem ko ostali delci, ki dosežejo KLM, v njem sprožijo hadronski plaz.

8.2.2 *Računalniška simulacija in programska orodja*

Za namene testiranja analize in odziva detektorja na razne procese se v okviru raziskovalne skupine Belle uporabljajo različni Monte Carlo (MC) simulirani podatki. MC metode so v splošnem računalniški algoritmi, ki *naključno* generirajo dogodke iz dane začetne verjetnostne porazdelitve.
MC simulacija je razdeljena na dva dela: simulacijo golih fizikalnih procesov (kjer glede na znane porazdelitve, denimo kotne odvisnosti, razvejitvena razmerja, ipd. opišemo fizikalno ozadje iskanih procesov) in simulacijo odziva detektorja (kjer preučujemo, kako simulirani proces poteka v detektorju).
MC simulacije ločimo tudi glede na to, katere procese opisujejo. Tako signalna MC simulacija opisuje zgolj izbrani proces; s tem tipom simulacije določimo sprejemnost za izbrani tip dogodkov (torej kolikšen delež dogodkov analiza dejansko rekonstruira. Generična MC simulacija pa je namenjena oceni prispevkov k signalu, ki prihajajo iz ozadja, ne pa iz izbranega procesa. S tem tipom simulacije pridobimo tudi podatke o ločljivosti količin, ki nas bodo zanimale na pravih podatkih.
Rekonstrukcija dogodkov je narejena v okviru programskega orodja BASF (Belle Analyisis Software Framework), ki omogoča, da v celotni zbirki podatkov analiziramo vsak dogodek posebej. Dobljeni rezultati so zapisani v formatu, ki omogoča delo s programom ROOT. Vsi nadaljni postopki, priprava grafov porazdelitev, prilagajanje funkcij porazdelitvem, statistični testi, ipd. so ravno tako izvedeni s programom ROOT in njegovim posebnim okoljem RooFit.

8.3 OSNOVE POSTOPKA ANALIZE

Tako zaradi nepoznavanja kvarkovske strukture X(3872) kot tudi zaradi relativne neraziskanosti področja takojšnje produkcije X(3872) uvedemo kontrolni kanal. Stanje $\psi(2S)$ je dobro poznano vezano stanje $c\bar{c}$, ki z X(3872) deli kvantno število J^{PC}, z njim pa deli tudi izbrani kanal za rekonstrukcijo, $J/\psi\pi^+\pi^-$.
Analiza poteka na treh različnih setih podatkov - $\Upsilon(4S)$ (711 fb^{-1}), $\Upsilon(5S)$ (121 fb^{-1}) in ti. podatki kontinua (60 MeV pod $\Upsilon(4S)$, 89 fb^{-1}). Analiza je narejena posebej na vsakem setu podatkov.
Izbrani rekonstrukcijski kanal je $J/\psi\pi^+\pi^-$, kjer J/ψ rekonstruiramo v leptonskih kanalih (e^+e^- ali $\mu^+\mu^-$). Izbrana spremenljivka za rekonstrukcijo je razlika mas, definirana kot

$$\Delta m = m_{X(3872)} - m_{J/\psi} - m_{\pi^+} - m_{\pi^-}, \tag{54}$$

kjer sta $m_{X(3872)}$ in $m_{J/\psi}$ invariantni masi, medtem ko sta masi pionov kar nominalni masi, pripisani ob identifikaciji delca.

Pričakujemo, da se bo kinematika X(3872), ki izvirajo iz takojšnje produkcije, razlikovala od kinematike X(3872), ki so posledica razpada mezonov B. Zato biniramo Δm glede na p_X^* v 10 binov v območju od 0-4 GeV.

8.3.1 *Signalna MC simulacija*

MC simulacije skupine Belle v času nastanka tega dela niso vsebovale opisa takojšnje produkcije čarmonija; še več, v okviru orodij za pripravo MC simulacij takšne produkcije ni bilo možno simulirati. Kakršna koli rešitev bi morala izpolniti naslednje zahteve: X(3872) mora izvirati iz takojšnje produkcije, gibalna količina X(3872) mora pokriti celoten razpoložljivi fazni prostor in slediti Petersonovi fragmentacijski funkciji, poleg X(3872) pa morajo biti producirani tudi D mezoni. Rešitev uporablja poenostavitev problema - X(3872) je produciran neposredno, ne v hadronizaciji $c\bar{c}$, poleg njega pa je produciran dodatni $c\bar{c}$, ki pa hadronizira neodvisno. Dobljeni dogodki so nato uteženi tako, da ustrezajo Petersonovi fragmentacijski funkciji.
Dipionska masa je simulirana tako, da kar najbolj ustreza rezultatom nekaterih meritev [29]; razpad X(3872) je torej simuliran kot X(3872)$\rightarrow \rho\ J/\psi$.
Za potrebe analize so bili simulirani trije podobni vzorci: X(3872) $+c\bar{c}$, $\psi\,(2S) + c\bar{c}$ in $J/\psi + c\bar{c}$, prva dva kot signalni MC vzorec in slednji kot pomemben dodatek za generični MC. Število generiranih dogodkov izračunamo preko enačbe:

$$N_{\text{signal}} = \mathcal{L} * N_{\text{streams}} * \sigma_{\text{prod}} * BR(X(3872) \rightarrow J/\psi\rho) * BR(J/\psi \rightarrow l^+l^-) \quad (55)$$

za X(3872) oz. $\psi\,(2S)$ ali kot

$$N_{\text{signal}} = \mathcal{L} * N_{\text{streams}} * \sigma_{\text{prod}} * BR(J/\psi \rightarrow l^+l^-) \quad (56)$$

za J/ψ.
V vseh primerih za σ_{prod} vzamemo 0.74 pb^{-1}.
Generični MC, uporabljen v tej analizi, je bil produciran l. 2009, ko še niso bile znane vse lastnosti X(3872). Tako je X(3872) v simulacijo vključen zgolj v razpadih B mezonov v razpadnem kanalu $B^+ \rightarrow$X(3872)K. V generičnem MC je vrednost razvejitvenega razmerja BR(X(3872)$\rightarrow J/\psi\pi\pi$) postavljena na 0.366, medtem ko [50] postavlja spodnjo mejo na 5×10^{-2}; slednji rezultat je uporabljen tudi za študije na MC v tej analizi. Vsi razpadi X(3872) so skalirani, da dosežejo podano spodnjo mejo.

8.3.2 *PID*

Rekonstrukcija se začne z identifikacijo štirih tipov končnih delcev: dveh leptonov in dveh pionov. Identifikacija hadronov združi informacije iz meritve $\frac{dE}{dx}$ v CDC, iz detektorja TOF in iz meritve fotoelektronov. Verjetnost, da je rekonstruirani delec enak kot identifikacijska hipoteza, je zmnožek verjetnosti iz poddetektorjev.

$$P_f = P_f^{dE/dx} \times P_f^{ACC} \times P_f^{TOF} \quad (57)$$

vzorec	spremenljivka	$X(3872)_{ee}$	$X(3872)_{\mu\mu}$	$\psi(2S)_{ee}$	$\psi(2S)_{\mu\mu}$
$\Upsilon(4S)$	$\Delta\, m_{J/\psi}$	[-0.102,0.018]	[-0.021,0.021]	[-0.1,0.03]	[-0.03,0.03]
	$m_{\pi\pi}$	> 0.72	> 0.68	/	/
kontinuum	$\Delta\, m_{J/\psi}$	[-0.069,0.027]	[-0.015,0.015]	[-0.099,0.021]	[-0.024,0.024]
	$m_{\pi\pi}$	>0.62	>0.66	/	/
$\Upsilon(5S)$	$\Delta\, m_{J/\psi}$	[-0.132,0.03]	[-0.054,0.054]	[-0.12,0.056]	[-0.052,0.052]
	$m_{\pi\pi}$	>0.68	>0.68	/	/

Tabela 37: Rezi za vse rekonstruirane vzorce in kanale po optimizaciji FOM. Vse vrednosti so v enotah GeV.

Elektrone identificiramo z združevanjem informacij iz treh poddetektorjev: oblike plohe v ECL, meritve ionizacijske izgube $\frac{dE}{dx}$ v CDC, primerjave sledi iz CDC in položaja plohe v ECL ter števila fotoelektronov v ACC. Podobno velja za mione, le da dodatno informacijo dobimo iz povezave meritve v CDC in KLM.

8.3.3 *FOM*

Namen optimizacije FOM je določitev selekcijskih kriterijev za izbrani razpadni kanal. Selekcijski kriteriji morajo biti določeni tako, da kar najbolje ločijo signal od ostalih procesov, ki predstavljajo ozadje; to storimo z iskanjem maksimuma ti. FOM (figure-of-merit), definiranega kot

$$\mathrm{FOM} = \frac{N_{\mathrm{sig}}}{\sqrt{N_{\mathrm{sig}} + N_{\mathrm{bkg}}}}. \tag{58}$$

8.3.3.1 *Predizbor HadronB*

Prvi korak pri optimizaciji predstavlja predizbor HadronB, ki izloči procese, ki eksperimentalno niso zanimivi (npr. $\tau\tau$, $\gamma\gamma$), in obdrži procese, kot sta npr. $B\overline{B}$ in $q\overline{q}$. Selekcijski kriteriji so število nabitih sledi, energijska izguba v detektorju, vsota gibalnih količin v z-smeri ter točka prvotne interakcije.

8.3.3.2 *Uporabljeni rezi*

Pri optimizaciji selekcijskih kriterijev je bilo izbranih pet različnih količin. Tri količine so optimizirane ne glede na vzorec in končni rekonstruirani delec. Tako velja, da je $PID_{leptons} > 0.8$, $PID_{pions} < 0.3$ in $\chi^2_{\text{vertex fit}} < 20$. Rezultati za preostala dva reza, omejitev mase J/ψ in rez po dipionski masi, so zbrani v tabeli 37.

8.3.3.3 *Sprejemnost*

Za vsakega od naštetih kanalov in vzorcev v vsakem razdelku glede na $p^*_{rec.particle}$ izračunamo sprejemnost kot količnik med številom pravilno rekonstruiranih dogodkov in številom vseh dogodkov. Rezultati so podani v sliki 82.

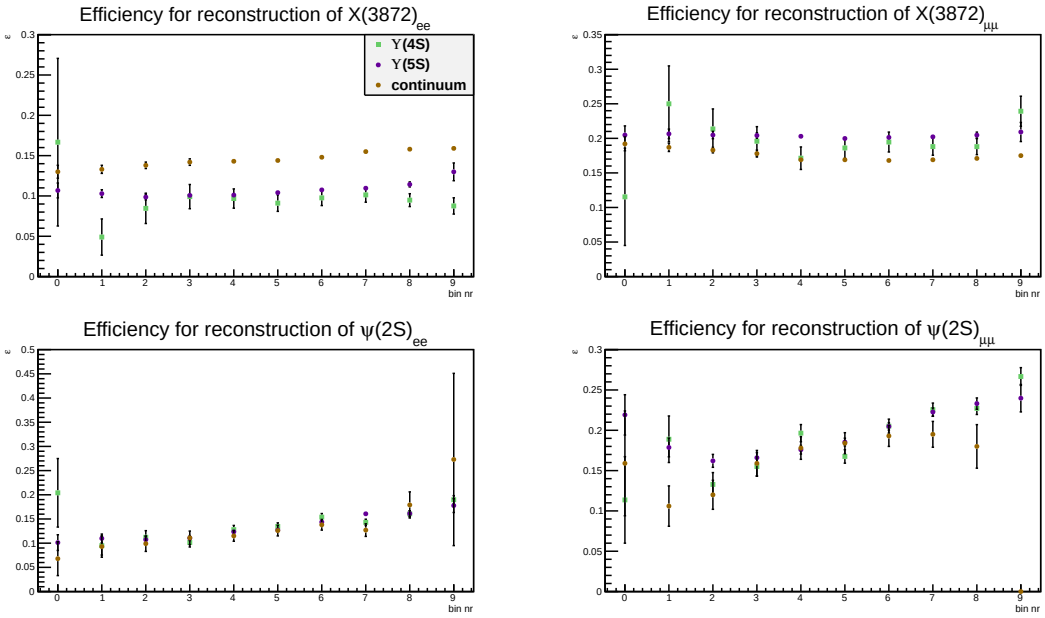

Slika 82: Sprejemnost za vse kanale in vzorce.

8.3.4 *Rezultati rekonstrukcije na MC vzorcu*

Pričakovani vrednosti za vrh v porazdelitvi Δm sta za X(3872) 0.495 GeV ter za $\psi(2S)$ 0.31 GeV. Vsi grafi za rekonstruirane dogodke sledijo enakemu vzorcu - bolj ali manj poudarjen vrh, ki izvira iz pravilno rekonstruiranih signalnih dogodkov, ter gladko (polinomsko) ozadje. Še dodaten vzorec je posebej viden v rekonstrukciji $\psi(2S)$: v prvih 4 razdelkih prevladujejo $\psi(2S)$, ki izvirajo iz razpadov mezonov B, v nadaljnih pa je dominantni prispevek iz takojšnje produkcije. Če podrobneje preverimo sestavo ozadja, lahko ugotovimo, da večina ozadja izvira iz pravilno rekonstruiranih J/ψ, ki jim dodamo naključne pione. J/ψ izvirajo iz razpadov mezonov B. [manjka še kakšna slikica]

8.4 PRILAGAJANJE FUNKCIJ REKONSTRUIRANIM PORAZDELITVAM

Prilagajanje funkcij dobljenim porazdelitvam je bilo opravljeno znotraj programskega orodja RooFit [52], ki za prilagajanje uporablja metodo največje zanesljivosti. Naj bo $P(X|\alpha)$ verjetnost, da na danem dogodku izmerimo X (α je set parametrov, od katerih je odvisna P). V splošnem napravimo več meritev, rezultate zapišemo kot set X_i. Namen prilagajanja funkcije je pridobiti vrednost α, ki maksimizira L.

$$L = \prod_{i=1}^{N} P(X_i|\alpha). \tag{59}$$

Namesto da bi funkcijo prilagajali posebej za elektronski in za mionski kanal, prilagajano funkcijo združimo tako, da lahko za obe porazdelitvi funkcijo pri-

lagajamo istočasno. To nam omogoča zveza med presekom za produkcijo in količinami v posameznih kanalih:

$$\sigma_{\text{prod}}\,\text{Br}(X(3872)\to J/\psi\pi^+\pi^-) = \frac{N_{ee}}{\mathcal{L}\,\text{Br}(J/\psi\to e^+e^-)\,\varepsilon_{ee}} = \frac{N_{\mu\mu}}{\mathcal{L}\,\text{Br}(J/\psi\to \mu^+\mu^-)\,\varepsilon_{\mu\mu}}. \tag{60}$$

Signalni del opišemo s tremi Gaussovimi funkcijami: m_{0i} in σ_i predstavljajo centralno vrednosti in varianco, f_i pa predstavljajo delež dogodkov, ki jih opiše i-ta Gaussova porazdelitev.

$$\text{S} = \text{N}_{\text{sig}}\left(\text{f}_1\,\text{G}_1(\Delta\text{m}_{01},\sigma_1) + \text{f}_2\,\text{G}_2(\Delta\text{m}_{02},\sigma_2) + (1-\text{f}_1-\text{f}_2)\,\text{G}_3(\Delta\text{m}_{03},\sigma_3)\right), \tag{61}$$

Za opis ozadja uporabimo polinome Čebiševa:

$$\begin{aligned}
T_0(x) &= 1\\
T_1(x) &= 2x\\
T_2(x) &= 4x^2-1\\
T_3(x) &= 8x^3-4x\\
T_4(x) &= 16x^4-12x^2+1\\
T_5(x) &= 32x^5-32x^3+6x.
\end{aligned}$$

RooFit v procesu prilagajanja funkcije podatkom vsakemu polinomu pripiše koeficient; funkcijo, ki opisuje ozadje, torej opišemo kot $N_{bkg} = \sum_i \alpha_i T_i$. Koeficienti α_i so definirani v intervalu [-1,1]. Za opis ozadja v pričujoči analizi zadostuje uporaba polinomov tretje stopnje.
Signalno MC simulacijo uporabimo za fiksiranje parametrov funkcije za opis signala. Fiksiramo srednje vrednosti in odklone Gaussovih funkcij; kot prosti parametri prilagajane funkcije ostanejo koeficienti Čebiševih polinomov, število dogodkov v ozadju ter $\sigma_{prod}Br$. Primer takšnega prilagajanja prikazuje slika 83.

Primerjava preštetih dogodkov in rezultatov prilagajanja pokaže, da se razlikujeta v okviru nenatančnosti 1σ, kar je vidno tudi na sliki. Za namene tega povzetka navajamo zgolj rezultat za rekonstrukcijo $\psi(2S)$ na vzorcu $\Upsilon(4S)$(glej sliko 84), a trditev velja tudi za vse ostale vzorce.

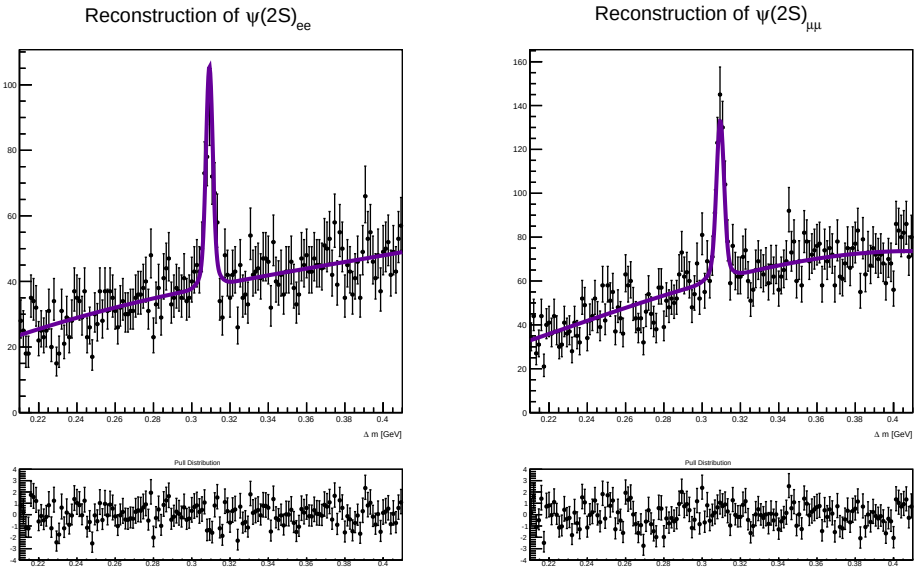

Slika 83: Primer prilagajanja funkcije podatkom. Točke so rezultat rekonstrukcije, vijolična črta kaže rezultat prilagajanja funkcije. Primer je vzet iz rekonstrukcije $\psi\,(2S)$.

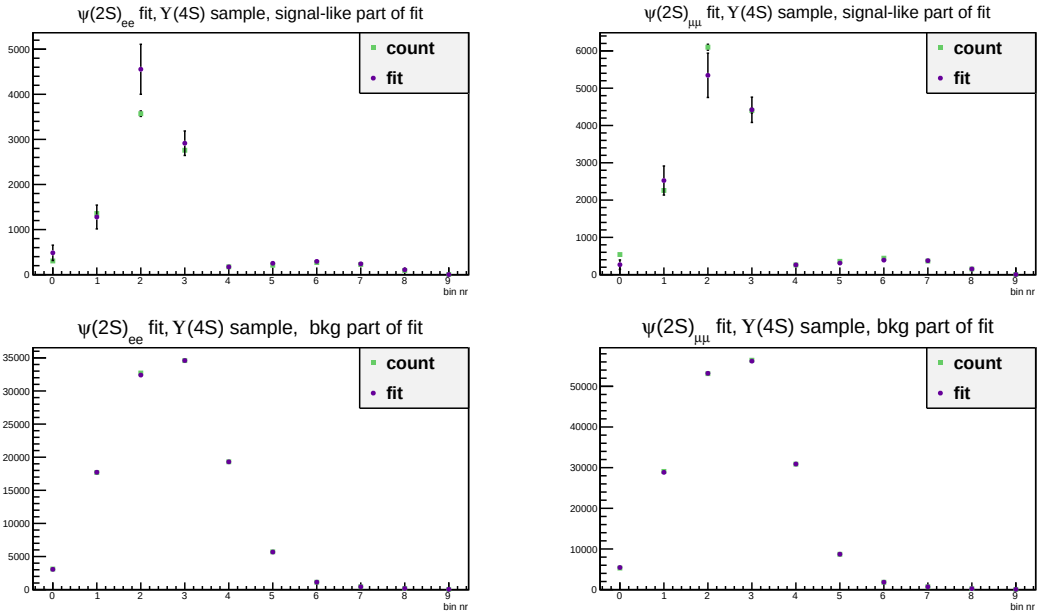

Slika 84: Rezultati prilagajanja funkcije dobljenim podatkom. Rekonstrukcija $\psi\,(2S)$ v vzorcu $\Upsilon\,(4S)$.

8.5 REKONSTRUKCIJA NA PRAVIH PODATKIH

Rekonstrukcijski postopek na pravih podatkih ostaja enak kot na simulaciji MC. Vsi rezi ostajajo enaki, tudi izbor najboljšega kandidata ostaja enak. Na sliki 85 lahko vidimo primerjavo med rekonstrukcijo $\psi(2S)$ na vzorcu $\Upsilon(4S)$ za simulacijo MC in za pogon na pravih podatkih. Neujemanje ozadja je posledica nezadovoljivega opisa gibalne količine J/ψ v simulaciji MC. Slika 86 pojasnjuje prejšnjo trditev - tokrat je primerjava med pravimi podatki in simulacijo MC narejena v izven signalnega okna J/ψ, torej na podatkih, kjer je pravi J/ψ večinoma izločen. V takem vzorcu se rekonstrukciji na pravih podatkih in na simulaciji MC ujemata izven signalnega okna (torej v pričakovanem ozadju za rekonstruirani signal). Tudi prilagajana funkcija ostaja enaka kot v primeru prilagajanja

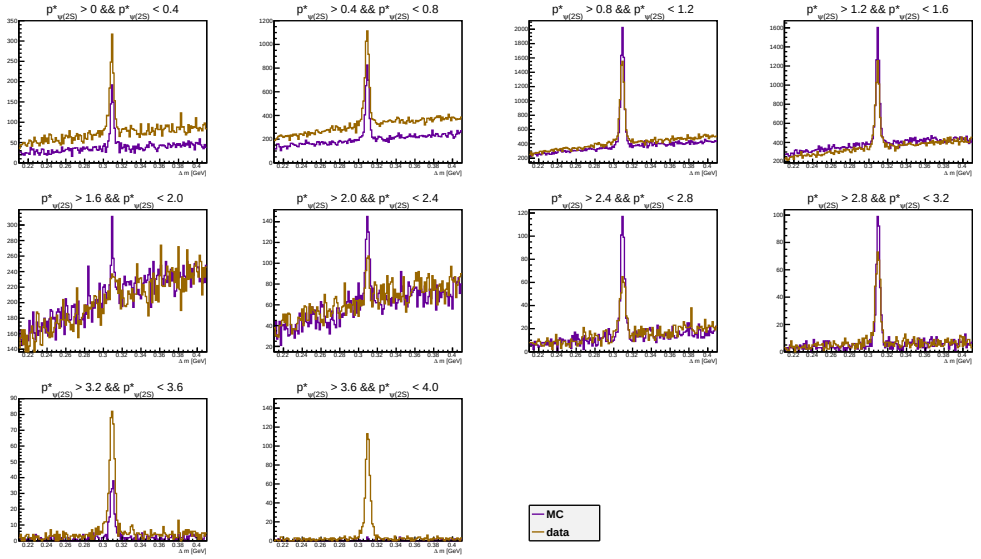

Slika 85: Primerjava med pravimi podatki (zlata) in simulacijo MC (vijolična). Rekonstrukcija $\psi(2S)$ na vzorcu $\Upsilon(4S)$.

podatkom iz simulacije MC. Rezultate prilagajanja prikazuje slika 87. Medtem ko za $\psi(2S)$ lahko podamo vrednost $\sigma_{prod}Br$ za vsak razdelek v gibalni kolicini, to za X(3872) ni mogoče in kot rezultat kasneje navedemo zgornjo mejo ob intervalu zanesljivosti 90%.

8.5.1 *Meritev razvejitvenega razmerja* $Br(B \to \psi(2S) + karkoli)$

Ker je bila meritev σBr narejena tako na vzorcu kontinua kot tudi na vzorcu $\Upsilon(4S)$, lahko izmerimo vrednost $Br \to \psi(2S)$ + karkoli. Medtem ko vzorec $\Upsilon(4S)$ vsebuje tudi $\psi(2S)$, ki izvirajo iz razpadov mezonov B, vzorec kontinua vsebuje zgolj $\psi(2S)$ iz takojšnje produkcije. Pod kinematsko mejo za $\psi(2S)$ iz razpadov mezonov B (1.6 GeV) tako lahko določimo vrednost razvejitvenega razmerja kot

$$\mathrm{Br}(B \to \psi(2S)\ \mathrm{karkoli}) = \frac{N_{ee,\,\Upsilon(4S)} - \frac{\mathcal{L}_{\Upsilon(4S)}}{\mathcal{L}_{cont}} N_{ee,\,\mathrm{continuum}}}{2\ N_{B\overline{B}}\ \varepsilon_{ee}\ \mathrm{Br}(\psi(2S) \to J/\psi\pi^+\pi^-)\ \mathrm{Br}(J/\psi \to e^+e^-)} \quad (62)$$

	elektronski kanal	mionski kanal
s	1.2677 ± 0.0257	1.0558 ± 0.0162
δm	$(-3.2583 \pm 0.4425)\ 10^{-4}$ GeV	$(-4.6269 \pm 0.3213)\ 10^{-4}$ GeV

Tabela 38: Rezultati spremenjene parametrizacije.

oziroma ekvivalentno za mionski kanal.
V okviru rekonstrukcije je potrebno upostevati še dva korekcijska faktorja. Prvi izvira iz razlike med sprejemnostjo za simulacijo MC in podatke pri identifikaciji nabitih sledi. Tako leptonske sledi utežimo s faktorjem 0.97 ± 0.017, pionske pa s faktorjem 1.00 ± 0.012. Drugi popravek sledi v parametrizaciji prilagajane funkcije. Tako zaradi razlik resolucije na MC in pravih podatkih dovolimo, da se središčna vrednost dveh Gaussovih krivulj premika za δm, medtem ko za spremembo širine Gaussovih krivulj dovolimo faktor s. Novo parametrizacijo preizkusimo na vzorcu $\Upsilon(4S)$, za prilagajanje podatkom kontinua pa vzamemo kar dobljene δm in s. Rezultate nove parametrizacije podajamo v tabeli 38, slika 88 kaže rezultate prilagajanja. Tudi prilagajanje samo je rahlo spremenjeno - namesto hkratnega prilagajanja uporabimo prilagajanje, ki ima za rezultat število signalnih dogodkov v vsakem kanalu posebej.

Izračun preko enačbe 62 daje

$$\begin{aligned} BR_{\text{elec}} &= (2.683 \pm 0.052)\ 10^{-3} \\ BR_{\text{muon}} &= (2.954 \pm 0.041)\ 10^{-3}, \end{aligned} \tag{63}$$

kjer je nezanesljivost zgolj statistična.

8.5.2 *Meritev razvejitvenega razmerja $Br(B \to X(3872) + karkoli) \times Br(X(3872) \to J/\psi\pi^+\pi^-)$*

Podobno kot za $\psi(2S)$ lahko tudi za X(3872) izvedemo meritev $\text{Br}(B \to X(3872) + \text{karkoli}) \times \text{Br}(X(3872) \to J/\psi\pi^+\pi^-)$. Kinematska meja za X(3872) iz mezonov B je 1.45 GeV. Korekcijski faktorji zaradi različne sprejemnosti so uporabljeni enako kot pri $\psi(2S)$, za prilagajanje funkcije pa vzamemo kar vrednosti δm in σ, dobljene pri obravnavi $\psi(2S)$. Rezultat računa je tako:

$$\begin{aligned} BR_{\text{elec}} &= (2.629 \pm 0.595)\ 10^{-5} \\ BR_{\text{muon}} &= (2.865 \pm 0.460)\ 10^{-5}, \end{aligned} \tag{64}$$

napaka je zgolj statisticna.

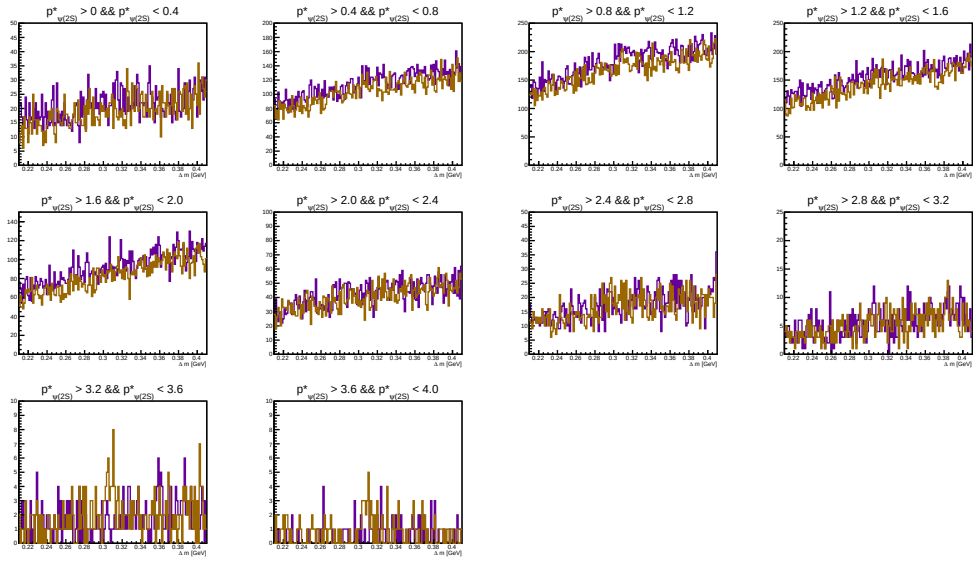

Slika 86: Primerjava med pravimi podatki (zlata) in simulacijo MC (vijolična) za dogodke izven signalnega okna J/ψ. Rekonstrukcija $\psi\,(2S)$ na vzorcu $\Upsilon\,(4S)$.

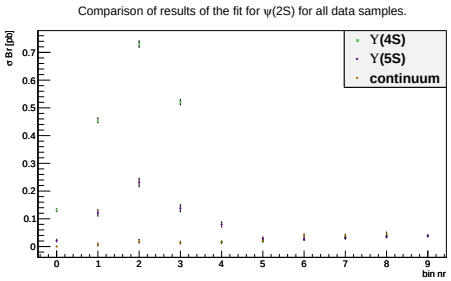

(a) $\psi\,(2S)$, vsi vzorci podatkov.

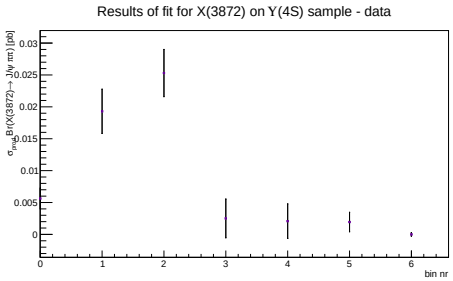

(b) X(3872), rezultati za $\Upsilon\,(4S)$.

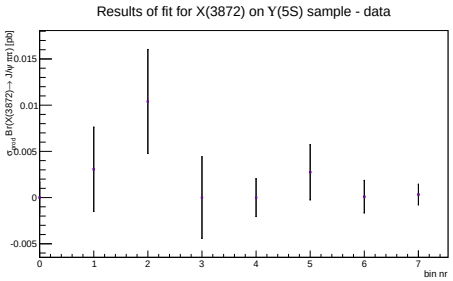

(c) X(3872), rezultati za $\Upsilon\,(5S)$.

Slika 87: Rezultati prilagajanja funkcije podatkom za različne rekonstruirane delce in različne vzorce podatkov.

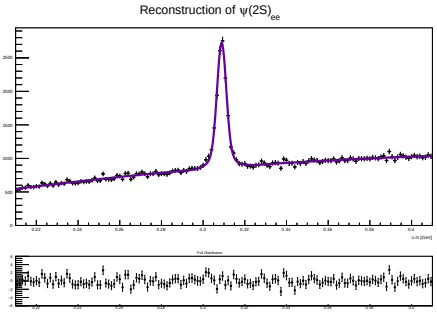

(a) $\psi\,(2S)_{ee}$, vzorec $\Upsilon\,(4S)$.

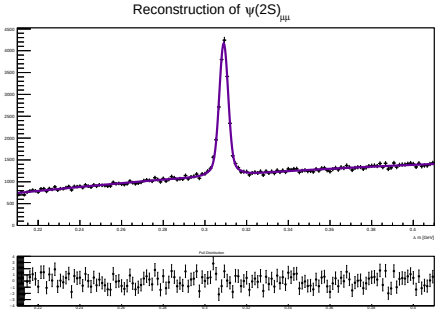

(b) $\psi\,(2S)_{\mu\mu}$, vzorec $\Upsilon\,(4S)$.

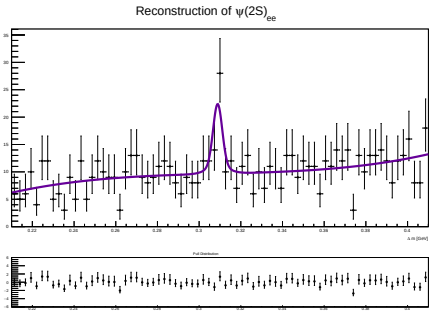

(c) $\psi\,(2S)_{ee}$, vzorec kontinua.

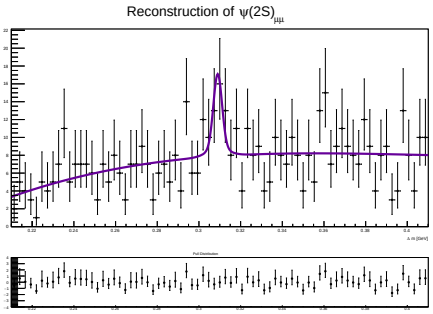

(d) $\psi\,(2S)_{\mu\mu}$, vzorec kontinua.

Slika 88: Rezultati prilagajanja funkcije za $p^*_{\psi(2S)} < 1.6$ GeV.

8.6 SISTEMATSKA NEZANESLJIVOST

V okviru dolocanja sistematske nezanesljivosti je bilo določenih pet izvorov nezanesljivosti:

- razlika v sprejemnosti zaradi identifikacije na pravih podatkih in na simulaciji MC,
- razlika v učinkovitosti določanja sledi pri MC simulaciji in pri podatkih,
- negotovost v stevilu zaznanih mezonov B,
- napaka v uporabljenih razvejitvenih razmerjih,
- napaka v sprejemnosti zaradi končne velikosti vzorca, uporabljenega za določitev sprejemnosti.

Tabela 39 podaja vrednosti za prve štiri navedene napake, medtem ko se tabeli 40 in 41 osredotočata na zadnji navedeni vir napake, napake sprejemnosti.

Identifikacija	mioni	3.4%
	elektroni	3.4%
	pioni	2.4%
Učinkovitost določanja sledi		1.4 %
Sekundarni BR	$J/\psi \to e^+e^-$	0.54 %
	$J/\psi \to \mu^+\mu^-$	0.55 %
	$\psi(2S) \to J/\psi\pi\pi$	0.87 %
Število parov B mezonov		1.4%

Tabela 39: Prispevki k sistematskim napakam.

	$\Upsilon(4S)$			$\Upsilon(5S)$			kont.		
st razdelka	ee	$\mu\mu$	skupaj	ee	$\mu\mu$	skupaj	ee	$\mu\mu$	skupaj
0	0.067	0.060	0.045	0.158	0.114	0.093	0.515	0.409	0.320
1	0.200	0.153	0.122	0.082	0.067	0.052	0.237	0.236	0.167
2	0.125	0.111	0.083	0.056	0.049	0.037	0.162	0.150	0.110
3	0.089	0.077	0.058	0.045	0.036	0.028	0.126	0.101	0.079
4	0.070	0.056	0.044	0.041	0.028	0.023	0.096	0.079	0.061
5	0.052	0.048	0.035	0.031	0.027	0.021	0.087	0.071	0.055
6	0.045	0.044	0.032	0.026	0.024	0.018	0.080	0.067	0.051
7	0.042	0.035	0.027	0.025	0.022	0.017	0.102	0.082	0.064
8	0.037	0.031	0.024	0.037	0.030	0.023	0.151	0.150	0.106
9	0.042	0.041	0.029	0.079	0.071	0.053	0.652	0.117	0.115

Tabela 40: Relativna negotovost sprejemnosti za razdelke v p^* za rekonstrukcijo $\psi(2S)$ v različnih vzorcih. *ee* zaznamuje elektronski kanal, $\mu\mu$ mionski kanal. Skupni rezultat je uporabljen v vseh primerih, kjer je bilo uporabljen hkratno prilagajanje.

	$\Upsilon(4S)$			$\Upsilon(5S)$		
	ee	$\mu\mu$	skupaj	ee	$\mu\mu$	skupaj
0	0.623	0.609	0.435	0.084	0.063	0.051
1	0.449	0.220	0.198	0.049	0.034	0.028
2	0.212	0.136	0.114	0.040	0.024	0.021
3	0.152	0.107	0.087	0.030	0.020	0.016
4	0.124	0.094	0.075	0.020	0.015	0.012
5	0.110	0.081	0.065	0.019	0.015	0.012
6	0.092	0.072	0.057	0.019	0.015	0.012
7	0.089	0.069	0.055	0.018	0.015	0.012
8	0.084	0.064	0.051	0.026	0.020	0.016
9	0.114	0.092	0.072	0.085	0.067	0.053

Tabela 41: Relativna negotovost sprejemnosti za razdelke v p^* za rekonstrukcijo X(3872) v različnih vzorcih. *ee* zaznamuje elektronski kanal, $\mu\mu$ mionski kanal. Skupni rezultat je uporabljen v vseh primerih, kjer je bilo uporabljen hkratno prilagajanje.

8.7 KONČNI REZULTATI

Z dodajanjem sistematske napake in oceno zgornje meje, kjer prilagajanje funkcije ni dalo od nič razlicnega rezultata, lahko navedemo končne rezultate te analize.

8.7.1 $Br(B \to \psi(2S) + karkoli)$

Ko združimo oba rekonstrukcijska kanala in upoštevamo propagacijo napake, lahko rezultat zapišemo kot:

$$\mathrm{Br}(\mathrm{B} \to \psi(2S) + \mathrm{karkoli}) = (2.817 \pm 0.032 \pm 0.104)\ 10^{-3},$$

kar je v skladu z rezultatom, ki je naveden v PDG [11]: $(3.07 \pm 0.21)\ 10^{-3}$. Rezultat je pomemben test smiselnosti analize in daje težo vsem nadaljnim rezultatom.

8.7.2 $Br(B \to X(3872) + karkoli) \times Br(X(3872) \to J\psi\pi^+\pi^-)$

Ko združimo oba rekonstrukcijska kanala in upoštevamo propagacijo napake, lahko rezultat zapišemo kot:

$$\mathrm{Br}(B \to X(3872) + \mathrm{karkoli}) \times \mathrm{Br}(X(3872) \to J\psi\pi^+\pi^-) = (2.79 \pm 0.37 \pm 0.11)\ 10^{-5}.$$

Primerjava med prejšnjimi meritvami inkluzivnega razvejitvenega razmerja za razpade mezonov B v čarmonij je podana v tabeli 42; zadnja navedena vrednost je zgornji rezultat, kjer smo za $Br(X(3872) \to J/\psi\pi\pi)$ vzeli $(5.5 \pm 2.0)\%$ [55]. Večina prejsnjih meritev za inkluzivno razvejitveno razmerje $B \to$ čarmonij + karkoli podaja red velikosti 10^{-3}, nedavni preliminarni rezultat skupine Belle ravno tako poroča o red velikosti manjšem rezultatu za $B \to \chi_{c2}$ + karkoli.

8.7.3 *Produkcija* $\psi\,(2S)$

Tabele 43 - 45 podajajo rezultate meritve $\sigma_{e^+e^- \to \psi(2S)}\mathrm{Br}(\psi(2S) \to J/\psi\pi\pi)$ v razdelkih $p^*_{\psi(2S)}$ za razne vzorce.

razpadni kanal	PDG vrednost [11]	preliminarni rezultat Belle
$B \to J/\psi$+ karkoli	$(7.8 \pm 0.4)\ 10^{-3}$	
$B \to \psi(2S)$ + karkoli	$(3.07 \pm 0.21)\ 10^{-3}$	
$B \to \chi_{c1}(1P)$ + karkoli	$(3.24 \pm 0.25)\ 10^{-3}$	$(3.03 \pm 0.04 \pm 0.22)\ 10^{-3}$
$B \to \chi_{c2}(1P)$ + karkoli	$(1.65 \pm 0.31)\ 10^{-3}$	$(0.70 \pm 0.05 \pm 0.07)\ 10^{-3}$
$B \to X(3872)$ + karkoli	$(5.1 \pm 2.0)\ 10^{-4}$	$(0.51 \pm 0.2)\ 10^{-3}$

Tabela 42: Primerjava razvejitvenih razmerij za inkluzivne razpade mezonov B v čarmonij.

bin nr	σBr [pb]	$\sigma_{\text{stat.}}$ [pb]	$\sigma_{\text{sist.}}$[pb]
0	1.31E-001	4.75E-003	7.90E-003
1	4.55E-001	8.51E-003	5.84E-002
2	7.30E-001	1.14E-002	6.73E-002
3	5.21E-001	9.69E-003	3.70E-002
4	1.73E-002	3.76E-003	1.03E-003
5	1.86E-002	2.51E-003	9.96E-004
6	2.47E-002	1.69E-003	1.27E-003
7	3.09E-002	1.64E-003	1.50E-003
8	3.68E-002	1.68E-003	1.72E-003
9	3.86E-002	1.54E-003	1.93E-003

Tabela 43: Rezultati za produkcijo $\psi(2S)$ v $\Upsilon(4S)$ vzorcu. σBr marks $\sigma_{e^+e^-\to\psi(2S)\text{ karkoli}}\text{Br}(\psi(2S) \to J/\psi\pi\pi)$. Vse navedene vrednosti so v enotah pb.

bin nr	σBr [pb]	$\sigma_{\text{stat.}}$ [pb]	$\sigma_{\text{sist.}}$[pb]
0	2.16E-002	4.68E-003	2.18E-003
1	1.21E-001	1.12E-002	7.95E-003
2	2.31E-001	1.55E-002	1.27E-002
3	1.38E-001	1.29E-002	6.80E-003
4	7.98E-002	9.22E-003	3.72E-003
5	2.88E-002	5.87E-003	1.30E-003
6	2.70E-002	4.46E-003	1.20E-003
7	3.08E-002	4.03E-003	1.35E-003
8	3.54E-002	4.17E-003	1.65E-003
9	3.86E-002	4.10E-003	2.56E-003

Tabela 44: Rezultati za produkcijo $\psi(2S)$ v $\Upsilon(5S)$ vzorcu. σBr oznacuje $\sigma_{e^+e^-\to\psi(2S)\text{ + karkoli}}\text{Br}(\psi(2S) \to J/\psi\pi\pi)$. Vse navedene vrednosti so v enotah pb.

bin nr	σBr [pb]	$\sigma_{\text{stat.}}$ [pb]	$\sigma_{\text{sist.}}$[pb]
0	3.42E-005	1.89E-003	2.25E-005
1	6.91E-003	5.15E-003	2.34E-003
2	1.91E-002	6.31E-003	4.32E-003
3	1.41E-002	5.01E-003	2.39E-003
4	1.52E-002	4.57E-003	2.04E-003
5	2.14E-002	4.84E-003	2.64E-003
6	4.00E-002	5.67E-003	4.65E-003
7	3.87E-002	5.74E-003	5.45E-003
8	4.63E-002	5.69E-003	1.01E-002
9	3.77E-002	4.54E-003	2.51E-002

Tabela 45: Rezultati za produkcijo $\psi(2S)$ v vzorcu kontinua. σBr oznacuje $\sigma_{e^+e^-\to\psi(2S)+\text{ karkoli}}\text{Br}(\psi(2S) \to J/\psi\pi\pi)$. Vse navedene vrednosti so v enotah pb.

Za vzorec kontinua lahko navedemo tudi rezultat za $\sigma_{e^+e^-\to\psi(2S)\text{ + karkoli}}$, če za $\text{Br}(\psi(2S) \to J/\psi\pi\pi)$ uporabimo 0.3445 :

$$\sigma_{e^+e^-\to\psi(2S)\text{ + karkoli}} = (0.694 \pm 0.046 \pm 0.083)\text{ pb}$$

8.7.4 *Produkcija X(3872)*

Tabele 46 - 48 podajajo rezultate meritve $\sigma_{e^+e^-\to X(3872)}\text{Br}(X(3872) \to J/\psi\pi\pi)$ v razdelkih p^*_X za razne vzorce.

bin nr	σBr [pb]	$\sigma_{\text{stat.}}$ [pb]	$\sigma_{\text{sist.}}$[pb]	zgornja meja (zgolj stat.)
0	5.63E-003	1.70E-003	2.46E-003	
1	1.93E-002	3.47E-003	3.89E-003	
2	2.53E-002	3.70E-003	3.06E-003	
3	2.51E-003	3.04E-003		7.12E-003
4	2.08E-003	2.71E-003		6.12E-003
5	1.94E-003	1.52E-003		3.71E-003
6	3.88E-022	2.82E-004		8.74E-004

Tabela 46: Rezultati za produkcijo X(3872) v $\Upsilon(4S)$ vzorcu. σBr oznacuje $\sigma_{e^+e^-\to X(3872)\text{ karkoli}}\text{Br}(X(3872) \to J/\psi\pi\pi)$. Vse navedene vrednosti so v enotah pb. Kjer je bil rezultat prilagajanja konsistenten z 0, je navedena zgornja meja (zgolj stat.) za interval zaupanja 90%.

bin nr	σBr [pb]	$\sigma_{\text{stat.}}$ [pb]	$\sigma_{\text{sist.}}$[pb]	zgornja meja (zgolj stat.)
0	1.28E-007	1.68E-003		3.51E-003
1	3.06E-003	4.56E-003	1.48E-004	
2	1.04E-002	5.63E-003	4.64E-004	
3	3.17E-007	4.42E-003		7.93E-003
4	1.00E-007	2.05E-003		5.37E-003
5	2.74E-003	2.99E-003		7.45E-003
6	9.83E-005	1.76E-003		3.29E-003
7	3.31E-004	1.11E-003		2.22E-003

Tabela 47: Rezultati za produkcijo X(3872) v $\Upsilon(5S)$ vzorcu. σBr oznacuje $\sigma_{e^+e^-\to X(3872)\text{ karkoli}}\text{Br}(X(3872) \to J/\psi\pi\pi)$. Vse navedene vrednosti so v enotah pb. Kjer je bil rezultat prilagajanja konsistenten z 0, je navedena zgornja meja (zgolj stat.) za interval zaupanja 90%.

bin nr	σBr [pb]	$\sigma_{\text{stat.}}$ [pb]	$\sigma_{\text{sist.}}$[pb]	zgornja meja (zgolj stat.)
0	9.67E-004	4.45-003		8.52E-003

Tabela 48: Rezultati za produkcijo X(3872) v vzorcu kontinua. σBr oznacuje $\sigma_{e^+e^-\to X(3872)\text{ karkoli}}\text{Br}(X(3872) \to J/\psi\pi\pi)$. Vse navedene vrednosti so v enotah pb. Ker je bil rezultat prilagajanja konsistenten z 0, je navedena zgornja meja (zgolj stat.) za interval zaupanja 90%..

BIBLIOGRAPHY

[1] S.-K. Choi, S. L. Olsen, et al. Observation of a narrow charmoniumlike state in exclusive $B^{\pm} \to K^{\pm}\pi^{+}\pi^{-}J/\psi$ decays. *Phys. Rev. Lett.*, 91:262001, Dec 2003. doi: 10.1103/PhysRevLett.91.262001. URL http://link.aps.org/doi/10.1103/PhysRevLett.91.262001. (Cited on pages xviii, 1, 14, 15, and 16.)

[2] B. Aubert et al. Study of the $B^{-} \to J/\psi K^{-}\pi^{+}\pi^{-}$ decay and measurement of the $B^{-} \to X(3872)K^{-}$ branching fraction. *Phys. Rev. D*, 71:071103, Apr 2005. doi: 10.1103/PhysRevD.71.071103. URL http://link.aps.org/doi/10.1103/PhysRevD.71.071103. (Cited on pages 1 and 119.)

[3] D. Acosta et al. Observation of the narrow state $X(3872) \to J/\psi\pi^{+}\pi^{-}$ in $\overline{p}p$ collisions at $\sqrt{s} = 1.96$ TeV. *Phys. Rev. Lett.*, 93:072001, Aug 2004. doi: 10.1103/PhysRevLett.93.072001. URL http://link.aps.org/doi/10.1103/PhysRevLett.93.072001. (Cited on pages 1 and 119.)

[4] V. M. Abazov et al. Observation and properties of the $X(3872)$ decaying to $J/\psi\pi^{+}\pi^{-}$ in $p\overline{p}$ collisions at $\sqrt{s} = 1.96$ TeV. *Phys. Rev. Lett.*, 93:162002, Oct 2004. doi: 10.1103/PhysRevLett.93.162002. URL http://link.aps.org/doi/10.1103/PhysRevLett.93.162002. (Cited on pages 1 and 119.)

[5] URL http://inspirehep.net/. (Cited on page 1.)

[6] J. Chadwick. Possible existence of a neutron. *Nature*, 129:312, 1932. doi: 10.1038/129312a0. (Cited on page 1.)

[7] H. Yukawa. On the interaction of elementary particles. *Proc.Phys.Math.Soc.Jap.*, 17:48–57, 1935. (Cited on page 1.)

[8] C. M. G. Lattes, H. Muirhead, G. P. S. Occhialini, and C. F. Powell. Processes involving charged mesons. *Nature*, 159:694–697, may 1947. doi: 10.1038/159694a0. (Cited on page 2.)

[9] G. Zweig. An SU(3) model for strong interaction symmetry and its breaking. version 1. 1964. (Cited on page 2.)

[10] M. Gell-Mann. A schematic model of baryons and mesons. *Phys.Lett.*, 8: 214–215, 1964. doi: 10.1016/S0031-9163(64)92001-3. (Cited on page 2.)

[11] K.A. Olive et al. *Chin. Phys. C*, 38:090001, 2014. (Cited on pages xxiii, xxiv, xxv, 3, 14, 51, 87, 110, 113, 114, and 137.)

[12] S. L. Glashow, J. Iliopoulos, and L. Maiani. Weak interactions with lepton-hadron symmetry. *Phys. Rev. D*, 2:1285–1292, Oct 1970. doi: 10.1103/

PhysRevD.2.1285. URL http://link.aps.org/doi/10.1103/PhysRevD.2.1285. (Cited on page 3.)

[13] J.E. Augustin et al. Discovery of a narrow resonance in e^+e^- annihilation. *Phys.Rev.Lett.*, 33:1406–1408, 1974. doi: 10.1103/PhysRevLett.33.1406. (Cited on page 3.)

[14] J.J. Aubert et al. Experimental observation of a heavy particle J. *Phys.Rev.Lett.*, 33:1404–1406, 1974. doi: 10.1103/PhysRevLett.33.1404. (Cited on page 3.)

[15] A.J. Bevan et al. The physics of the B factories. *Eur.Phys.J.*, C74(11):3026, 2014. doi: 10.1140/epjc/s10052-014-3026-9. (Cited on pages xvii, xviii, 4, 6, 11, and 16.)

[16] S. Okubo. φ-meson and unitary symmetry model. *Physics Letters*, 5 (2):165 – 168, 1963. ISSN 0031-9163. doi: http://dx.doi.org/10.1016/S0375-9601(63)92548-9. URL http://www.sciencedirect.com/science/article/pii/S0375960163925489. (Cited on page 6.)

[17] G. Zweig. *CERN Report*, No.8419/TH412, 1964. (Cited on page 6.)

[18] J. Iizuka. Systematics and phenomenology of meson family. *Prog.Theor.Phys.Suppl.*, 37:21–34, 1966. doi: 10.1143/PTPS.37.21. (Cited on page 6.)

[19] P. Artoisenet. Charmonium production at B-factories, unknown source. (Cited on page 11.)

[20] G. T. Bodwin. Theory of charmonium production. 2012. (Cited on page 12.)

[21] P. Pakhlov et al. Measurement of the $e^+e^- \to J/\psi c\bar{c}$ cross section at $\sqrt{s} \approx 10.6$ GeV. *Phys. Rev. D*, 79:071101, Apr 2009. doi: 10.1103/PhysRevD.79.071101. URL http://link.aps.org/doi/10.1103/PhysRevD.79.071101. (Cited on pages xviii, xix, xxiii, xxiv, xxvi, 12, 14, 24, 25, 26, 121, and 122.)

[22] M. Butenschoen and B. A. Kniehl. World data of J/ψ production consolidate nonrelativistic QCD factorization at next-to-leading order. *Phys. Rev. D*, 84:051501, Sep 2011. doi: 10.1103/PhysRevD.84.051501. URL http://link.aps.org/doi/10.1103/PhysRevD.84.051501. (Cited on pages xviii, 12, 13, and 121.)

[23] Y.-J. Zhang, Y.-Q. Ma, K. Wang, and K.-T. Chao. QCD radiative correction to color-octet J/ψ inclusive production at B factories. *Phys. Rev. D*, 81:034015, Feb 2010. doi: 10.1103/PhysRevD.81.034015. URL http://link.aps.org/doi/10.1103/PhysRevD.81.034015. (Cited on pages 12 and 121.)

[24] D. Acosta. Measurement of the J/ψ meson and B-hadron production cross sections in $p\bar{p}$ collisions at $\sqrt{s} = 1960$ GeV. *Phys. Rev. D*, 71:032001, Feb 2005. doi: 10.1103/PhysRevD.71.032001. URL http://link.aps.org/doi/10.1103/PhysRevD.71.032001. (Cited on pages xviii and 13.)

[25] E. Braaten and J. Lee. Exclusive double charmonium production from e^+e^- annihilation into a virtual photon. *Phys.Rev.*, D67:054007, 2003. (Cited on pages xxiii, 13, 14, and 121.)

[26] K. Abe et al. Evidence for $X(3872) \to \gamma J/\psi$ and the sub-threshold decay $X(3872) \to \omega J/\psi$. 2005. (Cited on pages 17, 23, and 119.)

[27] B. Aubert et al. Search for $B^+ \to X(3872)K^+, X(3872) \to J/\psi\gamma$. *Phys.Rev.*, D74:071101, 2006. doi: 10.1103/PhysRevD.74.071101. (Cited on pages 17 and 119.)

[28] R. Aaij et al. Determination of the $X(3872)$ meson quantum numbers. *Phys. Rev. Lett.*, 110:222001, May 2013. doi: 10.1103/PhysRevLett.110.222001. URL http://link.aps.org/doi/10.1103/PhysRevLett.110.222001. (Cited on pages xviii, 17, 19, 20, 21, and 120.)

[29] A. Abulencia et al. Measurement of the dipion mass spectrum in $X(3872) \to J/\psi\pi^+\pi^-$ decays. *Phys. Rev. Lett.*, 96:102002, Mar 2006. doi: 10.1103/PhysRevLett.96.102002. URL http://link.aps.org/doi/10.1103/PhysRevLett.96.102002. (Cited on pages xviii, 17, 18, 120, and 126.)

[30] S.-K. Choi et al. Bounds on the width, mass difference and other properties of $X(3872) \to \pi^+\pi^- J/\psi$ decays. *Phys. Rev. D*, 84:052004, Sep 2011. doi: 10.1103/PhysRevD.84.052004. URL http://link.aps.org/doi/10.1103/PhysRevD.84.052004. (Cited on pages 17, 19, 22, 23, and 120.)

[31] S. Prelovsek and L. Leskovec. Evidence for $X(3872)$ from DD^* scattering on the lattice. *Phys. Rev. Lett.*, 111:192001, Nov 2013. doi: 10.1103/PhysRevLett.111.192001. URL http://link.aps.org/doi/10.1103/PhysRevLett.111.192001. (Cited on page 19.)

[32] G. Gokhroo et al. Observation of a near-threshold $D^0\overline{D}^0\pi^0$ enhancement in $B \to D^0\overline{D}^0\pi^0 K$ decay. *Phys.Rev.Lett.*, 97:162002, 2006. doi: 10.1103/PhysRevLett.97.162002. (Cited on page 22.)

[33] B. Aubert et al. Study of resonances in exclusive B decays to $\overline{D}^* D^* K$. *Phys.Rev.*, D77:011102, 2008. doi: 10.1103/PhysRevD.77.011102. (Cited on pages 22 and 120.)

[34] T. Aushev et al. Study of the $B \to X(3872)(D^{*0}\overline{D^0}K)$ decay. *Phys.Rev.*, D81:031103, 2010. doi: 10.1103/PhysRevD.81.031103. (Cited on pages 22, 23, and 120.)

[35] L. Maiani, F. Piccinini, A.D. Polosa, and V. Riquer. Diquark-antidiquarks with hidden or open charm and the nature of $X(3872)$. *Phys.Rev.*, D71:014028, 2005. doi: 10.1103/PhysRevD.71.014028. (Cited on pages 22 and 120.)

[36] T. Aaltonen et al. Precision measurement of the $X(3872)$ mass in $J/\psi\pi^+\pi^-$ decays. *Phys.Rev.Lett.*, 103:152001, 2009. doi: 10.1103/PhysRevLett.103.152001. (Cited on page 22.)

[37] B. Aubert et al. A study of $B \to X(3872)K$, with $X(3872) \to J/\psi\pi^+\pi^-$. *Phys.Rev.*, D77:111101, 2008. doi: 10.1103/PhysRevD.77.111101. (Cited on pages 22 and 120.)

[38] R. Aaij et al. Evidence for the decay $X(3872) \to \psi(2S)\gamma$. *Nucl.Phys.*, B886: 665–680, 2014. doi: 10.1016/j.nuclphysb.2014.06.011. (Cited on page 23.)

[39] P. del Amo Sanchez et al. Evidence for the decay $X(3872) \to J/\psi\omega$. *Phys.Rev.*, D82:011101, 2010. doi: 10.1103/PhysRevD.82.011101. (Cited on page 23.)

[40] V. Bhardwaj et al. Observation of $X(3872)$ to $J/\psi\gamma$ and search for $X(3872)$ to $\psi'\gamma$ in B decays. *Phys.Rev.Lett.*, 107:091803, 2011. doi: 10.1103/PhysRevLett.107.091803. (Cited on page 23.)

[41] S. Chatrchyan et al. Measurement of the X(3872) production cross section via decays to $J/\psi\pi\pi$ in pp collisions at $\sqrt{s} = 7$ TeV. *JHEP*, 1304:154, 2013. doi: 10.1007/JHEP04(2013)154. (Cited on page 24.)

[42] A.V. Berezhnoy and A.K. Likhoded. Electroproduction and gluonic production of J/ψ mesons under the assumption of quark-hadron duality. *Physics of Atomic Nuclei*, 71(2):309–312, 2008. ISSN 1063-7788. doi: 10.1134/S1063778808020117. URL http://dx.doi.org/10.1134/S1063778808020117. (Cited on page 24.)

[43] S. Kurokawa and E. Kikutani. Overview of the KEKB accelerators. *Nucl. Instrum. Methods Phys. Res. A*, 499:1 – 7, 2003. (Cited on page 29.)

[44] A. Abashian et al. The Belle detector. *Nuclear Instruments and Methods in Physics Research Section A: Accelerators, Spectrometers, Detectors and Associated Equipment*, 479(1):117 – 232, 2002. ISSN 0168-9002. doi: http://dx.doi.org/10.1016/S0168-9002(01)02013-7. URL http://www.sciencedirect.com/science/article/pii/S0168900201020137. Detectors for Asymmetric B-factories. (Cited on pages xix, xxiii, 29, 32, 33, 34, 35, 36, 37, 38, 39, 40, 41, 42, and 124.)

[45] Z. Natkaniec, H. Aihara, Y. Asano, T. Aso, A. Bakich, et al. Status of the Belle silicon vertex detector. *Nucl.Instrum.Meth.*, A560:1–4, 2006. doi: 10.1016/j.nima.2005.11.228. (Cited on page 29.)

[46] D. J. Lange. The EvtGen particle decay simulation package. *Nucl. Instrum. Methods Phys. Res. A*, 462:152 – 155, 2001. (Cited on page 44.)

[47] Torbjorn Sjostrand, Stephen Mrenna, and Peter Z. Skands. A Brief Introduction to PYTHIA 8.1. *Comput.Phys.Commun.*, 178:852–867, 2008. doi: 10.1016/j.cpc.2008.01.036. (Cited on page 44.)

[48] R. Brun. Geant3. 1987. (Cited on page 44.)

[49] R. Brun and F. Rademakers. ROOT - An object oriented data analysis framework. *Nuclear Instruments and Methods in Physics Research Section A: Accelerators, Spectrometers, Detectors and Associated Equipment*, 389 (1â2):81 – 86, 1997. ISSN 0168-9002. doi: http://dx.doi.org/10.1016/S0168-9002(97)00048-X. URL http://www.sciencedirect.com/science/article/pii/S016890029700048X. New Computing Techniques in Physics Research V. (Cited on pages 45 and 116.)

[50] C.-Z. Yuan. Exotic hadron. 2009. (Cited on pages 51 and 126.)

[51] K. Abe et al. Measurement of inclusive production of neutral pions from $v(4S)$ decays. *Phys. Rev. D*, 64:072001, Sep 2001. doi: 10.1103/PhysRevD.64.072001. URL http://link.aps.org/doi/10.1103/PhysRevD.64.072001. (Cited on pages xxiv and 55.)

[52] W. Verkerke and K. Kirkby. The RooFit toolkit for data modeling. 2003. (Cited on pages 71 and 128.)

[53] A. Bala, Bhardway V., K. Trabelsi, and J.B. Singh. Observation of X(3872) in $B \to X(3872)K\pi$ decays. 2015. (Cited on pages 105 and 109.)

[54] URL http://belle.kek.jp/secured/nbb/nbb.html. (Cited on page 110.)

[55] N. Drenska, R. Faccini, F. Piccinini, A. Polosa, F. Renga, et al. New hadronic spectroscopy. *Riv.Nuovo Cim.*, 33:633–712, 2010. doi: 10.1393/ncr/i2010-10059-8. (Cited on pages 113 and 137.)